SYNTHESIS OF HYBRID NANOPARTICLES WITH COMBINED MAGNETO-PHOTOTHERMAL EFFECT FOR MEDICAL APPLICATIONS

Nina Kostevšek

Doctoral Dissertation
Jožef Stefan International Postgraduate School
Ljubljana, Slovenia

Supervisor: Asst. Prof. Dr. Kristina Žužek Rožman, Jožef Stefan Institute, Ljubljana, Slovenia

Evaluation Board:
Assoc. Prof. Dr. Sašo Šturm, Chair, Jožef Stefan International Postgraduate School and Jožef Stefan Institute, Ljubljana, Slovenia
Asst. Prof. Dr. Sašo Gyergyek, Member, Faculty of Chemistry and Chemical Engineering, University of Maribor, Slovenia
Asst. Prof. Dr. Goran Dražić, Member, Jožef Stefan International Postgraduate School and National institute of Chemistry, Ljubljana, Slovenia

MEDNARODNA PODIPLOMSKA ŠOLA JOŽEFA STEFANA
JOŽEF STEFAN INTERNATIONAL POSTGRADUATE SCHOOL



Nina Kostevšek

SYNTHESIS OF HYBRID NANOPARTICLES WITH COMBINED MAGNETO-PHOTOTHERMAL EFFECT FOR MEDICAL APPLICATIONS

Doctoral Dissertation

SINTEZA HIBRIDNIH NANODELCEV S KOMBINIRANIM MAGNETO-FOTOTERMIČNIM EFEKTOM ZA MEDICINSKE APLIKACIJE

Doktorska disertacija

Supervisor: Asst. Prof. Dr. Kristina Žužek Rožman

Ljubljana, Slovenia, October 2016

Acknowledgments

A PhD period is a special chapter in a life of each “scientist” when first real intellectual challenges are experienced. It is an individual research, however, there is always a group of people that importantly contribute to the PhD thesis and render possible its accomplishment. Therefore, I would like to use a few sentences to thank all of them who make my last four years memorable and helped me not only with my research but also to grow as a person.

Firstly, I would like to thank both supervisors, Asst. Prof. Kristina Žužek Rožman and Prof. Dr. Spomenka Kobe, for introducing me the world of nanotechnology and nanomaterials. It is already more than six years since I started working at the Department for Nanostructured Materials, first as an undergraduate student of chemistry and later as a PhD student, but I am still fascinated everyday by all the possibilities that a “nanoworld” can offer. Thank you for giving me the opportunity to work with you and to supporting and encouraging me to go abroad!

I would especially like to thank Asst. Prof. Kristina Žužek Rožman for always being supportive and encouraging. But the most I appreciate her fast response and efficacy when needed, eagerness to learn new topics with me and to be scientifically exact that motivated us all to achieve more than we otherwise would.

I would like to thank both, Prof. Dr. Sašo Šturm and Asst. Prof. Kristina Žužek Rožman, to influencing the development of my personality in a way of becoming a more independent person, who is not afraid to think out of the box, and for giving me the opportunity to work on different projects from the scratch till the end. Thank you for the numerous fruitful discussions that we had! No matter what problem, Sašo is a person that always sees a broader picture and has great suggestions. Sašo, thank you also for great microscopy work that contributed crucial results to my PhD work.

Special thanks go also to Prof. Dr. Mauro Comes Franchini from the Department of Industrial Chemistry "Toso Montanari”, University of Bologna, for giving me the opportunity to work with them. Mauro, Erica and Ilaria really did their best to teach me as much as possible in only 4 months. Although we were working on a different topic that was not related to my PhD thesis, I have gained there valuable knowledge in the field of nanomaterials and nanomedicine.

There were many other people that helped me during my PhD work. Thanks to Dr. Muhammad Shahid Arshad for a very helpful discussion on magnetic interactions and extremely important simulation work, Dr. Maarten Bloemen (Department of Chemistry, KU Leuven, Belgium) for the preparation of ZDS ligand and functionalization of FePt NPs, Prof. Dr. Igor Serša and Ana Sepe for MRI measurements, Prof. Dr. Zvonko Jagličić for the SQUID measurements, Dr. Kristina Žagar for the TEM lessons, Dr. Janez

Zavašnik for all the help with the microscopy, Dr. Matjaž Spreitzer for the photo-thermal experiments and Asst. Prof. Dr. Paul McGuiness for proofreading English in my articles. I have to mention the entire magnetic group from which I got many valuable comments and advice on every meeting. Thank you all for helping me with the instrumentation and for making the mystery of magnetism more understandable. Thanks to all my colleagues in the Department for Nanostructured Materials for their help and all the nice moments in the last years. Positive energy in the group is the reason why I like to come to work every day!

Finally, I would like to thank my father and mother for giving me the opportunity to study, for all the moral and financial support and for being patient in stressful moments. I deeply appreciate all the help and support from you!

Blaž Saksida, a very special person in my life, thanks for supporting all my crazy ideas, for being infinitely patient with me and for making me laugh on a "everything-goes-wrong day". Indeed, you made my writing period less stressful!

Abstract

Despite the increasing number of successful cancer treatments the number of newly discovered cancer cases is expected to rise. Therefore, new forms of therapy are urgently required in order to combat the disease. One of the promising approaches for the cancer treatment is photo-thermal therapy, where active component efficiently transform absorbed light into the heat. This generated heat can be then used to selectively destroy targeted cells, while healthy tissue remains intact. There are two general requirements for the most efficient photo-thermal treatment. Firstly, active component has to mediate strong plasmon induced surface heat flux upon absorption of the light. And secondly, maximum absorption of the light has to lie within the near-infrared region (NIR) at around 800 nm (biological window), where the penetration of light into the tissue is at a maximum. One of the most promising materials that fulfil these demands are Au nanostructures in form of Au shells or rods. On the other hand, superparamagnetic nanoparticles have shown great potential to be used as the contrast agents in the magnetic resonance imaging (MRI). Additionally, their magnetic nature can be beneficially used for the magnetic guidance, which can significantly reduce the unintended side effects and damage in the healthy tissues. The value of the material's magnetization and magnetic moment has a strong influence on the performance of the nanoparticles that act as the contrast-agent material for MRI and their ability to be magnetically manipulated, therefore magnetic material has to be selected accordingly. Combining a magnetic material with a high magnetic moment and a material that is plasmonically active in the NIR region of the light in a single nanostructure represents a novel approach of creating multifunctional nanoparticles. As such they allow diagnostics, i.e. magnetic resonance imaging (MRI), retention and manipulation as well as photo-thermal treatment in a controllable manner. In the scope of this thesis we have produced an innovative material based on hybrid magneto-plasmonically active FePt/SiO_2/Au nanoparticles. In the first part of the thesis, processing routes for the synthesis of superparamagnetic FePt nanoparticles of different sizes are described, which, as a result, exhibit different magnetization values. “Single-core” FePt nanoparticles of different sizes (3–10 nm) were prepared via one-step or two-step synthesis, i.e. the “seed-mediated growth”. The latter nanoparticles were found to exhibit twice the magnetization ($m_{(1.5T)}$ = 14.5 emu/g) of the nanoparticles formed via the one-step synthesis ($m_{(1.5T)}$ < 8 emu/g). In order to retain the superparamagnetism at further increase of the nanoparticles size we propose the synthesis of “multi-core” FePt nanoparticles, where 4-8 FePt nanoparticles were joined in one nanostructure. This was achieved by changing the ratio between the two surfactants (oleylamine and oleic acid). The step from smaller “single-core” FePt nanoparticles towards the larger, “multi-core” FePt nanoparticles (>20 nm), led to an increase in the magnetization $m_{(1.5T)}$ from 8 to 19.5 emu/g, without exceeding the superparamagnetic limit, that was attributed to the exchange interactions within one “multi-core” FePt nanoparticle. A step toward biomedical implementation was done via preparing stable water suspensions of FePt nanoparticles. We propose two different approaches: a) functionalization with biocompatible, catechol-based ligands (zwitterionic

dopamine sulphonate or hydrocaffeic acid), which were used on the FePt nanoparticles for the first time, and b) coating with SiO_2 shells of various thicknesses. Homogeneous and heterogeneous nucleation in the SiO_2 coating process was systematically studied to obtain optimal reaction conditions where only SiO_2-coated FePt nanoparticles without core-free SiO_2 nanoparticles were obtained. These FePt-based nanostructures, the cathechol- and SiO_2-coated "single-core" and "multi-core" FePt nanoparticles, were investigated in terms of the relaxation rates (r_1 and r_2) to assess their potential as contrast agents for MRI. The higher r_2 values obtained for the "multi-core" FePt nanoparticles compared to the "single-core" ones indicate the superiority of the "multi-core" FePt nanoparticles as T_2 contrast agents based on their higher magnetization values. Furthermore, it was shown that the SiO_2 coating reduces the r_1 and r_2 relaxation values for both the "single-core" and "multi-core" FePt nanoparticles. This can be attributed to the fact that the SiO_2 layer increases the distance between the water protons and the magnetic FePt core and, therefore, the effective magnetic relaxations of the water protons around the nanoparticles are reduced, which influences the shortening of the T_2 relaxation times. The high r_2/r_1 ratios obtained in our study put FePt nanoparticles near the top of the list of candidate materials for the use in MRI. SiO_2 layer was introduced on the surface of FePt nanoparticles not only to prepare stable water suspension, but also to obtain appropriate core-to-shell ratio of final hybrid FePt/SiO_2/Au nanoparticles to shift the maximum absorption of the light in the NIR region. To implement the multi-functionality of photo-termia with the already proven MRI contrast agent ability of FePt nanoparticles in further steps the hybrid FePt/SiO_2 nanoparticles were covered with Au shell via two different approaches. In the first approach Au nanoparticles were seeded on the SiO_2 surface and then subsequently additional Au was reduced with a strong reducing agent, $NaBH_4$, to form the Au shell. Such hybrid FePt/SiO_2/Au nanoparticles showed a high absorption in the NIR region of the light, which is essential for the photo-thermal therapy. However, this synthesis approach led to a formation of coarse Au shells with several connected cores. Therefore, we proposed the second synthesis approach, i.e. double Au seeding, where Au shells can be prepared in a more controllable manner. Even though the as-prepared hybrid FePt/SiO_2/Au nanoparticles obtained with the two-step Au seeding method have absorption peak at the edge of the biological window, absorption of the light is continued to be high also within this window, which is essential to obtain strong photo-thermal effect. In order to obtain stable and biocompatible water suspension, hybrid nanoparticles were functionalized with a polyethylene glycol-based ligand. Photo-thermal effect was demonstrated by irradiating the water suspension of the hybrid polyethylene glycol-functionalized FePt/SiO_2/Au nanoparticles with different concentrations with a low-energy laser (P=0.9 W, λ=808 nm). Furthermore, the results of experiments performed on a suspension of hybrid nanoparticles in a flow of water confirmed that they can be magnetically manipulated and retained at a targeted location under realistic dynamic conditions. Demonstrated dual magnetic and photo-thermal effect makes the FePt/SiO_2/Au hybrid nanoparticles excellent candidates for the theranostic system (therapy and diagnostics). Their magnetic properties allow them to be used as the contrast agents in MRI, while plasmonically active Au shells enables photo-thermally induced cancer therapy.

Povzetek

Kljub povečanemu številu uspešnih zdravljenj rakavih obolenj se število novo odkritih primerov povečuje, zato so nove oblike zdravljenja nujno potrebne za uspešen boj proti tej bolezni. Med izredno obetavne pristope za zdravljenje rakavih oboljenj sodi tudi fototermično zdravljenje, kjer aktivna komponenta učinkovito pretvori absorbirano svetlobo v toploto. Toplota, ki se pri tem sprošča, se lahko učinkovito uporabi za selektivno uničenje rakavih celic, medtem ko zdrave celice ostanejo nepoškodovane. Za učinkovito fototermično zdravljenje morata biti izpolnjeni dve poglavitni zahtevi. Aktivna komponenta mora omogočati močan foto-termičen efekt in maksimalna absorpcija svetlobe mora biti dosežena znotraj t. i. biološkega okna, kjer je penetracija svetlobe v tkivo najgloblja. To področje svetlobe se nahaja v bližnjem infra-rdečem delu spektra (okrog valovne dolžine 800 nm). Eden izmed najbolj obetavnih materialov, ki izpolnjujejo te zahteve, so zlate nanolupine in nanopalčke. Po drugi strani pa superparamagnetni nanodelci kažejo velik potencial kot kontrastna sredstva pri slikanju z jedrsko magnetno resonanco. Njihova magnetna narava pa prav tako omogoča magnetno vodenje, ki lahko pomembno zmanjša nezaželene stranske učinke, ki bi vodili do poškodb zdravih celic. Vrednost magnetizacije ima močan vpliv na učinkovitost delcev, ki se uporabljajo kot kontrastna sredstva pri slikanju z jedrsko magnetno resonanco in na njihovo uspešno magnetno manipulacijo, zato je izbira ustreznega magnetnega materiala izredno pomembna. Združitev magnetnega materiala, ki ima visok magnetni momement, z materialom, ki izkazuje plazmonske lastnosti v bližnjem infra-rdečem področju svetlobe, znotraj ene nanostrukture, predstavlja inovativen prostop za pripravo multifunkcionalnih nanodelcev. Tako pripravljeni nanodelci združujejo magnetne in foto-termične lastnosti znotraj enega delca, kar omogoča njihovo uporabo za lokalno hipertermično zdravljenje, vizualizacijo in magnetno manipulacijo. Osredotočili smo se na pripravo inovativnega materiala na osnovi hibridnih magneto-plazmonsko aktivnih $FePt/SiO_2/Au$ nanodelcev. V prvem delu te disertacije je opisana sintezna pot za pripravo superparamagnetnih FePt nanodelcev različnih velikosti, ki posledično kažejo različne vrednosti magnetizacije. “Eno-jedrni” FePt nanodelci različnih velikosti (3–10 nm) so bili pripravljeni bodisi v enem koraku bodisi v dveh (uporaba FePt nanodelcev kot kali). Nanodelci, pripravljeni v dveh korakih, kažejo dvakrat višjo magnetizacijo ($m_{(1.5\mathrm{T})}$ = 14,5 emu/g) kot delci, pripravljeni v enem koraku ($m_{(1.5\mathrm{T})} < 8$ emu/g). V želji, da bi povišali magnetizacijo in hkrati obdržali delce v superparamagnetnem režimu, smo v nadaljevanju predlagali sintezo “več-jedrnih” FePt nanodelcev, kjer je 4-8 delcev združenih v eno nanostrukturo. To smo dosegli s spreminjanjem razmerja med surfaktantoma (oleinska kislina in oleilamin). Korak od “eno-jedrnih” FePt nanodelcev k večjim, “več-jedrnim” FePt nanodelcem (>20 nm), pripelje do porasta v magnetizaciji $m_{(1.5\mathrm{T})}$ od 8 do 19,5 emu/g, kot posledica izmenjalnih interakcij znotraj “več-jedrne” FePt nanostrukture, brez prestopa superparamagnetne meje. Naslednji korak proti uporabi FePt nanodelcev v biomedicini je priprava stabilnih vodnih suspenzij. To smo pripravili po dveh postopkih: a) funkcionalizacija z biokompatibilnimi ligandi na osnovi kateholne funkcionalne skupine (zwitterionski dopaminski sulfonat ali hidrokofeinska kislina), ki so bili na FePt nanodelcih uporabljeni

prvič, in b) različno debele prevleke FePt nanodelcev na osnovi SiO_2. Homogena in heterogena nukelacija med procesom tvorbe SiO_2 prevleke sta bili sistematično preučevani, da smo določili optimalne sintezne pogoje za nastanek le FePt delcev, prevlečenih s SiO_2 prevleko, in ne tudi "praznih" SiO_2 delcev. Tako pripravljene nanostrukture, FePt nanodelci funkcionalizirani s kateholnimi ligandi ali prevlečeni s SiO_2 prevleko, so bili uporabljeni pri meritvah relaksivnosti (r_1 in r_2), s čimer smo ocenili njihovo potencialno uporabo kot kontrastna sredstva. Višje vrednosti r_2 so bile dosežene pri "več-jedrnih" FePt, kar kaže na njihovo superiornost pri uporabi kot kontrastna sredstva v primerjvi z "eno-jedrnimi" FePt nanodelci. Prav tako smo pokazali, da SiO_2 prevleka zmanjša vrednosti r_1 in r_2 tako pri "eno-jedrnih" kot tudi pri "več-jedrnih" FePt nanodelcih. Prisotnost SiO_2 plasti poveča razdaljo med protoni molekul vode in magnetnimi jedri in posledično se efektivna magnetna relaksacija protonov okrog nanodelcev zmanjša, kar pa vpliva na zmanjšanje relaksacijskih časov, T_2. Visoko razmerje r_2/r_1, doseženo pri teh meritvah, umešča FePt nanodelce visoko na seznam potencialnih kandidatov za uporabo kot kontrastna sredstva. SiO_2 prevleka ne služi samo za pripravo stabilnih vodnih suspenzij, ampak tudi za pripravo hibridnih $FePt/SiO_2/Au$ nanodelcev z ustreznim razmerjem med jedrom in lupino, ki omogoča maksimalno absorpcijo svetlobe v bližnjem infra-rdečem delu spektra. Za pripravo hibridnih $FePt/SiO_2/Au$ nanodelcev sta bila uporabljena dva postopka. Pri prvem postopku smo uporabili najprej zlate kali na $FePt/SiO_2$ nanodelcih, na katere smo nadalje reducirali plast zlata z močnim reducentom, $NaBH_4$. Tako pripravljeni hibridni delci kažejo visoko absorpcijo svetlobe v NIR delu spektra, kar je nujno potrebno za uspešno foto-termično terapijo. Ker poleg individualnih hibridnih nanodelcev nastanejo tudi skupki več $FePt/SiO_2$ jeder, ki so prekrita s skupno plastjo zlata, smo, da bi dosegli bolj monodisperzne hibridne delce in bi jih bolj kontrolirano prekrili s tanjšo plastjo zlata, uporabili nov pristop, v katerem smo uporabili dvakratno dodajanje zlatih kali na površino SiO_2. Delci, pripravljeni na takšen način, imajo absorpcijski vrh na robu biološkega okna z izmerjeno visoko absorpcijo tudi znotraj tega okna, kar je izrednega pomena za doseganje učinkovitega foto-termičnega efekta. Stabilne in biokompatibilne vodne suspenzije hibridnih nanodelcev smo dosegli z njihovo funkcionalizacijo z ligandom na osnovi polietilen glikola. Foto-termičen učinek hibridnih $FePt/SiO_2/Au$ nanodelcev smo demonstrirali tako, da smo obsevali vodne suspenzije z različnimi koncentracijami z nizko-energijskim laserjem (P=0,9 W, λ=808 nm). Prav tako smo pokazali, da je možno hibridne delce v toku tekočine magnetno manipulirati in zadržati na želenem mestu. Zaradi magnetno-plazmonske aktivnosti lahko hibridne $FePt/SiO_2/Au$ nanodelce uvrstimo med izredno obetajoče multifunkcionalne materiale za teranostiko (terapijo in diagnostiko). Magnetne lastnosti FePt jeder omogočajo njihovo uporabo kot kontrastna sredstva pri slikanju z jedrsko magnetno resonanco, medtem ko plazmonsko aktivne zlate lupine naredijo takšne delce primerne za uporabo pri foto-termičnem zdravljenju raka.

Contents

List of Figures **xv**

List of Tables **xix**

Abbreviations **xxi**

Symbols **xxiii**

1 Introduction **1**
1.1 Magnetism Basics, from Bulk to Nano ... 5
1.1.1 Magnetic anisotropies ... 7
1.1.1.1 Magnetocrystalline anisotropy ... 8
1.1.1.2 Surface anisotropy ... 9
1.1.1.3 Shape anisotropy ... 10
1.1.2 Magnetic interactions and ZFC/FC measurements ... 11
1.1.3 Superparamagnetic size limit ... 13
1.2 Fe-Pt Alloy ... 15
1.2.1 Synthesis of FePt NPs ... 16
1.2.2 Nanoparticles as contrast agents in magnetic resonance imaging ... 18
1.2.3 Magnetic manipulation of nanoparticles ... 20
1.3 Surface Functionalization of NPs ... 21
1.3.1 Functionalization of FePt NPs ... 24
1.3.1.1 Functionalization of FePt NPs with dopamine-based ligands ... 24
1.4 Plasmonic Properties of Au Nanostructures ... 25
1.4.1 Surface plasmon resonance ... 25
1.4.2 Photo-thermal therapy using Au nanostructures ... 30
1.4.3 Nanostructures with combined magneto-optical effect ... 32
1.4.3.1 SiO_2 coating of FePt NPs ... 32
1.4.3.2 Formation of Au complexes and their role in the Au shell formation ... 35
1.4.3.3 Functionalization of hybrid FePt/SiO_2/Au NPs ... 36

2 Aims and Hypothesis **37**
2.1 Aims ... 37
2.2 Hypotheses ... 38
2.2.1 Hypothesis 1 ... 38
2.2.2 Hypothesis 2 ... 39
2.2.3 Hypothesis 3 ... 40

3 Materials and Methods **41**
3.1 Materials Used in the Synthesis Procedures ... 41
3.2 Synthesis Procedures ... 42
3.2.1 Synthesis of FePt NPs ... 42
3.2.1.1 “Single-core” FePt NPs ... 42
3.2.1.2 “Single-core” FePt NPs produced via seed-mediated growth ... 42
3.2.1.3 “Multi-core” FePt NPs ... 42

3.2.2 Functionalization of FePt NPs with zwitterionic dopamine sulfonate ligand ... 42
3.2.3 Functionalization of FePt NPs with hydrocaffeic acid ... 43
3.2.4 SiO_2 coating of FePt NPs ... 43
3.2.5 Au shell formation ... 43
3.2.5.1 Functionalization of FePt/SiO_2 NPs with APTES ... 43
3.2.5.2 One-step Au seeding ... 43
3.2.5.3 Au shell formation with NaBH4 ... 44
3.2.5.4 Au shell formation via two-step Au seeding ... 44
3.2.6 PEGylation of hybrid NPs ... 44
3.2.7 Summary over the formation of hybrid NPs ... 44
3.3 Characterization Techniques and Experimental Set-Up ... 45
3.3.1 Nanoparticles characterization ... 45
3.3.2 Simulation of UV-VIS spectra for hybrid NPs ... 46
3.3.3 Photo-thermal efficiency of the hybrid NPs ... 46
3.3.4 Hybrid NPs magnetic extraction ... 46

4 Results and Discussion 49
4.1 Synthesis of FePt NPs ... 49
4.1.1 "Single-core" FePt NPs synthesis based on varying the amount of surfactants ... 49
4.1.2 "Single-core" FePt nanoparticles synthesis based on seed-mediated growth ... 51
4.1.3 "Multi-core" FePt NPs synthesis ... 52
4.1.4 HRTEM analysis of FePt NPs ... 59
4.1.5 Magnetic properties of "single and multi-core" FePt NPs ... 61
4.2 Ligand Exchange Reactions on FePt NPs ... 66
4.2.1 Functionalization of FePt NPs with zwitterionic dopamine sulfonate ... 66
4.2.2 Functionalization of FePt NPs with hydrocaffeic acid ... 67
4.3 SiO_2 Coating of FePt NPs ... 72
4.4 Relaxivity Measurements ... 76
4.5 Hybrid FePt/SiO_2/Au NPs ... 79
4.5.1 Simulations of UV-Vis spectra for hybrid FePt/SiO_2/Au NPs ... 79
4.5.2 Synthesis of hybrid FePt/SiO_2/Au NPs ... 83
4.5.2.1 Functionalization of SiO_2 surface for effective Au decoration ... 83
4.5.2.2 Au seeding ... 84
4.5.2.3 Au shell formation with $NaBH_4$ ... 85
4.5.2.4 Au shell formation via two-step Au seeding ... 87
4.5.3 Functionalization of hybrid FePt/SiO_2/Au NPs with PEG ... 89
4.5.4 Photo-thermal effect studies on hybrid FePt/SiO_2/Au NPs ... 90
4.5.5 Magnetic extraction studies on hybrid FePt/SiO_2/Au NPs ... 91

5 Conclusions 95

References 101

Bibliography 113

List of Figures

Figure 1.1: Absorption coefficient at different wavelength for hemoglobin and water. 4
Figure 1.2: M-H curves for different types of materials. 6
Figure 1.3: Schematic drawing of a) disordered face centered cubic (*fcc*) and b) ordered face centered tetragonal (*fct*) crystal phase FePt. 9
Figure 1.4: Estimation of the blocking temperature T_b from the temperature dependent field-cooled (FC) and zero-field-cooled (ZFC) magnetic susceptibility curves. 12
Figure 1.5: Binary phase diagram of Fe-Pt [49]. Reprinted with permission. 15
Figure 1.6: Schematic representation of the proposed growth mechanism of FePt NPs. ..17
Figure 1.7: Relaxation process of the hydrogen atoms in MRI. 19
Figure 1.8: Schematic representation of the electric double layer at a charged interface in an aqueous solution. 22
Figure 1.9: Structural formula of a) hydrocaffeic acid (HCA) and b) zwitterionic dopamine sulphonate (ZDS) ligand. 25
Figure 1.15: Schematic of electronic cloud displacement in NPs induced by an oscillating electric field. 26
Figure 1.16: UV−Vis absorption spectra of 9, 22, 48, and 99 nm Au NPs in water. All spectra are normalized at their absorption maxima, which are 517, 521, 533, and 575 nm, respectively. Reprinted with permission [108].....28
Figure 1.17: Tunable optical properties of Au nanorods by changing the aspect ratios. ..30
Figure 1.18: Sequence of events and approximate time scales following absorption of photons by a metal nanoparticle [12]. Reprinted with permission. 31
Figure 1.10: Structural formula of a) TEOS (tetraethyl orthosilicate), b) Igepal CO-520 (polyoxyethylene (5) nonylphenylether) and c) cyclohexane. 33
Figure 1.11: Schematic representation of the SiO_2 coating process. 33
Figure 1.12: a) La Mer diagram for the nucleation and growth of a SiO_2 shell on a Fe_3O_4 core NPs. 34
Figure 1.13: Functionalization of SiO_2 surface with APTES. 35
Figure 1.14: Structural formula of polyethylene glycol (PEG) and thiolated methyl-PEG (mPEG-SH). 36
Figure 2.1: Summary of all experiments performed in each step of the synthesis of hybrid FePt/SiO_2/Au NPs. 38
Figure 3.1: Schematic presentation of the four steps in the synthesis of the hybrid FePt/SiO_2/Au NPs. 45
Figure 3.2: Experimental set-up for measuring the photothermal effect. 46
Figure 3.3: Schematic representation of the experimental set-up for studying the manipulation of hybrid NPs in a water suspension with the use of an applied external field. 47
Figure 4.1: TEM images for a) 3-nm (S2), b) 6-nm (S7) and c) agglomerated (S8) “single-core” FePt NPs. d) Graph indicating the size of “single-core” FePt NPs for different amounts of added surfactants and e) comparison of the magnetic properties for 3- and 6-nm “single-core” FePt NPs measured at 300 K. 51

Figure 4.2: a) Schematics of the synthesis of »single-core« FePt NPs in two steps, b) TEM image of NPs obtained after 2. step of the seed-mediated growth with c) the corresponding magnetic measurements for the NPs after 1. and 2. step at 300K. 52
Figure 4.3: TEM images of "multi-core" FePt NPs for different OLA:OA ratios with magnetic measurements at 300 K for the sample with OLA:OA ratio = 6:2 (S12). 54
Figure 4.4: Graph indicating variation in composition of FePt by changing the amount of added OA while all other parameters are kept constant: OLA (6 mL), $Fe(acac)_3$ (1 mmol, 70 mg) and $Pt(acac)_2$ (0.5 mmol, 40 mg) were used in dibenzyl ether (20 mL) and 1,2-hexadecanediol (2.3 mmol, 0.012 g). 55
Figure 4.5: TEM images of "multi-core" FePt NPs at constant OLA:OA ratio = 3 but the overall volume of added surfactants was varied with magnetic measurements at 300 K for the sample with OLA:OA ratio = 6:2 (S12). 56
Figure 4.6: The weight-loss curves for a) pure oleylamine (OLA), b) pure oleic acid (OA) and c) OLA/OA-coated FePt NPs measured by TGA in the temperature range 25-600°C.57
Figure 4.7: a) TEM image and b) SAED pattern of the sample 22, where Pt:Fe salt ratio = 1:8 was used. FePt and Fe oxide phases are indicated with red and blue dotted lines, respectively. 58
Figure 4.8: HR-TEM images of a) "single-core" and b) "multi-core" FePt nanoparticles with corresponding SAED patterns shown as insets. 59
Figure 4.9: High-resolution HAADF-STEM images of individual a) "single-core" and b) "multi-core" FePt nanoparticles. The inset shows the enlarged region of the particle's edge. 60
Figure 4.10: a) Bright-field and b) HAADF-STEM image of a"multi-core" FePt NP with the corresponding elemental map for c) Fe (green, Fe K line) and Pt (red, Pt M line). . 61
Figure 4.11: Temperature dependent field-cooled and zero-field-cooled (FC/ZFC) magnetic susceptibility curves for "single-core" and "multi-core" FePt NPs performed with an applied field 8 kA/m. 62
Figure 4.12: Initial magnetization at low low H (0-32 kA/m) for "single-core" and "multi-core" FePt NPs measured at 300 K. 63
Figure 4.13: Graph indicating theoretically calculated and experimentally obtained saturation magnetization for "single-core" FePt NPs with different diameters. 65
Figure 4.14: a)-c) Synthesis route of the ZDS ligand, d) oleic acid/oleylamine stabilized FePt NPS in hexane phase before the ligand exchange and e) ZDS-functionalized FePt NPs in the water phase after the ligand-exchange reaction. 67
Figure 4.15: a) Schematic representation of a ligand exchnage reaction with HCA in THF and b) chelate bonding of a HCA on FePt NPs. 67
Figure 4.16: Zeta potential measurements of an aqueous suspensions of the »single-core« and »multi-core« FePt NPs after ligand exchange with HCA. 68
Figure 4.17: FTIR spectrum of pure oleic acid. 69
Figure 4.18: FTIR spectrum of pure oleylamine. 69
Figure 4.19: FTIR spectra of pure oleic acid, pure oleylamine and oleic acid- and oleylamine-coated FePt NPs. 70
Figure 4.20: FTIR spectrum of pure hydrocaffeic acid. 71
Figure 4.21: FTIR spectra of pure HCA and HCA-functionalized FePt NPs. 72
Figure 4.22: a) La Mer diagram for nucleation and growth of SiO_2 and SiO_2-coated FePt NPs. TEM images of samples obtained at TEOS : NH_3 ratio a) 1:25, b) 1:5, c) 1:2 and d) 1:1. 74
Figure 4.23: Growth of SiO_2 shell with the reaction time and TEM images of SiO_2-coated b) "single-core" and c) "multi-core" FePt NPs. 74
Figure 4.24: Magnetic measurements at 300 K of SiO_2-coated a) "single-core" and b) "multi-core" FePt NPs (reaction time 24 hours). 75

Figure 4.25: Schematic representation of the samples used for MRI measurements;.....76
Figure 4.26: Graph indicating a) T_1 relaxation times and b) inverse longitudinal $1/T_1$ – $1/T_1(0)$ relaxation rate increase for "single-core" (S), "multi-core" (M), SiO_2-coated "single-core" (S-SiO_2) and SiO_2-coated "multi-core" FePt NPs (M-SiO_2).....77
Figure 4.27: Graph indicating a) T_2 relaxation times and b) inverse longitudinal $1/T_2$ – $1/T_2(0)$ relaxation rate increase for "single-core" (S), "multi-core" (M), SiO_2-coated "single-core" (S-SiO_2) and SiO_2-coated "multi-core" FePt NPs (M-SiO_2).....77
Figure 4.28: Simulated UV-Vis spectra for hybrid NPs with different core sizes (20-100 nm) and Au shell thickness 5 nm. 79
Figure 4.29: Simulated UV-Vis spectra for hybrid NPs with different core sizes (35-150 nm) and Au shell thickness 10 nm.....80
Figure 4.30: Simulated UV-Vis spectra for hybrid NPs with different core sizes (35-225 nm) and Au shell thickness 15 nm.....80
Figure 4.31: SPR peak positions extracted from simulated UV-Vis spectra for hybrid NPs with different core-to-shell ratios. 81
Figure 4.32: Simulated UV-Vis spectra for hybrid NPs where standard deviation in the core and shell size was applied.Black and red curves: Au shell thickness is 10±5nm and core size is a) 150 nm and b) 200 nm. Blue curve represents ideal sample where no standard deviation in the shell and core size is considered. 82
Figure 4.33: Simulated UV-Vis spectra for hybrid NPs where standard deviation in the core and shell size was applied. Au shell thickness is set to be 10±5nm and core size is 150 nm or 200 nm with standard deviation 15 or 45 nm.....83
Figure 4.34: Zeta-potential measurements of the untreated FePt/SiO_2 NPs and the APTES functionalized FePt/SiO_2 NPs in water.....84
Figure 4.35: Au seeding on SiO_2 surface obtained at different pH values of $HAuCl_4x3H_2O$ water solution : a) 4, b) 6 and 8. 85
Figure 4.36: Au seeding on SiO_2 surface obtained at pH=7 at different reaction times (1-30 minutes). 85
Figure 4.37: TEM images of FePt/SiO_2/Au core/shell NPs and b) corresponding UV-VIS spectra of water suspensions containing gold-seeded FePt/SiO_2 NPs and hybrid FePt/SiO_2 NPs with a Au shell. 86
Figure 4.38: Simulated UV-Vis spectra for Au shells with different core sizes (35 - 125 nm) and comparison with experimental UV-Vis spectrum measured for hybrid NPs in water. 87
Figure 4.39: TEM images of a) SiO_2-coated »multi-core« FePt NPs, b) hybrid NPs after first Au seeding step and c) after second Au seeding step. 88
Figure 4.40: UV-Vis spectra of water suspension of hybrid NPs after first Au seeding step and after second Au seeding step are shown.....89
Figure 4.41: Zeta potential measurements of hybrid NPs before and after PEGylation...90
Figure 4.42: a) Graph of the temperature increase for pure water and a water suspension of hybrid NPs with different concentrations (0.1 - 0.8 mg/mL), irradiated by laser light with an output power of 0.9 W for approximately 10 minutes and b) temperature increase normalized with the suspension concentration. 91
Figure 4.43: a) Magnetic properties of hybrid »multi-core« FePt/SiO_2/Au NPs suspension at 300 K and b) graph indicating the normalized concentration drop of hybrid NPs in the water suspension as a function of time. 92
Figure 5.1: Schematic representation of multimodal hybrid FePt/SiO_2/Au NPs′ functionalities for nanomedical applications by combining photothermal stimulation and manipulation with an external magnetic field [154]. Reprinted with permission. 98
Figure 5.2: Internalization of hybrid NPs into high-grade cancer urothelial cells *in vitro* (A and B). 99

List of Tables

Table 1.1: List of T_b and K_{eff} values from the literature for the spherical *fcc* FePt NPs with different sizes that were used in the caluclation of D_{SPL}. 14
Table 1.2: List of possible complexes present in an aquous solution of $HAuCl_4$ in dependence of the pH. 35
Table 4.1: Sample list of »single-core« FePt NPs, including the amounts of OLA and OA used and the resulting OLA/OA ratio for FePt samples 1 to 8; $Fe(acac)_3$ (1 mmol, 70 mg) and $Pt(acac)_2$ (0.5 mmol, 40 mg) were used in dibenzyl ether (20 mL) and 1,2-hexadecanediol (2.3 mmol, 0.012 g). 50
Table 4.2: Sample list of »multi-core« FePt NPs, including the amounts of OLA and OA used and the resulting OLA/OA ratio for FePt samples 9 to 17; $Fe(acac)_3$ (1 mmol, 70 mg) and $Pt(acac)_2$ (0.5 mmol, 40 mg) were used in dibenzyl ether (20 mL) and 1,2-hexadecanediol (2.3 mmol, 0.012 g). 53
Table 4.3: Sample list of »multi-core« FePt NPs, including the OLA : OA ratio and $Pt(acac)_2$: $Fe(acac)_3$ ratio with the resulting composition for FePt samples 18 to 22. Samples were prepared in dibenzyl ether (20 mL) and 1,2-hexadecanediol (2.3 mmol, 0.012 g). 58
Table 4.4: List of SiO_2 coated samples prepared by changing the TEOS : NH_3 ratio while all other parameters are kept constant; i.e. 170 mL of cyclohexane, 8 mL of Igepal CO-520, 20 mg of »single-core« FePt NPs and 1 mL of 25% NH_3 solution. Reaction time was 24 hours. 73
Table 4.5: Calculated longitudinal (r_1) and transverse (r_2) relaxivities for “single-core” (S), “multi-core” (M), SiO_2-coated “single-core” (S-SiO_2) and SiO_2-coated “multi-core” (M-SiO_2) FePt NPs with corresponding r_2/r_1 ratios. 78

Abbreviations

NP	... nanoparticles
JSI	... Jožef Stefan Institute
IPS	... International Postgraduate School
fcc	... face-centered cubic
fct	... face-centered tetragonal
SPR	... surface plasmon resonance
NIR	... near-infrared region
MRI	... magnetic resonance imaging
SPIO	... superparamagnetic iron oxide
SPL	... superparamagnetic limit
FC	... field-cooled
ZFC	... zero-field-cooled
OLA	... oleylamine
OA	... oleic acid
ZDS	... zwitterionic dopamine sulphonate
HCA	... hydrocaffeic acid
FTIR	... Fourier transform infrared spectroscopy
APTES	... (3-aminopropyl)thiethoxysilane
MAR	... motional average regime
SDR	... static dephasing regime
ELR	... echo-limiting regime
TEOS	... tetraethyl orthosilicate
PEG	... polyethylene glycol
mPEG-SH	... thiolated methyl-PEG
DMF	... N,N-dimethylformamide
THF	... tetrahydrofuran
TEM	... transmission electron microscopy
EDXS	... energy-dispersive X-ray spectroscopy
EELS	... Electron energy-loss spectroscopy
VSM	... vibrating-sample magnetometer
NPU	... Normal porcine urothelial cells
RT4	... low-grade cancer urothelial cells
T24	... high-grade cancer urothelial cells
SAED	... selected-area electron diffraction
HAADF	... high-angle annular dark-field
STEM	... Scanning transmission electron microscopy

Symbols

K ... magnetocrystalline anisotropy
M ... magnetization
B ... magnetic induction
H ... magnetic field strength
χ ... volumetric magnetic susceptibility
μ_0 ... permeability of free space
m ... magnetic moment
V ... volume
E_a ... Anisotropy energy
τ_N ... Néel relaxation time
k_B ... Boltzmann constant
T ... temperature
T_B ... blocking temperature
τ_m ... measurement time
D_{SPL} ... superparamagnetic size limit
H_c ... coercive force
T_c ... Curie temperature
m_s ... saturation magnetization of the NPs
R_1 ... longitudinal relaxation rates
R_2 ... transverse relaxation rates
r_1 ... longitudinal relaxivity coefficient
r_2 ... transverse relaxivity coefficient
T_1 ... longitudinal relaxation time
T_2 ... transverse relaxation time
γ ... gyromagnetic ratio of the protons
D ... diffusion coefficient
F_d ... hydrodynamic drag force
η ... is medium viscosity
r_{hp} ... diameter of hybrid NP
v_p ... velocity of the particle
v_f ... velocity of the media
F_m ... magnetic force
$m_{(1.5T)}$ ... magnetization at 1.5 T
C_s ... solubility concentration
C_{homo} ... concentration threshold for the homogeneous nucleation
σ_{abs} ... absorption cross-section
σ_{sca} ... scattering cross-section
σ_{ext} ... extinction cross-section
ε_m ... medium's dielectric function
n_m ... refractive index of the medium
ε_1 ... real component of the dielectric function

ε_2 . . . imaginary component of the dielectric function
ω_p . . . plasma frequency
γ . . . damping parameter of the bulk metal
ω_{max} . . . SPR peak frequency
λ_{max} . . . SPR peak wavelength
λ_p . . . wavelength corresponding to the plasma frequency of the bulk metal
R . . . aspect ratio of nanorods (length/width)
ε_{core} . . . complex dielectric function of the core metal
ε_{shell} . . . complex dielectric function of the shell
k . . . wavenumber
g . . . volume fraction of the shell layer
ν . . . wavenumber

Chapter 1

Introduction

Surgical incisions along with chemotherapy are the doctrine therapies for cancer. Although effective in termination of cancer, these pose a variety of unwanted side effects due to the delocalized performance of chemotherapy, raising the desire for less invasive and local treatments to avoid damaging interventions to surrounding healthy tissue. Recently emerging cancer treatment routes go into the direction of a using multi-functional/hybrid "nano-systems" that enable such targeted treatment. Using such therapeutic routes, medical treatment is pronounced while keeping the drug doses and the toxicity to the surrounding healthy tissues at minimum.

Definition of hyperthermia is a condition where a body temperature is higher than normal, which can be caused by illnesses, such as fever or heat stroke. But hyperthermia can also refer to a heat treatment, where use of heat is carefully controlled for medical purposes. Hyperthermia is considered as a non-invasive, anti-cancer approach for the selective destruction of abnormal cells in which biological tissues are exposed to temperatures higher than the normal body temperature (41-47 °C)[1]. Such a high temperature causes irreversible cell damage due to the protein denaturation and disruption of the cell's membrane permeability [2]. Very high temperatures can kill cancer cells, but they can also injure or kill normal cells and tissues. Therefore, in order to reduce possible side effects, employing a localized temperature increase in a controllable manner (so-called local hyperthermia) is essential to selectively overheat and therefore kill only the cancerous cells, while preserving the surrounding healthy tissues intact. Not only that hyperthermia by itself can be used for the cancer treatment, but it was also shown that it significantly increases the effectiveness of other treatments, such as chemotherapy or radiation therapy. Besides damaging cells directly, local hyperthermia increases the pore size of the cells, which makes the cells more radiosensitive and improve the delivery of chemotherapeutic and immunotherapeutic agents [3]. There are several techniques by which hyperthermia can be induced locally, such as microwaves, ultrasound waves, radio frequency waves, NIR laser light, oscillating magnetic field, etc. [3].

As the first example, heating can be induced by high intensity focused **ultrasounds**. As an acoustic wave propagates through the tissue, part of it is absorbed and converted to heat. The penetration depth is frequency dependent and can vary from a few mm to a few cm. Frequency used for this type of therapy is usually in the range of 0.5 to 3 MHz. The biggest advantage of this technique comes from the use of an acoustic lens, which can very precisely localize ultrasounds on a target location in the body [4]. **Radio frequency** represents the electromagnetic waves that lie in the range extending from around 3 kHz to 300 GHz. For the treatment of the tumor, frequencies of 10-120 MHz are generally used and those wavelengths are long compared to the body dimensions and,

thus, deposit energy over a sizeable region. Therefore, in order to achieve a more local effect a two-electrode system was designed. Alternating electric current that oscillates in the radio frequency range is used as a heating source for tumor destruction purposes. Radio frequency current passes through the target tissue from the tip of an active electrode (radio frequency generator) towards a dispersive electrode which serves as the grounding pad. Needle-shaped active electrode is inserted into the tumor, where the radio frequency current at the electrode leads to ionic agitation with subsequent conversion of friction into heat [5]. Frictional heating occurs as the consequence of the tissue ions attempting to follow the changes in the direction of the alternating electric current. Inserting an electrode directly into the tumor minimizes the side effects on the surrounding healthy tissue. With this approach tumors with a size up to 5 cm can be treated and is most often used to treat tumors that cannot be removed with surgery or for patients who are not able to go through the stresses of surgery. Thirdly, hyperthermia can be induced by using **microwaves**. Microwaves represent the portion of the electromagnetic spectrum between 300 MHz and 300 GHz. Most commonly used frequencies for microwave thermal therapy are 915 MHz and 2.45 GHz where the penetration depth is 2 - 4 cm in most tissues [6]. The most significant effect of an electromagnetic field applied to biological tissue is conversion of electromagnetic radiation to thermal energy. The greatest constituent of most biological tissues is water. When the electromagnetic field is applied, water molecules continually rotate to align with the direction of the applied field. This continual realignment increases kinetic energy that reflects in the increase of the temperature. How efficiently microwave energy is converted to heat depends on the type of tissue, its water content, and the frequency of the applied field [6]. In comparison with the ultrasound technique, microwave-based hyperthermia suffers from less precise control over the heating rate and a broader heating area.

Further, another approach called **magnetic fluid hyperthermia** has been developed for local hyperthermia using magnetic NPs as mediators of heat. In the magnetic fluid hyperthermia magnetic NPs are internalized by the cancer cells via passive or active targeting [7]. The heating effect of a magnetic fluid is a result of absorbing energy from *ac* magnetic field and converting it into heat by hysteresis losses, relaxation and resonance losses. The latter usually occurs at very high frequencies (e.g. GHz range) and can be neglected in this case. The electromagnetic radiation used in magnetic hyperthermia is in the range of the radio frequency (between several kHz and 1 MHz). Radiation in that range is not harmful for the human body and shows enough penetration depth to access inner organs or tissues [8]. Besides the therapeutically useful heating effect of magnetic particles the alternating magnetic field can causes also an unwanted non-selective heating of both, cancerous as well as healthy tissue due to the generation of eddy currents. Therefore, due to the biomedical reasons a strict limitation $H \cdot f < C$ should be considered. H and f are the amplitude and the frequency of the alternating magnetic field, respectively. C=$4.85 \cdot 10^8$ $Am^{-1}s^{-1}$ was experimentally determined as the value that for a loop with a diameter of about 30 cm the test persons were able to withstand the treatment for more than one hour without major discomfort [9]. For smaller diameter of the exposed body region this value may be exceeded. Therefore, the milder conditions with lower C value should be used to avoid possible side effects. For example, at f=400 kHz and f=700 kHz, H should not exceed 12.5 kA/m and 7.1 kA/m, respectively. Hysteresis losses are important for the multi-domain NPs, which can be seen as the amount of energy dissipated during a magnetization cycle. For biomedical applications, magnetic NPs are preferred to show a superparamagnetic behaviour, which is typically achieved when the size of the NPs is reduced below 20 nm. In this size range the prevailing heating mechanisms are the relaxation losses. This

relaxation can correspond either to the physical rotation of the particles themselves within the fluid (Brownian relaxation), or rotation of the atomic magnetic moments within each particle (Néel relaxation) [10]. The mechanism of relaxation depends on the size of the NPs (volume of NPs) and also on the properties of magnetic material (due to its anisotropy constant). In the recent years, extensive research has been done in testing different materials for their potential use in magnetic hyperthermia, such as Fe, Co, and Ni metallic NPs and their oxides. Pure metals have the highest saturation magnetization, but have limited use in biomedical applications due to their inherent toxicity and poor chemical stability; therefore, ferrites are the most studied materials, among them, the highest number of publications can be found on iron oxide NPs. Fe oxide NPs indeed satisfy both; the MRI ability [15] as well as the hyperthermia treatment in oscillating magnetic field [16]. However, despite their advantages they have been shown to have some weaknesses with regards to their rapid clearance by macrophages that hinder their trans-endothelia passage and tissue penetration [18]. Seeking for a novel system with an "inverse approach" shows that an alternative system to Fe oxides, should have a better biocompatibility, and in order to surpass magnetic properties of Fe oxides, also a larger magnetization. Here, FePt-based alloys with a face-centred cubic (*fcc*) crystal structure represent an alternative, since they possess a three-times-higher bulk saturation magnetization [19] (about 1140 emu/cm^3) when compared to iron oxides [11]. Furthermore, in the search of new candidates for the magnetic hyperthermia with superior heating performance some theoretical calculations were done. Maenosono et al. [11] estimated the performance of magnetite, maghemite, FeCo and $L1_0$ and *fcc* FePt NPs and showed that *fcc* FePt NPs have superior heating capability compared with others. The reason for their superiority lies in the high magnetic anisotropy constant of the FePt alloy. Besides usage as the contrast agent for MRI and drug delivery applications, also theoretically predicted superior heating capability puts *fcc* FePt NPs high on the list of the most promising materials for use in nanomedicine. Advantage of the magnetic fluid hyperthermia it is that is not limited to surface tumors, but also deeper tissues are accessible. Furthermore, same superparamagnetic NPs that are used as the heat mediators can be used at the same time as the contrast agent for MRI, which enables direct monitoring of the treatment process.

Finally, also laser light can be used for the cancer therapy. Photo-dynamic therapy uses a drug that is not active until it is exposed to a certain type of laser light, to kill cancer cells. **Photo-thermal therapy** is the extension of photodynamic therapy, which exploits light to excite active components that in turn release vibrational energy (heat). The generated heat can be used to either kill targeted cells at the application site or to trigger release of incorporated drugs in case of use of photosensitive coatings. The absorbed photon energy is rapidly converted into heat by going through a process of internal relaxation of the electrons via electron-electron scattering and electron-phonon coupling, resulting in the dissipation of heat into the environment [12]. For better understanding of this conversion of absorbed light into the heat, the sequence of events following photon absorption and their time scales will be discussed in the chronological order in the section 1.4.2.

In order to use light most effectively for the photo-thermal therapy, the absorption peak of the active component needs to be shifted either to the region of the first biological window in the near-infrared region (NIR) at around 800 nm or the second biological window at around 1750 nm, where the penetration of light into the tissue is at a maximum. For comparison, in the visible part of the spectrum the penetration depth of the light is up to a few millimetres, while in the NIR range penetration depth of a few centimeters can be achieved, depending on the type of the tissue. In order to use the plasmonic particles for body-treatments we have to be aware that human body consists

of different types of light absorbers. In blood two types of hemoglobin can be found, i.e. oxyhemoglobin (HbO_2) and deoxyhemoglobin (Hb), that exhibit different absorption spectra [22] as evident from Figure 1.1. The absorption coefficient of Hb (green curve, Figure 1.1) has its highest absorption peak at 420 nm and a second peak at 580 nm. With increasing the wavelength its spectrum then gradually decreases. On the other hand, HbO_2 (red curve, Figure 1.1) shows its highest absorption peak at 410 nm, and two peaks at 550 nm and 600 nm. At wavelengths larger than 600 nm, HbO_2 absorption decays much faster than Hb absorption, but starts to increase again within the NIR window. Another major absorber of light in the human body is water. Although water is nearly transparent in the range of visible light, its absorption becomes significant with increasing wavelength over the NIR region (blue curve, Figure 1.1). Moreover, water is present in high concentration in human tissue; therefore, its contribution to the overall absorption of the tissue is large. Other tissue components with less significant contributions to the total absorption spectrum of tissue are fat and melanin, which is a chromophore in the human epidermal layer of skin and is responsible for the protection from harmful UV radiation. From Figure 1.1 it can be seen that the major absorbers of visible and infrared light have their lowest absorption coefficient in the NIR region around 650–900 nm. This NIR region of the light is also called a "biological window". Light in the visible range is routinely used for intravital microscopy, where living cells are observed at high resolution through an attached window preparation. However, imaging of deeper tissues (>500 μm to cm) requires the use of NIR light [22]. Besides imaging, light can be used also for the therapy.

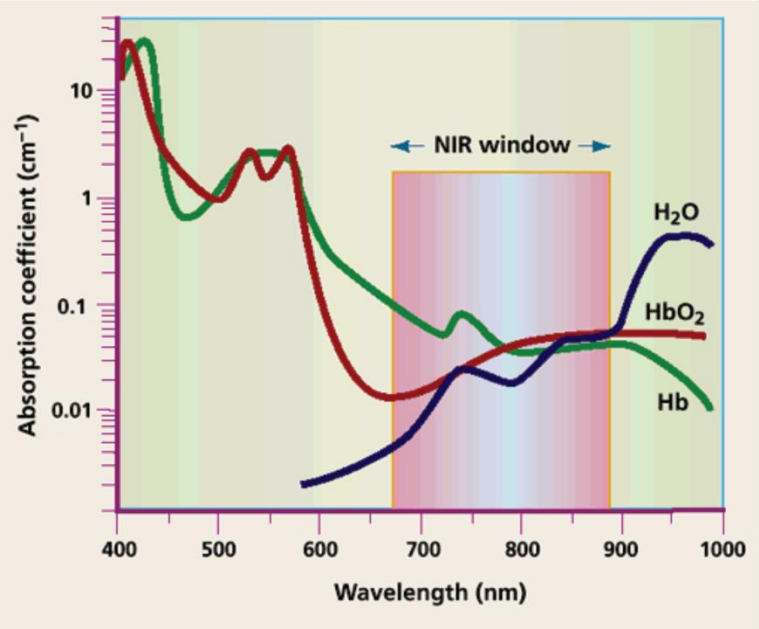


Figure 1.1: Absorption coefficient at different wavelength for hemoglobin and water. In NIR window the absorption of light by hemoglobin (<650 nm) and water (>900 nm) is minimal [22]. Reprinted with permission.

One of the most promising materials in photo-thermal therapy are Au NPs because they mediate strong plasmon induced surface heat flux upon absorption of NIR light [20], [21], prerequisite for the body-treatments. Spherical Au NPs show the highest absorption of the light in the visible region. Increase in the NP diameter from 20 to 80 nm results in a small red-shift in the maximum absorption peak position from ~520 to 550 nm [21].

However, if Au NPs are fabricated in the form of rods or shells, maximum absorption peak can be shifted towards the NIR region of the light. Moreover, fabrication of Au rods or shells enables relatively simple positioning of the absorption peak by changing their dimensions and morphology [20], [21].

The difference between the traditional hyperthermia and the photo-thermal therapy with a plasmonically active NPs and, at the same time the biggest advantage, is that the photo-thermal heating with NPs can be very precisely localized in the tumor cells, because a small dimension of NPs enables them to enter every individual cell. Thus, selective internalization of NPs enables destruction of all cancer cells, while with other approaches, except for the magnetic fluid hyperthermia where NPs are used as well, a certain tissue area is destructed without distinction between the healthy and cancerous cells. Hence it follows that both plasmonic and magnetic NPs can be used in the hyperthermia therapy. In both cases, the size and the shape of the NPs are crucial. Au nanostructures in form of the nanoshells and nanorods are often preferred due to their strong absorption in the NIR region. For magnetic NPs, fine-tuning the shape, magnetization and anisotropy is necessary to enhance the heat-generating capacity. Furthermore, if plasmonic and magnetic NPs are combined in a hybrid magneto-plasmonic nanostructure, a cumulative heating effect can be expected. It was shown on the example of "multi-core" iron oxide/gold branched shell NPs that a combination of high thermal capabilities for both magnetic hyperthermia and photo-thermia can strongly enhance the heat generation in comparison with only either magnetic hyperthermia or photo-thermia [13]. Furthermore, magnetic NPs can be used as contrast agents in MRI and Au NPs induce a strong X-ray attenuation, which make them an ideal candidate for computed tomography (CT) contrast agents and, therefore, therapy and imaging can be performed simultaneously. Such "hybrid" systems represents the concept of a "theranostic" device, in which both diagnostic and therapeutic functions can be administered in a single dose [14]. For NPs, an advantage of combining imaging with therapeutic functions is that the biodistribution of the materials can be monitored in vivo, reducing the potential for unintended side effects of drug toxicity or hyperthermia-induced damage in healthy tissues.

1.1 Magnetism Basics, from Bulk to Nano

First reports on magnetism date back to ancient Greece, India and China. A word magnet derives from the Greek "magnítis líthos", which means "Magnesian stone". By definition, a magnet is a material that produces its own magnetic field. If a magnetic material is placed in a magnetic field of strength $\vec{H}$, the individual atomic moments in the material contribute to its overall response, which is called magnetic induction $\vec{B}$ [10]:

$$\vec{B} = \mu_0(\vec{H} + \vec{M}), \tag{1.1}$$

where μ_0 is the permeability of free space, $\vec{M}$ is the magnetization, which is given as the sum of the magnetic moments ($\vec{m}$) per unit volume (V) ($\vec{M} = \vec{m}/V$). All materials interact with the applied magnetic field to some extent and are classified in terms of their volumetric magnetic susceptibility (χ). The magnetization induced in a material by $\vec{H}$ is specified as:

$$\vec{M} = \chi\vec{H} \tag{1.2}$$

In SI units, $\vec{M}$ and $\vec{H}$ are expressed in A m^{-1} and χ is dimensionless. Some materials display some magnetism only in the presence of an applied field; these are classified either as paramagnetic ($\chi = 10^{-6}$ to 10^{-1}) or diamagnetic materials ($\chi = -10^{-6}$ to -10^{-3}). However, some materials are magnetic even without a field applied, due to the ordered magnetic states; these are classified as ferromagnetic, ferrimagnetic and antiferromagnetic materials. Here the prefix refers to the nature of the coupling interaction between the electrons within the material, which is responsible for large spontaneous magnetizations [23].

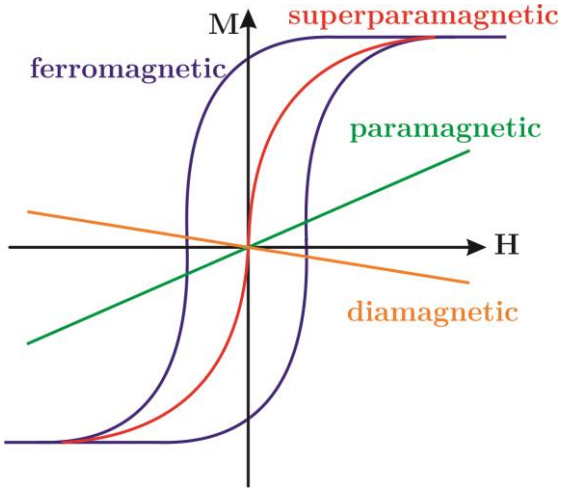


Figure 1.2: M-H curves for different types of materials.

The magnetic behaviour of the materials is characterized with the *M–H* curve. From Figure 1.2 it can be seen that the susceptibility depends not just on temperature, but also on *H*, with *M* approaching a saturation value at large values of *H*. Open *M–H* curves, called hysteresis loops, are observed in ferromagnetic and ferrimagnetic materials as the consequence of the irreversibility in the magnetization process, which is related to the pinning of the magnetic domain walls at impurities or grain boundaries within the material, as well as to intrinsic effects such as the magnetic anisotropy of the crystalline lattice [10]. In the initial demagnetized state, without an applied field, the magnetic domains of ferromagnetic material are arranged in a way that the magnetization is averaged to zero. The reason lies in the formation of magnetic domains, which are small regions of magnetic alignment, and this minimizes the magnetostatic energy within a bulk ferromagnet. Material with multiple magnetic domains is in the so-called multi-domain ground state, which appears when large particles are present (micron size or more). When a magnetic field is applied, the energy of the field can overcome the magnetostatic energy associated with the domain formation, and the magnetization of the material increases until all of the moments are aligned with the field and the maximum magnetization is referred to as the saturation magnetization, or M_s [24]. Once the saturation magnetization is achieved, if the magnetic field is switched back to zero, the magnetization will not return to zero. Some magnetic domains remain in a parallel orientation, but some portion of them aligns randomly, consequently, the material will maintain some net magnetization, which is called the remanent magnetization, M_r. In order for the magnetization to return to zero, a field must be applied in the opposite direction. The field at which the magnetostatic energy is minimized and moments of the domains are again in different directions is called the coercivity, H_c. The full cycle of the magnetic field can be achieved by saturating the magnetization in the opposite direction, reverse and going back through the zero until the magnetization is once again saturated

in the initial direction. Complete hysteresis loop is shown in Figure 1.2, blue curve. The material in a multi-domain ground state has a narrow hysteresis loop (low value of H_c) because it takes relatively little field energy to make the domain walls move.

If the size of the particles is decreased below a certain critical size, generally below 1 micrometer, the energy required to form a domain wall becomes too high, therefore, a single domain ground state appears, where all spins in a particle are aligned in the same direction [24]. This manifests in a broader hysteresis loop (large value of H_c). Single domain diameter particle size (d_s) depends on the chemical composition, shape and crystal structure of the material. For a spherical particle d_s can be calculated using the following equation:

$$d_s = \frac{36\sqrt{A\,K_{eff}}}{\mu_0 M_s} \tag{1.3}$$

where A is the exchange constant, K_{eff} is the effective anisotropy constant and μ_0 is the vacuum permeability. For example, single domain diameter for *fcc* Fe_3O_4, *fct* FePt and *fct* CoPt is 82, 340 and 610 nm, respectively [25].

At even smaller sizes (of the order of tens of nanometers or less) superparamagnetism arises, where the magnetic moments of the particles are randomly oriented and are free to fluctuate due to the high thermal energy. This reflects on the anhysteretic, but still sigmoidal, *M–H* curve shown in Figure 1.2, red curve. It can be seen that superparamagnetic particles each with its own moment can be easily saturated in the presence of a field, but the magnetization returns to zero upon removal of the field, i.e., both M_r and H_c are zero. Therefore, materials in a superparamagnetic state are of great interest for biomedical applications because magnetic interactions between any two NPs in the dispersion are minimized, which reduces the possibility for NPs agglomeration. As well as single domain diameter also superparamagnetic size limit (SPL) is chemical composition, shape and crystal structure dependent. For example, SPL for *fcc* Fe_3O_4, *fct* FePt and *fct* CoPt is 24, 3 and 3.6 nm, respectively [25]. SPL in *fcc* FePt NPs will be discussed in Section 1.1.3.

1.1.1 Magnetic anisotropies

The magnetic anisotropy energy, Ea, is the energy needed to reverse the magnetization from one stable state to the other [24]. This energy tends to keep the magnetization in a particular crystallographic orientation, which is called the easy axis. This easy axis dictates where the magnetization will be pointing at in the absence of the external magnetic field [26]. Important contribution to the magnetic anisotropy energy derives from the crystal structure of the material, i.e. cubic, tetragonal, hexagonal, etc. This contribution is called magnetocrystalline anisotropy. Moreover, for non-spherical structures also shape of the structure has to be considered in the total anisotropy energy. This term is called shape anisotropy. Furthermore, in the nanoregime, due to the increased surface-to-volume ratio, also surface anisotropy becomes significant. These three anisotropies will be described in the following sections.

1.1.1.1 Magnetocrystalline anisotropy

Magnetocrystalline anisotropy (MCA) is the tendency of the magnetization to align itself along a preferred crystallographic direction. The easy and hard directions arise from the interaction of the spin magnetic moment with the crystal lattice (spin-orbit coupling) [27]. In the presence of the external magnetic field the spin of the electron tends to orient in the direction of the magnetic field. Consequently, also the orbit of the electron tries to follow this reorientation. However, orbit is strongly coupled to the lattice and therefore resists the rotation of the spin axis. The energy necessary to deflect the magnetic moment in a single crystal from the easy to the hard direction is called magnetic anisotropy energy (EMCA). In most materials spin-orbit coupling is weak and, therefore, MCA is not particularly strong.

For the cubic crystal structure, the E_{MCA} can be calculated using the first and second order anisotropy constants (K_0, K_1 and K_2) and the direction cosines (α_i) of the angles between the magnetization and the axes parallel to the fourfold axes [28]:

$$E_{\mathrm{MCA}}(\theta)=K_0 + K_1\,(\alpha_1^2\alpha_2^2 + \alpha_2^2\alpha_3^2 + \alpha_3^2\alpha_1^2) + K_2\,(\alpha_1^2\alpha_2^2\alpha_3^2) + \cdots \tag{1.4}$$

Anisotropy constants are temperature dependent and are expressed in J/m^3. Higher powers are generally not needed, because already K_2 can be so small that the term containing it can be neglected. K_0 is angle-independent and is usually ignored.

In uniaxial magnetic NPs, the terms above first order are usually neglected. Therefore, the anisotropy energy per particle is given by a simpler expression:

$$E_{\mathrm{MCA}}(\theta)=K_1 V \sin^2\theta, \tag{1.5}$$

where V is the volume of the particle and θ is the angle between the magnetization and the easy magnetization axis of the particle. The maximum energy barrier that separates the two energetically equivalent easy magnetization directions i.e., the energy barrier to moment reversal, is equal to $K_1 V$ [29].

FePt alloy for example belongs to the group of the high MCA materials in dependence of its crystal structure. The most investigated FePt crystal structures are *fcc* and *fct*, which are schematically shown in Figure 1.3. In the face-centered cubic crystal (*fcc*) phase, Fe and Pt atoms are chemically disordered (Figure 1.3a), the material has a low magnetocrystalline anisotropy and is magnetically soft. In contrast, the *fct*-structured FePt is chemically ordered (Figure 1.3b). Alternating atomic layers of Fe and Pt are stacked along the [001] direction (c axis) of the fct crystal structure. The phase change from the high symmetry cubic structure to the low symmetry tetragonal structure causes a preferential magnetization orientation along the c-axis and in high magnetocrystalline anisotropy. This high effective anisotropy constant (K_1 = 6.6 - 10 · 10^6 J/m^3 at room temperature) arises due to the large spin-orbit coupling of the Pt site and the hybridization between Fe 3d and Pt 5d states [30].

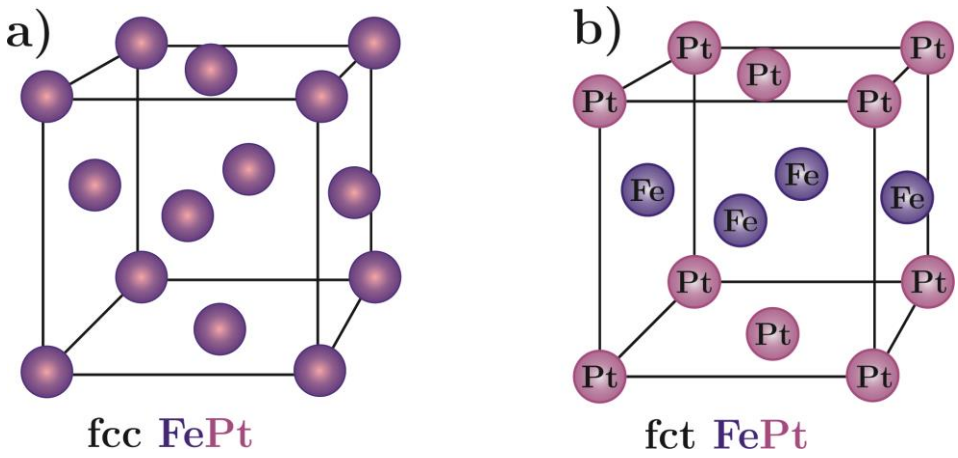


Figure 1.3: Schematic drawing of a) disordered face-centered cubic (*fcc*) and b) ordered face-centered tetragonal (*fct*) crystal phase FePt.

1.1.1.2 Surface anisotropy

When tuning the magnetization in nanosize regime, we have to take into account that the magnetic properties of NPs are strongly influenced by the so-called finite-size and surface effects whose relevance increases with decreasing the particle size [31]. Finite-size effects result from the quantum confinement of the electrons. Upon that increasing the surface-to-volume ratio a contribution of the surface to the overall magnetization becomes significant. The surface atoms experience different environments than those in the core of the particle, therefore, several types of defects might exist on the surface such as atomic vacancies, changes in the atomic coordination, dangling bonds and lattice disorder [29]. These surface defects result in an uncompensated disordered spins, which influence the magnetization of the surface. Spins at the surface of NP undergo nonlinear coupling, forming disordered shell around an ordered core. This phenomenon is called spin canting [26]. Because the surface contribution is significant anisotropy constant is not directly proportional to the particle's volume and differs from the bulk values (K_v) [29]. Therefore, term effective anisotropy constant (K_{eff}) was introduced for the materials with the reduced size [32]:

$$K_{\text{eff}} = K_{\text{v}} + \frac{S}{V} K_{\text{s}}, \tag{1.6}$$

where K_v is a bulk anisotropy constant, K_s is a surface anisotropy and S/V is the particle's surface-to-volume ratio. Magnetic anisotropy is larger for NPs (by a factor 10^1-10^2) than for bulk materials due the large contribution of the surface anisotropy [31].

The saturation magnetization of the NPs (m_s) is known to be proportional to the NPs' size, according to the relation:

$$m_s = M_s\ [(r-d)/r]^3, \tag{1.7}$$

where M_s is the saturation magnetization of the bulk, r is the radius of the NP, and d is the thickness of the disordered surface spin layer [33]–[35]. Application of surface-functionalization groups on NPs (surfactants), either for the NP suspension stability

and/or for their biocompatibility [34], can influence the thickness of the disordered surface spin layer. It was shown that the formation of the bond between the surfactant molecule and the surface atoms might lead to a charge transfer from the surfactant molecule to the Fe site, which is the primary contributor to the magnetization in FePt, thereby lowering the atomic magnetization by 60 % [33]. 3-nm-sized FePt NPs exhibit a dramatic increase in the value of m_s from 210 emu/cm^3 to 850 emu/cm^3 when annealed at 400°C, due to the removal of the surfactant layer, which is known to be magnetically "dead" [33]. At temperature higher than 400°C the bonding between the surfactant and the surface atoms is broken, which leads to the increase in the surface magnetization and, consequently, increase in the overall NP magnetization. However, the removal of the surfactant causes the agglomeration of the NPs in a suspension, which is not desirable in biomedical applications for which our synthesis was aiming. In order to determine the influence of the chain length and the type of the functional group of the ligands on the magnetic properties of NPs, six different ligands (octanoic acid, dodecanoic acid, 1-octanethiol, 1-dodecanethiol, 1-octylamine and 1-dodecylamine) were introduced on the *fcc* FePt NPs surface using the ligand exchange technique [34]. The thinnest dead layer was found for the 1-dodecanethiol molecules (d=1.5 nm), while the thickest was in the case of dodecanoic acid (d=1.85 nm). In accordance with the Eq. (1.7) the thinner dead layer corresponded to the higher m_s values (m_s for 1-dodecanethiol is 22.3 emu/g and m_s for dodecanoic acid is 15.3 emu/g). Possible explanation for the origin of the difference in m_s among NPs capped with different ligands can be found in the difference in the electron donation ability of the ligand to the Fe d bands [34] as discussed in [33]. Longer alkyl chain length regardless of the functional group leads to a higher magnetization decrease. This can be explained by the chain-length effect of hydrocarbons on the electron donating ability. This means that ligands with longer alkyl chain length have higher electron donating ability and, therefore, stronger effect on the magnetization reduction. On the other hand, at the same size of the alkyl chain length the ability of the reduction of the magnetization is also functional group dependent. The reason lies in the difference in its basicity. If comparing alkylamine, alkanethiol and fatty acid, their basicity constants pK_b are 3, 4 and 9, respectively. It was confirmed that among them the NPs capped with alkylamines have the largest surface dead layer. From the pK_b values it would be expected that the NPs capped with alkanethiols would have larger surface dead layer than the fatty acid, however, results revealed the opposite effect. This can be attributed to the fact that thiols form weaker bonds with iron than the carboxylic group; on the other hand, thiols strongly bond to the Pt sites. Therefore, a significant fraction of thiol molecules is bonded on Pt sites, which influence the magnetic properties of FePt much less than the ligands binding to the Fe sites. Moreover, the thickness of the dead layer depends not only on the basicity of the ligand but also on the number of the Fe-ligand binding sites. It was concluded that the up to 10 % of increase in the m_s of the *fcc* FePt NPs can be achieved with high pK_b ligands and/or reducing the number of Fe-ligand binding sites.

1.1.1.3 Shape anisotropy

Besides the magnetocrystalline and surface anisotropy also the shape anisotropy (K_{shape}) has an important contribution to the magnetic properties of nanostructures. Shape anisotropy originates from the nanostructures′ demagnetizing field and depends on the shape of the nanostructure. In a non-spherical particle the demagnetizing field (H_d) will not be equal for all the directions. The H_d is smaller for the long and larger for the short axes and can therefore create one or more easy magnetization axes. The demagnetizing

field can be expressed as $H_d = \Delta N \cdot M_s$, where ΔN is the difference in the demagnetizing factors for different axes. For spherical particles ΔN is 0, therefore there is no shape anisotropy present. It was shown that the variation in the magnetic properties between spherical, cubic, star and rod shaped *fcc* FePt NPs arise from the different shape anisotropies [36]. Due to the same volume of the particles, the contribution of the surface anisotropy to the K_{eff} is in all cases similar, thus difference in the K_{eff} can be attributed to the different shape anisotropies. Because spherical NPs have no shape anisotropy, the K_{shape} for other geometries can be calculated. It was determined that rods with a dimension (8.5 x 4 nm) have $K_{shape} = 2.7 \cdot 10^5$ J/m^3. Furthermore, it was shown that $K_{eff,cubic}$ ($1.3 \cdot 10^5$ J/m^3) is lower than $K_{eff,spherical}$ ($1.6 \cdot 10^5$ J/m^3). Due to the aspect ratio of 1 the shape anisotropy in cubic NPs is negligible. However, due to the more symmetric coordination of the atoms in the cubic crystals, their surface anisotropy should be lower than in the spherical ones, therefore, cubic NPs have lower K_{eff}. When NPs with different shapes have similar surface-to-volume ratio also their m_s value is expected to be similar. However, the coercivity H_c depends on the K_{eff} and, consequently, different values of H_c are expected for NPs with different shapes. Measurements done at 10 K, where *fcc* FePt NPs show ferromagnetic response, confirmed that the highest H_c is obtained in the case of FePt rods, which has the highest K_{eff}.

1.1.2 Magnetic interactions and ZFC/FC measurements

With decreasing particle size the energy barrier ($E_B = K_{eff}\ V$) that separates the two energy minima, where the magnetization is parallel or antiparallel to the easy axis, is also decreased. In a very small NPs the thermal energy fluctuations ($E_{th} = k_b T$) overcome this energy barrier and spontaneously reverse the magnetization of a particle from one easy direction to the other, even in the absence of an applied field [26]. This phenomenon is called superparamagnetic relaxation. A rotation of the atomic magnetic moments within each particle is called Néel relaxation. Néel relaxation time (τ_N) is the characteristic time for the thermal fluctuations of the magnetization in a NP with uniaxial anisotropy and is described by the relation:

$$\tau_N = \tau_0 \exp\left(\frac{K_{eff}\ V}{k_b T}\right), \tag{1.8}$$

where K_{eff} is the effective anisotropy constant, V is the volume of the particle, k_B is the Boltzmann constant and T is the temperature. τ_0 is called attempt time and depends on different parameters, such as temperature, saturation magnetization and applied field. It usually has a value in the range of $\tau_0 = 10^{-9}$ - 10^{-13} s.

The state of the NP (superparamagnetic or blocked) depends as well on the measurement time τ_m [10]. The temperature for which $\tau_m = \tau_N$ is called the blocking temperature T_b, which can be determined from the temperature dependent field-cooled and zero-field-cooled (FC/ZFC) magnetic susceptibility curves as is shown in Figure 1.4. If $\tau_m >> \tau_N$ NPs appear to be superparamagnetic; while if $\tau_m << \tau_N$, flipping of the magnetization is slow in comparison with the measurement time and NPs are in the so-called blocked state, where particles' magnetization is blocked along their individual anisotropy easy axes. In the ZFC measurements, the sample is cooled from room temperature to a temperature of a few K in the absence of the magnetic field. Then a small magnetic field (about 8 kA/m) is applied and the magnetization is measured as the function of the increasing temperature [29]. With the increasing temperature also the thermal energy is increased. If thermal energy overcomes anisotropy energy, magnetic

moments are released from the blocked state, which causes the alignment of the moments along the direction of the applied magnetic field. The number of these aligned moments will increase until reaching a maximum magnetization at T_B. As the temperature is raised above T_B, the thermal energy becomes large enough to cause the magnetic moments to flip again randomly and the magnetization of the particle is suppressed. A peak in the ZFC measurement occurs at T_B. A sample with a large particle size distribution will show a broad peak. On the contrary, in a sample with a small size distribution a narrow peak is observed because the NPs of nearly equal sizes will have nearly the same T_B. In FC measurements the magnetization is measured during the cooling. At $T > T_B$, the thermal energy is large enough that the magnetic moments are randomly oriented and a very small net magnetization is observed. With decreasing the temperature the thermal energy decreases and more and more magnetic moments align along the field direction leading to an increase in the magnetization. If the NPs in the sample are not monodispersed and/or are interacting with each other (i.e. not isolated) this will manifest in the change in the shape of the ZCF/FC curve.

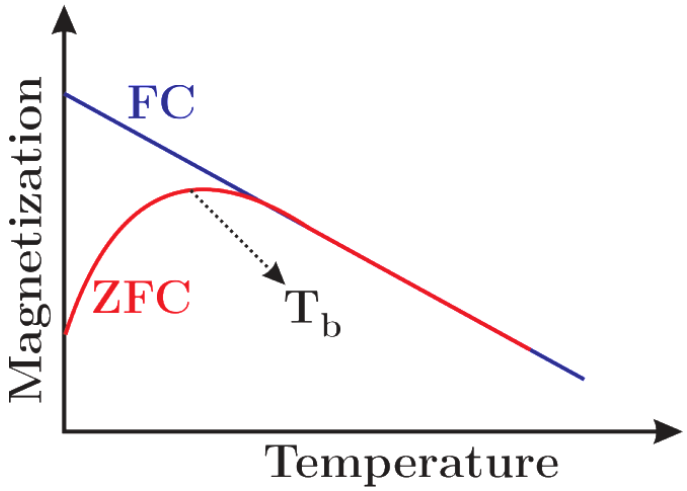


Figure 1.4: Estimation of the blocking temperature T_b from the temperature dependent field-cooled (FC) and zero-field-cooled (ZFC) magnetic susceptibility curves.

On the nanoscale magnetism many possible intra- and inter-particle interactions might occur [37]–[39]. Namely, a NP's magnetism is strongly influenced by the inter-particle dipolar (long-range) and/or intra-particle exchange (short-range) interactions [38]. Non-interacting NPs follow Néel-Brown relaxation theory, however when interactions are not negligible, they can have a significant effect on the superparamagnetic relaxation.

For most magnetic materials with magnetic moments of few Bohr magnetrons magnetic dipole interactions between atoms in a crystal are so small that cannot induce magnetic ordering at temperatures above 1 K. This means that magnetic dipole interactions have a negligible influence on the magnetic order in bulk materials at higher temperature. However, when the dimensions of ferromagnetic or ferromagnetic materials is decreased down to 10 nm, the magnetic moments can achieve values of 10^4 Bohr magnetrons and therefore, dipole interactions between NPs can have significant influence on the magnetic properties. The dipole interaction energy (E_d) of a particle can be expressed as [38]:

$$E_d \approx \frac{\mu_0 \mu^2}{4 \pi d^3} \tag{1.9}$$

where μ_0 is the permeability of free space, μ is the average magnetic moment, d is the average separation between two particles. From this equation it can be seen that in concentrated samples where NPs are in close proximity dipole interactions can significantly influence magnetic behaviour. This means that magnetic ordering might occur and superparamagnetic relaxation may be even suppressed. Dipole interactions can have a significant effect on the magnetization measurements. For example, in ZFC measurement shift in T_b towards higher temperature can indicate the presence of dipolar interactions [39]. Furthermore, the temperature-independent ZC curve, which reaches a saturation at $T<<T_b$, indicates the presence of the inter-particle dipole and/or exchange interactions. However, in the non-interacting system ZC curve increases monotonously with decreasing temperature achieving maximum value at the lowest temperature (blue curve, Figure 1.4) [39], [40]. When talking about the overall magnetic properties, the numerical simulations have showed that the global magnetization of the cluster consisting of several magnetic NPs is decreased by the NPs' dipolar interactions [41], [42]. Inter-particle dipolar interactions can be prevented by coating NPs with surfactants. However, this is not necessarily enough to achieve fully non-interacting system [26].
When surface atoms of neighbouring NPs are in a close contact, another type of magnetic interactions, i.e. exchange interactions, might arise. Magnetic energy of a particle that is interacting with its neighbours is expressed as [38]:

$$E = K_{eff} V \sin^2\theta - \sum_{i,j} J_{ij} \overrightarrow{S_i} \cdot \overrightarrow{S_j} \tag{1.10}$$

The first term represents the magnetic anisotropy energy and the second term in the exchange interaction energy, where $\overrightarrow{S_i}$ and $\overrightarrow{S_j}$ are the surface spins of two neighbouring particles and J_{ij} is the exchange coupling constant. J > 0 is valid for ferromagnetic interaction that couples the spins parallel (↑↑) and can be found in ferromagnetic materials. On the other hand, J < 0 is valid for antiferromagnetic interactions where spins are coupled antiparallel (↑↓) and is found in both ferromagnetic and antiferromagnetic materials [26]. From this equation it can be seen that the presence of the exchange interaction can significantly alter the magnetic behaviour in contrast to the non-interacting system. If individual NPs are coated with the surfactant, exchange interaction between NPs can be neglected. However, in "multi-core" NPs, where particles or cores are in a close contact, exchange interactions are expected to act and can have a significant influence on the magnetic properties. For example, it was shown in the case of Fe oxide NPs that in "multi-core" morphology the global magnetization can increase upon a decrease in surface spin disorder and increase in intra-particle exchange interactions in comparison with the "single-core" sample [37].

1.1.3 Superparamagnetic size limit

When T_b and size of the NPs are known, then the effective anisotropy constant K_{eff} for the non-interacting monodispersed NPs can be calculated using the following equation:

$$K_{eff} = \frac{25\, k_b\, T_b}{V}, \tag{1.11}$$

where k_B is the Boltzmann constant, T_b is the blocking temperature and V is the volume of the particle. Furthermore, Eq. (1.8) describing the Néel relaxation time can be used for the estimation of the SPL. The superparamagnetic behaviour occurs when $k_b T >> K_{eff} V$ is valid and Eq. (1.8) can be rearranged into:

$$\left(\frac{K_{eff}\, V}{k_b T}\right) \geq \ln\left(\frac{\tau_m}{\tau_0}\right) \tag{1.12}$$

For the materials with high K_{eff}, such as *fct* FePt, *fct* CoPt, etc., in order to maintain the thermal stability of a single-domain NPs, which is important, for example, in information storage [24], this ratio should be larger than 60:

$$\left(\frac{K_{eff}\, V}{k_b T}\right) \geq 60 \tag{1.13}$$

The diameter of a NP at the superparamagnetic size limit (D_{SPL}) can be calculated from the following equation:

$$D_{\mathrm{SPL}} = \sqrt[3]{\frac{60\, k_b T_b}{K_{eff}}} \tag{1.14}$$

Because in the literature no information about D_{SPL} for *fcc* FePt can be found, we used experimentally determined T_b and K_{eff} values from the literature for the spherical *fcc* FePt NPs with different sizes and Eq. (1.14) to estimate the D_{SPL}. Because value of K_{eff} is shape dependent [36], therefore, to make more solid comparison, only data for spherical *fcc* FePt NPs were used.

Table 1.1: List of T_b and K_{eff} values from the literature for the spherical *fcc* FePt NPs with different sizes that were used in the caluclation of D_{SPL}.

NPs size	T_b **(K)**	K_{eff} **(J/m^3)**	D_{SPL} **(nm)**	**Ref.**
3 nm	15	3.7 · 105	8.8	[43]
3 nm	15	2.0 · 105	9.2	[11][40]
4 nm	25	2.6 · 105	9.9	[44]
4.6 nm	53	3.6 · 105	8.8	[45]
5 nm	30	1.6 · 105	11.2	[46]
5 nm	26	1.4 · 105	11.4	[36]
8 nm	70	9.0 · 104	11.2	[46]
9 nm	140	1.3 · 105	12.5	[34], [47]

Calculated D_{SPL} values listed in Table 1.1 are in the size range 8.8 – 12.5 nm. Deviation in the results can be contributed to the errors coming from the determination of T_b. Broader size distribution means broader peak in the ZFC curve and, consequently, less accurate determination of T_b. Moreover, the position of T_b depends also on the measurement time, which brings additional error in the calculation. However, from the obtained data we can conclude that D_{SPL} for spherical *fcc* FePt NPs is approx. 10 nm, therefore, in order to keep NPs in the superparamagnetic regime, this size should not be exceeded.

1.2 Fe-Pt Alloy

Among the magnetic NPs, it is mainly superparamagnetic Fe_3O_4 NPs (SPION) that has been studied for the use in biomedical applications. FePt-based alloys with a face-centred cubic (*fcc*) crystal structure represents an alternative, since they possess a three-times-higher bulk saturation magnetization [19] (about 1140 emu/cm^3) when compared to iron oxides [11]. According to the phase diagram of the Fe-Pt, which is shown in Figure 1.5, the equiatomic FePt exists in the ordered *fct* phase ($L1_0$) at low temperature, suggesting that it is a more energetically stable state. In $Fe_{100-x}Pt_x$ alloys deviating from the $35 \leq x \leq 55$ stoichiometry, formation of the stable and chemically ordered cubic structures $FePt_3$ ($L1_2$) and Fe_3Pt ($L1_2$) is expected at temperatures below 850 °C and 1350 °C, respectively. However, in the synthesis with the thermal decomposition of metal salts that were used in the work for this thesis, the kinetic constrains the diffusion reaching the equilibrium phases as set in the phase diagram. Therefore, chemically disordered cubic *fcc* FePt phase is produced [48].

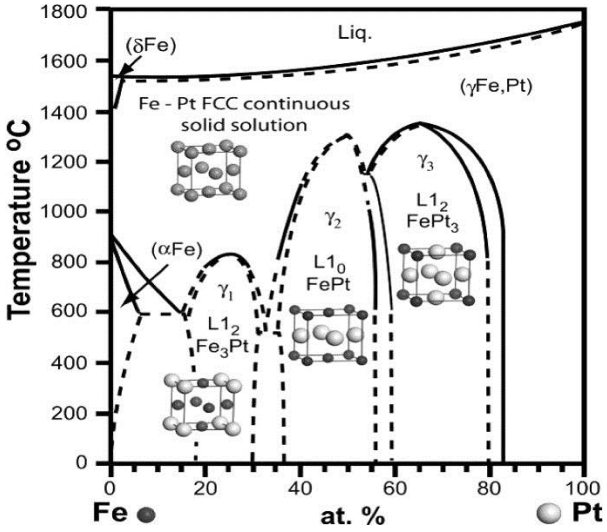


Figure 1.5: Binary phase diagram of Fe-Pt [49]. Reprinted with permission.

FePt NPs with the *fct* crystal structure preserve the ferromagnetic properties at 300 K down to the grain size of 3 nm [19]. This makes *fct* FePt a promising candidate for ultra-high density recording media, but not for the medical applications. Not only that obtaining so small particles is challenging from the synthesis perspective, but also they are way below the optimal size for biomedical applications.

1.2.1 Synthesis of FePt NPs

The chemical synthesis of *fcc* FePt NPs can be divided into the high-temperature and low-temperature route. The first approach is conducted in organic solvents at temperatures above 200°C, while the second is carried out close to room temperature. The latter is often performed in aqueous phases stabilized by amphiphilic molecules [19]. For example, synthesis of FePt NPs in an aqueous phase was carried out as the co-reduction of $FeCl_2$ and H_2PtCl_6 with $NaBH_4$ in a cetyltrimethyl ammonium bromide (CTAB)/water/butanol/octane system [50]. Despite the use of CTAB surfactant, NPs were strongly agglomerated. Another example of an aqueous approach is $FeCl_2/H_2PtCl_6$/hydrazine in a triton/water/cyclohexane system, which again resulted in polydispersed and aggregated FePt NPs [51]. It seems that surfactants used in these aqueous systems cannot sufficiently stabilize NPs, which leads to an agglomeration that can occur during the synthesis or later, in the purification step. Because the low-temperature aqueous route offers poor control over the size and stability of FePt NPs suspension, we selected the first approach, i.e. high-temperature route. It was reported that *fcc* FePt and partially ordered *fct* FePt NPs can be prepared from $Fe(acac)_3$ and H_2PtCl_6 in a solution consisting of tetraethylene glycol that acts as a solvent and polyvinyl pyrolidone (PVP) as a stabilizer [52]. However, such as-prepared FePt NPs are polydispersed and agglomerated.

The first successful synthesis of monodispersed and well separated *fcc* FePt NPs was reported in 2000 [53]. This synthesis was based on the reduction of platinum acetylacetonate $Pt(acac)_2$ and the thermal decomposition of iron pentacarbonyl $Fe(CO)_5$ in high boiling point solvents e.g. dioctyl ether or benzyl ether. The oleic acid (OA) and oleylamine (OLA) were used as stabilizers. It was shown that OA is a coordinative ligand for the Fe atoms (Fe-oleic acid complex) and OLA is believed to coordinate Pt atoms (Pt-oleylamine complex) [54]. In order to replace the $Fe(CO)_5$ which is toxic with less volatile iron precursor, iron acetylacetonate $Fe(acac)_3$ [55]–[57] and iron (III) ethoxide $Fe(OEt)_3$ [54] were also investigated. Among those, in order to have similar Fe and Pt salt precursors, for our work the $Fe(acac)_3$ in the synthesis of FePt NPs was selected.

In order to fine tune the FePt composition the FePt NPs nucleation and growth mechanism was studied [57] and is schematically shown in Figure 1.6. Pt rich nuclei are formed at ~ 160°C due to the reduction of $Pt(acac)_2$. When the temperature is further increased (180-200°C) the thermal decomposition of $Fe(acac)_3$ occurs and Fe cluster species are attached on the Pt nuclei forming a core-shell structure. In this temperature range pure Pt nuclei, Fe oxide particles and Pt-Fe oxide core-shell particles can be detected. The presence of the Fe oxide phase instead of the elemental Fe can be explained as follows. Thermal decomposition temperature of $Fe(acac)_3$ is 182°C and the reduction potential of the used diol (1,2-hexadecanediol) is not high enough to complete the reduction of $Fe^{3+} \rightarrow Fe^0$, but promotes only partial reduction to Fe^{2+}. However, when the temperature is further increased (230°C) the thermal decomposition of $Fe(acac)_3$ leads to carbon monoxide formation (CO), which is a strong reducing agent, and the reduction of the Fe oxide species takes place. Therefore, spherical FePt NPs without Fe oxide can be detected, meaning that the Fe atoms are incorporated in the Pt structure. In addition the catalytic activity of the Pt surface induces the oxidation of CO to CO_2 and promotes the iron reduction. Finally, FePt NPs with homogeneous distribution of Fe and Pt atoms are obtained through the atomic diffusion at high temperature (>250°C).

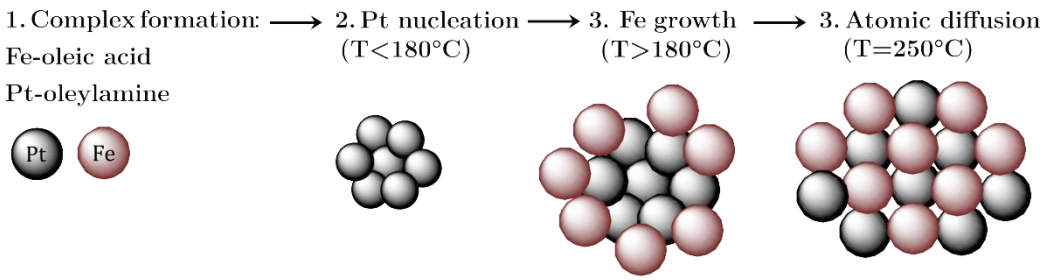


Figure 1.6: Schematic representation of the proposed growth mechanism of FePt NPs.

Besides the concentration of metal precursors ($Fe(acac)_3$ and $Pt(acac)_2$) a very important parameter in the synthesis is also the concentration of the used surfactants (OLA and OA) and the ratio between them. The concentration of the surfactant has a significant effect on the NPs size, while changes in the surfactants ratio influence the NPs morphology. The influence of the surfactant concentration on the NPs size can be attributed to the change in the number of nuclei at the first step of particle formation [46]. An increase in the surfactant concentration to the metal salt concentration most probably results in the formation of a larger amount of stable metal-surfactant complexes like: Fe-oleic acid and Pt-oleylamine complexes. Therefore, an increase in the surfactant concentration is expected to suppress the nucleation process with larger particles being produced. However, the surfactant concentration cannot be increased infinitely because at very high surfactant concentrations the free surfactant molecules can cause flocculation of the already surfactant-stabilized NPs, which leads to NPs agglomeration [46], [58].

The magnetization of the NPs can be manipulated via different synthesis procedures that are known to affect the particle size. One of the approaches that enables further increase of NPs size is the so-called seed-mediated synthesis [59]. In this approach the NPs prepared with a »regular« synthesis procedure are used as the seeds in the second step of the synthesis. The addition of a metal precursor leads to an increase of the NPs size via heterogeneous nucleation on the existing NPs seeds. It is however essential to precisely control the metal salt concentration. According to the LaMer diagram, large addition of metal salts might lead not only to the growth of the NPs but also to the occurence of the homogeneous nucleation, which reflects in a larger polydispersity of the final sample. Therefore, metal salt concentration has to be kept below the threshold concentration for the homogeneous nucleation [60].

Not only size but also shape of the NPs can be varied by changing the reaction conditions. Different surfactants have different binding affinities towards different crystal planes. A combination of such surfactants can be used to suppress growth of one crystal growth and facilitate growth of the others. For example, Wang et al. [61] have demonstrated preparation of FePt nanorods and nanowires using a mixture of OLA and octadecene. Furthermore, size and shape of the nanowires/nanorods can be tailored tuning the ratio of OLA to octadecene. Different binding affinities towards different crystal planes in the *fcc* FePt crystal structure were observed also for the case of OLA and OA. It was shown that the amine group of OLA binds more strongly on the {100} planes than on the {111} planes, which causes the formation of slightly elongated structures. On the other hand, OA binds on both planes equally and therefore spherical structures are formed [61], [62].

Controlled aggregation of individual superparamagnetic NPs into larger »multi-core« clusters can be beneficially used for the improvement of the magnetic properties. It was

already shown on the example of Fe oxide NPs that the formation of »multi-core« NPs leads to an increase in the magnetization due to the increase in the effective magnetic moment with regards to the "single-core" NPs [37]. However, only one report about preparation of "multi-core" FePt NPs can be found in the literature [63]. Authors have shown that "multi-core" FePt NPs can be prepared by changing the amount and the ratio of the used surfactants (OA/OLA). It has been suggested that the availability of Fe could play an important part in causing the NPs to aggregate into "multi-core" FePt NPs. The availability of Fe atoms during the nucleation and growth of NPs can be regulated with the concentration of OA surfactant because it was shown that OA is a coordinative ligand for the Fe atoms [54]. Such FePt "multi-core" NPs were proven to exhibit larger m_s values than their "single-core" counterparts.

1.2.2 Nanoparticles as contrast agents in magnetic resonance imaging

Magnetic resonance imaging (MRI) has been recognized as one of the most important imaging techniques in medicine because of its high spatial resolution, strong soft-tissue contrast and the absence of radiation risk [64], [65]. With this imaging technique we obtain a noninvasively cross-sectional view of a human body by utilizing the nuclear magnetic resonance of protons. In other words, we visualize the water in the body and this is done in all three directions, x, y and z, which gives us a 3D image. All biological tissues are mainly composed of carbon, oxygen, hydrogen and nitrogen atoms. Among them, the most abundant atom in the biological tissue is hydrogen, the majority of which is in water. Hydrogen has the largest and most significant magnetic moment, therefore is used for the visualization in MRI [66]. Hydrogen nucleus contains a positively-charged single proton that precesses around an axis. This spinning generates its own tiny magnetic field, giving the proton its own north and south poles. In the absence of the magnetic field magnetic moments of the hydrogen atoms are randomly oriented (Figure 1.7a). However, when the high external magnetic field is applied, the majority of the atoms align parallel to the direction of the magnetic field (Figure 1.7b). This is called Larmor precession. Then, the radio-frequency pulse with a frequency equal to the Larmor frequency is applied perpendicular to the magnetic field (Figure 1.7c). Consequently, the magnetic moment of the nuclei tilt away from the direction of the magnetic field. Once the radio-frequency pulse is removed, the nuclei return to their equilibrium. This process is known as relaxation (Figure 1.7d) and the time that is needed for this process is called relaxation time. The echo time refers to the time between the application of radio-frequency excitation pulse and the peak of the signal induced in the coil.

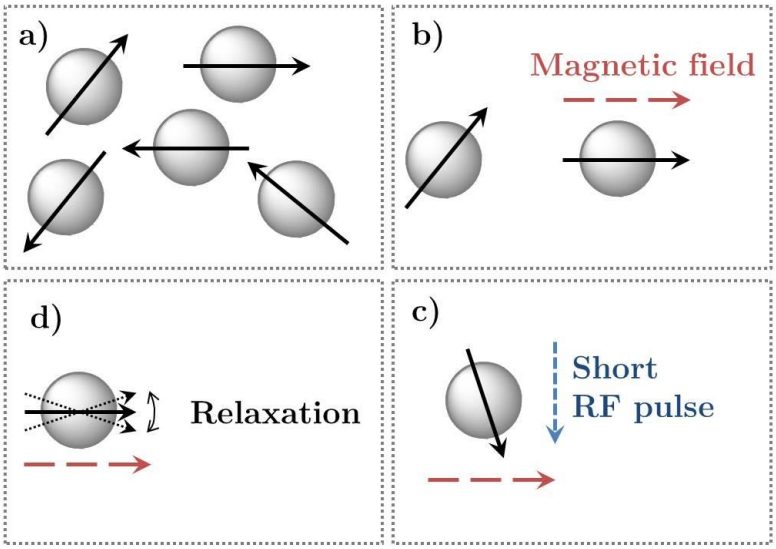


Figure 1.7: Relaxation process of the hydrogen atoms in MRI. a) Hydrogen atoms with randomly oriented magnetic dipoles in the absence of the magnetic field. b) When high external magnetic field is applied, the majority of the atoms align parallel to the direction of the magnetic field. c) Radio-frequency pulse applied perpendicular to the magnetic field tilts nuclei away from the direction of the magnetic field. d) After the removal of the radio-frequency pulse, relaxation occurs and the nuclei return to the direction parallel to the magnetic field.

There are two independent relaxation processes that occur during the relaxation, longitudinal (spin-lattice) or T_1 relaxation and transverse (spin-spin) or T_2 relaxation [66]. T_1 relaxation time ranges from a few hundred milliseconds to a few seconds. Tissues with shorter T_1 relaxation time will appear on the MRI image whiter than tissues with longer T_1 relaxation time. T_2 relaxation time ranges from a few milliseconds to a few hundred milliseconds. Tissues with longer T_2 relaxation time will appear brighter than that of shorter T_2 relaxation time. MRI images can be T_1 weighted images or T_2 weighted images. In general, anatomical details can be depicted very well in T_1 weighted images whereas T_2 weighted images are useful for identifying pathological conditions. In order to improve the contrast of the image, a contrast agent are applied during the imaging. Depending on which relaxation process they influence (T_1 or T_2), we classify contrast agents in two groups, T_2- or T_1-type contrast agents, depending on their relaxivity coefficients (r_2 or r_1, $mM^{-1}\ s^{-1}$), which are the terms that define the ability to accelerate the relaxation rates (R_2 or R_1, s^{-1}) [64]. The r_2/r_1 ratio is an important parameter to estimate whether a given contrast agent can serve as a T_1 or T_2 contrast agent. T_1 MRI contrast agents need to have a high r_1 and a low r_2/r_1 ratio, e.g., paramagnetic chelates (e.g. Gd^{3+} paramagnetic complex) usually have r_2/r_1 ratios of 1-2. In contrast, to be an effective T_2 MRI contrast agent, a high r_2 value is a prerequisite, with the r_2/r_1 ratio equal to 10 or even more [67]. Depending on the magnetic properties and surface effects the magnetic NPs can serve as effective T_2 or T_1 MRI contrast agents [68]. The relationship between the magnetization and the T_2 relaxation rate R_2 is described as follows.

$$R_2 = \frac{1}{T_2} = \frac{256\ \pi^2\gamma^2}{405}\ {m_s}^2\ V \frac{r^2}{D\ \left(1+\frac{L}{r}\right)} \tag{1.15}$$

where γ is the gyromagnetic ratio of the protons, m_s is the saturation magnetization of the NP, V is the NP's volume fraction, r is the radius of the magnetic NP, D is the diffusion coefficient of the water molecules, and L is the thickness of the surface coating [69]. The equation states that the shortening of T_2 is directly proportional to the square of the saturation magnetization, which suggests that systems exhibiting large saturation magnetization, like FePt, would be of interest. A bulk saturation magnetization (M_s) is an intrinsic magnetic property; however, by reducing the size of the material to the nanoscale, the surface effects on the magnetization (m_s) become significant or even decisive [64]. The size of the magnetic NPs used for MRI is therefore very important, since it influences the m_s and, consequently, the R_2. Theoretical studies indicate that there are three different NP size regimes: i) the motional average regime (MAR), ii) the static dephasing regime (SDR) and iii) the echo-limiting regime (ELR). In the MAR regime the diffusion length of the proton, i.e. average distance that the proton travels during the one echo time, is comparable or larger than the scale of the magnetic field inhomogeneities that arise from one particle. This means that T_2 values are not dependent on the echo time. This is valid for relatively small NPs and in this regime R_2 increases with the NP size increment. However, at a certain size the R_2 plateau is reached and NPs enter in the so-called SDR. For the case of Fe oxide NPs it was calculated that the plateau is reached at NPs diameter of approx. 50 nm [70]. In SDR regime proton diffusion is not a dominating factor for the signal decay any more, because the magnetic field coming from the particles is stronger. Therefore, R_2 becomes independent on proton diffusion and will not increase with the particle size [68]. With any further size increment NPs enter into ELR where an echo-dependant decrease of R_2 is observed. Accordingly, the highest R_2 is achieved for the NPs in the SDR, but the size of the NPs used for MRI usually falls into the MAR in order to limit their uncontrolled aggregation, induced by strong ferromagnetic dipolar interactions [64].

One of the options for improving the NPs' effect on the T_2-relaxation times is to use the materials with high saturation magnetization and further to produce controlled clusters of such magnetic NPs with an increased m_s to fit the SDR regime. The enhancements of the longitudinal and transverse relaxation rates of the protons in the water are quantified by the relaxivities r_1 and r_2, respectively. Success in increasing the r_2 was achieved for iron oxide NPs (7.4 nm) combined into clusters (163 nm) in block-polymer micelles [71], where the increase in the loading of iron oxide NPs in the micelles from 12 to 42% causes an increase in the r_2 from 90 to of 229 $mM^{-1}s^{-1}$, which surpasses that of commercial Feridex® (41 $mM^{-1}s^{-1}$ at 1.5 T, 37 °C). Alternatively, silica can be used to synthesize the nanoclusters, and improvements in r_2 were achieved for Fe-oxide NPs [72].

1.2.3 Magnetic manipulation of nanoparticles

Manipulation of magnetic particle suspensions has found place in several applications ranging from self-assembled manufacturing to the life science analytical tools [10]. Because external magnetic field can act on larger distances, the magnetic manipulation has an advantage to be a non-contact technique and, therefore, biologically inert. This fact led researchers to propose the use of magnetic carriers to target specific sites, e.g. cancerous tumours, within the body. This approach is called magnetic drug delivery and has two advantages. First, the amount of distribution of the cytotoxic drug in the body is reduced, reducing also the possible side-effects. And second, the drug dosage is reduced due to the more efficient and localized targeting of the drug [10]. Moreover, if the magnetic entity can be removed from the tissues after the treatment using the external

magnetic field, the accumulation of the NPs in different tissues in the body can be minimized. Furthermore, it was demonstrated on mice that magnetic NPs can be engineered to capture free-floating ovarian cancer cells [73]. This was done by using an outside-the-body magnetic filtration device, which can remove a large portion of the cancer cells that often create secondary tumors in a single treatment.

Magnetic NPs can be separated from the flowing liquid through a region in which there is a magnetic field gradient which can attract the NPs via the magnetic force. For the successful manipulation of the magnetic NPs the magnetic force on the magnetic NPs must exceed the fluidic drag force [10]. The hydrodynamic drag force (F_{d}) can be calculated using Stokes' law for drag on a sphere:

$$\vec{F}_d = = \ -6\ \eta\ r_p(\overrightarrow{\nu_p} - \overrightarrow{\nu_f}), \tag{1.16}$$

where η is medium viscosity, r_{p} is diameter of NP, $\overrightarrow{\nu_p}$ is velocity of the particle and $\overrightarrow{\nu_f}$ is velocity of the media. This definition is valid in a laminar flow with a Reynolds number smaller than 1. The minimum magnetic force ($\overrightarrow{F_m}$) needed to manipulate a particle must exceed the hydrodynamic drag force ($\overrightarrow{F_d}$) of the NPs under the dynamic flowing conditions. The magnetic force $\overrightarrow{F_m}$ on a particle due to an external magnetic flux $\vec{B}$ can be assumed to be equal to the force experienced by a point-like magnetic dipole ($\vec{m}_p$). This magnetic force is defined by:

$$\vec{F}_m = \ \nabla(\vec{m}_p \cdot \ \vec{B}), \tag{1.17}$$

If we equalize both equations for the drag and the magnetic force, the required z component of the magnetic field gradient $\frac{dB_z}{dz}\,[T/m]$ can be calculated. Since the magnetic flux decreases exponentially with the distance, it is important to achieve sufficient magnetic forces for a controlled manipulation on larger distances. This can be done by using high magnetic field gradient externally or using magnetic implants. Those can be located in the vicinity of the target using minimally invasive surgery [74]. Thus, a strong enough local magnetic field can be created to overcome the hydrodynamic forces in the blood stream [75]. As an example, gold-coated Nd–Fe–B magnets were already inserted into the kidneys of New Zealand rabbits and were proven to be more effective at attracting the nanoparticles than externally positioned magnets [76]. Furthermore, according to the Eq. (1.17) high $\overrightarrow{F_m}$ can be achieved with a selection of the material with a high magnetic moment.

1.3 Surface Functionalization of NPs

NPs possess a large fraction of surface atoms per unit volume; therefore, also the total surface energy increases with decreasing the dimensions. For example, when the particles change from a centimeter size to a nanometer size, the surface area and the surface energy increase by seven orders of magnitude [77]. Surface atoms possess fewer nearest neighbours and lower coordination numbers. This creates dangling bonds on the surface. Consequently, the bond distance between the surface atoms and the sub-surface atoms becomes smaller than is the bond distance between the interior atoms. This makes surface atoms more unstable or reactive. Hence, those atoms possess an extra energy, which is called surface energy [77]. To decrease the overall surface energy the individual

NPs can combine into larger structures via sintering, where individual NPs merge together, or via Oswald ripening, where larger structures grow in the expense of smaller ones. In general, sintering is negligible at room temperature, while Oswald ripening can occur at any temperature. Agglomeration of NPs is another way to reduce the systems′ overall surface energy. In agglomerates the NPs are connected together through chemical bonds and physical attraction forces at interfaces. Once formed, agglomerates are very difficult to disperse [77]. Therefore, it is very important to prevent NPs from agglomeration when dispersed in a liquid because stable colloidal suspensions are crucial for successful implementation of NPs in numerous applications. One of the biggest challenges in the fabrication of NPs is to overcome this surface energy and retain NPs's size small. In that way the special physical and chemical properties that originate from their small size are preserved.

The most important factors that influence the NPs colloidal stability are the shape and the NPs size and their surface characteristics, which dictate the inter-particle and the particle-solvent interactions. When a solid particle is immersed in a polar solvent or electrolyte, a surface charge is developed, which is determined by the ions adsorbed on the NP's surface. In the solution, both the surface charge determining ions and the counter ions, which are oppositely charged, exist. In the proximity of the solid surface the distribution of both, charge determining ions and counter ions, is inhomogeneous with large variation in concentration, which leads to a formation of a so-called double layer structure. Electric double layer at a charged interface in an aqueous solution is schematically shown in Figure 1.8. The thickness of the double layer is typically around 10 nm or larger. Double layer consists of two layers, Stern layer and the diffuse layer (or Gouy layer) that are separated by the Helmholtz plane [77]. Stern layer is the layer between the NP surface and the Helmholtz plane. At the surface of NP the concentration of the charge determining ions is the highest and the electric potential drops linearly through the Stern layer, which contains also solvent and counter ions. Beyond the Helmholtz plane is the diffuse layer that extends until the counter ions reach the average concentration in the solvent. In this layer the counter ions diffuse freely and the electric potential does not reduce linearly. Zeta potential is defined as the average electrostatic potential at the hydrodynamic plane of shear, somewhere between the Stern plane and the end of the diffuse layer. The latter is normally considered to be 0.2 nm from the surface [78].

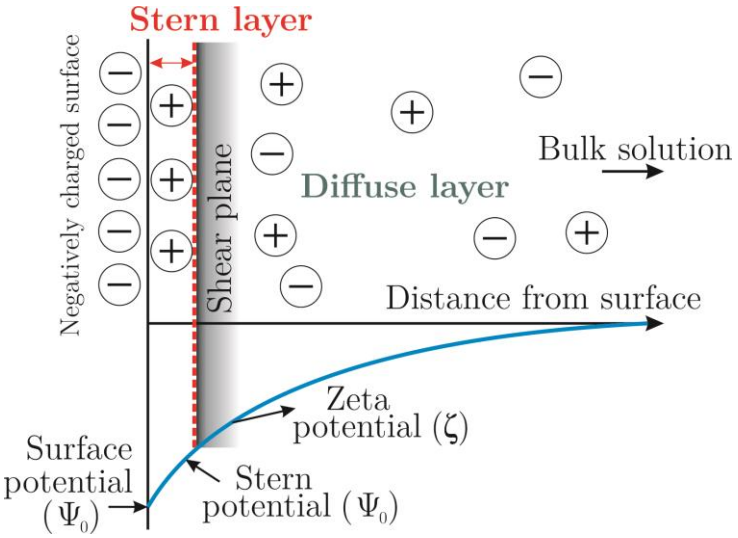


Figure 1.8: Schematic representation of the electric double layer at a charged interface in an aqueous solution.

When more NPs are present in the solution, interactions between NPs occur. In the case that two particles are far apart, there is no overlap of two double layers and, therefore, the electrostatic repulsion between two particles is zero. On the other hand, if the distance between two particles is reduced to extent that two double layers start to overlap, a repulsive force develops. The total interaction between two particles in the suspension is the combination of van der Waals attraction forces and electrostatic repulsive forces. Far from the NP surface, both van der Waals and repulsive forces reduce to zero. Van der Waals force is a weak force and becomes significant only at a very short distance. Moreover, in the suspension of NPs Brownian motion also plays and important role and it ensures that NPs are colliding with each other. A combination of van der Waal forces and Brownian motion can results in an agglomeration of NPs. Therefore, in order to obtain a stable suspension, repulsive barrier has to be introduced into the system. At sufficient high repulsive barrier, the collisions of two NPs will not overcome this barrier and agglomeration will not occur. In the theory of colloidal chemistry such repulsive forces can be achieved by electrostatic or steric stabilization.

The electrostatic repulsive force is formed when the electrical double layers of two particles overlap. The resulting repulsion forces between the particles decay exponentially with the inter-particle distances. This **electrostatic stabilization** of the NPs can be achieved by introduction of charged functional groups on the NP's surface. The protonation state of a functional group is strongly pH dependent, hence it follows that also the electrostatic repulsion force is pH dependent. Therefore, the molecule that will be used for the surface functionalization should be carefully selected to fulfil the requirements of the pH range, where suspension is expected to be stable. Surface potential is not directly measurable. However, measurement of the zeta potential is available and is currently the simplest and most straightforward way to characterize the surface of charged colloids. Larger absolute value of zeta potential indicates good suspension stability due to the strong electrostatic repulsion force. On the other hand, if the zeta potential value is close to zero, the particles become unstable and are likely to aggregate. In zeta potential measurements, an electrical field is applied across the sample and the movement of the charged NPs (electrophoretic mobility) towards the oppositely charged electrode is measured. Light scattering is one of the most commonly used techniques for determining the electrophoretic mobility of particles.

Steric stabilization is achieved by adsorption of large molecules at the particle surface, such as polymers or surfactants, which provide a protective layer. The proposed mechanism of stabilization is as follows. When two particles approach one another, the attached polymers can interact only when the particles are separated for less than twice the thickness of the polymer layer. With decrease in the inter-particle distance the number of the adsorbed molecules in the inter-particle space increase tremendously. This causes a decrease in entropy (an increase of the Gibbs free energy), which is thermodynamically not favorable, and causes repulsion between two particles. When the distance between two particles is less than the thickness of the polymer layer, a further reduction in the distance produces a repulsive force and an increase in the Gibbs free energy. Steric interaction is a short range interaction and does not significantly depend on the particle size. Colloidal stability is mainly determined by parameters such as polymer concentration, average chain length, the solubility of the polymer and temperature [79].

Electro-steric stabilization is a combination of steric and electrostatic stabilization. Electrosteric stabilization can be achieved by introducing polyelectrolytes on the particle surface. Polyelectrolytes are polymers whose repeating units contain functional group that dissociates in aqueous solutions, making the polymers charged. When such a polymer is attached on the charged particle surface, an electric potential adjacent to the

particle surface is retained [77]. In that way, when two particles approach one another, agglomeration is prevented by both, electrostatic and steric stabilization.

In the scope of this work, both types of stabilization, i.e. electrostatic and steric, were explored to obtain stable NPs suspension. First, FePt NPs were functionalized with dopamine-based ligands that provide effective electrostatic stabilization. Second, steric stabilization was used for the stabilization of hybrid FePt/SiO_2/Au NPs with polyethylene glycol (PEG).

1.3.1 Functionalization of FePt NPs

Stabile NPs suspensions are a prerequisite for further biological applications, where besides the suspension stability, a coating of the material should also provide NP's biocompatibility. When using FePt NPs for biomedical applications, the positive effects on human health have to be balanced with the possible toxicity [80]. Up to now, only a limited number of studies have been performed on FePt NPs [80]–[82], with no significant cytotoxic effect. In order to evaluate the performance of the as-synthesized FePt NPs for biomedical applications, water suspensions are desired, which pose an additional functionalization step, since the syntheses of FePt NPs are performed in organic solvents. The as-synthesized FePt NPs are hydrophobic due to the use of oleylamine (OLA) and oleic acid (OA) as the surfactants. Only few attempts were reported for the preparation of water suspensions of FePt NPs via ligand exchange reaction using tetramethylammonium hydroxide [47], cysteamine [18] and mercaptoalkanoic acids [83].

1.3.1.1 Functionalization of FePt NPs with dopamine-based ligands

Ligand that is selected for the ligand exchange reaction has to provide a strong coordination to the NP surface in order to replace initial ligands and to enable stabilization of NPs for a longer period of time. One of the candidates for this task is a dopamine-based ligand. It was demonstrated on the example of iron oxide NPs that dopamine-based ligands show strong interaction between the vicinal diol groups and the iron oxide surface, which makes ligand exchange possible and NPs are transfered from organic to water phase [84]. Two different biocompatible dopamine-based ligands, i.e. hydrocaffeic acid (HCA) and zwitterionic dopamine sulphonate (ZDS), will be described in this section.

HCA was selected as a ligand due to its natural origin. Polyphenol-rich foods, such as vegetables and fruits, contain HCA [84], [85]. Moreover, HCA is a metabolite of caffeic acid and with potent antioxidant properties, even more effective than the caffeic acid. This ligand was found to be suitable for Fe oxide NPs [84] due to the strong interaction between the vicinal diol groups and the iron oxide surface, as well as the hydrophilicity of the carboxyl group, but no attempts to functionalize the FePt NPs with it were reported yet. Furthermore, it was shown that Fe oxide NPs coated with HCA has no immune-stimulating properties for dendritic cells, which is necessary for NPs to have sufficient half-life in blood [24]. Structural formula of HCA is shown in Figure 1.9a.

The benefits of using the ZDS ligand lie in its chemical character, since it is composed of three active moieties [86]. The dopamine part of the molecule provides a strong coordination to the NP surface [87], the sulfonate group (R-SO_3^-) is responsible for the high water solubility, and the combination of a quaternary amine group (NR_4^+) and a sulfonate group gives the ligand a zwitterionic character, which enables its buffer

capacity, i.e., a high pH stability, which decreases the NPs' non-specific interactions with proteins. Structural formula of ZDS ligand is shown in Figure 1.9b.

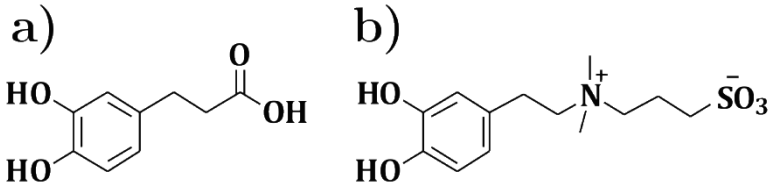


Figure 1.9: Structural formula of a) hydrocaffeic acid (HCA) and b) zwitterionic dopamine sulphonate (ZDS) ligand.

1.4 Plasmonic Properties of Au Nanostructures

Au NPs are interesting for several applications in the fields of catalysis [102], electronics [103], photovoltaics [104], biosensing [105] and photo-thermal therapy [20]. Many of those applications are inspired by the unique light induced plasmonic properties of Au nanostructures, which derive from the surface plasmon resonance (SPR). Firstly, this chapter will provide an overview of the fundamentals of the SPR phenomena in spherical noble metal NPs (focus on Au NPs) by using Mie theory and expansion of Mie theory to other shapes of Au NPs. Secondly, factors such as dielectric constant, material, size and shape of NPs that influence the SPR will be discussed with the view towards the final application of photo-thermia.

1.4.1 Surface plasmon resonance

The term plasmon refers to a longitudinally collective oscillation of the electron plasma relative to the crystal lattice. In general, one has to distinguish between bulk, surface and localized surface plasmon resonance at the surface of NPs (Mie resonance) [106]. The *bulk plasmon* denotes a collective excitation of the electron gas in the bulk metal. Due to its longitudinal nature of the excitation of bulk plasmons the interaction with light is not possible. *Surface plasmons* can be found on the surface of the metal and can be optically excited. The mobility of the electrons in a plane parallel to the surface is high. However, due to the surface border the mobility is limited in the perpendicular direction. If the size of metal NPs is smaller than the wavelength of light, then all atoms in the particle can be collectively excited, which is called *localized surface plasmon resonance* (LSPR). Consequently, the electric field near the particle's surface is greatly enhanced, which is schematically shown in Figure 1.10. Plasmon resonant frequency has a maximum in a visible wavelengths for noble metal NPs [106]. This reflects in a high absorption in the visible region (SPR band) and is also referred to as Mie resonance from the name of one of the most prominent contributors to the SPR theory: Gustav Mie [107]. All metals feature this property; however, Au, Ag and Cu exhibit the strongest SPR band. The SPR band intensity and wavelength depends on the factors affecting the electron charge density on the particle surface such as metal type, particle size, shape, structure, composition, and the dielectric constant of the surrounding medium [105].

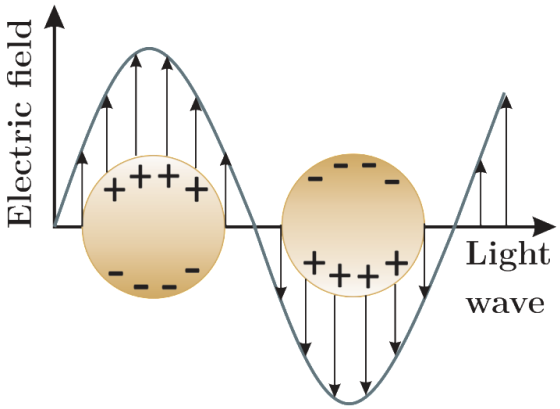


Figure 1.10: Schematic of electronic cloud displacement in NPs induced by an oscillating electric field.

Gustav Mie proposed an analytical solution to Maxwell's equations that describes the scattering and absorption of light by spherical particles [107]. The optical properties of the metal particle in terms of absorption and scattering cross-sections σ_{abs} and σ_{sca} are related to the intensity loss of the incident light due to absorption and elastic scattering. Both absorption and scattering contribute in a total cross-section:

$$Q_{\text{abs}} = Q_{\text{ext}} - Q_{\text{sca}} \tag{1.18}$$

For very small particles ($d<<\lambda$), absorption and scattering cross-sections σ_{abs} and σ_{sca} can be written as:

$$Q_{sca} = \frac{32\, V^2 \pi^4\, V\, \varepsilon_m^2}{\lambda^4} \frac{(\varepsilon_1 - \varepsilon_m)^2 + (\varepsilon_2)^2}{(\varepsilon_1 + 2\varepsilon_m)^2 + (\varepsilon_2)^2} \tag{1.19}$$

$$Q_{ext} = \frac{18\ V\, \varepsilon_m^{3/2}}{\lambda} \frac{\varepsilon_2(\lambda)}{(\varepsilon_1(\lambda) + 2\varepsilon_m)^2 + \varepsilon_2(\lambda)^2} \tag{1.20}$$

where V is the particle volume and ε_m is medium's dielectric function and is related to the refractive index of the medium $\varepsilon_m = n_m^2$. Complex metal dielectric function ε is composed of real $\varepsilon_1(\omega)$ and imaginary part $\varepsilon_2(\omega)$ and is given by $\varepsilon = \varepsilon_1(\omega) + i\varepsilon_2(\omega)$ and is frequency (ω) dependent. The real part of the dielectric constant of the metal determines the SPR position and the imaginary part determines its bandwidth. The extinction cross-section will be maximized when $\varepsilon_1 = -2\varepsilon_m$. This explains the dependence of the SPR extinction peak on the surrounding dielectric environment. For example, for Au particles in water ($\varepsilon_m \approx 1.7$) with a diameter in a range 5 - 15 nm, the expected wavelength where $\varepsilon_1 = -2\varepsilon_m$ is about 520 nm. This coincides with the experimentally observed absorption spectrum of Au colloid. The SPR peak wavelength's dependence on the dielectric function of the medium can be described as:

$$\varepsilon_1 = 1 - \frac{\omega_p^2}{\omega^2 + \gamma^2} \tag{1.21}$$

Plasma frequency (ω_p) is a material property that is based on the number density of conduction electrons, and γ is the damping parameter of the bulk metal (scattering frequency of the electron as it travels through the metal). For visible and near-infrared frequencies, $\gamma << \omega_p$ so the above equation can be simplified to:

$$\varepsilon_1 = 1 - \frac{\omega_p^2}{\omega^2} \tag{1.22}$$

Using this expression for ε_1 and setting the resonance condition $\varepsilon_1 = -2\varepsilon_m$, one obtains the expression for the SPR peak frequency (ω_{max}):

$$\omega_{max} = \frac{\omega_p}{\sqrt{2\varepsilon_m + 1}} \tag{1.23}$$

Conversion from frequency to wavelength via $\lambda = 2\pi c/\omega$, where c is the speed of light, and then from dielectric constant to index of refraction via $\varepsilon_m = n^2$ gives this useful correlation:

$$\lambda_{max} = \lambda_p \sqrt{2n_m^2 + 1} \tag{1.24}$$

where λ_{max} is the SPR peak wavelength and λ_p is the wavelength corresponding to the plasma frequency of the bulk metal [106]. With increasing the particle size the SPR peak wavelength is red shifted and also the intensity is increased [108]. For example, from the UV-Vis absorption spectra shown in Figure 1.11 it can be seen that 9, 22, 48, and 99 nm large Au NPs in water have SPR peak at 517, 521, 533, and 575 nm, respectively. For particles larger than 100 nm, the absorption band is strongly broadened due to the dominating contributions from higher order electron oscillations. Furthermore, the maximum red-shift obtained for spherical Au NPs is approx. 600 nm. Beyond this the absorption drops to negligible amounts due to the reduction of the dielectric function of gold at longer wavelengths.

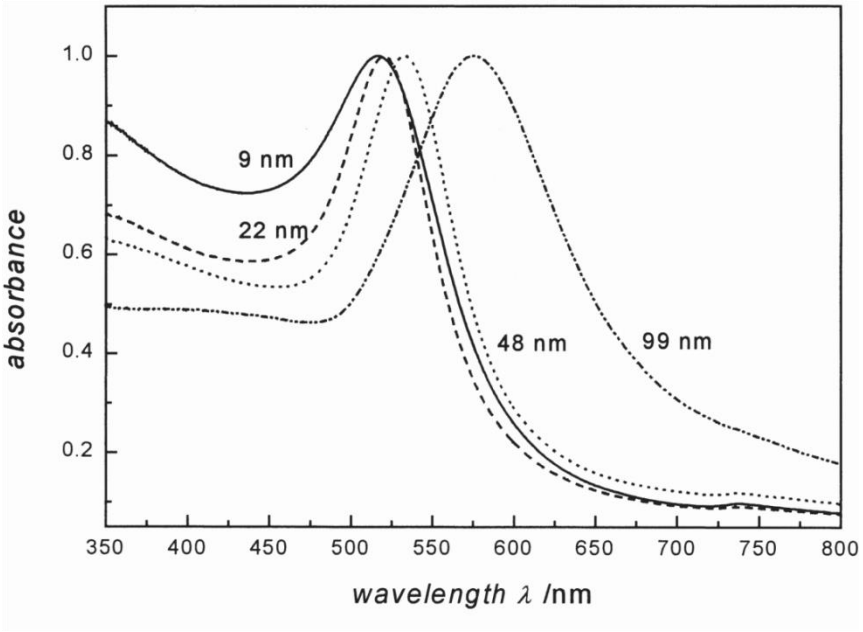


Figure 1.11: UV−Vis absorption spectra of 9, 22, 48, and 99 nm Au NPs in water. All spectra are normalized at their absorption maxima, which are 517, 521, 533, and 575 nm, respectively. Reprinted with permission [108].

Mie theory holds in terms of spectra for relatively large particles (>3 nm for gold) but does not agree with the experimental results when applied to the smaller sizes where quantum effects are predominant and, consequently, no SPR is observed [109]. Already for a 5 nm particles the plasmon oscillation is strongly damped and its absorption becomes weak and broad, however, it completely disappears for NPs less than about 2 nm in diameter. When the number of atoms in a cluster becomes so small the fundamental assumption of infinite lattice periodicity fails and a continuous energy level band will separate into individual levels [110]. Furthermore, the smaller the particles, the larger is the energy level spacing between the adjacent levels. This effect is very pronounced for semiconductor NPs where NPs with diameter of several nanometers are expected to undergo the transition from the bulk to the quantum confined state. Quantum size effects also occur in metal NPs. In order to observe the localization of the energy levels, the level spacing has to exceed the thermal energy (about 26 meV), which occurs when the size of metal NPs is well below 2 nm [110]. In semiconductor NPs, the energy separation between the completely filled valence band and the empty conduction band is of the order of a few eV and increases rapidly with decreasing size. However, in a metal, the conduction band is half filled and the density of energy levels is so high that a noticeable separation in energy levels within the conduction band is observed in very small NPs, i.e. when the NP is composed of just a few atoms (N = 100) [110]. Thus, in metal NPs quantum size effects become predominant at such small sizes (< 2 nm in diameter).

The energy loss of electromagnetic wave after passing through a matter results from two contributions: absorption and scattering. Light absorption results from the photon energy dissipation due to inelastic processes. Light scattering occurs when the photon energy of the incident light causes electron oscillations in the material and photons are emitted in the form of scattered light either at the same frequency as the incident light (Rayleigh scattering) or at a shifted frequency (Raman scattering) [20]. Presence of the SPR oscillation strongly enhances the light absorption and scattering, which are 5-6

orders of magnitude stronger than most strongly absorbing organic dye molecules or than the emission of most strongly fluorescent molecules, respectively [105].

The optical absorption and scattering in NPs is strongly depends on their size. For smaller NPs, e.g. 20 nm Au NP, the main contribution to the total extinction is coming from the absorption. When the size of NPs increases to 40 nm, also the scattering appears. For larger NPs (> 80 nm) both, absorption and scattering, contribute to the total extinction in similar degrees [105]. Taking all this into consideration the size of the Au NPs determine their biomedical applications or vice versa for a certain bio application a certain NPs size should be selected. For example, for imaging, larger NPs are preferred because of higher scattering efficiency, whereas for photo-thermal therapy, light should be efficiently converted into the heat, which can be achieved with smaller NPs due to their high absorption.

The position and intensity of SPR band can also be tuned by changing the shape of Au NPs. Richard Gans extended the Mie theory with a geometrical factor which is valid for spheroidal particles of any aspect ratio in the small particle approximation, meaning that the NPs size is much smaller in comparison to the wavelength of light [111]. TEM images of Au nanorods with aspect ratios of 2.4, 4 and 6 are shown in Figure 1.12a. Changes in the absorption spectra are consistent also with the color of the Au nanorods suspension. In Figure 1.12b it is demonstrated that the variation in the aspect ratio of nanorods from 2.4 to 5.7 reflects in the suspension color change from green to red. Gans theory predicted that SPR band is split into two bands if the shape of NP changes from spheres to rods. Strong absorption band in NIR region appears due to the electron oscillations along the long axis (longitudinal band) and a second, weaker band in the visible region at a similar wavelength to that of spheres (transverse band). Transverse band is insensitive to the size change (Figure 1.12c), while the longitudinal band is red shifted with increasing the aspect ratio of rods. Linear proportional relationship between the longitudinal SPR absorption maximum and the aspect ratio of nanorods R (length/width) in aqueous solution was proposed in the form of an equation:

$$\lambda_{\max} = 95\mathrm{R} + 420, \tag{1.25}$$

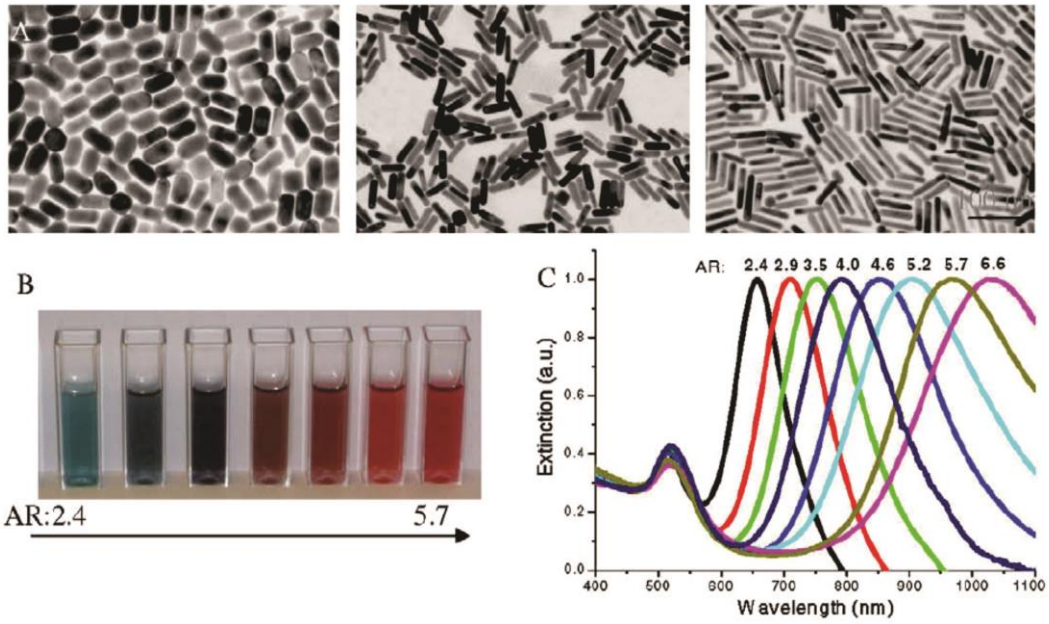


Figure 1.12: Tunable optical properties of Au nanorods by changing the aspect ratios. Au nanorods of different aspect ratios exhibit a) different dimensions as seen by TEM, b) different color and c) different SPR wavelength. Reprinted with permission [112].

Another extension of the Mie theory was done for the core-shell NPs. For the calculation of the extinction cross-section for the small-core shell NP both, complex dielectric function of the core $\varepsilon_{\text{core}}$ and that of the shell $\varepsilon_{\text{shell}}$ should be considered, as well as the volume fraction of the shell layer and the radius of the core [113]. Equation for the calculation of the Q_{ext} for the core-shell NPs is as follows:

$$Q_{ext} = 4\pi r^2 k\, Im\left\{\frac{(\varepsilon_{shell}-\varepsilon_m)(\varepsilon_{core}-2\varepsilon_{shell})+(1-g)(\varepsilon_{core}-\varepsilon_{shell})(\varepsilon_m+2\varepsilon_{shell})}{(\varepsilon_{shell}+2\varepsilon_m)(\varepsilon_{core}+2\varepsilon_{shell})+(1-g)(\varepsilon_{shell}-2\varepsilon_m)(\varepsilon_{core}-\varepsilon_{shell})}\right\}, \quad (1.26)$$

where r is the radius of the coated particle, k is the wavenumber, g is the volume fraction of the shell layer and ε_{core}, ε_{shell} and ε_m are the complex dielectric functions of the core material, shell material and surrounding medium, respectively.

All equations listed in this chapter can serve as a powerful tool for the theoretical prediction of the optimal size and shape of the nanostructures in order to achieve desirable optical properties.

1.4.2 Photo-thermal therapy using Au nanostructures

As already mentioned above, in small Au nanostructures the absorbed photon energy is rapidly converted into heat, which is called the photo-thermal effect. Conversion of absorbed light into the heat happens through the sequence of events that will be described in this section and is schematically shown in Figure 1.13. After the exposure of Au NPs to the light, the collective electron oscillation or SPR takes place. The time scale on which the decay of the SPR occurs is defined with the dephasing time and is on the order of 4 - 20 fs. Dephasing time is a function of particle size, shape and its dielectric

properties. Dephasing of the SPR leads to the absorption of photons. This deposited energy creates excited electrons that are spread over different levels in the conduction band. This energy can also cause interband transitions (transition between the conduction and valence bands - electrons and holes; blue shift of the LSPR), or the intraband transitions (transitions between the quantized levels within the conduction or valence band; red-shift of the SPR). Next, the excited electrons rapidly equilibrate via electron-electron scattering on a few 100 fs time scale to create a hot electron distribution. Hot electrons are electrons that have gained very high kinetic energy. The hot electron distribution then relaxes via phonon emission (electron-phonon interactions) in a few picoseconds, resulting in a hot lattice with a temperature rise on the order of a few tens of degrees. Finally, the hot lattice cools off by passing its heat to the surrounding medium via phonon-phonon relaxation within ~ 100 ps [12]. In order to allow heat dissipation from particles to surrounding medium the continuous wave laser should be used. High energy pulsed laser generally leads to particle structure changes and ablation due to rapid massive heat creation in a very short time [105].

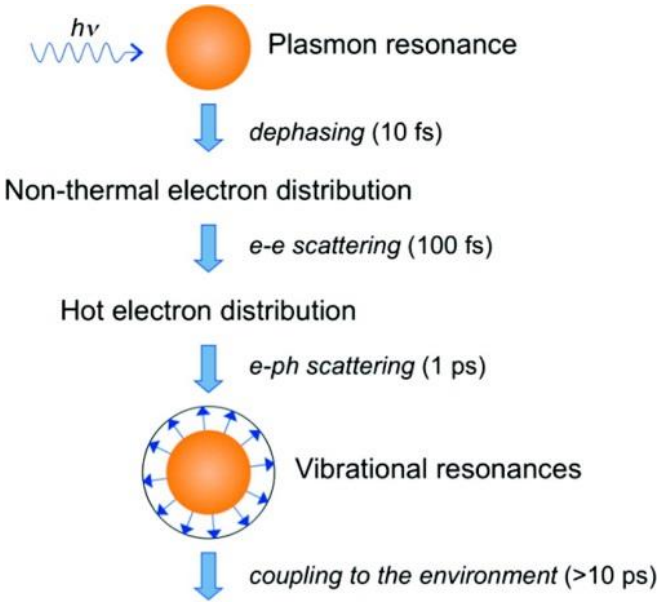


Figure 1.13: Sequence of events and approximate time scales following absorption of photons by a metal nanoparticle [12]. Reprinted with permission.

This conversion of light into the heat allows the successful use of Au NPs in photo-thermal therapy for the selective ablation of targeted cells, where laser excitation is used as the source of the light. In order to use Au NPs most effectively for photo-thermal therapy, the absorption peak needs to be shifted either to the region of the first biological window in the near-infrared region (NIR) at around 800 nm or the second biological window at around 1750 nm, where the penetration of light into the tissue is at a maximum [22]. As such, Au NPs were fabricated in the form of rods or shells, which enabled relatively simple positioning of the absorption peak by changing the dimensions and morphology of the appropriate nanostructures [105]. Furthermore, the heating rate can be controlled by varying the power of the laser and by the concentration of the photo-thermally active NPs in the target tissue. In the concentration range we are limited with the maximum concentration of the NPs that can be internalized in the cell. Selection of the appropriate power of the laser is of vital importance. Power of the laser should be selected in that range that irradiation of the tissue without NPs does not show

any heating effect in order to reduce a possible side effect, while NPs-containing tissues will undergo significant increase in the temperature.

1.4.3 Nanostructures with combined magneto-optical effect

Combined magnetically and optically active hybrid nanosystems were up to now prepared on the basis of Fe_3O_4-Au nanostructures with different morphologies, e.g. Fe_3O_4-Au core/shell NPs, with a superparamagnetic response and a significant absorbance in the NIR region of the light [114]. Only few reports can be found in the literature where superparamagnetic FePt component is combined with the Au nanostructure. Polycrystalline FePt-Au tadpole-, dumbbell, bead- and necklace-like heterostructures were prepared by growing Au NPs on FePt nanorods [115] with the aim to explore their catalytic activity. However, no effort was put into the investigation of its biomedical potential. Furthermore, synthesis of FePt/Au core/shell NPs was reported [44], [116]. However, due to their small size and, consequently, non-optimal core-to-shell ratio, the maximum absorption of the light was obtained in the visible spectrum, which is not suitable for the photo-thermal therapy, however besides the synthesis no further tests were performed on these FePt/Au core/shell NPs. Optimization of the core-to-Au shell ratio is the key factor to shift the maximum absorption of the light into the NIR region. For example, addition of an intermediate layer between the core and the Au shell can be an effective approach to fine tune the core-to-shell ratio and, consequently, position of the absorption maximum. In order to implement this literature suggests a SiO_2 layer as the intermediate layer. The choice of SiO_2 as the material for the intermediate layer is beneficial, because of its biocompatibility, the possibility for subsequent functionalization and the easy regulation of the coating process [88], [89]. Further, it is believed that the optimum size for NPs involved in biomedical applications ranges from 20 nm to 100 nm. NPs in that optimum size range are thought to be easily internalized by the cells [117]. Therefore, controlling the size of the SiO_2 intermediate layer between the FePt core and the Au shell is of vital importance if the goal is to achieve a suitable size for biomedical applications and, at the same time, to shift the SPR peak into the range of the NIR spectrum (i.e., the biological window).

1.4.3.1 SiO_2 coating of FePt NPs

SiO_2 layer was introduced on the surface of FePt NPs not only to prepare stable water suspension, but also to obtain appropriate core-to-shell ratio of final hybrid FePt/SiO_2/Au NPs. The choice of SiO_2 as the coating material is beneficial because of its biocompatibility, the possibility for subsequent functionalization and the easy regulation of the coating process [88], [89]. Moreover, every single FePt NP should be coated with a homogeneous SiO_2 shell without magnetic core-free SiO_2 particles; therefore, suitable synthesis procedure should be selected. SiO_2 coating on the NPs is usually prepared by two different synthetic routes: a) the Stöber process or b) water-in-oil microemulsion system [90]. In the Stöber process SiO_2 layer is formed on the NPs *in-situ* through the hydrolysis and condensation of a silicon alkoxide precursor in a basic water-ethanol solution. However, f the Stöber process cannot be applied to the core NPs that are soluble in the non-polar media because this procedure offers less control over the size and the number of the entrapped NPs cores. Therefore, the second procedure of water-in-oil microemulsion is more suitable to coat the NPs, which are dispersed in the non-polar media, since it enables the formation of a thinner coating layer and more monodispersed

final particles. In the water-in-oil microemulsion system, the hydrolysis and condensation of a silicon alkoxide precursor occurs around NPs that are stabilized with surfactants [91] as will be discussed further.

By definition, a microemulsion is a dispersion made of water, oil, and surfactant(s) that is an isotropic and thermodynamically stable system with dimensions of micelles varying approximately from 1 to 100 nm, usually 10 to 50 nm [92]. In water-in-oil microemulsions, the micelles of the aqueous phase are surrounded by a monolayer of surfactant molecules and dispersed in the hydrocarbon (oil) phase. Those micelles in the oil phase serve as the nanoreactors for the synthesis and/or coating of NPs. The size of the micelles is determined by the molar ratio of water to surfactant [93]. By the addition of the antisolvent (e.g. acetone or ethanol) to the microemulsions, the formed NPs can be extracted from the reaction mixture with filtration or centrifugation.

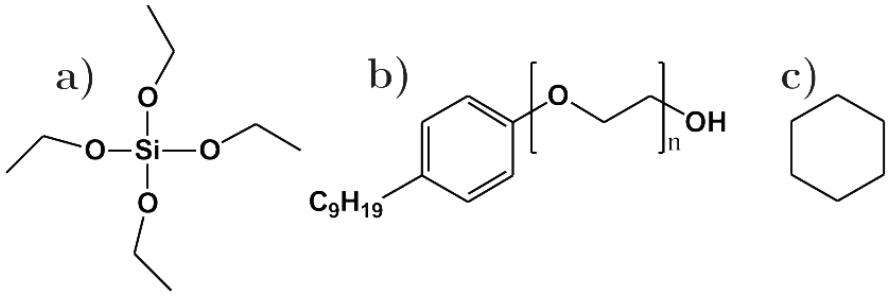


Figure 1.14: Structural formula of a) TEOS (tetraethyl orthosilicate), b) Igepal CO-520 (polyoxyethylene (5) nonylphenylether) and c) cyclohexane.

It is known that the water-in-oil microemulsion approach described in [90] would allow the synthesis of SiO_2-coated FePt NPs. In this system cyclohexane has a function of an oil phase, Igepal CO-520 (polyoxyethylene (5) nonylphenylether) is a surfactant and ammonia solution acts as a water phase. TEOS (tetraethyl orthosilicate) has a function of a SiO_2 precursor. Structural formulae of TEOS, surfactant Igepal CO-520 and cyclohexane are shown in Figure 1.14. Proposed reaction mechanism is as follows [90] and is schematically showed in Figure 1.15. First, surfactant (Igepal CO-520) is homogeneously distributed in the solvent (cyclohexane). When cores of NPs are added in the solution, the ligand exchange reaction occurs where new surfactant (Igepal CO-520) replaces chemically absorbed surfactants on the NPs surface. Next, the addition of an aqueous phase (ammonia solution) causes the formation of micelles. After the addition of SiO_2 precursor (TEOS), the hydrolyzed TEOS monomers replace the chemically absorbed surfactant (Igepal CO-520) on the NPs surface and NPs are transferred to the aqueous phase. In the final stage, condensation of hydrolyzed TEOS occurs and SiO_2 shells are formed [90].

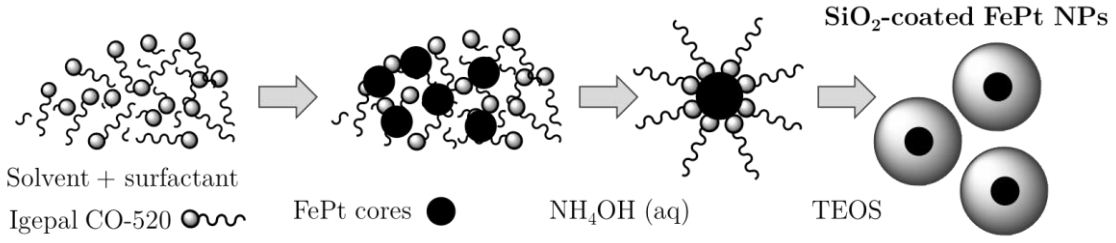


Figure 1.15: Schematic representation of the SiO_2 coating process.

La Mer theory for the nucleation and growth of NPs can be used to describe the SiO_2 coating process [90]. La Mer diagram for this process is shown in Figure 1.16. The energy barrier for the heterogeneous nucleation is lower than the energy barrier for the homogeneous nucleation and it depends on the supersaturation of the solution, i.e. the concentration of hydrolyzed TEOS. In the first stage the hydrolyzed TEOS monomers are formed and its concentration depends on the concentration of TEOS. By increasing the TEOS concentration also the number of hydrolyzed TEOS monomers is increased. When the solubility concentration (C_s) is exceeded, a heterogeneous nucleation occurs on the surface of core NPs. With further increase of the monomers concentration the threshold for the homogeneous nucleation is reached (C_{homo}, stage II). Consumption of the monomers leads to a decrease in its concentration and eventually it drops below the C_{homo}, which reflects in the reappearance of the heterogeneous nucleation (stage III). It is evident that if $C > C_{homo}$ both, core/shell NPs and core-free SiO_2 NPs, are present (Figure 1.16b). In order to avoid formation of a core-free SiO_2 NPs the condition $C_s < C < C_{homo}$ must be fulfilled through the whole reaction process (Figure 1.16c).

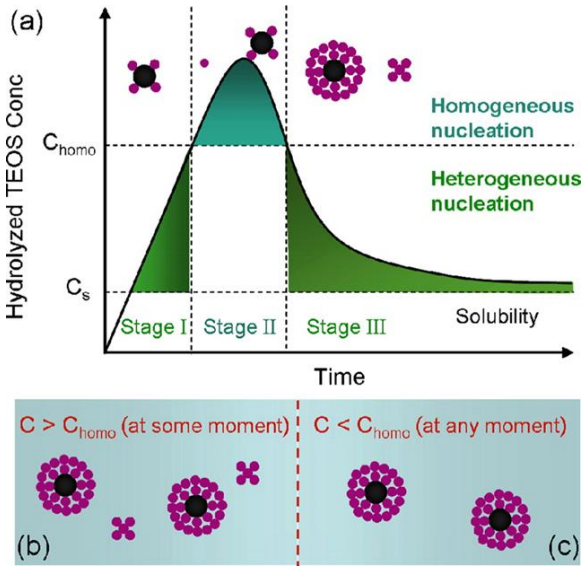


Figure 1.16: a) La Mer diagram for the nucleation and growth of a SiO_2 shell on a Fe_3O_4 core NPs. b) the existence of Fe_3O_4/SiO_2 core/shell NPs and SiO_2 NPs in the reaction when $C > C_{homo}$ at some moment and c) only the existence of Fe_3O_4/SiO_2 core/shell NPs in the reaction production when $C < C_{homo}$ at any moment [90]. Reprinted with permission.

Several parameters influence the SiO_2 coating process. The thickness of the SiO_2 layer is a strong function of the water-to-surfactant ratio and the ammonia concentration in the aqueous phase [94]. It is important to match the number of cores NPs to the water-to-surfactant ratio to avoid the formation of core-free SiO_2 NPs [90]. Increased ammonia concentration leads to an increase of the size of the micelles that are formed in the microemulsion. However, enlarged aqueous phase accelerates the hydrolysis of TEOS and the rate of the formation of the hydrolyzed TEOS monomers exceeds the consumption rate. Then the condition $C_s < C < C_{homo}$ is not valid anymore and core-free SiO_2 NPs might appear. Therefore, in order to keep the system balanced with increased ammonia concentration the TEOS content should be appropriately decreased [90]. Additionally, the thickness of the SiO_2 shell is increased as the amount of TEOS increases. However, when reaching a certain concentration of TEOS, a core-free SiO_2 NPs may appear.

1.4.3.2 Formation of Au complexes and their role in the Au shell formation

Isoelectric point of SiO_2 is at pH~2 [95]. At pH<2 SiO_2 NPs exhibit positive zeta potential, around pH=2 the zeta potential approaches zero value, while at pH>2 the surface is negatively charged, which is not suitable for the deposition of cationic gold species, which are used in the process of Au shell formation. This problem can be overcome with the anionic gold species, such as $[Au(en)2]_3^+$, however, those complexes are difficult to prepare [96]. Stable anionic gold species, e.g. $[AuCl_x(OH)_{4-x}]^-$, can be easily prepared from an aqueous solution of $HAuCl_4$. In order to facilitate deposition of those species, SiO_2 surface should be modified to achieve positive surface charge in the broad pH range. For that purpose SiO_2 surface can be functionalized for example with APTES ((3-aminopropyl)thiethoxysilane) as is schematically shown in Figure 1.17. as proposed in [95]. End functional amino groups of APTES provide positive surface charge up to the pH =10, in which point pK_a of amine is achieved [97].

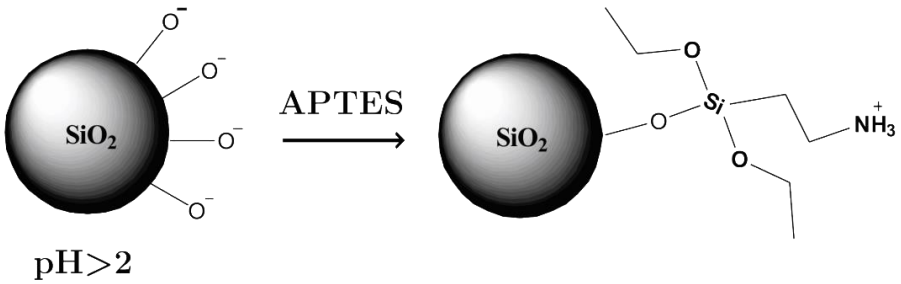


Figure 1.17: Functionalization of SiO_2 surface with APTES.

Table 1.2: List of possible complexes present in an aquous solution of $HAuCl_4$ in dependence of the pH.

Dominant complex	**pH**
$[AuCl_4]^-$	pH<3
$AuCl_3xH_2O$	pH=3
$[AuCl_x(OH)_{4-x}]^-$	pH=4-10
$[Au(OH)_4]^-$	pH>10

Complex formation from an aqueous solution of $HAuCl_4$ is strongly pH dependent. Complexes that are formed at different pH are listed in Table 1.2. The extent of hydrolysis of chloroauric ion $[AuCl_4]^-$ depends on the pH, which dictates the amount of OH^- available for hydrolysis and six different complexes can be formed ($[AuCl_x(OH)_{4-x}]^-$). In order to promote the hydrolysis, i.e. exchange of Cl^- and OH^- ions, the solution should be heated above 60°C [88]. In the mildly basic pH range $[AuCl_3(OH)]^-$ complex is predominant [88]. However, among them only $Au(OH)_3$ precipitates [98]. At pH = 3 - 4, hydrolysis of Au-Cl bond is not preferable, therefore, the major species are soluble $AuCl_3 \cdot H_2O$ with traces of $[AuCl_x(OH)_{4-x}]^-$ [88]. With increasing pH more Au-Cl is replaced with Au-OH as the consequence of increased hydrolysis. Therefore, denser Au seeding can be observed on the SiO_2 surface. At higher pH $Au(OH)_3$ dissolves and $[Au(OH)_4]^-$ is predominant species and, consequently, the efficiency of Au seeding is reduced. All these facts indicate that the precise control of the pH of the solution is crucial to obtain uniform deposition of particles (i.e. Au seeding) on the SiO_2 surface.

Once the $Au(OH)_3$ is deposited on the SiO_2 surface, mild heating leads to a decomposition to Au oxide in accordance with the Eq. (1.27). Finally, due to the oxide instability, according to the Eq. (1.28), elemental Au is formed. Typical temperature range for the decomposition bulk gold oxide Au_2O_3 was found to be 360-450 K, however, on the nano-level due to the prevailing surface effects these temperatures could be lower [99].

$$2\ Au(OH)_3 \rightarrow Au_2O_3 + 3H_2O \tag{1.27}$$

$$2\ Au_2O_3 \rightarrow 4Au + 3O_2 \tag{1.28}$$

1.4.3.3 Functionalization of hybrid $FePt/SiO_2/Au$ NPs

Polyethylene glycol (PEG), also poly(ethylene oxide) or polyoxyethylene, is a linear polymer consisting of repeated units of–CH_2–CH_2–O–. It is well soluble in water and several organic polar and non-polar solvents. PEGylation is a surface modification of NPs or molecules with polyethylene glycol (PEG), which is known to be biocompatible, prevents particle aggregation, non-specific protein adsorption and improves in vivo stability of NPs [100]. Moreover, its stealth behaviour inhibits the fast recognition by the immune system (opsonization) and generally leads to a reduced blood clearance by the reticuloendothelial cells. PEG molecules on the NPs surface repel other molecules by steric effects. PEG coating is very suitable for further bioconjugation (targeting ligands for maximizing interaction with specific cells or tissues). Molecular structure of PEG is shown in Figure 1.18. PEG can be modified to have different chain length and different functional groups on one or both sides of the chain, which strongly influence the surface binding and suspension stability. It was shown that thiol compounds can efficiently improve the stability and dispersity of colloidal Au NPs in aqueous solution [101]. This can be attributed to the fact that the surface of Au NPs forms strong, stable Au—S bonds to molecules with thiol (-SH) or disulfide (S-S) groups. Structural formula of mPEG-SH is shown in Figure 1.18. A nonreactive methoxy (CH_3O-) group that is pointing to the solution enables steric stabilization of NPs, which is more efficient than ionic stabilization.

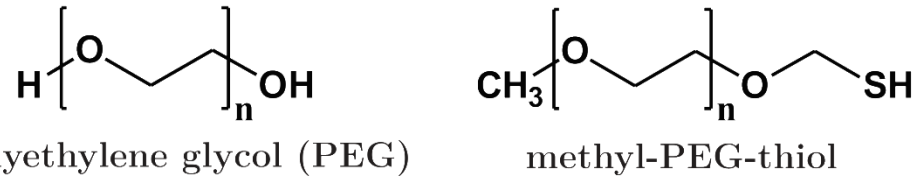


Figure 1.18: Structural formula of polyethylene glycol (PEG) and thiolated methyl-PEG (mPEG-SH).

Chapter 2

Aims and Hypothesis

2.1 Aims

Purpose of the dissertation was preparation of stable suspension of hybrid FePt/SiO_2/Au NPs with adequate magnetic properties (high saturation magnetization in a superparamagnetic state) ensured via FePt core. This would enable the magnetic manipulation and the imaging (MRI) (large effect on T_2 relaxation times). The optical modality with desired absorption in the near NIR region would be achieved via SiO_2 interlayer covered with Au shell that would enable a photo-thermal cancer treatment, the effect of which would be proven *ex-vitro.*

Main goals of the dissertation:

1. Optimization of the synthesis of superparamagnetic FePt NPs to achieve high saturation magnetization in a superparamagnetic state. For that purpose we have improved the magnetic properties of "single-core" FePt NPs (known from the literature) either by increasing their size by using either a one-step or two-step approach, or by formation of "multi-core" FePt NPs, where several FePt NPs were joined in aggregates via surfactant-assisted synthesis in a controlled way.

2. Preparation of stable water suspensions of "single-core" and "multi-core" FePt NPs via ligand exchange reactions and evaluation of their applicability for being used as the contrast agent for MRI.

3. Coating of "single-core" and "multi-core" FePt NPs with SiO_2 layer of controlled thicknesses, which acts as an intermediate layer between magnetic FePt and optically active Au component. SiO_2 shell thickness plays a vital role in controlling the position of the SPR peak by the varying core-to-Au shell ratio.

4. Formation of Au shell that enables high absorption of the light in the NIR region, which is essential for the photo-thermal treatment.

5. Preparation of stable water suspensions of hybrid FePt/SiO_2/Au NPs via surface functionalization with biocompatible PEG-based ligands.

6. Testing if hybrid FePt/SiO_2/Au NPs can be magnetically manipulated and retained at a targeted location under realistic dynamic conditions (*ex-vitro*).

7. Testing of the hybrid FePt/SiO_2/Au NPs suspensions to assess their photo-termal potential.

For reasons of clarity and comprehensibility, a short overview of the performed experiments is given in Figure 2.1. The first part of the thesis is dedicated to the synthesis and characterization of superparamagnetic "single-core" and "multi-core" FePt

NPs with focus on the improvement of their magnetic properties (left part of Figure 2.1). The effect of those NPs on the shortening of the relaxation times of water protons was the aim, therefore stable water suspensions were required. "Single-core" and "multi-core" FePt NPs were successfully transferred from organic into water phase via ligand exchange reaction using two different catechol based ligands (ZDS and HCA). Another approach to prepare water dispersible FePt NPs is coating them with SiO_2 layer (middle part of Figure 2.1). Where, again, the magnetic properties and the ability of SiO_2-coated "single-core" and "multi-core" FePt NPs to shorten water protons relaxation times were measured. In order to obtain positively charged SiO_2-coated "single-core" and "multi-core" FePt functionalization with APTES was used. This step was essential to successfully continue with the third part of the thesis aims, which was the formation of the Au shell, and the preparation of the final product, hybrid magneto-optically active FePt/SiO_2/Au NPs (right part of Figure 2.1). Optical response of hybrid FePt/SiO_2/Au NPs was first theoretically predicted through the simulations of absorption spectra. In that way an optimal core-to-Au shell ratio was determined and aimed at. Once hybrid FePt/SiO_2/Au NPs were synthesized optical properties were measured experimentally and compared to the theoretical predictions. Furthermore, in order to achieve stable water suspensions hybrid FePt/SiO_2/Au NPs were functionalized with a biocompatible ligand (polyethylene glycol). As-prepared hybrid FePt/SiO_2/Au NPs showed a high absorption of the light in the NIR part of the spectrum, therefore, measurements of the photo-thermal effect were performed. Finally, the magnetic properties of hybrid FePt/SiO_2/Au NPs were measured and it was shown that those NPs can be magnetically manipulated under realistic dynamic conditions.

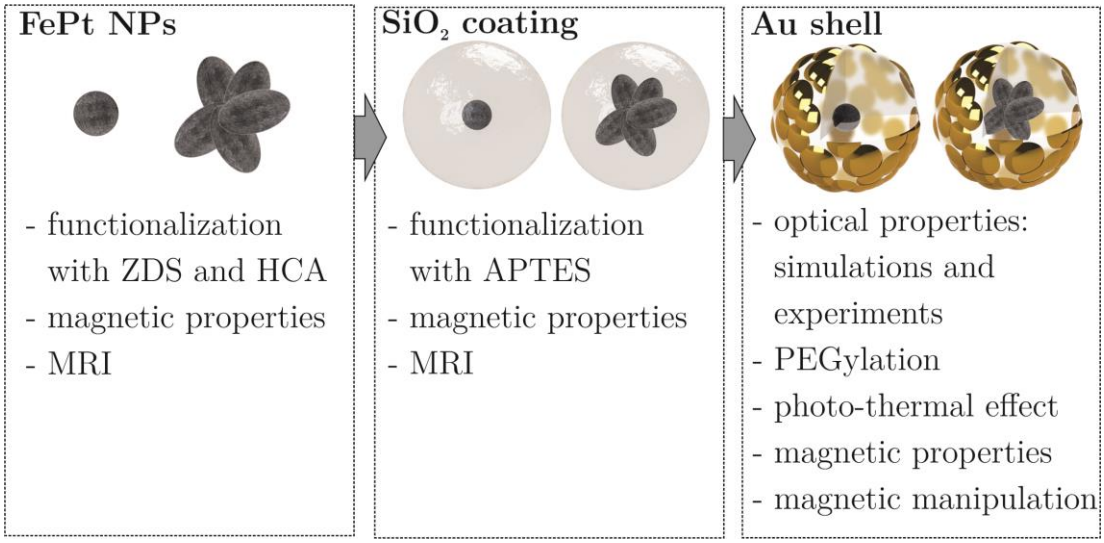


Figure 2.1: Summary of all experiments performed in each step of the synthesis of hybrid FePt/SiO_2/Au NPs.

2.2 Hypotheses

2.2.1 Hypothesis 1

A bulk saturation magnetization (M_s) is an intrinsic magnetic property; however, by reducing the size of the material to the nanoscale the surface effects (that include reduced surface and its changed surface due to the functionalization with ligands) on the

magnetization of a nanostructure (m_s) become significant or even decisive [64]. Even though the M_s of a FePt alloy is high, it is very difficult to achieve this value when the material is in a NP form due to the magnetically dead layer on the surface of NPs. This disordered layer thickness is usually in the range below 1 nm to several nm. For example in 9-nm FePt NPs it is estimated to be 1.5-1.8 nm, depending on the surface ligand (functional group and length of the chain) [34]. Consequently, the m_s of the NPs is to a large extent proportional to the NPs' size. By increasing the size of the FePt NPs the nanoparticle magnetization (m_s) value can be increased via reducing the ratio between the bulk magnetization (M_s) and its magnetically dead surface layer [46], while remembering to keep the NPs in the superparamagnetic state necessary for biomedical applications. We have calculated that the SPL for *fcc* FePt NPs is approx. 10 nm. We hypothesize that the m_s of FePt NPs can be increased by increasing their size, however, in this direction we are limited by the SPL. In order to overcome this limitation "multi-core" FePt NPs, which are controlled aggregates of smaller superparamagnetic FePt NPs, are hypothesized to possess larger m_s than their single components due to the collective magnetic behaviour of the FePt cores [37]. However, there are several questions that arise and have to be answered. How large "multi-core" NPs can be prepared that will still behave superparamagnetically? And further, to what extent the magnetization of the NPs can be improved with the formation of "multi-core" NPs. Having NPs with high m_s is important for the following applications.

According to the Eq. (1.15) the T_2 relaxation times can be efficiently shortened via larger values of saturation magnetization. Upon that the "multi-core" FePt NPs expressing higher saturation magnetization should result in higher relaxivity values in MRI in comparison with their "single-core" counterparts.

For the successful manipulation of the hybrid NPs under the dynamic flowing conditions, the magnetic force on the magnetic nanoparticles ($\overrightarrow{F_m}$) must exceed the fluidic drag force ($\overrightarrow{F_d}$). According to the Eq. (1.16) the hydrodynamic drag force ($\overrightarrow{F_d}$) depends on the medium viscosity, size of NP, velocity of the particle and velocity of the media. Because in the human body the medium viscosity and velocity are "fixed" values, we can influence the $\overrightarrow{F_d}$ only by changing the size of the NPs. From this it can be concluded that the smaller the size of NPs the smaller should be the $\overrightarrow{F_d}$. However, from the perspective of a successful magnetic manipulation, it is essential to have a high magnetic force $\overrightarrow{F_m}$. According to the Eq. (1.17) high $\overrightarrow{F_m}$ can be achieved by having NPs with high magnetization values and/or high external magnetic flux gradients $\nabla \vec{B}$. We are limited with the maximum $\nabla\vec{B}$ that can be achieved with the commercial magnets, therefore, it is essential to have NPs with high magnetic moment. The magnetic dipole moment of the particle ($\vec{m}_p$) depends on the magnetization M and the volume of the particle Vp (mp = Vp M), therefore, by increasing the size of the NPs also the magnetic moment is increased. On the other hand, it was stated that in order to minimize $\overrightarrow{F_d}$, smaller NPs are required. $\overrightarrow{F_d}$ increases linearly with increasing particle radius, however, because the NP's volume increases to the third power of the radius r (Vp =4πr3/3), the increase in the NP's size has a bigger effect on the increase of $\overrightarrow{F_m}$ than on $\overrightarrow{F_d}$. Therefore, if the magnetic moment of the particle is sufficiently increased, also bigger NPs can be successfully manipulated under the dynamic flowing conditions.

2.2.2 Hypothesis 2

Stable water suspensions of "single-core" and "multi-core" FePt NPs are needed for the evaluation of their applicability for being used as the contrast agent for MRI. Among the appropriate ligands to replace OLA and OA on the NP's surface, two dopamine based

ones (ZDS and HCA) were selected for the following reasons. It is essential that ligand provides a strong coordination to the NP surface. In that way initial ligands can be successfully replaced and NPs remained functionalized/stabilized for a longer period of time and even after being exposed to harsh conditions, such as purification and sterilization. It was shown on the example of iron oxide NPs that dopamine-based ligands show strong interaction between the vicinal diol groups and the iron oxide surface, which makes ligand exchange possible and NPs are transferred from organic to water phase. We postulate that a strong chemical bond might be formed also between FePt NP's surface and dopamine part of the molecule. This can be confirmed with a detailed FTIR study. There are several dopamine-based molecules available. We have selected ZDS ligand due to its zwitterionic character, which enables buffer capacity, i.e., a high stability in a broad pH range. Furthermore, we have selected HCA due to its natural origin and because it was shown that Fe oxide NPs coated with HCA have no immune-stimulating properties for dendritic cells, which is necessary for NPs to have sufficient half-life in blood.

Another approach to transfer FePt NPs into the aqueous phase is to coat them with SiO_2 layer. SiO_2 was selected because of its biocompatibility, the possibility for subsequent functionalization and the easy regulation of the coating process [88], [89]. It was shown that SiO_2-coated FePt NPs can be prepared via water-in-oil microemulsion procedure. However, in order to obtain uniform coating of every single NP without core-free SiO_2 NPs present, a fine tuning of the reactants' concentration is essential. In order to determine the optimal conditions for the formation of SiO_2-coated FePt NPs, without any FePt-free SiO_2 NPs or bare FePt NPs, an influence of the TEOS concentration on the formation of SiO_2-coated FePt NPs has to be systematically studied. On the basis of La Mer theory, which is described in Section 1.4.3.1, we postulate that with the precise control over the nucleation and growth process (e.g. varying TEOS concentration reaction time) every individual FePt NP can be coated with a SiO_2 layer of desired thickness, without having core-free SiO_2 NPs. Our aim was to determine C_s and C_{homo} for a given system to better understand the nucleation process, which enabled us to determine optimal reaction conditions. Not only to obtain SiO_2-coated FePt NPs, without any FePt-free SiO_2 NPs, also thickness of the SiO_2 shell has to be carefully controlled to obtain appropriate core-to-shell ratio of final hybrid FePt/SiO_2/Au NPs.

2.2.3 Hypothesis 3

According to Eq. (1.26) the absorption spectra for core/Au shell NPs depends on the complex dielectric function of the core (ε_{core}) and (ε_{shell}) material, as well as the core-to-shell ratio. In order to obtain optimum optical response for the photo-thermal effect, i.e. high absorption in the NIR region of the light (details can be found in Section 4.5.1), appropriate dimensions of the core-shell structure have to be determined. For that purpose simulated absorption spectra for FePt/SiO_2/Au hybrid NPs with different core (FePt/SiO_2) sizes and Au shell thicknesses were used as a guideline. Simulations revealed suitable geometries that fit in the optimum range (wavelength approx. 680 – 880 nm). We postulate that hybrid NPs with FePt-SiO_2 core-to-Au shell ratio 7-11 should show high absorption in the NIR region and, consequently, would give significant photo-thermal effect. However, real samples would suffer from imperfection and we hypothesise that any degree of polydispersity or agglomeration would influence the optical properties, which has to be taken into account when discussing the results.

Chapter 3

Materials and Methods

3.1 Materials Used in the Synthesis Procedures

For the synthesis of the FePt nanoparticles, platinum acetylacetonate $Pt(acac)_2$ (Merck), iron acetylacetonate $Fe(acac)_3$ (>99.9% Sigma-Aldrich), benzyl ether (>98%, Merck), oleic acid (OA, >99%, Sigma-Aldrich), oleylamine (OLA, 70%, Sigma-Aldrich), 1,2-hexadecanediol (90%, Sigma-Aldrich), hexane (>95%, Sigma Aldrich) and ethanol absolute anhydrous (> 99.9%, Carlo Erba Reagents) were used.

For the synthesis of the SiO_2 shells around "single-core" and "multi-core" FePt NPs cyclohexane (>99.9%, Fisher Chemical), Igepal CO-520 (Polyoxyethylene (5) nonylphenylether, Sigma-Aldrich), 25% ammonia solution (Merck), tetraethyl orthosilicate (TEOS, 99.9%, Alfa Aesar) and methanol (> 99.9%, Carlo Erba Reagents) were used. SiO_2 surface was functionalized with APTES (>98%, Merck).

For the ligand-exchange reaction and the functionalization of the FePt surface with zwitterionic dopamine sulfonate ligand the following reagents were used: dopamine hydrochloride (pure, Sigma Aldrich), ammonium hydroxide (28%, Acros Organics), 1,3-propanesultone (99%, Sigma Aldrich), N,N-dimethylformamide (99.8% on molecular sieves, Sigma Aldrich), anhydrous sodium carbonate (99.8%, Chemlab), iodomethane (99% with copper inhibitor, Sigma Aldrich), ethyl acetate (99.9%, VWR), tetrahydrofuran (99.9% with 250ppm BHT inhibitor, Sigma Aldrich) and acetone (99%, Nyssens Graphics).

For the ligand-exchange reaction and the functionalization of the FePt surface with hydrocaffeic acid the following reagents were used: tetrahydrofuran (THF, anhydrous, >99.9%, Sigma Aldrich), hydrocaffeic acid (HCA, 3-(3,4-Dihydroxyphenyl)propionic acid, >98%, Sigma Aldrich) and NaOH (anhydrous, >98%, Sigma Aldrich).

For the gold shells formation $HAuCl_4x3H_2O$ (>99.9%, Alfa Aesar), K_2CO_3 (>99%, Sigma-Aldrich), NaOH (anhydrous, >98%, Sigma Aldrich) and $NaBH_4$ (>99%, Fluka) were used. Hybrid $FePt/SiO_2/Au$ NPs were functionalized with methyl-PEG-SH (poly(ethylene glycol) methyl ether thiol, average M_n 6000, Sigma Aldrich).

3.2 Synthesis Procedures

3.2.1 Synthesis of FePt NPs

3.2.1.1 "Single-core" FePt NPs

At room temperature, 0.5 mM of $Pt(acac)_2$ and 1 mM of $Fe(acac)_3$ were added into a round-bottom flask containing 20 mL of benzyl ether. The ratio of the surfactants OLA:OA was 1:1, while the volume of added OLA and OA was varied from 0.5 to 6 mL (S1–S8) as listed in Table 4.1 and discussed in Section 3.2.1.1. Before heating to 260°C for 30 min the reducing agent 1,2-hexadecanediol (2.3 mmol) was added at 160°C. The black product was precipitated by adding absolute ethanol and separated by centrifugation (6000 rpm/10 min) and then redispersed in hexane.

3.2.1.2 "Single-core" FePt NPs produced via seed-mediated growth

For the first step in the synthesis the experimental procedure for sample 7 (volume of OLA and OA is 4 mL) was used. After the reaction the mixture in the first step was cooled to room temperature, in the second step, half of the initial volume of the metal salts was added and the same heating regime (260°C/30 min) was used as in the first step. After cooling to room temperature the black product was precipitated by adding absolute ethanol and separated by centrifugation (6000 rpm/10 min) and then redispersed in hexane.

3.2.1.3 "Multi-core" FePt NPs

Samples were prepared by changing the OLA:OA ratio while all the other parameters were kept the same as in the case of the "single-core" FePt NPs synthesis. The OLA:OA ratio was varied between 0.08 and 0.75. The volume of OLA was constant (6 mL), while the volume of OA was varied: 0.5 mL, 1 mL, 2 mL, 3 mL and 4.5 mL (S10–S14) as listed in Table 4.2 and discussed in Section 3.2.1.3. Additional two experiments were performed where only OLA (6 mL, S9) or OA (6 mL, S15) was used.

3.2.2 Functionalization of FePt NPs with zwitterionic dopamine sulfonate ligand

Dopamine hydrochloride (2.26 g, 12 mmol) was dissolved in 200 mL of ethanol in a flask, equipped with an Ar balloon. Ammonium hydroxide (832 μL, 6 mmol) and 1,3-propanesultone (1.14 mL, 13 mmol) were added and the mixture was stirred at 50°C for 16 hours. Dopamine sulfonate precipitates as a white solid, which was collected by centrifugation (10000 rpm/5 min) and washed three times with ethanol. The product was collected as a white powder (1.581 g, 40% yield). In the next step dopamine sulfonate (0.656 g, 2 mmol) was dissolved in 100 mL of dry N,N-dimethylformamide (DMF) and anhydrous sodium carbonate (0.508 g, 4.8 mmol) was added. After purging the system with argon gas, iodomethane (4.4 mL, 70 mmol) was added and this mixture was stirred for 16 h at 50°C. The mixture was filtered and the solvent was removed using a rotary evaporator. A mixture of DMF (4.4 mL) and ethyl acetate (45 mL) was added to precipitate the zwitterionic dopamine sulfonate, which was collected by centrifugation

(10000 rpm/5 min). This procedure was repeated three times to finally obtain a final solid product (364 mg, 51% yield).

Stable water suspensions of "single-core" and "multi-core" FePt NPs were achieved by a ligand-exchange process, where FePt NPs were functionalized with the ZDS ligand using the following procedure. FePt NPs (12 mg) were dissolved in 12 mL of tetrahydrofuran and the zwitterionic catechol was added (18 mg), dissolved in 1.2 ml of MilliQ water. This mixture was sonicated for 3 hours in an ultrasonication bath (Branson 5510). To purify the particles, 2 mL of MilliQ water and 10 mL of ethyl acetate were added to induce phase separation. The functionalized particles remained in the bottom aqueous phase, which was collected. This layer was washed three times with 10 mL of ethyl acetate to remove any residual tetrahydrofuran. A small volume of acetone was added to the aqueous layer (until turbid), which was subsequently centrifuged (10000 rpm, 5min) to collect the NPs. These functionalized NPs were dissolved in MilliQ water.

3.2.3 Functionalization of FePt NPs with hydrocaffeic acid

As-prepared hydrophobic FePt NPs (20 mg) were dispersed in 1 mL of THF. Solution of ligand was prepared by dissolving 50 mg of HCA in 5 mL of THF. Hydrophobic NPs were added dropwise to the solution of the ligand and the reaction mixture was then and stirred at 50 °C for 3 h to complete the reaction. Upon cooling the reaction mixture to room temperature, 0.5 mL of 0.5 M NaOH was added to precipitate the NPs, which were collected by centrifugation and redispersed in water.

3.2.4 SiO_2 coating of FePt NPs

FePt "single-core" or "multi-core" nanoparticles (20 mg) were added to a mixture of 170 mL of cyclohexane and 8 mL of surfactant Igepal CO-520. Then 1 mL of 25% ammonia solution and 0.2 mL of TEOS (tetraethyl orthosilicate) were added drop-wise and the whole mixture was vigorously stirred at room temperature for different reaction times (6, 12, 18 and 24 h) and deposited on TEM grids, and subsequently the thickness of the SiO_2 shell was measured.

3.2.5 Au shell formation

3.2.5.1 Functionalization of FePt/SiO_2 NPs with APTES

In order to induce positively charged aminopropylsilane groups on the SiO_2 surface 5 mL of 12 mM APTES solution (water:ethanol=1:3) was added to the suspension of the FePt/SiO_2 nanoparticles. The reaction mixture was stirred at 80°C for 3h before cooling to room temperature. Any excess of APTES was removed with five cycles of centrifugation (7500rpm/20min) and redispersion in water. Successful functionalization with APTES was monitored by measuring the zeta-potential on the surface of the FePt/SiO_2 NPs in water as discussed further in results.

3.2.5.2 One-step Au seeding

Small gold NPs, i.e. Au seeds, were deposited on SiO_2 surface by using the following procedure. First, to adjust the pH value to 7, 0.1-M NaOH was added to 4 mL of 6.35-mM $HAuCl_4x3H_2O$ in a water solution. The amine functionalized surface of the silica was seeded with $Au(OH)_3$ by mixing FePt/SiO_2 NPs with a $HAuCl_4x3H_2O$ solution and stirred at 70°C for 5 minutes. The colour change from yellow to orange-brown indicates

the attachment of the $Au(OH)_3$ to the SiO_2 surface [88]. The product was then centrifuged (950rpm/30min) and washed several times and finally dispersed in distilled water.

Size of gold seeds and coverage of the SiO2 surface strongly depends on the pH of the gold solution ($HAuCl_4x3H_2O$) and time of the synthesis. In order to find optimal conditions, solutions with different pH values were tested (4, 6 and 8). Growth of gold seeds was evaluated by extracting samples from the reaction mixture at different times (1, 5, 10 and 30 minutes).

3.2.5.3 Au shell formation with NaBH4

The gold shell is finally formed by reducing the additional gold on the gold-seeded SiO_2 surface. 50 mL of the gold solution with the pH=10.2 contained 30 mg of K_2CO_3 and 7 mg of $HAuCl_4x3H_2O$. To the mixture of gold solution and gold-seeded $FePt/SiO_2$ core/shell NPs 3 mL of ice-cold 6.6-mM $NaBH_4$, which is a strong reducing agent, was added. The reaction mixture was cooled to 0°C to slow down the reaction because at room temperature larger Au particles were grown, which aggravate the formation of Au shells. An almost immediate color change from colourless to blue indicated the formation of the Au shells.

3.2.5.4 Au shell formation via two-step Au seeding

Au shells were also prepared by using a novel approach of Au double seeding, which enables the preparation of thinner Au shells in a more controllable manner. By using synthesis procedure with a strong reducing agent, $NaBH_4$, larger Au NPs were grown, which offers less control over the shell thickness. In the first step, small (1-3 nm in diameter) Au NPs are deposited on the surface of the SiO_2 layer as described in Section 3.2.5.2. In order to achieve denser Au seeding, i.e. fill the gaps between the Au seeds from the first run and to obtain more uniform Au shell, in the second step, Au seeding step was repeated using the same conditions as in the first Au seeding step.

3.2.6 PEGylation of hybrid NPs

Hybrid $FePt/SiO_2/Au$ NPs were functionalized with mPEG-SH using the following procedure. Into the suspension of hybrid NPs in water (2 mL, 5 mg) 2 mL of mPEG-SH (0.5mg/mL) was added. Reaction mixture was then stirred for 30 min at 60°C. The sample was then centrifuged (7000rpm/10min) and washed several times to remove excess of mPEG-SH and finally dispersed in distilled water.

3.2.7 Summary over the formation of hybrid NPs

The overall synthesis route for the hybrid FePt/SiO2/Au NPs NPs consisting of four described “sub”-routes is schematically shown in Figure 3.1. First, FePt NPs, either “single-core” or “multi-core”, are coated with SiO2 layer. Such NPs (FePt NPs and SiO2 coated FePt NPs) were tested for their MRI performance. Further, these SiO2 coated NPs were functionalized with APTES. Au shells were subsequently formed on these NPs

by using two different approaches; a) via one-step Au seeding (described in Section 3.2.5.2) and consequent NaBH4 reduction process (described in Section 4.5.2.3) or b) via two-step Au seeding process (described in Section 3.2.5.4). In order to prepare stable and biocompatible water suspensions, hybrid NPs were functionalized with mPEG-SH. Finally the hybrid NPs were tested towards their photo-termal ability and magnetic separation.

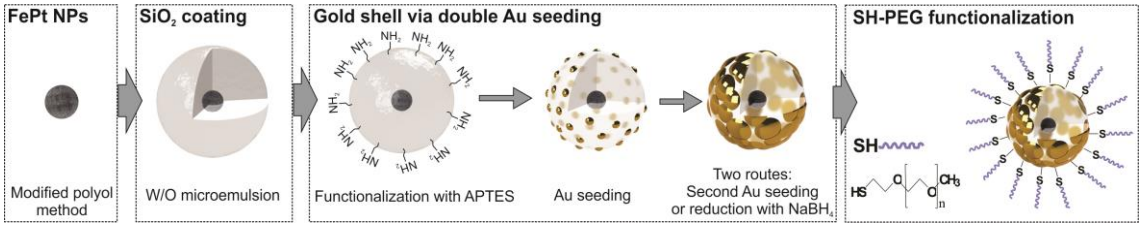


Figure 3.1: Schematic presentation of the four steps in the synthesis of the hybrid FePt/SiO_2/Au NPs. Syntesis of FePt NPs is followed by SiO_2 coating, functionalization of SiO_2 surface with APTES and then Au shells were formed either via one-step Au seeding and consequent $NaBH_4$ reduction process or via two-step Au seeding. Finally, hybrid NPs were functionalized with mPEG-SH.

3.3 Characterization Techniques and Experimental Set-Up

3.3.1 Nanoparticles characterization

Morphology, size and composition of the synthesized samples were characterized using a transmission electron microscope (Jeol JEM-2010F) equipped with a STEM unit, energy-dispersive X-ray spectroscopy (EDXS) and electron energy-loss spectroscopy (EELS) and transmission electron microscope (Jeol JEM-2100) equipped with EDXS, both operating at 200 kV. The bright field (BF) and high-angle annular dark-field (HAADF) images of FePt NPs were obtained with JEOL ARM 200 CF probe Cs corrected STEM with high resolution pole piece. Samples for the transmission electron microscopy analysis were prepared by adding a drop of NPs suspension on a lacey, carbon-coated TEM grid. For the magnetic characterization FePt NPs were prepared in a form of a dry powder. Magnetic measurements were performed with a vibrating-sample magnetometer (VSM MicroSense model FCM 10) at room temperature. Low-temperature magnetic measurements were performed on SQUID (Quantum Design MPMS-XL-5). Thermogravimetric analyses (TG analyser NETZSCH STA 449 C/6/G Jupiter) on OLA, OA and OLA/OA-coated FePt NPs were performed to determine the amount of organic matter in the FePt sample in a temperature range from 25 – 600°C in a Al_2O_3 crucible with a heating rate 20°C/min in Ar:O_2=4:1 atmosphere. Relaxation times measurements on water suspensions of "single-core" and "multi-core" FePt and FePt/SiO_2 NPs were made on an NMR/MRI system consisting of a 2.35-T superconducting magnet (Oxford Instruments, Abingdon, UK) and an Apollo NMR spectrometer (TecMag, Houston TX, USA). The concentration of Fe in the samples (water suspensions of "single-core" and "multi-core" FePt and FePt/SiO_2 NPs for MRI measurements) was determined using the atomic absorption spectrometer (model SpectrAA 110, Varian, USA). For the preparation of the calibration curve ICP multi-element standard solution XVI (Certipur, Merck Millipore, USA) was used. Fourier transform infrared spectroscopy (FTIR) measurements were performed in order to evaluate the success of the ligand bonding to

the NPs′ surface. This was done by using a Spectrum 400 spectrometer (Perkin Elmer, USA). The spectra were recorded on the dried samples in the wavenumber range 4000-650 cm^{-1}. The UV-VIS spectroscopy on a water suspension of hybrid $FePt/SiO_2/Au$ NPs was performed using a PerkinElmer Lambda 950 spectrometer. For the zeta potential measurements on the water suspensions of FePt NPs, SiO_2-coated FePt NPs and PEG-coated hybrid $FePt/SiO_2/Au$ NPs ZetaPALS (Brookhaven Instruments Corporation,U.S.A.) was used.

3.3.2 Simulation of UV-VIS spectra for hybrid NPs

For hybrid NPs, the efficiency of the absorption, Q_{abs}, was calculated on the basis of the Aden and Kerker theory for coated spheres [113] using computer software (MieLab) developed by O. P. Rodriguez et al. [118] Software is based on improved recursive algorithm by Yang [119] and freely available for download here [120]. The input parameters for the code were the values of the thickness and refractive indices of each layer in hybrid NPs. For gold, the values of the complex dielectric function at different wavelengths were used from Johnson and Christy [121]. The embedded media for hybrid NPs was considered to be water with a refractive index of 1.33+0i. The calculations were performed in the wavelength range from 300 to 1300 nm.

3.3.3 Photo-thermal efficiency of the hybrid NPs

The photo-thermal experiments were performed by using a continuous-wave laser source with a wavelength of 800 to 820 nm and power of 0.9 W (HighLight FAP 100, Coherent, Inc., USA). Figure 3.2 shows the experimental set-up that was used to determine the photo-thermal effect in a water suspension containing the hybrid NPs. Continuous-wave diode light was focused on a quartz cuvette (size: 1 x 1 x 3 cm) using an optical lens with a spot size of about 8 mm. The temperature of the suspension was measured with a J-type Teflon thermocouple that was immersed in the cuvette and connected to a computer to collect the data in real time.

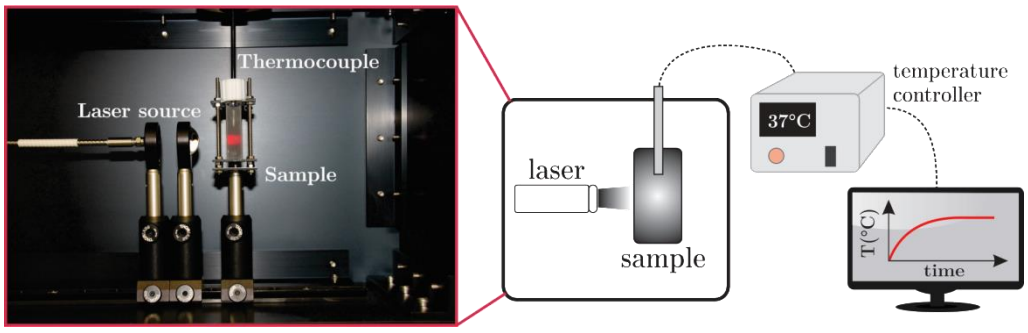


Figure 3.2: Experimental set-up for measuring the photothermal effect.

3.3.4 Hybrid NPs magnetic extraction

In order to test whether the hybrid $FePt/SiO_2/Au$ NPs can be magnetically manipulated and retained at a targeted location under realistic dynamic conditions the following experimental set-up was used which is shown in Figure 3.3. The fluid flow was simulated by using a peristaltic pump (Ismatec Reglo), which was connected with tubes (diameter

= 0.5 mm) to the spectrophotometer containing a flow cuvette. Two tubes with a length of 25 cm were used to connect the peristaltic pump, the spectrophotometer and a chamber with a magnet to a closed circuit. Both tubes were connected together outside the spectrophotometer with a slightly broadened connector (1 cm), which served as a chamber to collect the hybrid NPs with a commercial Nd−Fe−B permanent magnet ($\mu_0 H$ = 0.3 T measured right on the top of the magnet) with a disc shape (radius = 1 cm, height = 1 cm) that was placed next to the chamber to attract the hybrid NPs during their flow. Simultaneously, the absorption spectra were measured with UV-VIS spectrophotometer.

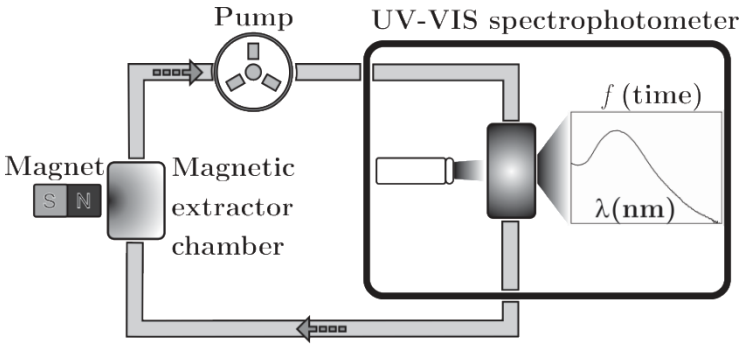


Figure 3.3: Schematic representation of the experimental set-up for studying the manipulation of hybrid NPs in a water suspension with the use of an applied external field.

Chapter 4

Results and Discussion

4.1 Synthesis of FePt NPs

4.1.1 "Single-core" FePt NPs synthesis based on varying the amount of surfactants

FePt NPs are very promising candidates to be used in several applications; therefore improvement of its magnetic properties is of wide interests. In this chapter different processing routes for the synthesis of FePt NPs of different sizes are described, which, as a result, exhibit different magnetization values. "Single-core" FePt NPs were synthesized using a modification of the polyol method, reported by Sun's group, in an argon atmosphere [53]. As it was discussed in Section 1.1., the saturation magnetization of the NPs (m_s) is known to be proportional to the NPs' size, therefore, increase in the size is crucial for the improvement of the magnetic properties. FePt NPs with different size were prepared by changing the amount of the added surfactants; oleylamine (OLA) and oleic acid (OA) from 0.15 - 6 mL. List of the samples (S1 - S8) is shown in Table 4.1. The TEM images in Figure 4.1 represent the FePt NPs prepared by the addition of different volumes of both surfactants, 0.5 mL (S2) and 4 mL (S7), where the sizes of the FePt NPs were found to be 3 nm (Figure 4.1a) and 6 nm (Figure 4.1b), respectively. For the largest added volume (6 mL, S8), the size is increased to 7.5 nm (Figure 4.1c); however, the NPs started to agglomerate, since at higher surfactant concentrations the free surfactant molecules can cause flocculation of the already surfactant-stabilized NPs, which is in accordance with the literature observations [46], [58]. A graph indicating the linear dependence of the particle size on the volume of the added surfactants is shown in Figure 4.1d. Influence of the surfactant concentration on the NPs size can be attributed to the change in the number of nuclei at the first step of particle formation [46]. Increase in the surfactant concentration with regards to the metal salt concentration most probably resulted in the formation of a larger amount of stable metal-surfactant complexes in the solution (Fe-oleic acid and Pt-oleylamine complexes), therefore, an increase in the surfactant concentration is expected to suppress the nucleation process and, as a consequence, larger particle size is produced.

The elemental analysis obtained using the energy-dispersive X-ray spectroscopy (EDXS) was performed on the S7 sample, where the addition of both surfactants was 4 mL. Three separately prepared samples were examined for their elemental composition in order to estimate the reproducibility of the synthesis procedure and five spectra were

recorded for each sample in different areas. All three S7 samples had very similar compositions, with the maximum deviation between them being ±1 at.%. The elemental composition determined from the obtained EDXS data was $Fe_{25\pm1}Pt_{75\pm1}$.

The magnetic hysteresis loops measured at 300 K for the furthest-apart samples in terms of their size (3 nm and 6 nm) are shown in Figure 4.1e. Both samples exhibit superparamagnetic behaviour, with the magnetizations $m_{(1.5T)}$ 2 emu/g and 8 emu/g, respectively. Our measured values for the magnetization are comparable to the values reported in the literature for similarly sized FePt NPs [46], [80]. However, the still relatively low m_s values, in comparison with the bulk FePt M_s value (75 emu/g), are most probably due to the particle size reduction according to Eq. (1.16) or due to the functionalization of the NPs with the surfactants, which causes a magnetically "dead" surface layer due to the oxygen bonds of the surfactant polar end group (OA/OLA) with Fe [33]. It was reported that by removing/decomposing the surfactant layer the M_s of the FePt NPs can be fully recovered [33], but this causes the agglomeration of the NPs, which is not desirable for biomedical applications. Upon that, dealing with an improvement of the magnetic properties should be considered for the whole suspension system and should not be limited to the raw/unfunctionalized NPs only.

Table 4.1: Sample list of »single-core« FePt NPs, including the amounts of OLA and OA used and the resulting OLA/OA ratio for FePt samples 1 to 8; $Fe(acac)_3$ (1 mmol, 70 mg) and $Pt(acac)_2$ (0.5 mmol, 40 mg) were used in dibenzyl ether (20 mL) and 1,2-hexadecanediol (2.3 mmol, 0.012 g).

Sample	**OLA / mL**	**OA / mL**	**Ratio OLA:OA**
1	0.15	0.15	1:1
2	0.5	0.5	1:1
3	0.6	0.6	1:1
4	1.5	1.5	1:1
5	2.5	2.5	1:1
6	3	3	1:1
7	4	4	1:1
8	6	6	1:1

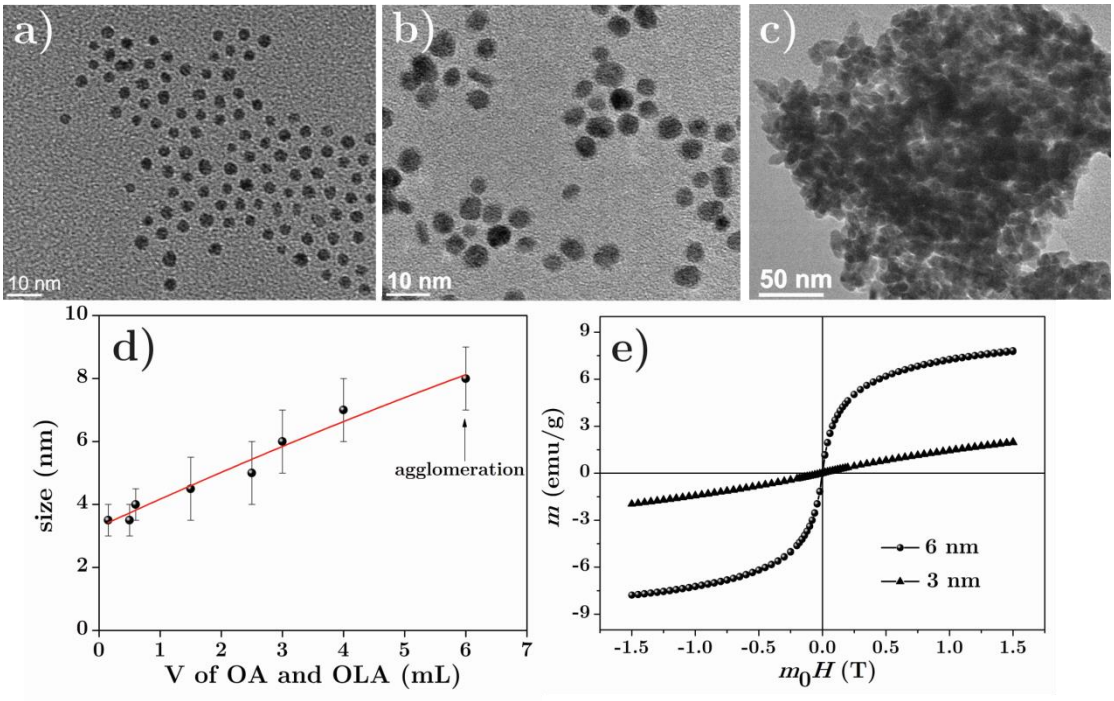


Figure 4.1: TEM images for a) 3-nm (S2), b) 6-nm (S7) and c) agglomerated (S8) "single-core" FePt NPs. d) Graph indicating the size of "single-core" FePt NPs for different amounts of added surfactants and e) comparison of the magnetic properties for 3- and 6-nm "single-core" FePt NPs measured at 300 K.

4.1.2 "Single-core" FePt nanoparticles synthesis based on seed-mediated growth

In order to grow larger NPs with higher m_s, a two-step synthesis, i.e. seed-mediated growth [59], was performed, as is schematically shown in Figure 4.2a. In this approach the NPs prepared with a »regular« synthesis procedure (sample S7) are used as the seeds in the second step of the synthesis. The addition of a metal precursor in the second step leads to a heterogeneous nucleation on the NPs seeds, which reflects in an increase in the initial particle (seed) size. According to the La Mer diagram that describes the nucleation and growth of NPs in the solution (see Section 1.4.3.1), it is essential to precisely control the metal salt concentration. A too large addition might lead to the occurence of the homogeneous nucleation as well, which can be seen as the presence of the new nuclei in the final sample. Homogeneous nucleation is not desirable because it contributes to a larger polydispersity of the final sample due to the presence of the new nuclei and seeds that were further grown at the same time.

For the first step in the synthesis the experimental conditions for the formation of 6-nm-sized FePt NPs were used (S7, Figure 4.1b). In the second step, metal salt precursors ($Pt(acac)_2$ and $Fe(acac)_3$) were added and the same heating regime was used as in the first step. Optimal regulation of the rate between heterogeneous and homogeneous nucleation was achieved when in the second step only a half of the initial concentration of the metal precursors that was used in the first step was added. TEM micrograph (Figure 4.2b) of the NPs formed in the second step clearly shows that the NPs grew to sizes slightly above 10 nm after the second step with very few smaller seeds remaining; however, the NPs developed are of an irregular shape. This irregular shape might be

contributed to the fact that no additional surfactants were added in the second reaction step as it was shown that irregularly shaped FePt NPs can be formed if metal atoms are not sufficiently stabilized by the surfactant molecules [54]. The elemental composition determined from the obtained EDXS data was $Fe_{27\pm2}Pt_{73\pm2}$, which is comparable to the NPs's composition prepared in the first synthesis step. This indicates that the addition of the metal precursors in the second step in the same ratio that was used in the first step does not influence the NPs composition.

Despite the shape, the magnetization value after the second step was almost twice as large (14.5 emu/g) as after the first step (8 emu/g), which can be attributed to the larger size of the NPs. The hysteresis loop presented in Figure 4.2c shows that the larger particles maintained their superparamagnetic behaviour; however, the size of the formed NPs is already close to the SPL, which could restrict their use in biomedical applications.

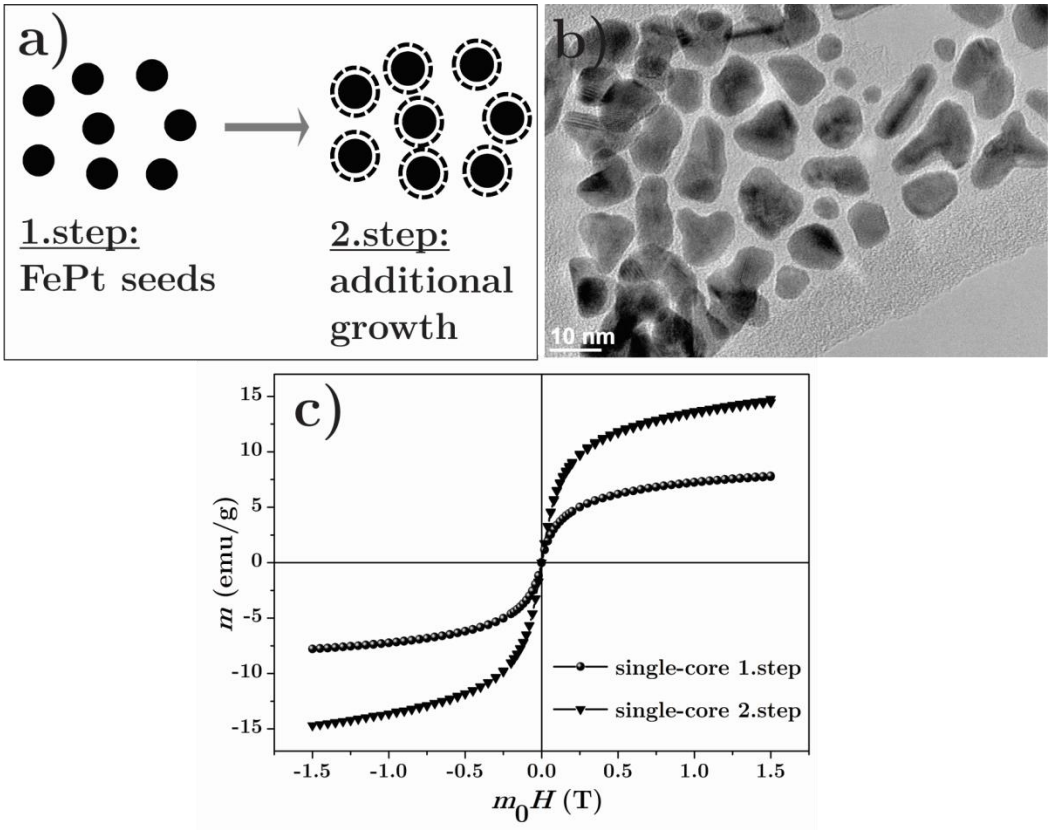


Figure 4.2: a) Schematics of the synthesis of »single-core« FePt NPs in two steps, b) TEM image of NPs obtained after the 2nd step of the seed-mediated growth with c) the corresponding magnetic measurements for the NPs after 1st and 2nd step at 300K.

4.1.3 "Multi-core" FePt NPs synthesis

Formation of "multi-core" NPs was shown to be an important step towards improving the magnetic properties. However, due to only one literature report this field is still unexplored and optimization in the preparation of "multi-core" FePt NPs can be achieved. This publication (Green et al. [51]) served us as the guideline and on its basis we have suggested a few improvements in the synthesis of "multi-core" FePt NPs. First, in the work of Green et al., a thin iron oxide layer around "multi-core" FePt NPs is reported. We have suggested that introducing a reducing agent (e.g. 1,2-hexadecanediol)

into the reaction mixture might prevent the oxidation of FePt NPs and the formation of the oxide phase. Further, we have selected a different Fe precursor in order to have similar metal salts ($Pt(acac)_2$ and $Fe(acac)_3$), which facilitate the formation of a pure FePt phase (solid solution).

According to the literature [63] "multi-core" FePt NPs can be prepared by the changing ratio of the used surfactants (OA/OLA). It has been suggested that the availability of Fe atoms could play an important role in causing the NPs to aggregate into multi-core« FePt NPs [63]. Availability of Fe atoms during the nucleation and growth of NPs can be regulated with the concentration of OA surfactant, because it was shown that OA is a coordinative ligand for the Fe atoms, while OLA coordinated Pt atoms [54]. Therefore, in order to systematically study the formation of "multi-core" FePt NPs, the ratio between the OLA and the OA was varied from 0.08 to 0.75. The volume of OLA was constant (6 mL), while the volume of OA was varied: 0 mL, 0.5 mL, 1 mL, 2 mL, 3 mL, 4.5 mL (S9 -S14). All samples are listed in Table 4.2.

Table 4.2: Sample list of »multi-core« FePt NPs, including the amounts of OLA and OA used and the resulting OLA/OA ratio for FePt samples 9 to 17; $Fe(acac)_3$ (1 mmol, 70 mg) and $Pt(acac)_2$ (0.5 mmol, 40 mg) were used in dibenzyl ether (20 mL) and 1,2-hexadecanediol (2.3 mmol, 0.012 g).

Sample	**OLA / mL**	**OA / mL**	**Ratio OLA:OA**
9	6	0	6:0
10	6	0.5	6:0.5
11	6	1	6:1
12	6	2	6:2
13	6	3	6:3
14	6	4.5	6:4.5
15	0	6	0:6
16	4	1.3	6:3
17	2	0.66	6:3

When the amount of added OA was larger than the amount of OLA (OA>OLA), "single-core" FePt NPs were always obtained (data not shown). TEM images of the prepared samples with different OLA-to-OA ratios are shown in Figure 4.3. It is evident that a small amount of OLA is needed to stabilize the NPs and to prevent agglomeration, which occurs when only OA is used as the surfactant (S15, Figure 4.3; OLA:OA ratio=0:6). It is clear from the TEM images in Figure 4.3 that when the amount of added OLA is larger than the amount of OA (OLA>OA), "multi-core" FePt NPs can be obtained. Moreover, a higher OLA:OA ratio leads to a slight decrease in the size of the "multi-core" NPs, with a smaller size (approx. 10 nm) being obtained when only OLA was used (Figure 4.3; OLA:OA ratio=6:0). In all of the cases when OLA>OA "multi-core" NPs with slightly elongated "single-core" NPs shapes were formed, the NP aspect ratio was found to decrease with OA addition. The observed elongated shape of

the synthesized NPs has its roots in OLA-induced, one-dimensional growth as observed in the literature [61], [62]. The latter group reported that the growth rates for the {111} and {100} planes in the FePt fcc crystal structure can be affected by changing the OLA:OA ratio. The amine group of OLA binds more strongly on the {100} planes than on the {111} planes, which causes the formation of slightly elongated structures. On the other hand, OA binds on both planes equally and therefore spherical structures are formed.

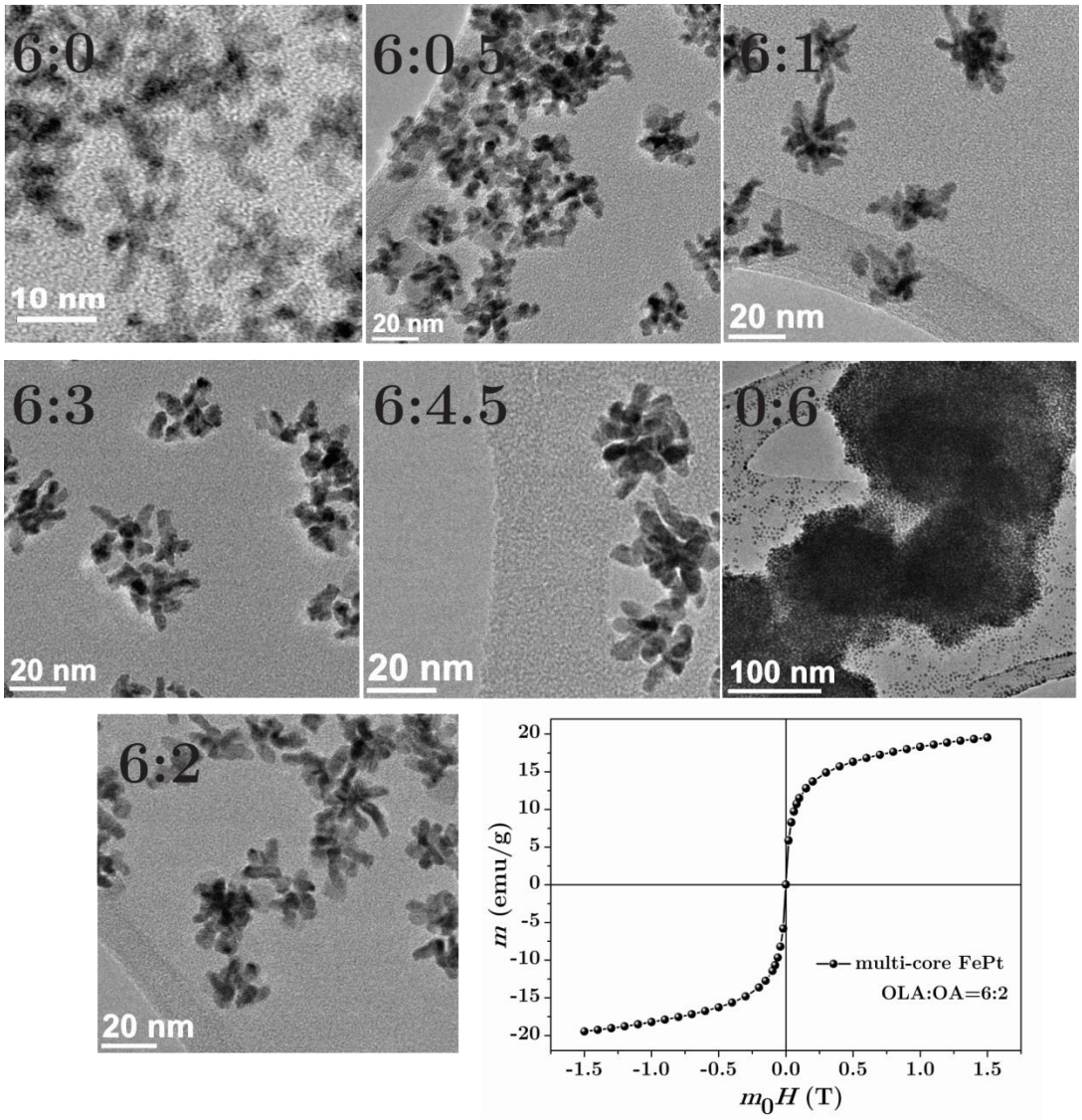


Figure 4.3: TEM images of "multi-core" FePt NPs for different OLA:OA ratios with magnetic measurements at 300 K for the sample with OLA:OA ratio = 6:2 (S12).

In order to study the composition of "multi-core" FePt NPs prepared from different OLA:OA ratios, EDXS analysis on the samples presented in Figure 4.3 was done. From Figure 4.4 it is evident that decrease in the addition of OA in the reaction mixture results in the increase in the final Fe content in the FePt NPs. Because OA is a coordinative ligand for the Fe atoms, a smaller amount of OA results in a fewer coordinated Fe metal intermediates in the reaction mixture and hence NPs with a slightly higher Fe content. The highest amount (54 at.% of Fe) is achieved when no OA was used (S9) and, on the contrary, the lowest amount (12 at.% of Fe) at the highest OA

addition (S8). It is expected that a high amount of Fe in the sample will result in the highest m_s. However, sample with the highest amount of Fe (54 at.% of Fe) exhibit $m_{(1.5T)}$ only of 1.5 emu/g (not shown) due to the small core size (< 4nm). Increase in the OA addition to 2 mL (S12) leads to a decrease in Fe content to 30 at. % (detailed HRTEM, SAED and EDXS analysis of this sample is shown in Section 4.1.4). However, higher addition of OA caused an increase in the individual core size and, consequently, higher m_s ($m_{(1.5T)}$ = 19.5 emu/g, magnetic measurement is shown in Figure 4.3). Further increase in the OA content does not lead to a significant enlargement of the core size that would compensate loss in the Fe content, therefore, samples with a larger OA concentration (S13 and S14) exhibit lower $m_{(1.5T)}$ than the "optimal" sample (S12, V(OA) = 2mL). From those results it can be concluded that a trade-off between core size and Fe content in "multi-core" FePt NPs is needed in order to obtain the "optimal" magnetic properties. An increase in the core size in "multi-core" FePt NPs is of vital importance for achieving high m_s. However, even higher m_s can be expected for "multi-core" particles with larger core sizes and high Fe content at the same time. Therefore, to follow this goal, two sets of experiments were performed. In the first one, the effect of the total surfactant concentration at constant surfactant ratio (optimal conditions, OLA:OA=6:2) on the NPs size and their magnetic properties was studied. And in the second one, the influence of the Fe:Pt salt ratio on the NPs composition was investigated.

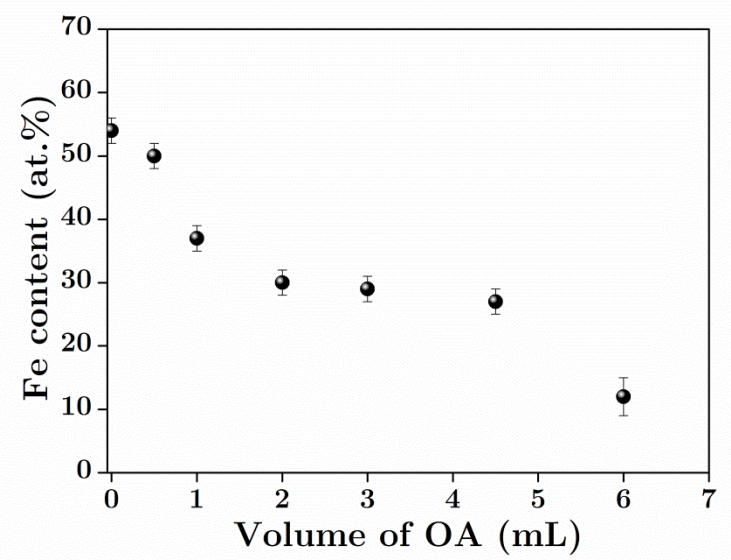


Figure 4.4: Graph indicating variation in composition of FePt by changing the amount of added OA while all other parameters are kept constant: OLA (6 mL), $Fe(acac)_3$ (1 mmol, 70 mg) and $Pt(acac)_2$ (0.5 mmol, 40 mg) were used in dibenzyl ether (20 mL) and 1,2-hexadecanediol (2.3 mmol, 0.012 g).

If the ratio between surfactants is kept constant (OLA : OA = 3) and the overall volume of added surfactants is varied, "multi-core" NPs are still formed. This can be seen in Figure 4.5 if comparing S12 (OLA : OA=6 mL : 2 mL), S16 (OLA : OA=4 mL : 1.3 mL) and S17 (OLA : OA=2 mL : 0.66 mL). Size of the "multi-core" FePt NPs is increased when higher volume of added surfactant is used. In the sample S17, where the lowest amount of both surfactants was used, but ratio is still kept OLA : OA = 3, the smallest "multi-core" FePt NPs are formed with size approx. 10 nm. However, in all three cases NPs are star-shaped, which indicates that OLA:OA ratio dictates the shape of

the NPs and volume of added surfactant is responsible for the size, as we already observed in the case of "single-core" FePt NPs. Magnetic properties follow the same trend as in the case of "single-core" FePt NPs; bigger "multi-core" NPs exhibit higher magnetization value, with the highest value when OLA = 6 mL and OA = 2 mL (S12, $m_{(1.5T)} = 19.5$ emu/g) and the lowest value when OLA = 2 mL and OA = 0.66 mL (S17, $m_{(1.5T)} = 12$ emu/g) was used. Magnetization value of S16 (OLA = 4 mL and OA = 1.33 mL) lies in between S12 and S17 ($m_{(1.5T)} = 14$ emu/g).

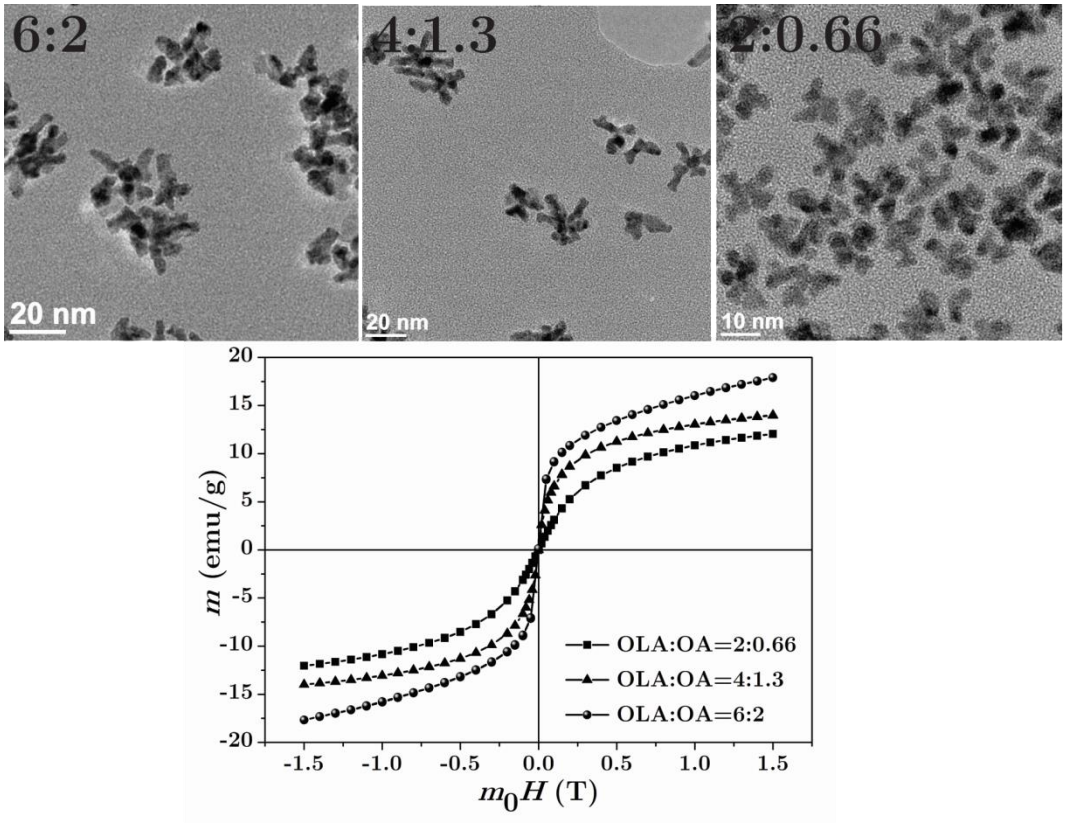


Figure 4.5: TEM images of "multi-core" FePt NPs at constant OLA:OA ratio = 3 but the overall volume of added surfactants was varied with magnetic measurements at 300 K for the sample with OLA:OA ratio = 6:2 (S12).

For accurate determination of m_s knowing the exact mass of the magnetic component is extremely important, otherwise a large error can be introduced in the results. For that purpose, thermogravimetric analyses on OLA, OA and OLA/OA-coated FePt NPs were performed to determine the amount of organic matter, i.e. OLA and OA content, in the FePt sample. The weight-loss curves for pure OLA, pure OA and OLA/OA-coated FePt NPs measured by TGA in the temperature range 25-600°C are shown in Figure 4.6. First only pure surfactants (OLA and OA) were investigated. In the case of OLA the decomposition starts at 200°C with a large drop in the mass up to 250° C followed by a slower weight reduction until reaching zero at about 300°C (Figure 4.6a). Decomposition of OA starts at a higher temperature (250°C) than in the case of OLA, again decomposition is very fast and almost the total mass is reduced up to 300°C and slowly reaches zero at about 400°C (Figure 4.6b). Temperature range for the OLA and OA decomposition is in good agreement with the literature report [33]. Determination of the

temperature range where surfactants decompose is important to interpret results for OLA/OA-coated FePt NPs. In order to ensure the reproducibility of the synthesis and measurement, TGA measurements were performed on two "single-core" and two "multi-core" FePt samples. Weight loss for all four samples was in the same weight range, therefore, only one, a representative graph, for all FePt NPs was selected and is shown in Figure 4.6c. It can be seen that the temperature range for the mass loss is very similar to that of the pure surfactants, reaching saturation at 400°C. The weight remained at higher temperatures can be attributed to the FePt NPs. The mass loss was determined to be 30 %, which is due to the decomposition of the surfactants. This mass correction was used in all magnetic measurements.

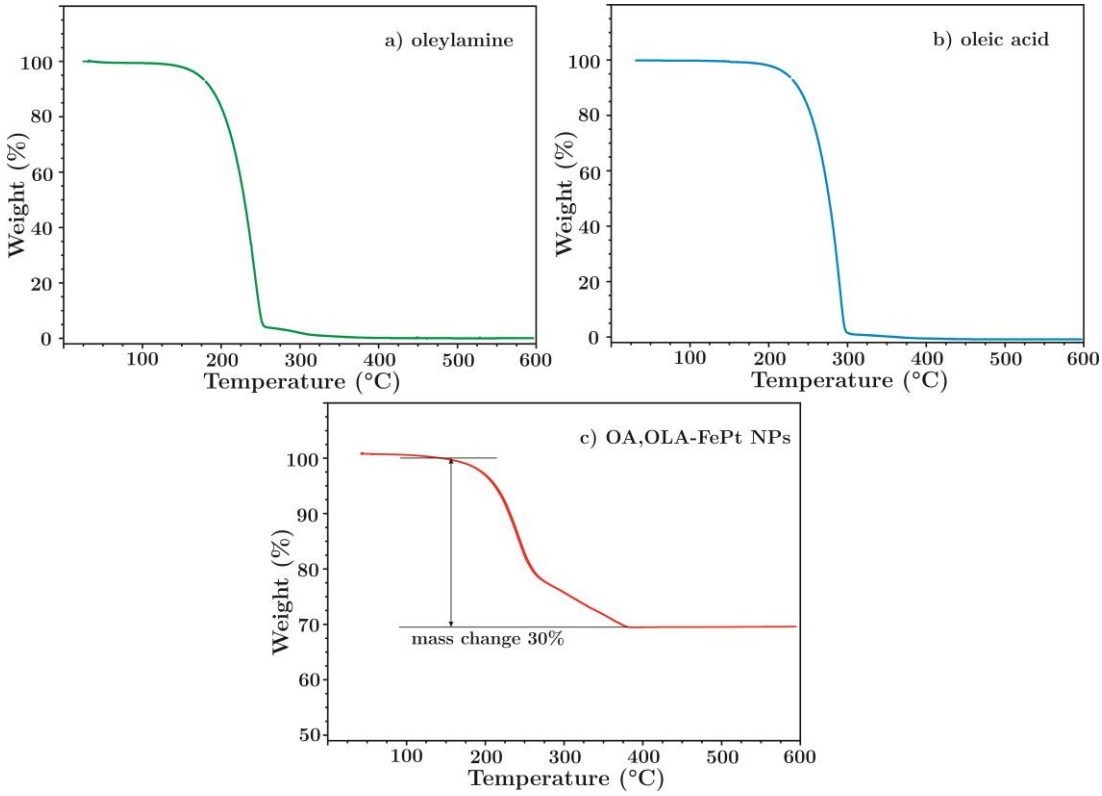


Figure 4.6: The weight-loss curves for a) pure oleylamine (OLA), b) pure oleic acid (OA) and c) OLA/OA-coated FePt NPs measured by TGA in the temperature range 25-600°C.

The composition of "multi-core" FePt NPs was studied by changing the Fe:Pt salt ratio. All investigated samples are listed in Table 4.3. OLA:OA ratio was initially selected to be 6:2 (S12, as in the case of optimal "multi-core" FePt NPs) and the Pt:Fe salt ratio was then varied from 1:1 up to 1:8 (S18-S21). With increasing Fe salt addition (Pt:Fe salt ratio 1:1 to 1:2, samples S18 and S12, respectively) also the amount of Fe in the samples increases from $Fe_{20}Pt_{80}$ to $Fe_{30}Pt_{70}$, respectively. TEM investigation together with the EDXS analysis showed that at higher addition of Fe salt (Pt:Fe salt ratio > 1:2) more OA is required to sufficiently stabilize all Fe atoms via Fe-oleate complex formation, otherwise besides the FePt phase also the Fe oxide phase is formed. When Pt:Fe salt ratio = 1:4 was used (S19), non-oxidised FePt alloy phase with a composition $Fe_{35}Pt_{65}$ can be achieved at the addition of OA=3.5 mL. However, at higher Pt:Fe salt ratio (1:6 and 1:8) even the addition of 4.5 mL of OA is not sufficient to prevent

formation of Fe oxide phase due to the large excess of Fe salt in the initial reaction mixture. This observation is in good agreement with the literature [122], where it was shown that the excess of Fe-oleate complex in the reaction mixture leads to the formation of iron oxide.

TEM image of FePt-Fe oxide NPs formed when Pt:Fe salt ratio 1:8 was used is shown in Figure 4.7a. Darker FePt phase in the dumbbell NP can be easily distinguished from the lighter Fe oxide phase. In Figure 4.7a the FePt phase is marked with the red dashed line and the Fe oxide phase with the blue dashed line. In order to determine the crystal structure of FePt-Fe oxide NPs SAED pattern was recorded, which is shown in Figure 4.7b. Comparison of the experimental results with the simulated diffraction patterns showed that two different phases are present in the sample. The first phase (Figure 4.7b, red simulated spectra) corresponds to the *fcc* crystal structure of the FePt phase and the second phase (Figure 4.7b, blue simulated spectra) can be ascribed to the Fe_3O_4 cubic inverse spinel structure (ICSD 65340).

Table 4.3: Sample list of »multi-core« FePt NPs, including the OLA : OA ratio and $Pt(acac)_2$: $Fe(acac)_3$ ratio with the resulting composition for FePt samples 18 to 22. Samples were prepared in dibenzyl ether (20 mL) and 1,2-hexadecanediol (2.3 mmol, 0.012 g).

Sample	**Pt:Fe salt ratio**	**OLA:OA ratio (mL)**	**Composition (at.%)**
18	1 : 1	6 : 2	$Fe_{20}Pt_{80}$
12	1 : 2	6 : 2	$Fe_{30}Pt_{70}$
19	1 : 4	6 : 3.5	$Fe_{35}Pt_{65}$
20	1 : 6	6 : 4.5	FePt + Fe oxide
21	1 : 8	6 : 4.5	FePt + Fe oxide

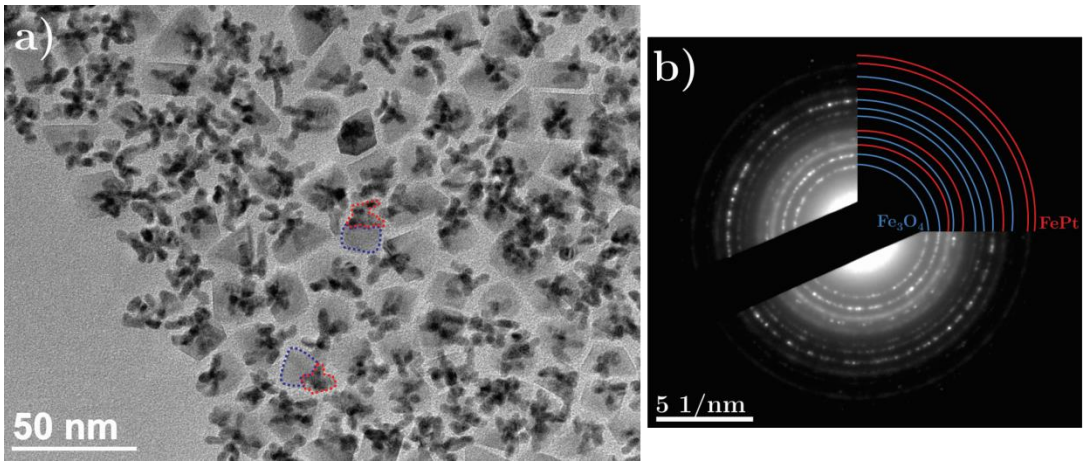


Figure 4.7: a) TEM image and b) SAED pattern of the sample 22, where Pt:Fe salt ratio = 1:8 was used. FePt and Fe oxide phases are indicated with red and blue dotted lines, respectively.

From this study it can be concluded that the composition of FePt NPs can be more precisely tuned by changing the OLA:OA ratio, while changes in the Pt:Fe salt ratio do not offer good control over the NPs 'composition and at higher concentration of Fe salt formation of Fe oxide phase cannot be avoided. Comparison of S12 and S19 revealed that in the latter case 100% increase in the amount of Fe salt and 75% increase in the OA amount in the reaction mixture led only to a slight increase of the Fe content in the sample (from $Fe_{30}Pt_{70}$ to $Fe_{35}Pt_{65}$), but no evident improvement in the magnetic properties. Due to the lower consumption of the materials and good magnetic properties, optimal conditions for the preparation of »multi-core« FePt NPs with the highest $m_{(1.5T)}$ (19.5 emu/g) were found to be OLA:OA ratio = 6:2 and Fe:Pt salt ratio = 1:2 (S12). Therefore, this sample will be used in all the following experiments.

4.1.4 HRTEM analysis of FePt NPs

Typical morphologies and size distributions of the "single-core" and "multi-core" FePt NPs are shown in Figure 4.8. The average size (defined as the average diameter) of the "single-core" (S7) NPs measured on the basis of 30 individual particles was 7±1 nm. In the case of the "multi-core" NPs (S12) the average size was estimated by measuring the average diameter of the body, using the dashed line, as indicated in Figure 4.8. The average particle size of the "multi-core" NPs was 20±3 nm.

The selected-area electron diffraction (SAED) patterns (superimposed in Figure 4.8), which were obtained for the "single-core" and "multi-core" samples, are in accordance with the *fcc* crystal structure of the FePt phase [123]. No additional phases could be detected, either using TEM/STEM imaging or electron-diffraction techniques (e.g., oxide phases etc.).

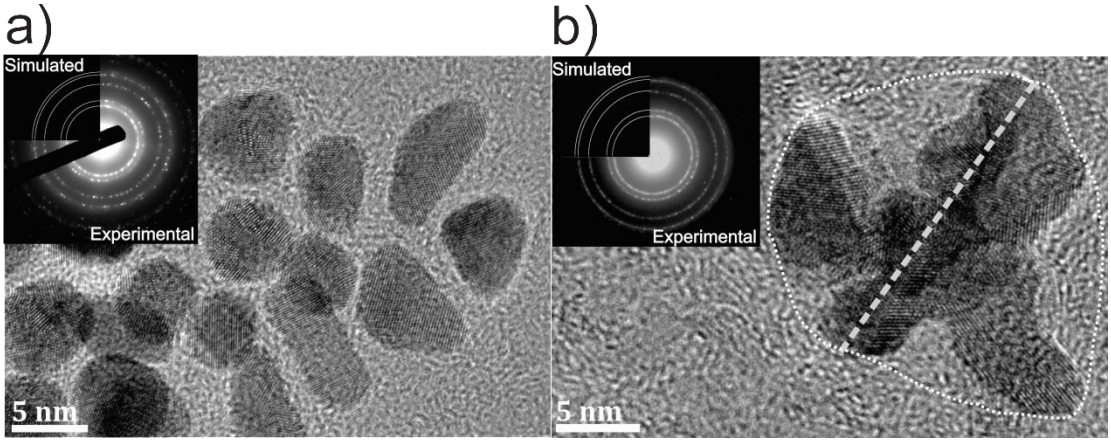


Figure 4.8: HR-TEM images of a) "single-core" and b) "multi-core" FePt nanoparticles with corresponding SAED patterns shown as insets.

In order to determine the crystallinity of the individual "single-core" and "multi-core" NPs, a series of atomic-resolution high-angle annular dark-field STEM (HAADF-STEM) images were acquired. Representative HAADF-STEM images are shown in Figure 4.9. The HAADF-STEM image acquired from the "single-core" NP in the [112] projection of the FePt *fcc* structure is shown in Figure 4.9a and the enlarged region of the particle edge is shown as an inset. The observed non-periodic variation of high and low intensity between the adjacent atomic columns, which is marked by white and grey arrows (Figure 4.9a), is directly related to the non-periodic variations in the atomic-column composition,

thus described as a FePt solid-solution with a *fcc* structure, which is in accordance with the SAED analysis. The HAADF-STEM images of the "multi-core" NP (Figure 4.9b) show that these aggregates are typically composed of radially grown, individual NPs. The structural characteristics of these individual particles are the same as described for the case of the "single-core" NPs. The results showed that controlled aggregates, i.e., "multi-core" FePt NPs, can be synthesized in-situ without any templates. Moreover, during our research it was ascertained that the addition of a small amount of a reducing agent (1,2-hexadecanediol) is necessary to avoid the oxidation of FePt NPs and the formation of oxide phases during the synthesis. TEM analyses confirmed a pure FePt phase without any oxide phase present. In contrast, in the work of Green et al. [63], a thin iron oxide layer around "multi-core" FePt NPs is reported, most probably due to the fact that no reducing agent was used during their synthesis.

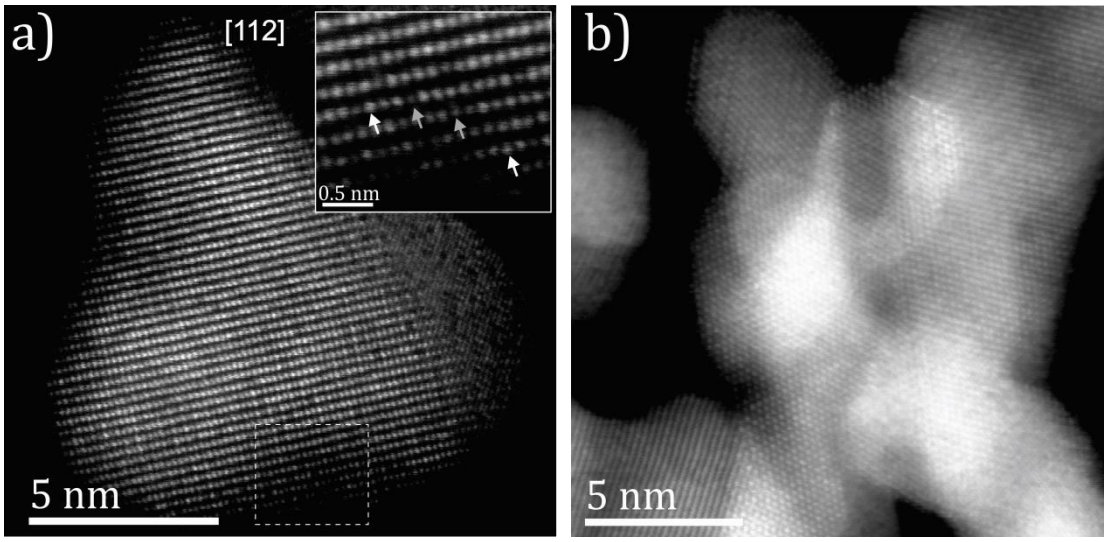


Figure 4.9: High-resolution HAADF-STEM images of individual a) "single-core" and b) "multi-core" FePt nanoparticles. The inset shows the enlarged region of the particle's edge.

The elemental analysis obtained using the energy-dispersive X-ray spectroscopy (EDXS) was performed on a "multi-core" (S12) sample. Three separately prepared samples were examined for their elemental composition in order to estimate the reproducibility of the synthesis procedure and five spectra were recorded for each sample in different areas. All three samples had very similar compositions, with the maximum deviation between them being ±1 at.%. The elemental composition determined from the obtained EDXS data was $Fe_{30\pm1}Pt_{70\pm1}$, respectively. As described in Section 3.2.1.1, composition of "single-core" FePt NPs (S7) was found to be $Fe_{25\pm1}Pt_{75\pm1}$. A slightly higher content of Fe in the case of the "multi-core" FePt NPs can be attributed to the lower content of OA during the synthesis, since it was suggested that OA is a coordinative ligand for the Fe atoms, and OLA is said to coordinate the Pt intermediates [54]. Therefore, a smaller amount of OA would result in a fewer coordinated Fe metal intermediates in the reaction mixture and hence NPs with a slightly higher Fe content.

The bright field (BF) and HAADF-STEM images of "multi-core" FePt NP are shown in Figure 4.10a and Figure 4.10b, respectively. In order to confirm the distribution of Fe and Pt atoms in the particles the energy dispersive X-ray spectrometry (EDXS)

elemental maps for Fe (K line) and Pt (M line) were recorded and are shown in Figure 4.10c and Figure 4.10d, respectively. Elemental maps confirmed a homogenous distribution of both atoms along the whole area of the particle.

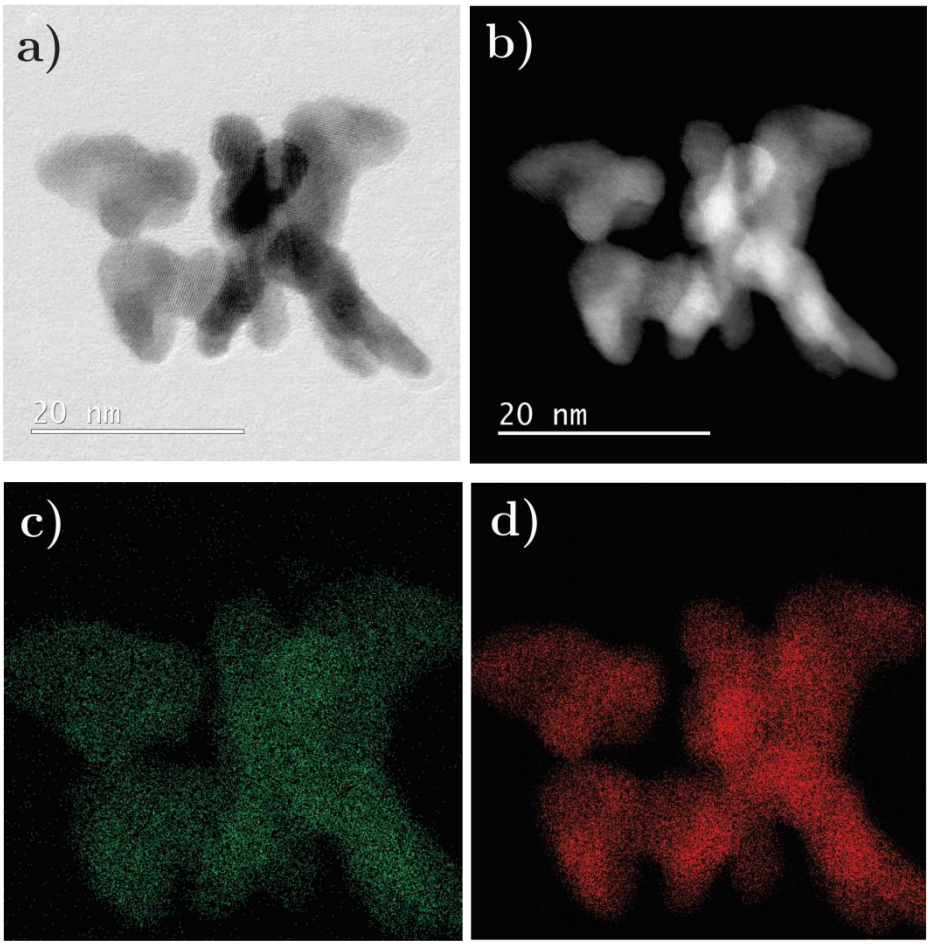


Figure 4.10: a) Bright-field and b) HAADF-STEM image of a“multi-core” FePt NP with the corresponding elemental map for c) Fe (green, Fe K line) and Pt (red, Pt M line).

4.1.5 Magnetic properties of “single and multi-core” FePt NPs

Magnetic properties of the as-synthesized “single-core“ and “multi-core” FePt NPs were assessed via temperature-dependent field-cooled and zero-field-cooled (FC/ZFC) magnetic susceptibility curves as shown in Figure 4.11. Measured samples were in a dry form. Blocking temperature (Tb) for the “single-core” (S7) and “multi-core” FePt NPs (S12) were determined to be 36 K and 121 K, respectively. This is in a good agreement with the Néel relaxation theory where larger particles have higher Tb. Broader peak in the case of “multi-core” FePt NPs indicates a broader size distribution, which is consistent with the results obtained by TEM analysis. Moreover, T_b can be shifted towards higher temperature due to the presence of the magnetic dipole interactions. The spin structure of the NPs can be affected by the inter-particle interactions, which are mainly long range dipole-dipole interactions and the exchange interactions through the surface of the particle. If the magnetic susceptibility (ZC curve) becomes temperature-independent at $T<<T_b$ and reaches saturation, this indicates the presence of the inter-particle dipole interactions. It can be seen from Figure 4.11 that for both samples ZC curves in the

range $T<<T_b$ increase with the decreasing temperature. Even though the complete saturation is not achieved, it can be inferred from the ZC curves that FePt NPs in a dry form are weakly interacting. "Multi-core" FePt NPs shows a less steep curve in that temperature range, which can be attributed to the stronger dipole interactions as in the case of sample "single-core" NPs. The larger dipole interactions in the case of larger NPs might arise due to the higher ms [40]. Similar behaviour was shown on the case of 3- and 9-nm sized *fcc* FePt NPs, where both samples have non-negligible dipole interactions, the effect being smaller in the smaller NPs [40]. It has to be pointed out that the samples for the ZFC/FC measurements were in a dry form with the inter-particle distance being reduced, therefore, significant dipole interactions at lower temperature could be expected. If however the magnetic dipolar interactions would be significant also at room temperature, they would compromise the superparamagnetic properties and colloidal stability of the suspension, which was not the case in our study.

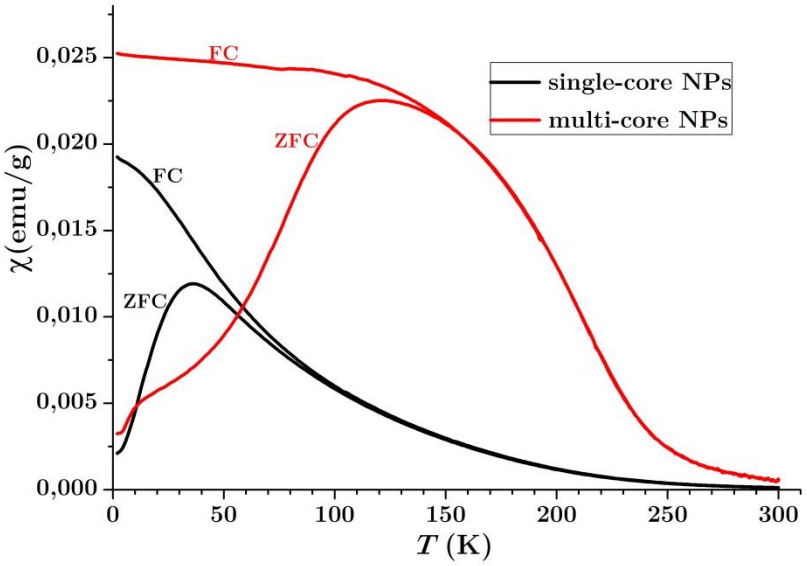


Figure 4.11: Temperature dependent field-cooled and zero-field-cooled (FC/ZFC) magnetic susceptibility curves for "single-core" and "multi-core" FePt NPs performed with an applied field 8 kA/m.

We additionally presume that in the case of "single-core" NPs in the suspensions the direct exchange interactions between the individual NPs might be neglected due to the surfactant coating, which prevents their direct contact [124]. However, in "multi-core" NPs the exchange interactions, i.e. intra-particle collective behaviour, can be present, which leads to the enhancement in the effective magnetic moment of "multi-core" NPs as was already observed by Lartigue et al. [37] in "multi-core" Fe-oxide NPs. Clustering of NPs would have an influence on the effective magnetic moment of the NP (μ_{eff}), which can be determined using the following procedure. From the magnetic hysteresis measurements the initial susceptibility of the samples (χ_0) can be calculated by using the slope of the M (kA/m) vs. H (kA/m) curve at low H.

Mass magnetization (emu/g) was converted to volumetric magnetization (emu/cm^3) by assuming density of FePt NPs 14 g/cm^3. For the calculation purposes in this case M (emu/cm^3) and H (T) were converted into SI units (kA/m). M - H curve at low H (0-32 kA/m) for "single-core" (S7) and "multi-core" FePt NPs (S12) is shown in Figure 4.12.

Initial susceptibility (χ_0) is found to be 0.89 and 3.93 for the "single-core" and "multi-core" NPs, respectively.

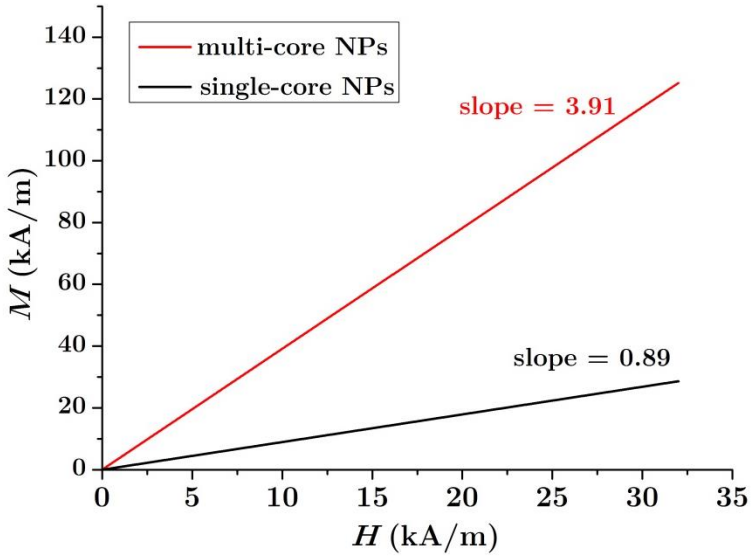


Figure 4.12: Initial magnetization at low low H (0-32 kA/m) for "single-core" and "multi-core" FePt NPs measured at 300 K.

Furthermore, by using the relation

$$\chi_0 = \mu_0 \frac{1}{V_{tot}} \frac{\mu_{eff}^2}{3\, k_b T}\,, \tag{4.1}$$

the effective magnetic moment for the nanostructure (μ_{eff}), can be calculated where V_{tot} is the total volume of a NP, k_b is the Boltzman constant (1.38 x 10^{-23} J/K), T is the temperature (K) and μ_0 is the permeability of a vacuum ($4\pi\times10^{-7}$ N/A^2) [41], [125]. Reorganization of the Eq.(4.1) gives an expression for the direct calculation of μ_{eff}:

$$\mu_{eff}^2 = \frac{V_{tot}\, \chi_0\, 3\, k_b\, T}{\mu_0}, \tag{4.2}$$

The effective magnetic moment of NPs (μ_{eff}) was then calculated by using the Eq. (4.2). Volume of FePt NPs was estimated to be $V_{(single\text{-}core)}$ and $V_{(multi\text{-}core)}$ 1.13 x 10^{-25} m^3 and 1.76 x 10^{-24} m^3, respectively. The calculated effective magnetic moments are $\mu_{eff\ (single\text{-}core)}$ =0.3 x 10^{19} A m^2 and $\mu_{eff\ (multi\text{-}core)}$ =2.6 x 10^{19} A m^2. From the above calculations it can be seen that the "multi-core" FePt NPs possess a higher effective magnetic moment than the "single-core" ones.

Moreover, if the cores in the "multi-core" structure are assumed to have the same magnetic moment (magnetic moment of the core, μ_c) and are magnetically non-interacting, one would expect that the effective magnetic moment of the "multi-core" particle (μ_{eff}) would follow the statistical relation for randomly oriented independent (non-interacting) core magnetic moments (μ_c) according to the relation [125]:

$$\mu_{eff} = \sqrt{N}\, \mu_c\,, \tag{4.3}$$

where N is the number of cores in the "multi-core" NP. If we assume that the average number of the cores in the "multi-core" NPs is 8, the $\mu_{\text{eff (multi-core)}} = 2.8\ \mu_{\text{eff (single-core)}}$, which is less than was shown experimentally ($\mu_{\text{eff (multi-core)}} \approx 8 \cdot \mu_{\text{eff (single-core)}}$). This can be attributed to the collective magnetic behaviour of the FePt cores [37] and/or to the slight increase in the core size, which was confirmed by TEM (please see discussion on surface effects later). We can say that the enhancement in the effective magnetic moment in FePt "multi-core" NPs has the origin in the intra-particle collective behaviour, i.e., the exchange interactions, as was already observed by Lartigue et al. (2012) in "multi-core" Fe-oxide NPs.

Furthermore, surface effects can also significantly influence the magnetic properties of the NPs. After determining the T_B for the "single-core" and "multi-core" FePt NPs the effective anisotropy constant K_{eff} was calculated using the Eq. (1.11) assuming spherical shape of NPs. It was found that the K_{eff} is larger for "single-core" FePt NPs ($6.9 \cdot 10^4$ J/m^3) than for "multi-core" FePt NPs ($1.3 \cdot 10^4$ J/m^3). Larger K_{eff} for the "single-core" FePt NPs is due to the smaller size and, consequently, increasing contribution from the surface anisotropy. Similar results were obtained in the work of Seehra et al. [40], where it was calculated that K_{eff} is $1.96 \cdot 10^5$ J/m^{3}and $4.3 \cdot 10^4$ J/m^{3}for FePt NPs with size 3 and 9 nm, respectively. Those calculations showed that the size dependence of the K_{eff} should be considered in the calculations when having magnetic NPs with a different size. Besides the magnetocrystalline and surface anisotropy also shape anisotropy (K_{shape}) has an important contribution to the magnetic properties of nanostructures. In the case of "single-core" NPs due to their spherical shape contribution of the K_{shape} to the K_{eff} can be neglected. However, "multi-core" FePt NPs have a complex structure and, therefore, their K_{shape} is more difficult to be evaluated. If we assume that "multi-core" FePt NPs are composed of slightly elongated, rod-shaped cores and the entire shape of the "multi-core" FePt NPs is irregular and slightly elongated, then the K_{eff} for "multi-core" NPs should lie in between $K_{eff,spherical}$ and $K_{eff,rod}$ due to the additional contribution from K_{shape}. For the same-sized *fcc* FePt NPs (approx. 4.5 nm in diameter) it was calculated that $K_{eff,spherical}$ ($1.6 \cdot 10^5$ J/m^3) < $K_{eff,rod}$ ($2.7 \cdot 10^5$ J/m^3) [36]. However, "single-core" and "multi-core" FePt NPs are not of the same size, therefore, larger contribution to the K_{eff} can be expected due to the size effects. Even though that the calculated value of K_{eff} does not take into account the dispersions of size and anisotropy of the FePt NPs, the magnetic anisotropy in both cases, i.e. "single-core" and "multi-core" NPs, is much higher than the one corresponding to the disordered cubic phase of the FePt bulk (K_{eff} is $6 \cdot 10^3$ J/m^3 [126]), which confirms that in FePt NPs the main contribution to the magnetic anisotropy comes from the atoms at the surface.

In the case of "multi-core" NPs, the surface-to-volume ratio is reduced due to the coalescence of individual cores, which could also contribute to the increase of the magnetization. This was already shown in the case of "single-core" NPs where a slight increase in the core size led to a significant improvement of the magnetic properties. According to the Eq.(1.7), the saturation magnetization of the NPs is proportional to the NPs' size. Furthermore, Eq.(1.7) shows that the maximum magnetization can be obtained when the disordered surface spin layer disappears. For example, for a "single-core" FePt NPs a disordered surface spin layer was estimated to be 1.5–1.8 nm, depending on the surface ligand [34]. The theoretically calculated m_s for "single-core" FePt NPs obtained from Eq.(1.7) are shown in Figure 4.13 (black line), where r = 1.6–7.5 nm, d = 1.5 nm and M_s = 75 emu/g were used. Experimental values (Figure 4.13, red line) are plotted for "single-core" FePt NPs in the range r = 1.6–4 nm, which correspond to m_s = 1.5–14 emu/g and a good match between the theory and experiment was obtained.

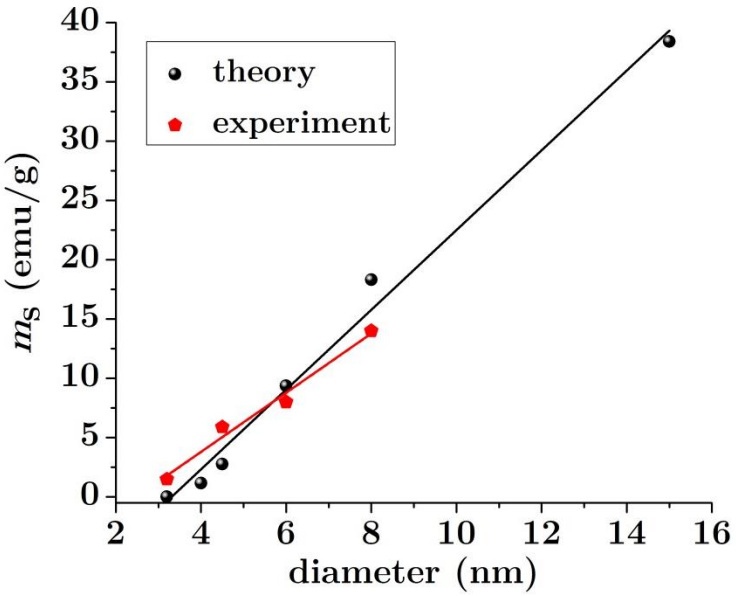


Figure 4.13: Graph indicating theoretically calculated and experimentally obtained saturation magnetization for "single-core" FePt NPs with different diameters.

By plotting the saturation magnetization value obtained for our FePt "multi-core" NPs (m_s = 19.5 emu/g) in Figure 4.13, a theoretical "single-core" NP with a diameter of 9.7 nm is obtained. This indicates that the multi-core nanoparticle magnetically behaves as a single-core particle with a size of 9.7 nm. TEM analysis of the "multi-core" NPs showed that the size of the individual cores is in the range 8±1nm, which is "slightly" less than it was calculated from the above equation. From this it could be assumed that the magnetic ordering due to the presence of the intra-particle exchange interactions increases the magnetic diameter of the cores. Therefore, we can conclude that the observed increment in the magnetization of the "multi-core" NPs has a basis in the reduction of their surface disorder (smaller surface-to-volume ratio) and/or in the magnetic exchange interactions between the individual cores.

Based on the presented results we can conclude that the highest possible magnetization for our FePt system would be theoretically obtained by fabricating "single-core" NPs with a core size just below the SPL (10 nm) and combine them together in a "multi-core" structure, introducing the collective magnetic behaviour without crossing the SPL. For example, the calculated m_s for a "single-core" NPs with a size around SPL (10 nm) is 23 emu/g. In our study "single-core" FePt NPs prepared via seed-mediated growth and size close to 10 nm possessed $m_{(1.5T)}$= 14.5 emu/g. Therefore, due to the presence of the exchange interactions between the individual cores, combining 10-nm sized cores in a "multi-core" structure would lead to an even further increase in m_s. However, this value is expected to still be much lower than the bulk saturation magnetization (75 emu/g) that cannot be obtained in a superparamagnetic regime due to the prevalent surface effects. An experimental hint about the maximum size of the "multi-core" NPs can be seen from the work of Green et al. [63], where "multi-core" FePt NPs with a size above approx. 40 nm and m_s = 29 emu/g already showed evidence of ferromagnetism at room temperature.

4.2 Ligand Exchange Reactions on FePt NPs

In order to evaluate the performance of the as-synthesized FePt NPs for biomedical applications, water suspensions are desired, which pose an additional functionalization step, since the syntheses of FePt NPs are performed in organic solvents. The as-synthesized FePt NPs are hydrophobic due to the use of OLA and OA as the surfactants. One of the ways for transferring the hydrophobic NPs into an aqueous phase is a ligand exchange method, in which new ligand molecules are used to replace the hydrophobic ligand. Ligand exchange method is typically performed in two phases: NPs in the hydrophobic phase and small molecules in the hydrophilic phase [127]. In order to prepare stable and biocompatible water suspensions of FePt NPs two different dopamine-based ligands were used: zwitterionic dopamine sulphonate (ZDS) ligand and hydrocaffeic acid (HCA). To the best of our knowledge, both ligands were used on the FePt system for the first time.

4.2.1 Functionalization of FePt NPs with zwitterionic dopamine sulfonate

The ZDS ligand was prepared according to a modified protocol described in the literature [86]. Dopamine hydrochloride was used as the starting material, with its chemical formula shown in Figure 4.14a. Ammonium hydroxide and 1,3-propanesultone were added to induce the sulfonation of the dopamine and the conversion to a dopamine sulfonate (Figure 4.14b). To form the final product (ZDS ligand), dopamine sulfonate was dissolved in DMF with the addition of anhydrous sodium carbonate, and the methylation of the amino group was achieved by the addition of iodomethane (Figure 4.14c). The excess of base was added to capture the hydrogen iodide that was released (H^+ from amine, I^- from iodomethane) and to keep the system basic, making sure that the amine and the sulphonic acid are not protonated. The protonation of the amine would hinder the nucleophilic attack on the iodomethane. The second methylation is less favorable because of steric hindrance; however, the higher temperature, the already deprotonated sulphonate (hence a more stable end product) and the removal of hydrogen iodide pulls the equilibrium to the side of the products. Strong coordination bonds between the –OH groups of the ZDS ligand and the Fe atoms on the surface of the NP were already proved in the case of SPIONs [86]. According to reports in the literature [128], that catechol-Pt complexes were formed by the coordination of Pt onto OH groups of catechol, we can assume that the catechol ligand is also coordinated to Pt atoms, similar to Fe. In Figure 4.14d it is clear that the suspension of OA/OLA stabilized the FePt NPs in the hexane phase before the ligand exchange with the NPs-free water phase below. After the ligand-exchange reaction the ZDS-functionalized FePt NPs are successfully transferred into the water phase and a NPs-free hexane phase is visible above (Figure 4.14e). Water suspensions of such ZDS ligand functionalized FePt “single-core” and “multi-core” NPs showed excellent stability and were subsequently checked for their MRI performance.

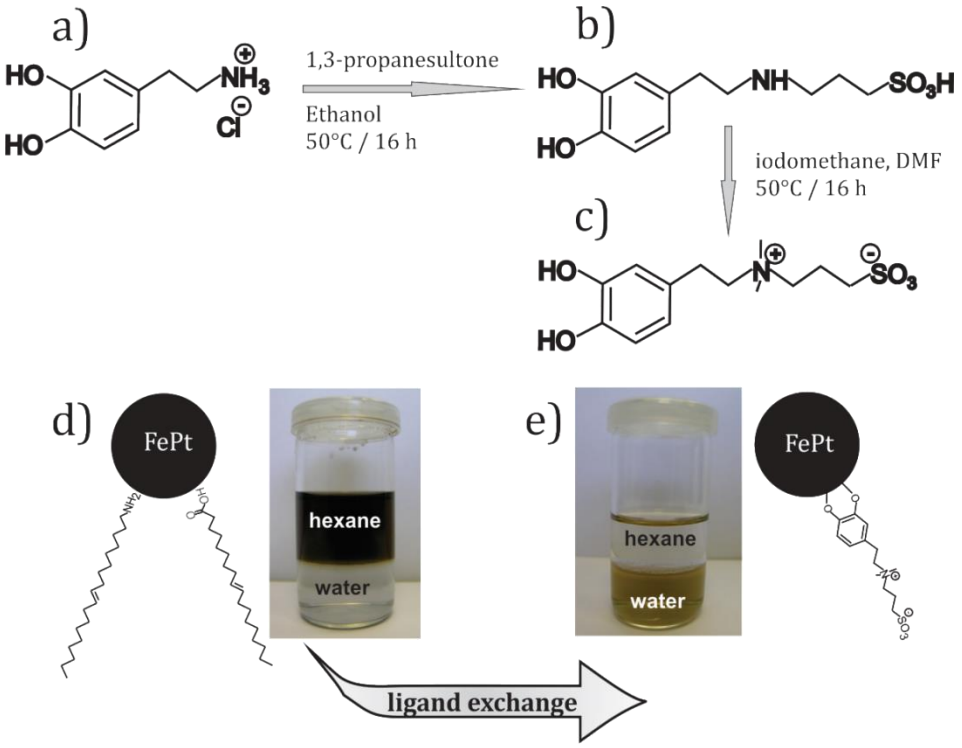


Figure 4.14: a)-c) Synthesis route of the ZDS ligand, d) oleic acid/oleylamine stabilized FePt NPS in hexane phase before the ligand exchange and e) ZDS-functionalized FePt NPs in the water phase after the ligand-exchange reaction.

4.2.2 Functionalization of FePt NPs with hydrocaffeic acid

Here we used a facile one-phase and highly efficient method to transfer hydrophobic FePt NPs to an aqueous phase [127] by using the HCA dissolved in tetrahydrofuran (THF). Ligand exchange reaction is schematically shown in Figure 4.15a. Literature reports on Fe oxide NPs have shown that the dopamine provides a strong coordination to the NP surface [87], [127], while the carboxylic group is responsible for the high water solubility and suspension stability in the wide pH range [127].

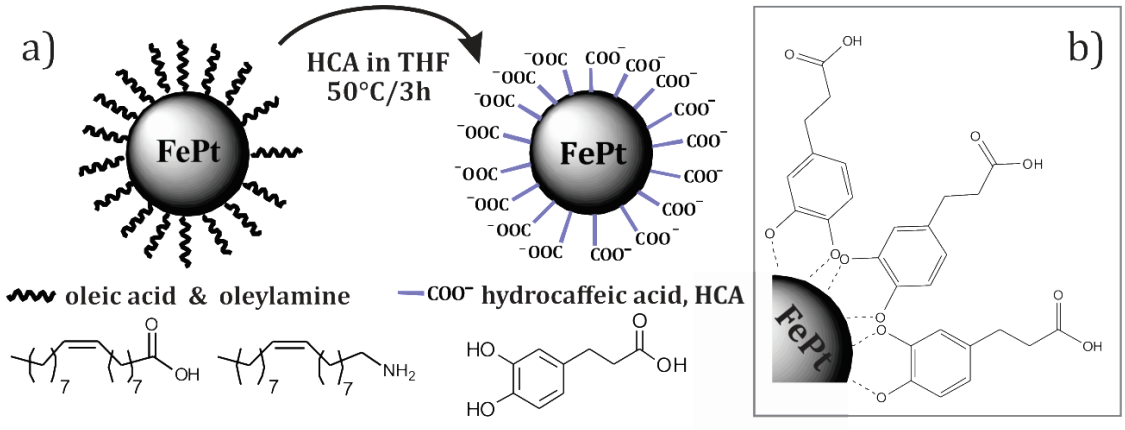


Figure 4.15: a) Schematic representation of a ligand exchange reaction with HCA in THF and b) chelate bonding of a HCA on FePt NPs.

Figure 4.16 evidently shows that after the ligand exchange reaction the FePt NPs are negatively charged (from -10 mV at pH=2 and -50 mV at pH=12) in the whole pH range that was used in the measurements. Negative zeta potential is related to the deprotonation of the carboxylic group of the HCA ligand. High measured values of the zeta potential enable a strong electrostatic repulsion between the NPs, which reflected in persistent suspension stability for a period of several months. Higher zeta potential values in the case of "multi-core" FePt NPs (from -38 mV at pH=2 – -70 mV at pH=12) can be attributed to a larger size of NPs where a larger surface allows attachment of more HCA molecules and, consequently, a higher surface charge can be obtained.

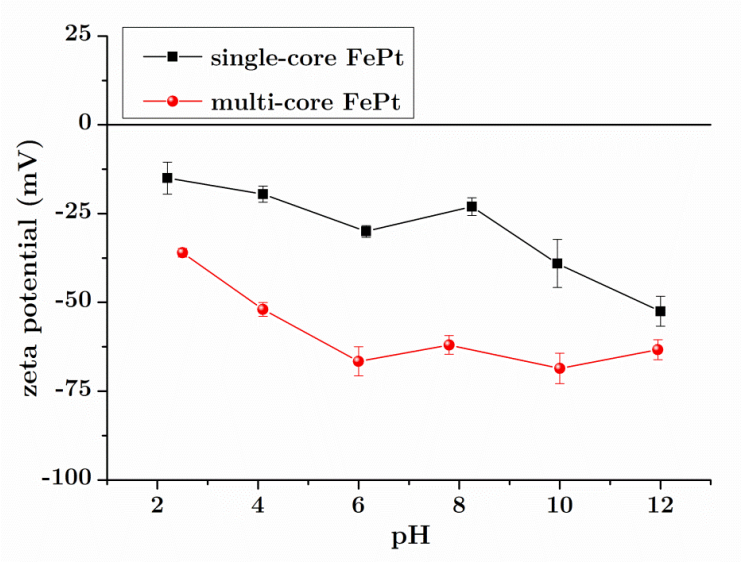


Figure 4.16: Zeta potential measurements of an aqueous suspensions of the »single-core« and »multi-core« FePt NPs after ligand exchange with HCA.

The usefulness of FTIR spectroscopy arises because different chemical structures (molecules) produce different spectral fingerprints and, therefore, any changes in the molecule structure due to the formation of a new bond can be detected. FTIR spectra recorded before and after the ligand exchange reaction are used to track the replacement of the initial ligand(s) with the new one. In order to examine the bonding between different ligands (OLA, OA and HCA) and NP's surface a detailed FTIR study was performed. Before the ligand exchange reaction OLA and OA ligands can be found in the FePt NPs surface. Individual FTIR spectra of pure ligands, i.e. oleic acid and oleylamine, with identified peaks are shown in Figure 4.17 and Figure 4.18, respectively. Detailed FTIR study of the OA and OLA bonding on the surface of FePt NPs can be found in the work of Shukla et al. [129]. FTIR spectra of as-synthesized OA- and OLA-stabilized FePt NPs together with FTIR spectra of pure OA and OLA are shown in Figure 4.19. From the observation of ν(COO) and ν(C=O) vibrational modes it can be seen that OA bonds to FePt NPs in both monodentate and bidentate forms (Figure 4.19). More precisely, the peak at 1709 cm^{-1} corresponds to the ν(C=O) stretch mode and indicates that OA is bonded on the FePt NPs either in monodentate form or as an acid. The peak at 1512 cm^{-1} corresponds to the ν(COO) mode and indicates the presence of the bidentate carboxylate bonding. Peak at 1590 cm^{-1} can be ascribed to the NH_2 scissoring which suggests that OA is adsorbed, i.e. bonds to FePt NPs molecularly with the NH_2 group intact. This means that the OLA bonds to the FePt NPs through electron donation from the nitrogen atom of the NH_2 group [129]. Moreover, a broad peak with low intensity in

the region from 3000-3500 cm^{-1} can be attributed to the ν(NH) stretching mode, which confirms the previous argument about the NH_2 groups staying/being intact. Peaks at 2800-3000 cm^{-1} correspond to the symmetric and asymmetric CH_2 stretching modes of the oleyl group; however, they give no useful information about the bonding of OA or OLA on the surface of FePt NPs.

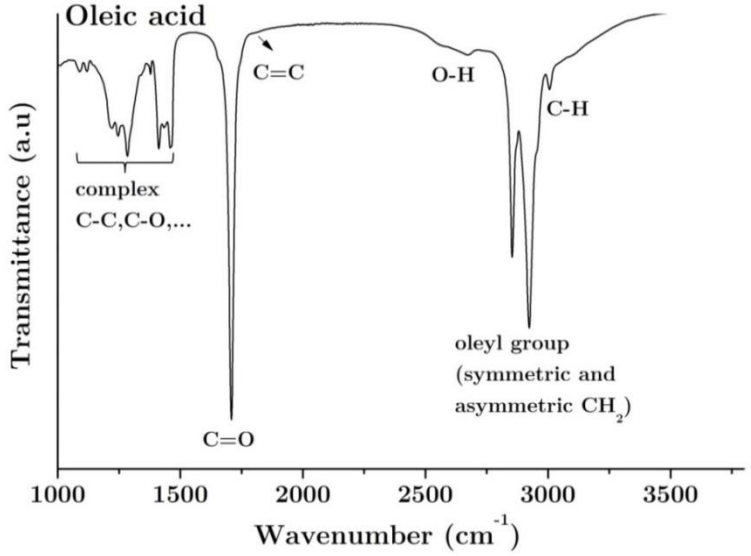


Figure 4.17: FTIR spectrum of pure oleic acid.

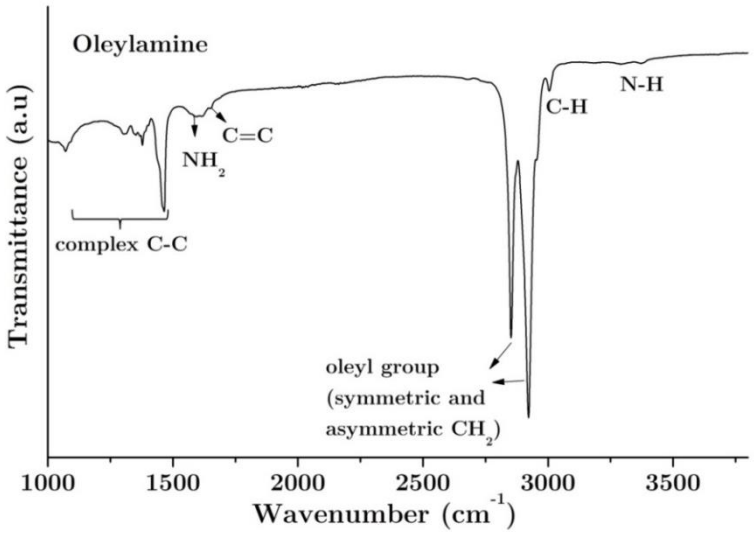


Figure 4.18: FTIR spectrum of pure oleylamine.

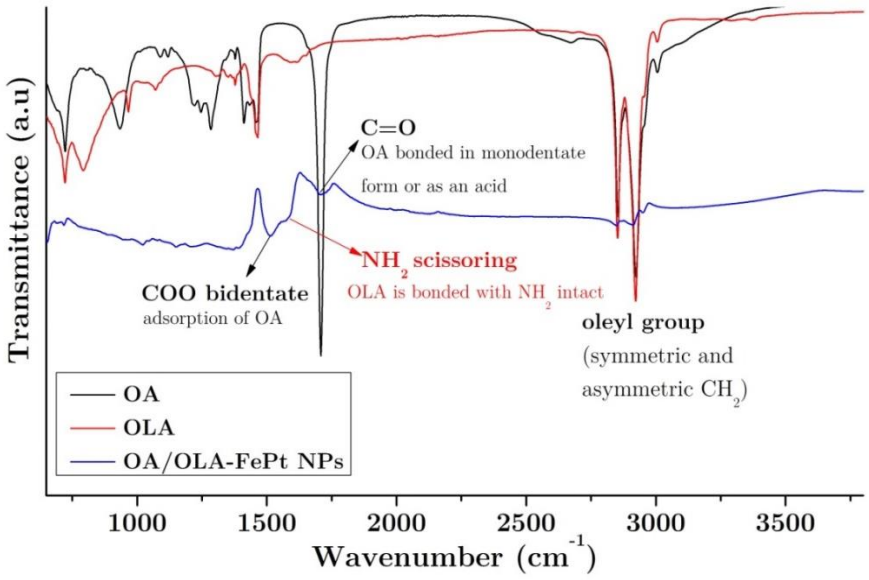


Figure 4.19: FTIR spectra of pure oleic acid, pure oleylamine and oleic acid- and oleylamine-coated FePt NPs.

Ligand exchange reaction with HCA was performed to transfer FePt NPs into the water phase. In order to study possible replacement of OLA and OA ligands with HCA on the NPs surface FTIR spectra were recorded. From Figure 4.20 it can be seen that FTIR spectrum of the pure HCA ligand is quite complex, which renders the determination of the individual peaks more difficult. Broad peak centered at 3350 cm^{-1} can be attributed to the stretching vibration of OH groups of HCA and peak at 1360 cm^{-1} can be assigned to the bending vibrations of catechol OH groups [130]. Peaks at 2800-3000 cm^{-1} correspond to the symmetric and asymmetric CH_2 stretching modes of the HCA molecule. Sharp peak at 1670 cm^{-1} corresponds to the ν(C=O) stretch mode of the carboxylic group, which is found at lower wavelength as expected for the monomeric acid (~1700 cm^{-1}) due to the intramolecular hydrogen bonding. Peaks from 1400-1600 cm^{-1} appear due to the C-C stretching in the aromatic ring. Peaks at 1290 cm^{-1} and 1200 cm^{-1} correspond to the ν(C-O) stretch mode of the carboxylic group and ν(C-OH) of the OH catechol group, respectively [131].

From Figure 4.21 it can be seen that the FTIR spectrum of the HCA-functionalized FePt NPs differs significantly from the FTIR spectra of pure HCA ligand. HCA ligand has two possible bonding sites with the NP's surface: COOH group and OH catechol groups; therefore, the major difference in the peak positions are expected to be related to the peaks correlated to those functional groups. The first distinct change in the spectrum of HCA-functionalized FePt NPs occurs due the deprotonation of the carboxylic group. More precisely, peaks correlated to the ν(C=O)=1670 cm^{-1} and ν(C-O)=1290 cm^{-1} stretch mode of the protonated carboxylic group diminish and new peaks for the symmetric at ν_{asym}(COO-)=1556 cm^{-1} and asymmetric stretching of carboxylate at ν_{sym}(COO-)=1370 and 1400 cm^{-1} appear [132]. Splitting of peaks often resulted from the formation of different carboxylate-metal inner-sphere complexes [133]. The separation in wavenumber $\Delta\nu_{(aysm-sym)}$ for the asymmetric and symmetric stretching of carboxylate bands can be used to elucidate bonding coordination. In general, Δν values greater than about 200 cm^{-1} are thought to indicate monodentate binding, whereas 180-150 cm^{-1} indicates binuclear bidentate (bridging) complexes, and <100 cm^{-1} indicates mononuclear bidentate binding

(chelation) [132]. The separation in wavenumber $\Delta\nu_{(aysm\text{-}sym)}$ was determined to be 186 and 156 cm^{-1} for the first and second symmetric peak, respectively. Therefore, it can be assumed that HCA ligand bonds to the NP's surface in the bidentate (bridging) form. Peak splitting might be attributed to the formation of HCA-Fe and HCA-Pt complexes at the FePt NP's surface. Presence of the peak that corresponds to the stretching mode (ν(C-OH)=1200 cm^{-1}) indicates that the aryl oxygen stretching is not affected by the catechol adsorption on the NP's surface. Moreover, peak at (ν(CO-M)=1250 cm^{-1}) occurs when catechol binds covalently to the metal as catechol anion. In the case of HCA-functionalized FePt NPs the disappearance of both peaks, stretching vibration of OH groups (broad peak at 3200-3500 cm^{-1}) and bending vibrations of catechol OH groups (ν(C-OH)=1360 cm^{-1}) that are present in pure HCA, indicates bonding of the HCA to the FePt NPs surface with the catechol OH groups [130]. From the obtained spectroscopic data it can be concluded that two types of binding structures for the HCA on the FePt NP's surface are possible, i.e. via carboxylic groups or catechol OH groups, which is in accordance with the literature data [134]. The deprotonation of HCA is indication of the bonding via the carboxylic groups. However, carboxylic groups at the outer surface do not bind to the FePt NP's surface providing good suspension stability and high negative zeta potential [134]. It is believed that the majority of the HCA molecules bind to the NP's surface via catechol groups [134] as is schematically shown in Figure 4.15b.

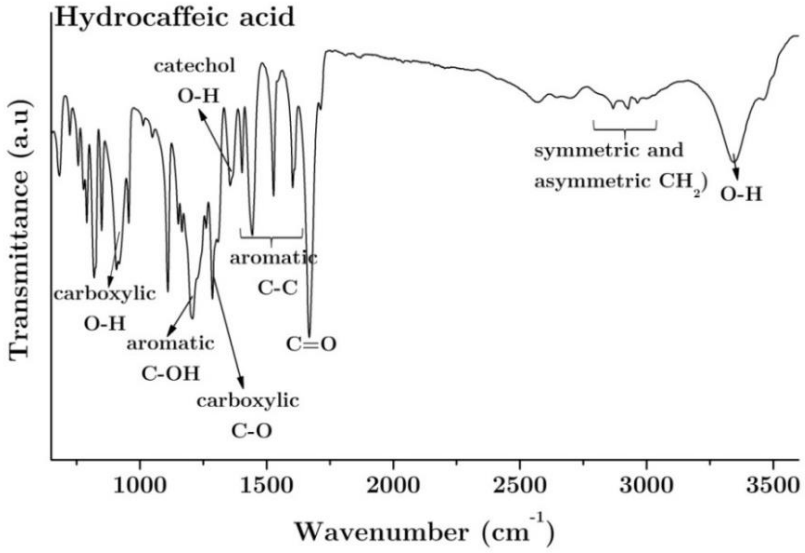


Figure 4.20: FTIR spectrum of pure hydrocaffeic acid.

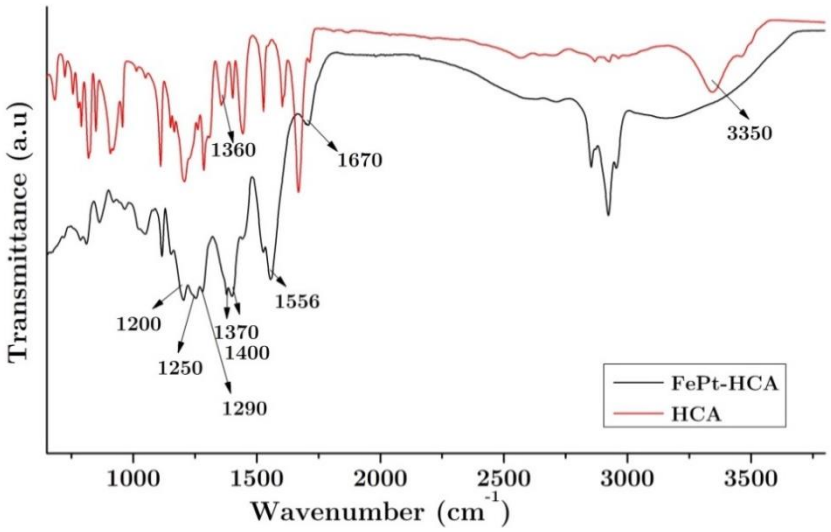


Figure 4.21: FTIR spectra of pure HCA and HCA-functionalized FePt NPs.

4.3 SiO_2 Coating of FePt NPs

SiO_2 layer was introduced on the surface of FePt NPs for two reasons; to prepare stable FePt/SiO_2 NPs water suspensions that were needed for the MRI measurements, and to obtain appropriate core-to-shell ratio for further photo-termal properties of the final hybrid FePt/SiO_2/Au NPs. The choice of SiO_2 as the coating material is beneficial because of its biocompatibility and the possibility for subsequent functionalization. Aim of this segment of work was to cover every individual FePt NP with a SiO_2 shell, without any FePt-free SiO_2 NPs or bare FePt NPs present. The latter has to be avoided before the final Au functionalization step, since only individual hybrid core-shell FePt/SiO_2/Au NPs are suitable for the magneto-optical application. For that purpose the water-in-oil microemulsion method was used [135]. Water-in-oil microemulsion is a suitable method to coat the NPs which are dispersed in the non-polar media since it enables the formation of a thinner coating layer and monodispersed final particles, i.e. similar thickness of the coating layer on all NPs.

In our study system based on a cyclohexane as an oil phase, Igepal CO-520 (polyoxyethylene (5) nonylphenylether) as a surfactant and 25% ammonia solution as a water phase were used. TEOS (tetraethyl orthosilicate) has a function of a SiO_2 precursor. Structural formula of TEOS, surfactant Igepal CO-520 and cyclohexane are shown in Figure 1.14. Proposed reaction mechanism and La Mer theory for the nucleation and growth of the SiO_2 layer on NPs was described in Section 1.4.3.1. In order to determine the optimal conditions for the formation of SiO_2-coated FePt NPs, without any FePt-free SiO_2 NPs or bare FePt NPs, an influence of the TEOS concentration on the formation of SiO_2-coated FePt NPs was systematically studied. Our aim was to determine C_s and C_{homo} for a given system to better understand the nucleation process, which enabled us to determine the optimal reaction conditions. Therefore, only TEOS concentration was varied in the reaction mixture, which is given as the TEOS : NH_3 ratio (1:1 sample D up to 1:25 sample A), while all other parameters were kept constant. Reaction time was selected to be 24 hours at room temperature. A list of the samples together with the description of the formed NPs is presented in Table 4.4. La Mer diagram for the nucleation and growth of SiO_2 and SiO_2-coated FePt NPs and TEM

images of samples obtained for different TEOS : NH_3 ratios (1:25, 1:5, 1:2 and 1:1) are shown in Figure 4.22. Results revealed that at the highest TEOS : NH_3 ratio (1:25), i.e. at lowest TEOS concentration, C_s is just exceeded, meaning all FePt NPs are coated with a SiO_2 layer with a diameter of approx. 25 nm. However, TEM analysis showed that FePt cores are not positioned in the center of the particle. Most probably the reason lies in the insufficient TEOS concentration, which reflects in the partially coated FePt cores. All TEOS monomers react immediately when entering the micelles and the reaction mixture runs out of the TEOS molecules before the complete coating is achieved. From this it can be concluded that a slightly lower concentration of TEOS than the one that was used in sample A should correspond to C_s. TEM image of sample B (TEOS : NH_3 ratio = 1:5) showed an uniform SiO_2 coating on the FePt cores, without core-free SiO_2 NPs present. This sample was positioned higher on the La Mer diagram, but still in the range of the heterogeneous nucleation, ($C < C_{homo}$). The size of the SiO_2-coated FePt NPs was determined to be approx. 40 nm. Further increase in TEOS concentration (sample C, TEOS : NH_3 ratio = 1:2) resulted in a slightly thicker SiO_2 shell, i.e. size of the SiO_2-coated FePt NPs was determined to be 45-50 nm, however already few core-free SiO_2 NPs appeared. This indicates that the threshold for the homogeneous nucleation was reached (C_{homo}), therefore, sample C was positioned on the La Mer diagram in the level of C_{homo}. Even higher TEOS concentration (sample D, TEOS : NH_3 ratio = 1:1) brought the system to the region of a significant homogeneous nucleation, which can be seen as the occurence of a larger amount of FePt core-free SiO_2 NPs. The size of the SiO_2-coated FePt NPs in sample D increased to 55-60 nm. From those results it can be concluded that optimal conditions for obtaining uniform SiO_2-coated FePt NPs without core-free SiO_2 NPs are at TEOS : NH_3 ratio = 1:5, which was used in all following experiments. Additionally, it was confirmed that the thickness of the SiO_2 shell is increased as the amount of TEOS increases. However, tuning of the SiO_2 shell thickness by changing the TEOS concentration offers less control over the coating process than varying the reaction time.

Table 4.4: List of SiO_2 coated samples prepared by changing the TEOS : NH_3 ratio while all other parameters are kept constant; i.e. 170 mL of cyclohexane, 8 mL of Igepal CO-520, 20 mg of »single-core« FePt NPs and 1 mL of 25% NH_3 solution. Reaction time was 24 hours.

Sample	**TEOS : NH_3 ratio**	**SiO_2 NPs**	**SiO_2-coated FePt NPs**
A	1 : 25	/	25 nm
B	1 : 5	/	40 nm
C	1 : 2	Few (35 nm)	45-50 nm
D	1 : 1	Many (40 nm)	55-60 nm

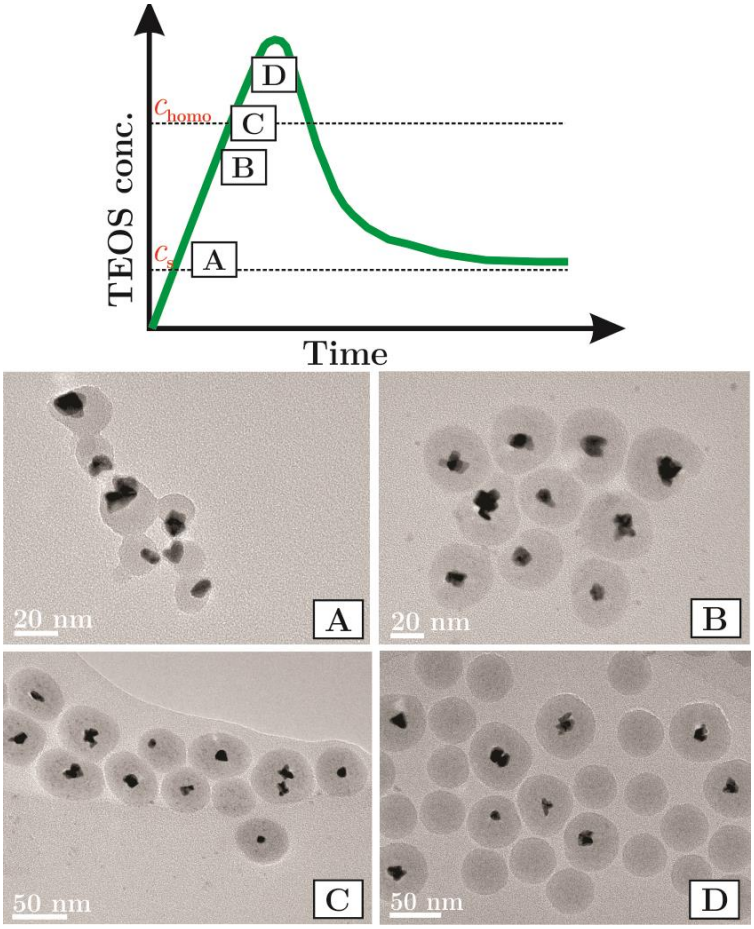


Figure 4.22: a) La Mer diagram for nucleation and growth of SiO_2 and SiO_2-coated FePt NPs. TEM images of samples obtained at TEOS : NH_3 ratio a) 1:25, b) 1:5, c) 1:2 and d) 1:1.

Using these optimal conditions, i.e. TEOS : NH_3 ratio = 1:5, "single-core" and "multi-core" FePt NPs were coated with SiO_2 shell. TEM images of as-prepared samples after 24 hours of synthesis are shown in Figure 4.23b and Figure 4.23c, respectively. All the FePt NPs are equally covered and no free FePt NPs were found, indicating the successful SiO_2 coating of all the magnetic cores.

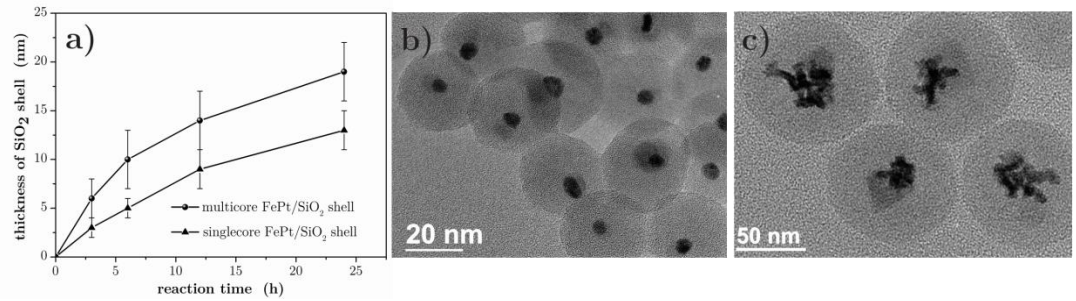


Figure 4.23: Growth of SiO_2 shell with the reaction time and TEM images of SiO_2-coated b) "single-core" and c) "multi-core" FePt NPs.

In Figure 4.23a the thickness of the SiO_2 shells measured after different reaction times (6, 12, 18 and 24 h) is presented for "single-core" or "multi-core" FePt NPs. The growth

of the SiO_2 shell is fast during the first 10 h of the reaction: the increase in the thickness of the SiO_2 shell is ~1 nm/h and ~2 nm/h for "single-core" and "multi-core" FePt NPs, respectively. Longer reaction times resulted in linear growth with an approximate growth rate of ~0.5 and ~0.8 nm/h for "single-core" and "multi-core" FePt NPs, respectively. After 24 hours of synthesis the thickness of the SiO_2 shell on the "single-core" and "multi-core" FePt NPs was ~12 and ~18 nm, respectively. The same mass of FePt NPs was used in both cases (20 mg). However, the same mass of FePt NPs equals a smaller number of NPs in the case of the "multi-core" sample. Therefore, for each "multi-core" NP a larger quantity of reagents is present and consequently a thicker shell is formed.

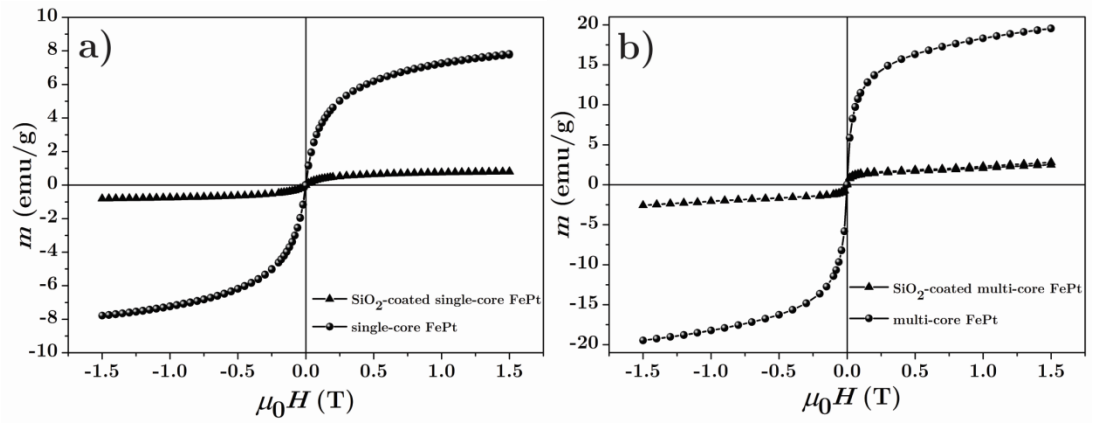


Figure 4.24: Magnetic measurements at 300 K of SiO_2-coated a) "single-core" and b) "multi-core" FePt NPs (reaction time 24 hours).

A comparison of the magnetic properties at 300 K before and after the SiO_2 coating for 24 h of "single-core" and "multi-core" FePt NPs is shown in Figure 4.24 and Figure 4.24b, respectively. The $m_{(1.5T)}$ of the SiO_2-coated FePt NPs is equal to ~1 emu/g and ~2.6 emu/g, for "single-core" and "multi-core" NPs, respectively, which is approximately 8 times lower than for the initial FePt NPs in both cases ("single-core" with $m_{(1.5T)} = 8$ emu/g, and "multi-core" with $m_{(1.5T)} = 19.5$ emu/g).

As discussed before, the NPs' surface chemistry can significantly modify their magnetic properties. A FTIR study of FePt NPs stabilized with OLA and OA and further coated with a SiO_2 shell [136] showed that the SiO_2 coating does not deteriorate the amine and carboxylate layer on the FePt surface. From this it can be concluded that the OLA and OA layer remain on the FePt surface even after the SiO_2 coating and no direct FePt-SiO_2 bonds are formed. Because the SiO_2-coating does not induce any change in the chemical bond on the surface of the FePt NP, the lower magnetization obtained for the SiO_2-coated FePt NPs is merely due to the dilution of the sample with the non-magnetic SiO_2 phase (the magnetization is based on the mass of the whole sample). However, as pointed out in the introduction, the targeted "hybrid" NP size was between 20 and 100 nm [117], which means that the magnetization reduction is inevitable in these kinds of "hybrid" systems with a constant trade-off between good magnetic properties (large m_s) and good biocompatibility.

Such prepared SiO_2-coated "single-core" and "multi-core" FePt NPs prepared with reaction time of 24 hours were used in the MRI measurements and are subsequently referred to as "sample S-SiO_2" and "sample M-SiO_2", respectively.

4.4 Relaxivity Measurements

The effectiveness of the ZDS-functionalized and silica-coated "single-core" and "multi-core" FePt NPs in a stable water suspension as MRI contrast agents was investigated by measuring the dependence of the longitudinal (T_1) and transverse (T_2) relaxation times on the FePt NPs' concentration. Water suspensions of ZDS-functionalized "single-core" and "multi-core" FePt NPs (sample S and sample M, respectively) and SiO_2-coated "single-core" and "multi-core" FePt NPs (sample S-SiO_2 and sample M-SiO_2, respectively) were prepared with different concentrations (0.01–0.08 mM) with respect to the Fe content. A schematic representation of the samples used for MRI measurements is shown in Figure 4.25.

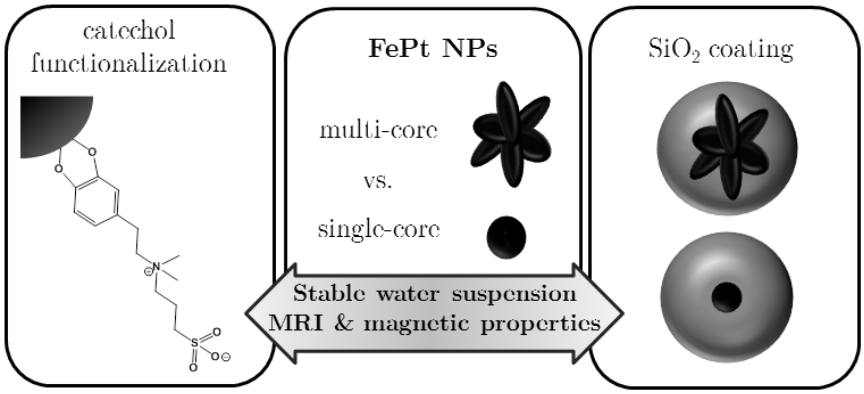


Figure 4.25: Schematic representation of the samples used for MRI measurements; ZDS-functionalized "single-core" and "multi-core" FePt NPs (sample S and sample M, respectively) and SiO_2-coated "single-core" and "multi-core" FePt NPs (sample S-SiO_2 and sample M-SiO_2, respectively).

The measured values of the T_1 relaxation times and longitudinal relaxation rate increase $1/T_1 - 1/T_1(0)$ for all four samples (S, M, S-SiO_2 and M-SiO_2) are presented in Figure 4.26a and Figure 4.26b, respectively. The corresponding calculated longitudinal relaxivities (r_1) are listed in Table 4.5. From the r_1 values it can be concluded that the "single-core" FePt NPs (sample S, $r_1 = 3.6 \pm 0.2$ mM^{-1} s^{-1}) have a weaker effect on the shortening of the T_1 time than the "multi-core" FePt NPs (sample M, $r_1 = 6.7 \pm 0.7$ mM^{-1} s^{-1}). The difference is found to be approximately 1.8-times in favour of sample M. In general, there are two relaxations of water protons nearby magnetic NPs, depending on whether the water protons merely diffuse through the magnetic NPs ("outer sphere") or temporarily bind to them ("inner sphere") [68]. T_1 relaxation enhancement is mainly related to the inner sphere regime that water protons chemically exchange with the surface centers directly. For the smaller magnetic NPs the spin-canting effect becomes stronger due to the higher fraction of surface metal ions relative to the core ones. This might lead to a decrease in the number of the effective metal centers on the surface and, consequently, less effective coordinating of the water molecules and chemical exchanging of the protons [68]; therefore, the resulting r_1 value for the smaller "single-core" NPs is lower than in the case of the larger "multi-core" ones. Furthermore, SiO_2-coating reduces the r_1 values for both the "single-core" (sample S-SiO_2, $r_1 = 1.2 \pm 0.1$ mM^{-1} s^{-1}) and "multi-core" FePt NPs (sample M-SiO_2, $r_1 = 1.2 \pm 0.1$ mM^{-1} s^{-1}) by approximately 3-times with respect to the uncoated ones.

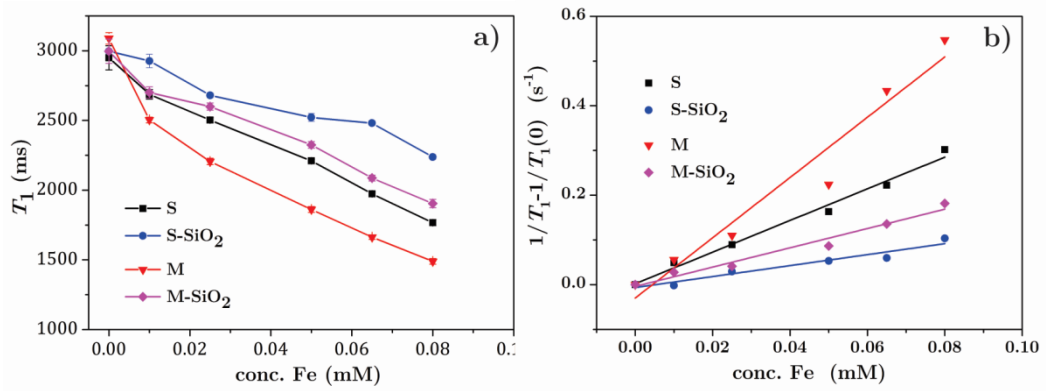


Figure 4.26: Graph indicating a) T_1 relaxation times and b) inverse longitudinal $1/T_1$ – $1/T_1(0)$ relaxation rate increase for "single-core" (S), "multi-core" (M), SiO_2-coated "single-core" (S-SiO_2) and SiO_2-coated "multi-core" FePt NPs (M-SiO_2).

The values of the T_2 relaxation times and transversal relaxation rate increase $1/T_2$ – $1/T_2(0)$ for all four samples (S, M, S-SiO_2 and M-SiO_2) can be found in Figure 4.27a and Figure 4.27b, respectively. The corresponding calculated transversal relaxivities (r_2) are listed in Table 4.5. From the relaxivity values r_2 it is clear that the "single-core" FePt NPs (sample S, $r_2 = 52 \pm 5$ mM^{-1} s^{-1}) have a weaker effect on the shortening of the T_2 time than the "multi-core" FePt NPs (sample M, $r_2 = 87 \pm 4$ mM^{-1} s^{-1}). As was clear from a comparison of the r_1 values, the r_2 values are also approximately 1.7-times higher in the case of sample M. This is in accordance with Eq. (4.4), where it is clear that R_2 is directly proportional, among other parameters, to $(m_s)^2$, meaning that NPs with higher m_s exhibit higher R_2 and r_2. Therefore, due to the higher magnetization, "multi-core" NPs (sample M) possess higher r_2 values than the "single-core" ones (sample S). The SiO_2-coating results in a 2- and 3-fold reduction in the r_2 values (sample S-SiO_2, $r_2 = 16 \pm 2$ mM^{-1} s^{-1} and sample M-SiO_2, $r_2 = 53 \pm 3$ mM^{-1} s^{-1}) in comparison with the non-coated samples (S and M). This can be attributed to the fact that the SiO_2 layer increases the distance between the water protons and the magnetic FePt core and, therefore, the effective magnetic relaxations of the water protons around the NPs are reduced, which influences the shortening of the T_2 relaxation times [64].

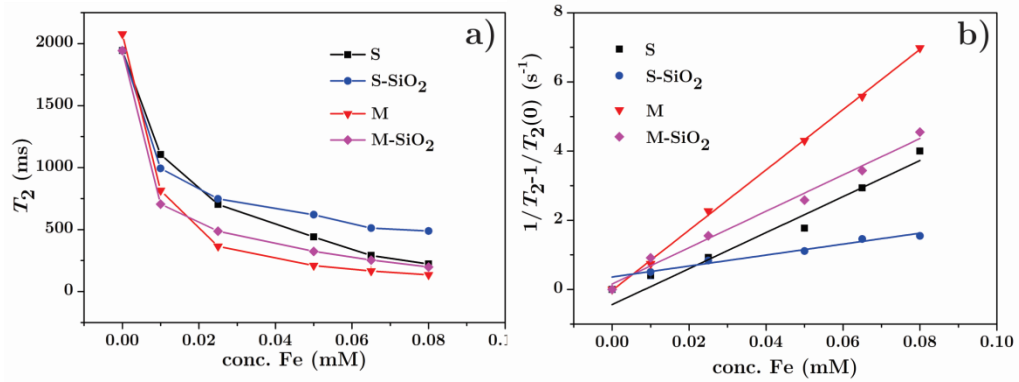


Figure 4.27: Graph indicating a) T_2 relaxation times and b) inverse longitudinal $1/T_2$ – $1/T_2(0)$ relaxation rate increase for "single-core" (S), "multi-core" (M), SiO_2-coated "single-core" (S-SiO_2) and SiO_2-coated "multi-core" FePt NPs (M-SiO_2).

Table 4.5: Calculated longitudinal (r_1) and transverse (r_2) relaxivities for "single-core" (S), "multi-core" (M), SiO_2-coated "single-core" (S-SiO_2) and SiO_2-coated "multi-core" (M-SiO_2) FePt NPs with corresponding r_2/r_1 ratios.

Sample	r_1 **(mM^{-1} s^{-1})**	r_2 **(mM^{-1} s^{-1})**	r_2 **/** r_1
S	3.6 ± 0.2	52 ± 5	14.4
S-SiO_2	1.2 ± 0.1	16 ± 2	13.3
M	6.7 ± 0.7	87 ± 4	12.9
M-SiO_2	2.1 ± 0.2	53 ± 3	25.2

As stated in the introduction, the r_2/r_1 ratio is an important parameter to estimate whether a given contrast agent can serve as a T_1 or T_2 contrast agent. Due to their large magnetization values, magnetic nanoparticles are usually classified as T_2 MRI contrast agents [64]. A high r_2/r_1 ratio is a prerequisite for an efficient T_2 contrast agent, where the r_2/r_1 ratio should be at least 10 [67]. From the r_2/r_1 ratios listed in Table 4.5 it can be concluded that all four samples possess a high r_2/r_1 ratio that even exceeds the required value of 10, which put FePt NPs high on the list of the most promising materials for use in MRI.

A direct comparison of r_1 and r_2, results of our "single-core" FePt NPs to the state-of-the-art literature on relaxivities ([81], [82], [137], [138]), is difficult, because of the large differences present in the experimental conditions. These include the applied magnetic field, surrounding medium, surface functionalization, etc. The applied magnetic field strength is known to influence the T_1 measurements; therefore, the absolute T_1 and r_1 values cannot be compared. However, T_2 relaxation times are less influenced by the applied magnetic field, and therefore a rough comparison with the literature can be made. Chou et al. [81] have tested the effect of the NPs' size on their ability to influence the MRI signal for 3-, 6- and 12-nm FePt NPs coated with cysteamine. It was shown that m_s increased from 1.7 to 12.7 emu/g Fe with the increasing size of the NPs. Consequently, 12-nm FePt NPs represented the most effective negative MRI contrast agent. Taylor et al. [137] measured for octadecylamine-coated 10-nm-sized FePt NPs in agarose an r_2 value of 62.2 mM^{-1}s^{-1}, which is comparable with the values obtained in our study. Liang et al. [138] studied cysteine-coated 3.8-nm-sized FePt NPs and obtained a low r_2 value in an aqueous solution (r_2 = 16.9 mM^{-1} s^{-1}), which favours the FePt NPs synthesized in our study. Furthermore, Yang et al. [82] showed in their work that tetraethylene glycol/oleic acid-coated 4-nm-large FePt NPs possess a high r_2 value in an aqueous solution (r_2 = 122 mM^{-1} s^{-1}, m_s = 25 emu/g). However, their r_2 value is found to be higher than in our case. The reason for this lies most probably, firstly, in the higher m_s and, secondly, in the different NP coatings, which was not quantitatively evaluated.

Our results show that "single-core" FePt NPs possess high r_2 values, which indicates that this material has a strong potential to become an excellent T_2 MRI contrast agent. A step towards increasing the m_s value of "single-core" FePt NPs was proven to work, and significant improvements of m_s were observed, which also reflected positively on the MRI material's performance. Additionally, we have successfully implemented the use of a dopamine-based ligand to transfer the FePt NPs to a water phase, while maintaining a high colloidal stability. This means that our study represents a crucial and positive step

towards water-based suspensions of biocompatible FePt NPs. We showed that the "multi-core" FePt NPs synthesized in our study exhibit higher r_2 values in comparison to the "single-core" particles and that the SiO_2 coating reduces both the r_1 and r_2 values. However the r_2/r_1 ratios are found to exceed the value of 10, which was reported to be ideally suited for quantitatively T_2-weighted MRI [67]. Our r_2 values for FePt NPs are, however, still inferior to "multi-core" iron oxides, mainly due to their higher m_s [139]–[142].

4.5 Hybrid FePt/SiO_2/Au NPs

4.5.1 Simulations of UV-Vis spectra for hybrid FePt/SiO_2/Au NPs

Optical response of hybrid magneto-plasmonically active NPs with different dimensions was theoretically calculated in order to estimate the optimal NPs structure and size for achieving the maximum absorption in the NIR region of the light. Eq.(1.26) was used to predict the optical behaviour of Au nanoshells with different dimensions. Hybrid NPs prepared in this work are composed of three layers; FePt core, SiO_2 intermediate layer and Au shell. With setting the FePt core size in the range of 10 nm - 20 nm for the "single-core" and "multi-core" FePt NPs, respectively, controlling the size of the SiO_2 intermediate layer between the core and the Au shell is of vital importance. The SiO_2 layer determines the suitable size for for biomedical applications and, at the same time, shifts the SPR peak into the range of the NIR spectrum (i.e., the biological window), but only for certain FePt-SiO_2-core to Au-shell ratios as it will be shown. In order to evaluate the effect of the Au shell thickness at different core-to-shell ratios on the UV-Vis spectrum, three sets of simulations with a different thickness of the Au shell (5, 10 and 15 nm) were performed.

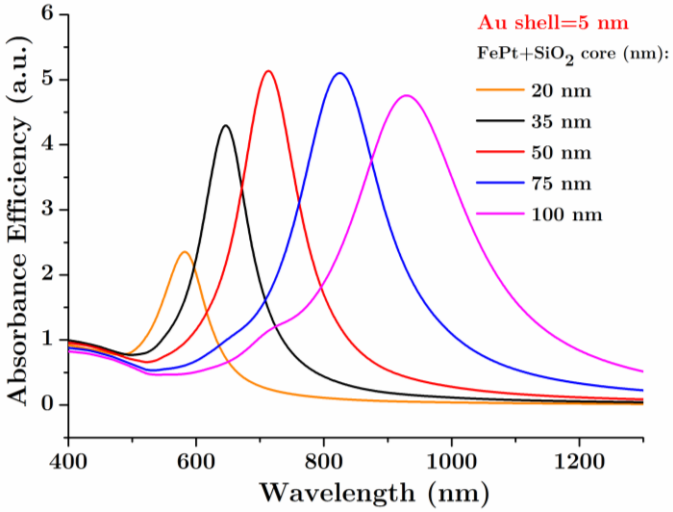


Figure 4.28: Simulated UV-Vis spectra for hybrid NPs with different core sizes (20-100 nm) and Au shell thickness 5 nm.

Simulated UV-Vis spectra obtained for hybrid NPs with different core sizes (core=FePt/SiO_2 NP with diameter 20-100 nm) and Au shell thickness 5 nm are shown in Figure 4.28. Increase in the core-to-shell ratio from 4 (core diameter 20 nm) to 20 (core diameter 100 nm) resulted in the shift of the SPR peak from 582 to 930 nm. Further, in the case of Au shell thickness 10 nm (Figure 4.29) SPR peak is shifted from

581 to 928 nm when core-to-shell ratio was increased from 3.5 (core diameter 35 nm) to 15 (core diameter 150 nm). Slightly larger core diameters were used in the calculations as in the previous case (Au shell 5 nm) to maintain core-to-shell ratio in the range 2-20, which facilitates the final comparison of all data. When the core radius is small, there is only one absorption peak (dipole resonance peak) present in the spectra, while two absorption peaks are observed when the core radius becomes large (>100 nm) due to the contribution of higher order resonances, i.e. quadrupole plasmon resonances [143]. In particles with a smaller core diameter (< 50 nm) the enhancement of the electric field near the particle's surface due to the interaction with the light is constant, meaning electric field is equally distributed, therefore only dipole resonance is observed. However, for larger core dimensions (> 50 nm) the distribution of the electric field within the structure becomes unequal, therefore also higher order resonances appear (quadrupole resonances), which reflects in the appearance of the additional absorption peak in the spectrum.

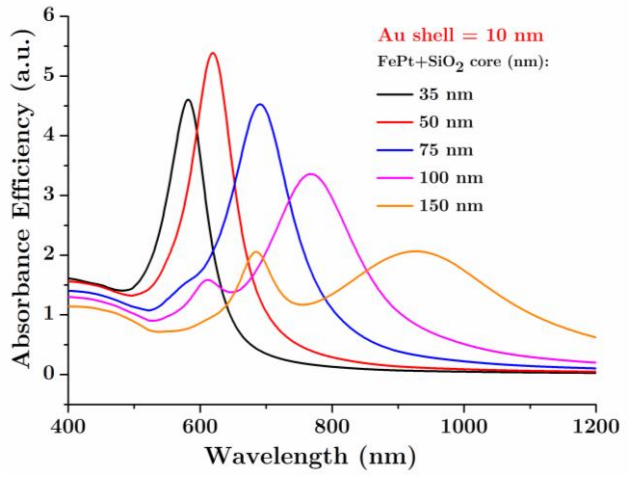


Figure 4.29: Simulated UV-Vis spectra for hybrid NPs with different core sizes (35-150 nm) and Au shell thickness 10 nm.

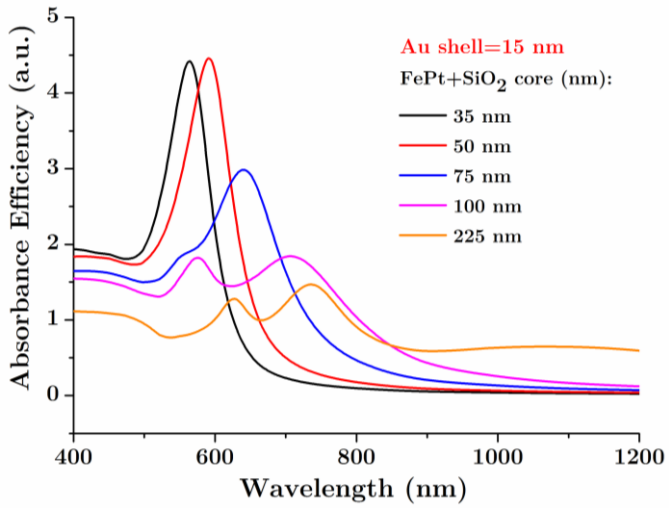


Figure 4.30: Simulated UV-Vis spectra for hybrid NPs with different core sizes (35-225 nm) and Au shell thickness 15 nm.

In the last set of simulations Au shell thickness was set to be 15 nm and core diameters were varied from 35 to 225 nm. Increase in the core-to-shell ratio from 2.3 (core diameter 35 nm) to 15 (core diameter 225 nm) resulted in the SPR peak shift from 563 to 1070 nm. It can be seen that increase in the NPs size causes a decay of the absorption efficiency due to the prevailing scattering effects and appearance of two absorption peaks due to the dipole and quadrupole resonances. All those calculations were done for a perfect system where hybrid NPs are isolated (no agglomeration) and all equal in size.

In order to determine the optimal core-to-shell ratio where hybrid FePt/SiO_2/Au NPs have the maximum absorption in the NIR region (biological window), all data were plotted in one graph (Figure 4.31), which indicates the position of the SPR peak in dependence on the core-to-shell ratio of the hybrid NPs. Part of the spectra where the biological window lies is colored gray on the graph. Comparison of all results revealed that only few NP's dimensions fit in this range. In the case of 5 nm thick Au shell, core diameter should be in the range of 45 - 80 nm, which corresponds to the core-to-shell ratio 9 - 16. Thicker Au shell requires larger core particles to fit in that range. For the 10 nm Au shell core diameter in the range of 70 - 140 nm is needed (core-to-shell ratio 7 - 14) and for 15 nm Au shell thickness required core diameter increases to 105 - 165 nm (core-to-shell ratio 7 - 11).

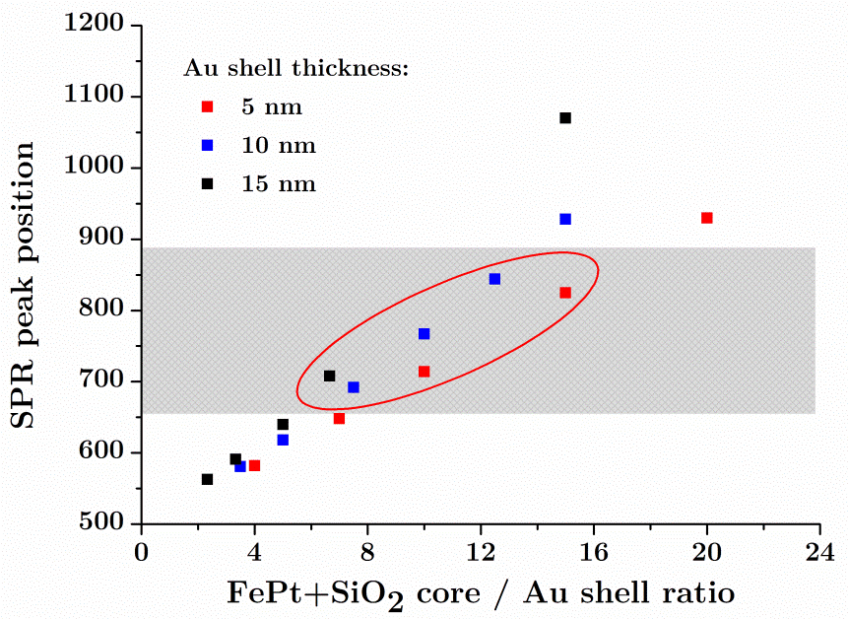


Figure 4.31: SPR peak positions extracted from simulated UV-Vis spectra for hybrid NPs with different core-to-shell ratios.

Those theoretical predictions served as the guidelines for the design of the synthesis experiments, which would give hybrid NPs with desired optical response, i.e. maximum absorption in the biological window. However, it has to be pointed out that real samples suffer from imperfections and any degree of polydispersity or agglomeration would influence the optical properties. Recently it was shown that gold NPs forming dimers or clusters exhibit a significant red-shift compared to individual gold NPs [144]. In this study the clusters were, in the first approximation, considered to be a single, large, uniform NP, for which the SPR modes can be theoretically predicted by using the computer software (Mielab) for a single-standing multi-layered NP. The obtained

theoretical values of the SPR modes were in good agreement with the experimental data, with some modifications, which were attributed to the irregular shapes of the individual particles within the cluster. Therefore, we took into account also polydispersity of the samples and simulations have shown that this factor has strong influence not only on the position of the spectra, but also on its shape.

For the simulation of UV-Vis spectra for polydispersed hybrid NPs two sizes of $FePt/SiO_2$ core (150 and 200 nm) were selected with the standard deviation in the core size 15 or 45 nm. Au shell thickness was set to 10 nm with standard deviation 5 nm. Obtained simulated spectra were then compared to the spectrum of monodispersed hybrid NPs with no standard deviation in the core or the shell size. Figure 4.32a represents simulated UV-Vis spectra for hybrid NPs with the core size 150 nm. It can be seen that monodispersed NPs possess two distinct peaks at 685 and 925 nm (quadrupole and dipole resonance peak, respectively), while in the case of polydispersed samples broadening of the peaks leads to the spectra with a broad hump. The larger the standard deviation, the more blurred original peak positions are until one very broad absorption hump prevails. Every single NP dimension has its own characteristic peak position, therefore, spectrum obtained from a polydispersed sample is a superposition of several spectra, each representing particular NPs dimensions. Hence it follows that larger polydispersity reflected in UV-Vis spectra as broadening of the peaks. This phenomenon is evidently seen in Figure 4.32a, where in the spectra with standard deviation in the core size 15 nm (black curve) original peaks at 685 and 925 nm can still be recognized, while in the spectra with larger standard deviation (45 nm, red curve) original peak positions are completely blurred. A similar trend can be seen in the case of larger core size (200 nm, Figure 4.32b). Monodispersed hybrid NPs with core size 200 nm and Au shell thickness 10 nm have two distinct peaks at 765 and 1076 nm, while polydispersed sample with standard deviation of 15 nm in the core size and 5 nm in the Au shell thickness showed spectrum with broader peaks than the original ones (black curve). Furthermore, UV-Vis spectra for the sample with standard deviation of 45 nm in the core size (red curve) showed no two distinct peaks, but one very broad absorption peak in a range 600-1300 nm.

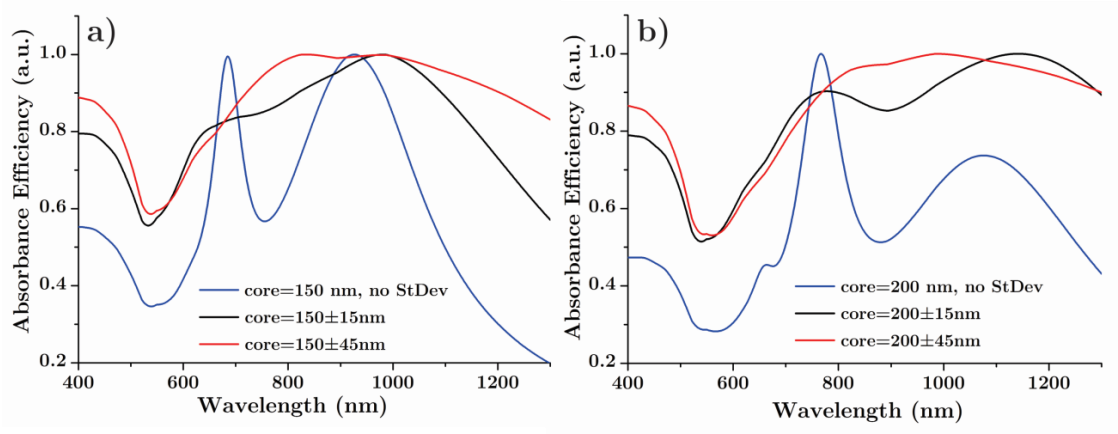


Figure 4.32: Simulated UV-Vis spectra for hybrid NPs where standard deviation in the core and shell size was applied. Black and red curves: Au shell thickness is 10±5nm and core size is a) 150 nm and b) 200 nm. Blue curve represents ideal sample where no standard deviation in the shell and core size is considered.

Simulated UV-Vis spectra in Figure 4.33 reveal that despite high size polydispersity core-to-shell ratio still has a significant effect on the absorption peak position. Au shell thickness is in all cases 15 nm with a standard deviation 5 nm. It can be seen that at the same standard deviation larger core-to-shell ratio shifts absorption peak towards longer wavelength in a similar fashion as it was shown for the monodispersed hybrid NPs. At lower wavelengths, i.e. 400 – 550 nm, the position of all spectra is comparable. However, at longer wavelengths the shift becomes more pronounced. Increase in the core-to-shell ratio from 15 to 20 at constant standard deviation 15 nm (black and blue curve, respectively) or 45 nm (red and purple curve, respectively) leads to a red-shift of a spectrum for approx. 60 nm in the range 600 – 1000 nm, and more than 100 nm in the region of wavelengths above 1000 nm. From this simulations it can be concluded that for interpretation of UV-Vis spectra obtained from complex samples all this possible contributions should be taken into account. Moreover, we have shown that theoretical simulations are a powerful tool that provide us useful information and facilitate insight into the real samples behaviour.

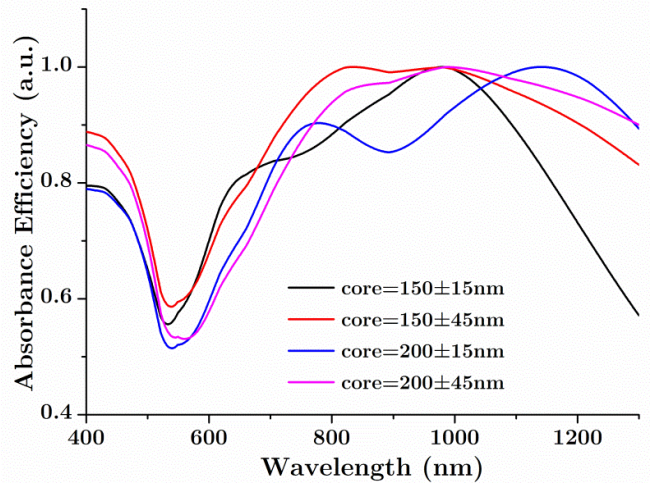


Figure 4.33: Simulated UV-Vis spectra for hybrid NPs where standard deviation in the core and shell size was applied. Au shell thickness is set to be 10±5nm and core size is 150 nm or 200 nm with standard deviation 15 or 45 nm.

4.5.2 Synthesis of hybrid FePt/SiO_2/Au NPs

4.5.2.1 Functionalization of SiO_2 surface for effective Au decoration

In order to obtain positively charged SiO_2, which enables depositing the anionic gold species, the FePt/SiO_2 NPs were functionalized with APTES, which was covalently bonded to the particle surface [145]. In order to induce positively charged aminopropylsilane groups on the SiO_2 surface APTES solution (water:ethanol=1:3) was added to the suspension of the FePt/SiO_2 NPs. Successful functionalization with APTES was monitored by measuring the zeta-potential on the surface of the FePt/SiO_2 NPs in water (Figure 4.34). From the zeta-potential measurements shown in Figure 4.34 it is clear that the SiO_2 surface before the APTES functionalization is negatively charged at a pH higher than 2 (Figure 4.34, black curve), which is in accordance with the literature [146]. This is due to the presence of the deprotonated -OH groups on the surface, as is schematically shown in Figure 1.17. A positive surface charge indicates the successful attachment of the aminopropylsilane groups to the particle surface (Figure 4.34, red

curve). From the obtained results it can be concluded that the optimum pH range for the Au seeding reaction on the APTES-functionalized FePt/SiO_2 NPs is between pH 3 and 7.5, where the surface charge has the highest positive value and so the largest coverage with gold seeds can be achieved.

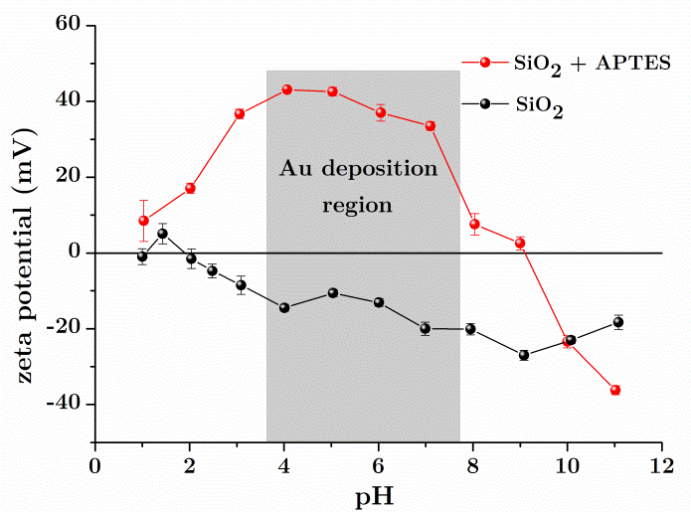


Figure 4.34: Zeta-potential measurements of the untreated FePt/SiO_2 NPs and the APTES functionalized FePt/SiO_2 NPs in water.

4.5.2.2 Au seeding

Experiment has shown that on the bare, non-functionalized SiO_2 surface no Au seeds can be attached because negative surface charge hinders the attraction of $[AuCl_x(OH)_{4-x}]^-$ species to the surface and its subsequent deposition. Au seeding on the APTES-functionalized SiO_2 surface was achieved by mixing FePt/SiO_2 NPs with a gold solution ($HAuCl_4x3H_2O$ dissolved in water) and stirred at 70°C. The colour change from yellow to brown indicated the attachment of the $Au(OH)_3$ to the SiO_2 surface [88]. The attached $Au(OH)_3$ decomposes to Au according to the Eq. (1.27) and Eq. (1.28) at elevated temperatures.

Size of the Au seeds and the coverage of the SiO_2 surface strongly depends on the pH of the gold solution ($HAuCl_4x3H_2O$) and the synthesis time. In order to find optimal conditions, solutions with different pH values were tested (pH = 4, 6 and 8). TEM images of obtained samples are shown in Figure 4.35. At pH=4 very small Au seeds with size of 1-2 nm are attached on the SiO_2 surface with a low coverage density. Increase in the pH coincide with the higher rate of the hydrolysis of the $[AuCl_4]^-$ that reflects in the increase of the size of Au seeds. At pH=6 the size of the Au seeds is only slightly increased to 1-3 nm. Evident difference in the sample appearance occurs at pH =8. In that case, much larger Au seeds are obtained (3-20 nm) with larger surface coverage density.

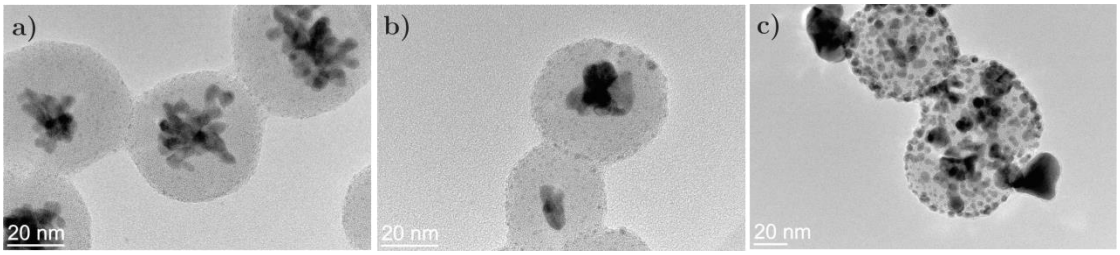


Figure 4.35: Au seeding on SiO_2 surface obtained at different pH values of $HAuCl_4x3H_2O$ water solution : a) 4, b) 6 and 8.

In order to obtain less polydisperse Au seeds and still retain high surface coverage, in the next experiments, the pH value was set to 7 to obtain predominantly $[AuCl_3(OH)]^-$ complex, where the size of the Au seeds appears to be smaller than at pH=8. Moreover, in order to determine the growth of the Au seeds samples were extracted from the reaction mixture at different times (1, 5, 10 and 30 minutes). TEM images of obtained samples are shown in Figure 4.36.

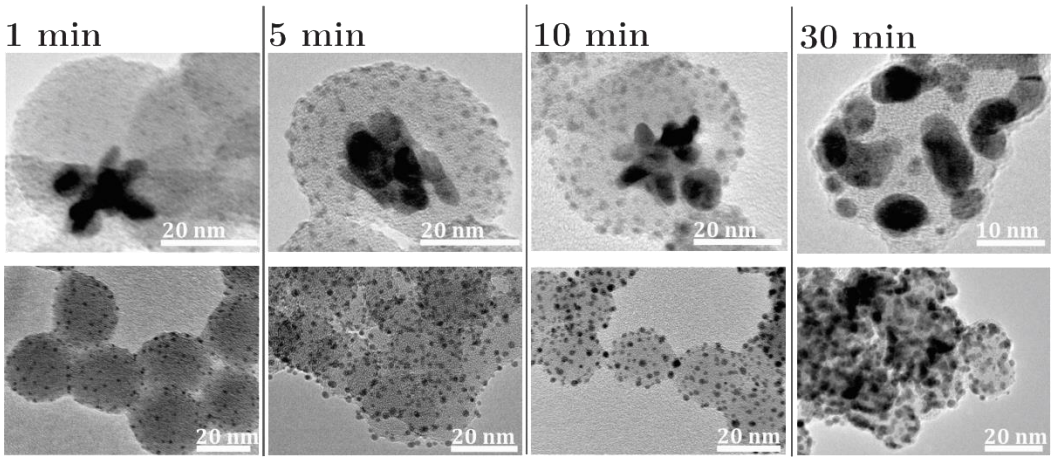


Figure 4.36: Au seeding on SiO_2 surface obtained at pH=7 at different reaction times (1-30 minutes).

The size of the Au seeds is increasing with time of the reaction. After 1 minute of the reaction size of the Au seed was measured to be 1-2 nm. After 5 minutes the size of the Au seeds reached 2-3 nm, while after 10 minutes Au seeds grew to 2-5 nm. Finally, when the reaction was stirred for 30 minutes, the size of the Au seeds increased to 3-20 nm with increased polydispersity. From those experiments it can be concluded that the optimum reaction time where monodispersed Au seeds with high surface coverage are obtained is 5 minutes. Therefore, all further samples, indicated as »Au seeding«, were prepared at pH=7 at 70°C for 5 minutes.

4.5.2.3 Au shell formation with $NaBH_4$

First route that was used for the preparation of Au shell was subsequent reduction of additional Au with the strong reducing agent $NaBH_4$ on the Au-seeded NPs. To the mixture of $HAuCl_4$ solution and gold-seeded $FePt/SiO_2$ core/shell NPs ice-cold solution of the reducing agent $NaBH_4$ was added. The reaction mixture was cooled to 0°C to slow down the reaction because at room temperature larger Au particles grew, which aggravated the formation of Au shells. TEM image of the Au nanoshells that were formed in his reaction step is shown in Figure 4.37a. The estimated thickness of the Au attached to the SiO_2 surface is up to 10 nm. Besides individually coated NPs, detailed TEM investigation revealed a partial agglomeration, where a cluster of few (from two to five) NPs was covered with gold. The UV-Vis absorption spectra acquired from the Au-seeded $FePt/SiO_2$ NPs (grey line) and the hybrid core-shell NPs (black line) are shown in Figure 4.37b. A suspension of Au-seeded $FePt/SiO_2$ NPs with the size of the gold seeds

being 1–3 nm, exhibited a very weak SPR peak at a wavelength λ=520 nm, which is in accordance with previous observations [147]. For Au NPs smaller than 5 nm, the plasmon oscillation is strongly damped, resulting in a broad and low-intensity absorption curve, which effectively disappears for NPs less than about 2 nm in diameter, because the electron density in the conduction band becomes very small [147]. In the case of the hybrid core-shell NPs the broad SPR peak saturates at λ=680 nm and remains nearly constant over the entire NIR spectrum region. This is a desirable effect, allowing us to select different laser-excitation sources from 600 nm up to 850 nm, depending on the required application in the area of photo-thermal cancer treatment.

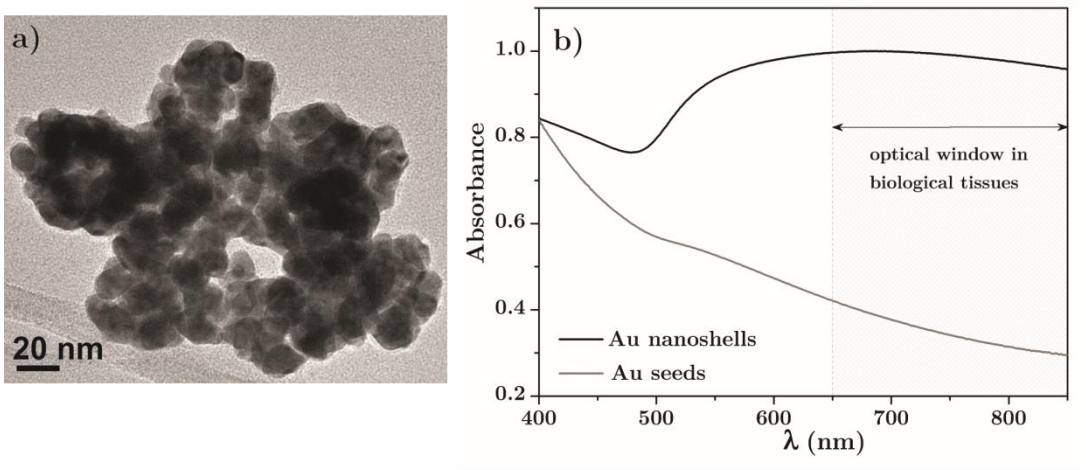


Figure 4.37: TEM images of $FePt/SiO_2/Au$ core/shell NPs and b) corresponding UV-VIS spectra of water suspensions containing gold-seeded $FePt/SiO_2$ NPs and hybrid $FePt/SiO_2$ NPs with a Au shell.

The observed broadening of the SPR peak can be attributed to the several interconnected morphological characteristics of the hybrid core-shell NPs, resulting from the fabrication route. In other words, the coverage of the SiO_2 surface with the Au might not be entirely perfect, for example, the thickness of the Au nanoshell may vary in size slightly [144] and the hybrid NPs can be partially clustered. It can be seen from the simulations of absorption spectra for hybrid NPs presented in Section 4.5.1 that introducing polydispersity in the sample brings significant broadening of the absorption peak. In order to theoretically assess the correlation between the agglomeration and the corresponding SPR absorption peak value, the series of calculations were performed by assuming several different sizes of clusters with diameter 35–125 nm and the thickness of the Au shell was assumed to be 10 nm. Figure 4.38 presents the comparison of the experimental curve (magenta curve) with the calculated ones for different size of the clusters. It can be speculated that when the distribution of the cluster sizes is not uniform, the resulting UV-Vis spectrum will reflect the averaged signal of a nearly uniform intensity over the whole NIR spectrum region, with the maximum peak positioned at around 700 nm, which is in good agreement with the experimental data.

It was shown that Au nanoshells can be prepared via $NaBH_4$ reduction method. However, even the finest tuning of the experimental conditions led to a formation of coarse Au shells with several connected cores. NPs that are suitable for the biomedical applications should have final size up to 100 nm. It was reported that it is very difficult to prepare Au nanoshells on cores with diameters below 60 nm [148]. With decreasing the core size also the thickness of the Au shell should decrease in order to retain desired core-

to-shell ratio, which brings SPR peak in the NIR region. Because we are limited with the size of the Au seeds (diameter 2-3 nm) the thinnest Au shell that can be theoretically prepared is 2-3 nm thick, which is not thin enough to fulfil this requirement. Furthermore, smaller Au nanoshells were found to be much more susceptible to aggregation than the larger ones. It is important to avoid agglomeration during the synthesis. Only in that way every individual core can be coated with Au shell. It was shown [148] that larger Au nanoshells are more stable during the synthesis due to the more effective charge double-layer repulsion. Calculations revealed that the 30 nm Au nanoshells are 10^7 more prone to agglomeration than the 120 nm-ones [148]. Therefore, with synthesis procedure described in this section, cores smaller than 50 nm will always aggregate together under the common layer of Au shell. In order to overcome this problem and to form thinner Au shell in a more controllable manner, a new approach, i.e. Au double seeding, was proposed, which will be described in the next section.

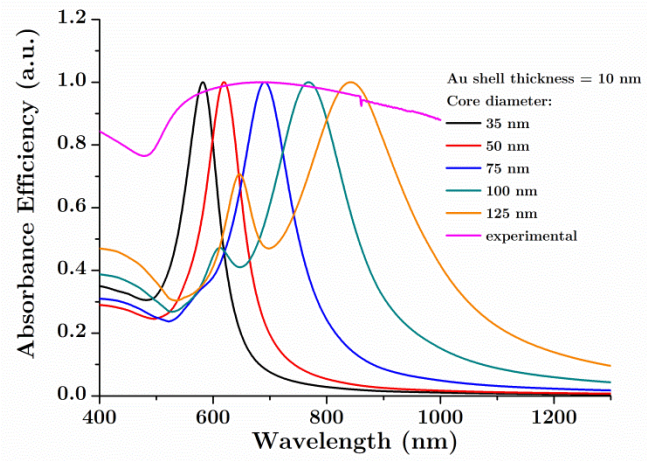


Figure 4.38: Simulated UV-Vis spectra for Au shells with different core sizes (35 - 125 nm) and comparison with experimental UV-Vis spectrum measured for hybrid NPs in water.

4.5.2.4 Au shell formation via two-step Au seeding

Au shells were prepared by using a novel approach, i.e. Au double seeding, where it is expected that thinner Au shells can be prepared in a more controllable manner. In the first Au seeding step, small Au NPs were deposited on the surface of the SiO_2 layer and in the second step, the gaps between Au NPs were filled, which results in a more uniform Au shell. Second Au seeding step was performed immediately after the first Au seeding step using the same conditions. TEM images of the samples in each step of the Au shell formation process; i.e. SiO_2-coated "multi-core" FePt NPs, hybrid NPs after first Au seeding step and after second Au seeding step, are shown in Figure 4.39. It can be seen that in the first Au seeding step SiO_2 surface is decorated with small Au seeds and in the second Au seeding step Au layer becomes thicker and denser. Moreover, comparing the previous synthesis procedure, i.e. reduction with $NaBH_4$, with this one, one can notice that in the latter case a more uniform deposition of Au on the SiO_2 surface can be achieved and individual FePt-SiO_2 cores remained dispersed. On the contrary, in the $NaBH_4$-reduction method, cores are fused together as the consequence of the Au shell formation reaction.

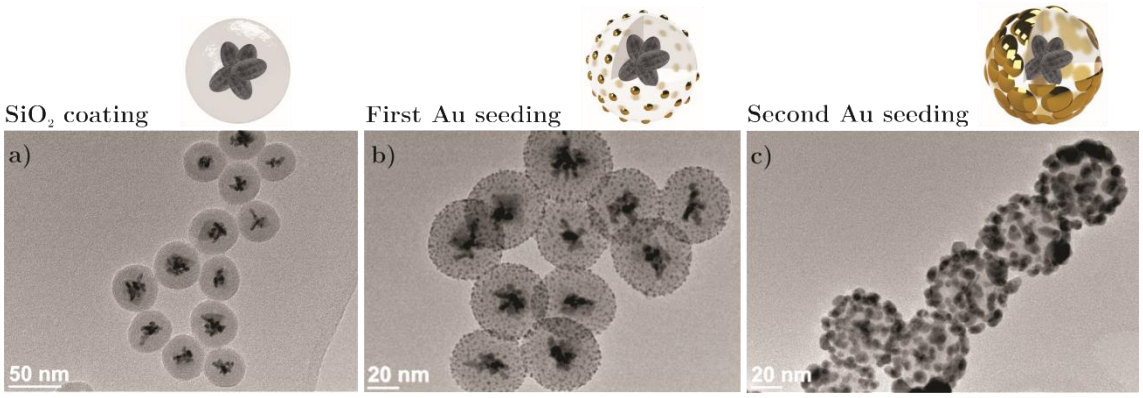


Figure 4.39: TEM images of a) SiO_2-coated »multi-core« FePt NPs, b) hybrid NPs after the first Au seeding step and c) after the second Au seeding step.

UV-Vis spectra of water suspension of hybrid NPs after the first Au seeding step and after the second Au seeding step are shown in Figure 4.40. It can be seen that hybrid NPs after the first Au seeding step exhibited a very weak SPR peak at a wavelength λ=520 nm due to the small seeds size (< 3 nm), which is in accordance with the literature [147]. However, in the second Au seeding step larger Au particles were introduced on the SiO_2 surface with large portion of them being fused together forming a non-continuous Au shell. This reflects in the absorption spectra as the appearance of the absorption peak with its maximum at the edge of the biological window (670 nm). Although the maximum absorption peak is not positioned within the biological window, high absorption in that region is still obtained. The size of the Au particles on the SiO_2 surface obtained after the second Au seeding step was determined to be between 6 – 10 nm and the core size (diameter of FePt+SiO_2 particle) is approx. 40 nm. Simulations have shown (see Figure 4.31) that for the monodispersed FePt/SiO_2/Au NPs with the core size 40 nm and the complete Au shell with thickness 5 or 10 nm it is expected to have maximum absorption at 680 or 600 nm, respectively. Even though the Au "shells" that are formed with the two-step Au seeding procedure are not complete, the experimental absorption fits well to the theoretical predictions. However, when discussing those results also possible polydispersity of Au NPs has to be taken into account, which influences the width of the SPR peaks and its position. Absorption spectrum for spherical Au NPs with size 5-10 nm has absorption maximum at 520 nm. Agglomeration of those particles would lead to the significant red-shift of the absorption peak [149] where absorption maximum can reach also wavelengths up to 700 nm. Therefore, rather than comparing experimental absorption spectra obtained after second Au seeding step with the simulated spectra for the ideal Au nanoshells we assume that this hybrid structure behaves as FePt/SiO_2 cores with the agglomerated Au NPs on the surface, which are forming non-continuous Au shell.

Even though the hybrid FePt/SiO_2/Au NP obtained with the two-step Au seeding method has an absorption peak at the edge of the biological window, absorption of the light is continued to be high also within this window, which is essential to obtain strong photo-thermal effect and will be demonstrated in Section 4.5.4.

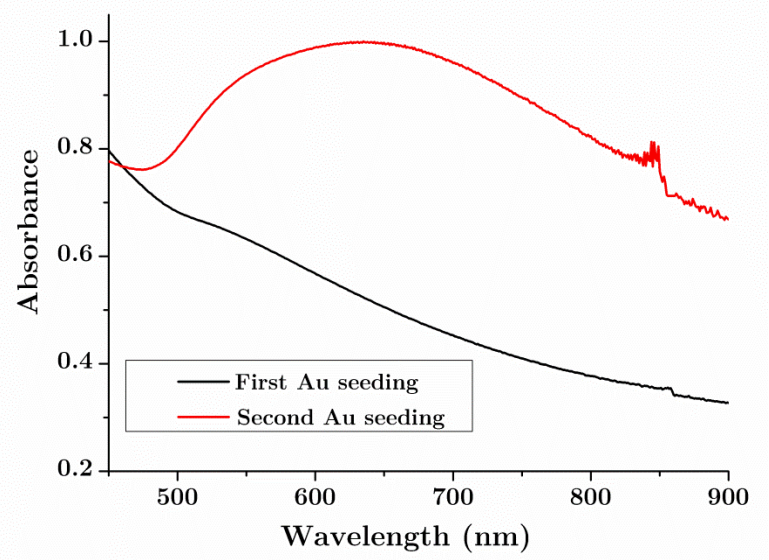


Figure 4.40: UV-Vis spectra of water suspension of hybrid NPs after first Au seeding step and after second Au seeding step are shown.

4.5.3 Functionalization of hybrid FePt/SiO_2/Au NPs with PEG

Hybrid FePt/SiO_2/Au NPs prepared via two-step Au seeding procedure showed better morphology and more uniform particle size, i.e. no clustering as in the case of hybrid NPs prepared via with $NaBH_4$-reduction method, therefore those hybrid NPs were selected for further experiments. Hybrid FePt/SiO_2/Au NPs were functionalized with mPEG-SH by stirring an aqueous suspension of NPs with an addition of mPEG-SH ligand for 30 min at 60°C. The final sample was washed several times to remove excess of mPEG-SH and finally dispersed in distilled water. TEM investigation of two samples, hybrid FePt/SiO_2/Au NPs before and after PEGylation step, showed no distinct changes in the structure of the NPs.

Results of the zeta potential measurement of an aqueous suspension of hybrid NPs before and after PEGylation are shown in Figure 4.41. Measurements were done in a pH range 5 - 9. It can be seen that the introduction of mPEG-SH molecules on the surface of hybrid NPs resulted in the decrease of the absolute zeta potential below -10 mV. This can be attributed to the neutralization of the NPs surface. mPEG-SH is a neutral capping ligand, i.e. has no charged functional groups, and neutralization of the surface charge occurs because the long polymer molecules are blocking the liquid flow towards the surface. Long polymer molecules cause a shift of the fluid slipping plane, as a result, the zeta potential is modified. The further the slipping plane from the particle surface, the smaller the zeta potential [150]. This effect is influenced by both, PEG chain length and the density of PEG molecules on the NPs surface. On the case of Au NPs it was shown that increase in the mPEG-SH chain length (M_w from 2100 to 51000 g/mol) leads to an increase in the hydrodynamic diameter of the Au NPs and, consequently, decrease in the absolute zeta potential to almost zero for the longest polymers [150]. Despite the fact that zeta potential after PEGylation almost approaches zero value, the suspension is stable and transparent without any evidence of agglomeration in the whole investigated pH range. On the contrary, despite the higher absolute zeta potential the suspension of non-modified hybrid NPs is less stable and after a short period of time agglomeration of NPs is visible.

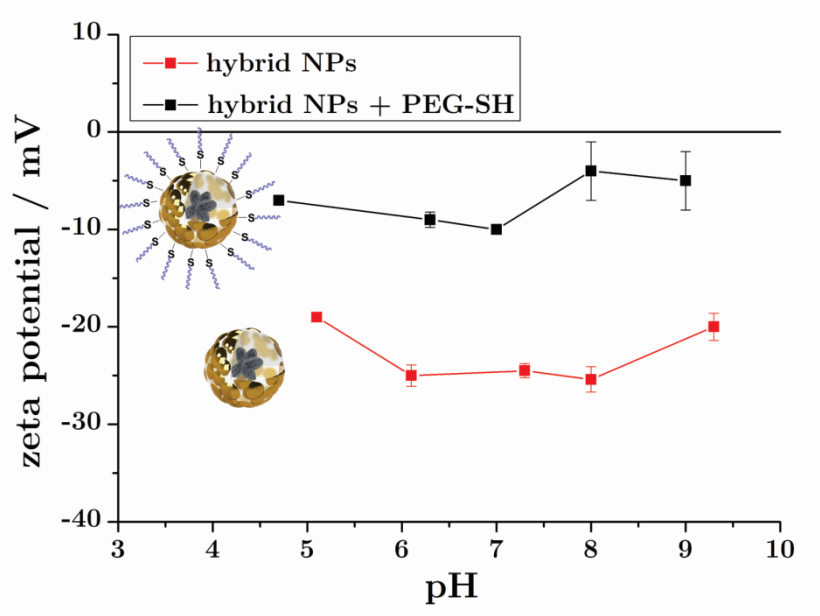


Figure 4.41: Zeta potential measurements of hybrid NPs before and after PEGylation.

4.5.4 Photo-thermal effect studies on hybrid FePt/SiO_2/Au NPs

Water suspension of PEGylated hybrid "multi-core" FePt/SiO_2/Au NPs, with Au shell prepared via two-step Au seeding procedure, was used for the determination of the photo-thermal effect. The experimental set-up that was used to determine the photo-thermal effect in a water suspension containing the hybrid NPs is shown in Figure 3.2. The wavelength of the laser light was fixed at 810 nm. A representative graph of the temperature difference, i.e., the temperature increase, for pure water and the water suspension of hybrid NPs with different concentrations (0.1 – 0.8 mg/mL) is shown in Figure 4.42a. The heating rate can be controlled by varying the power of the laser and/or by increasing the concentration of the photo-thermally active NPs in the water suspension. In the biological tissues a concentration of NPs is limited with the maximum concentration of the NPs that can be internalized in the cells. Laser should not induce heating of the cells that do not contain any NPs; therefore selection of the laser power is of vital importance. Power of the laser was selected in that range that irradiation of pure water gave no heating effect. Samples were irradiated with a laser that has an output power of 0.9 W for approximately 10 minutes. In the case of the pure water the temperature increase was negligible (black curve, Figure 4.42a). In contrast, in the case of suspension of hybrid NPs the temperature increase after 10 minutes of irradiation is significant with the highest heating rate (~ 0.8°C/min) at NPs concentration 0.8 mg/mL. Graph in Figure 4.42 indicates linear increase in the heating with increasing concentration. This observation is in accordance with the Beer-Lambert law, where it is stated, that the absorption is increasing linearly with the increasing concentration. As the consequence of increased absorption also larger heating rate is expected. Indeed, if the concentration of the NPs in the suspensions would continue to increase, at a certain point, heating rate will achieve saturation due to the limitations of the photo-thermal conversion and heat dissipation in the environment. However, we have tested NPs's photo-thermal efficiency only in the concentration range that is relevant for the biological

applications. Selected concentration range (<1 mg/mL) enables slow heating in a controllable manner, but efficient enough to raise the temperature above the hyperthermia level. Hyperthermia is considered as a non-invasive, anti-cancer approach for the selective destruction of abnormal cells in which biological tissues are exposed to temperatures higher than normal body temperature (41–47 °C) [1]. The heat capacity of water (4.2 kJ/kgK) is similar to the heat capacity of human tissue (3.8 kJ/kgK); therefore, it can serve as a good approximation [151]. These results revealed that hybrid NPs that were irradiated with a low energy laser showed high enough temperature increase in a short period of time that makes them promising candidates for the photo-thermal cancer therapy.

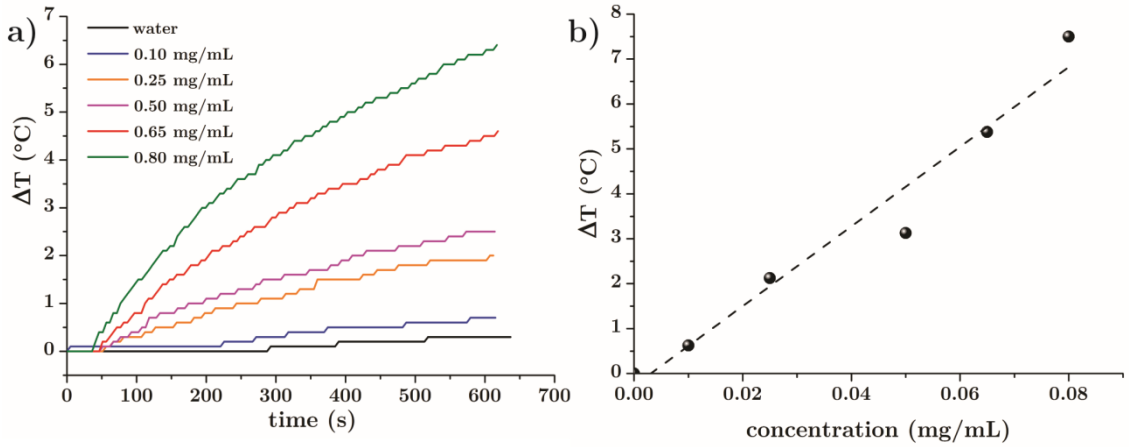


Figure 4.42: a) Graph of the temperature increase for pure water and a water suspension of hybrid NPs with different concentrations (0.1 - 0.8 mg/mL), irradiated by laser light with an output power of 0.9 W for approximately 10 minutes and b) temperature increase normalized with the suspension concentration.

4.5.5 Magnetic extraction studies on hybrid FePt/SiO_2/Au NPs

The magnetic properties of the PEGylated hybrid "multi-core" FePt/SiO_2/Au NPs in a dry form were measured at room temperature (300 K) and are presented in Figure 4.43a. It can be seen that hybrid NPs are in superparamagnetic state, which is a general requirement for nanomedical applications. Magnetization of the hybrid NPs was measured to be $m_{(1.5T)hybrid}$ = 2.4 emu/g, which is 8-times lower in comparison with the initial "multi-core" FePt suspension ($m_{(1.5T)}$ = 19.5 emu/g). This can be attributed to the dilution of the magnetic phase in the sample with the non-magnetic SiO_2 and Au component (the m_s is given by the mass of the sample).

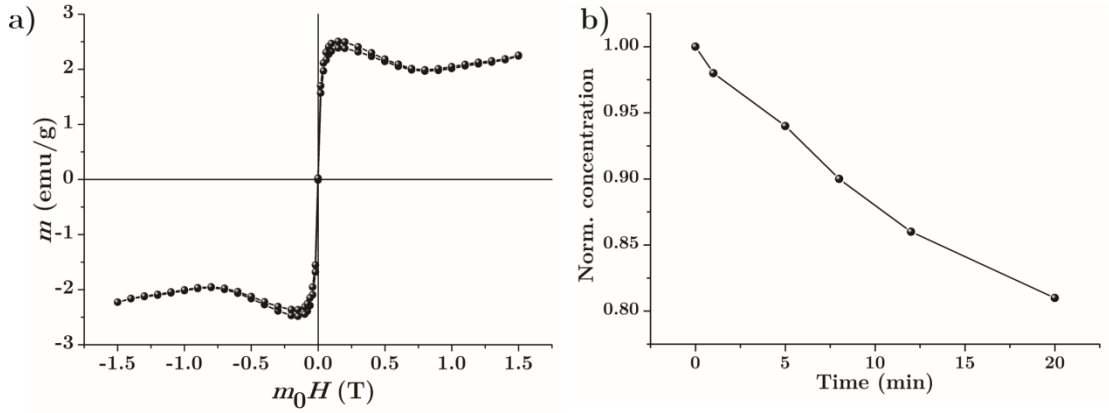


Figure 4.43: a) Magnetic properties of hybrid »multi-core« $FePt/SiO_2/Au$ NPs suspension at 300 K and b) graph indicating the normalized concentration drop of hybrid NPs in the water suspension as a function of time.

In order to test the hybrid NPs in a more realistic situation, an experiment was devised (Figure 3.3) to study their magnetic manipulation in a water-suspension flow using a permanent magnet. For this experiment water suspension of PEGylated hybrid "multi-core" $FePt/SiO_2/Au$ NPs was used with a concentration of 0.5 mg/mL. The blood flow rate in the capillaries of the human body is approximately 0.05 cm/s [152]; however, in our experiment a faster flow rate (0.15 cm/s) was selected in order to show that the NPs could be manipulated in harsh conditions. A commercial Nd–Fe–B permanent magnet ($\mu_0 H$=0.3 T measured right on the top of the magnet) was placed next to the chamber to attract the hybrid NPs during their flow. The resulting graph indicating the normalized concentration drop of the hybrid NPs in the water suspension as a function of time is shown in Figure 4.43b. The obtained results demonstrate that these hybrid NPs can be efficiently extracted from a water suspension using a permanent magnet during a water-suspension flow, reducing the initial NPs concentration in the solution by 19 % in just 20 minutes.

For the successful manipulation of the hybrid NPs (hp) the magnetic force on the magnetic NPs (p) must exceed the fluidic drag force [10]. The hydrodynamic drag force ($\overrightarrow{F_d}$) can be calculated using Stokes' law for drag on a sphere Eq. (1.18). This definition is valid in a laminar flow with a Reynolds number smaller than 1. The minimum magnetic force ($\overrightarrow{F_m}$) needed to manipulate a particle must exceed the hydrodynamic drag force of the NPs under the dynamic flowing conditions. The magnetic force $\overrightarrow{F_m}$ on a small particle due to an external magnetic flux B can be assumed to be equal to the force experienced by a point-like magnetic dipole (Eq.(1.19)). If we equalize both equations for the drag and the magnetic force, the required magnetic field gradient can be calculated. For the present case of hybrid NPs in a water-suspension flow with the parameters: $\eta(H_2O_{\ 25°C}) = 8.9\text{x}10^{-5}\ P_{as}$, $r_{hp} = 20$ nm, $\overrightarrow{\nu_p}= 0$ cm/s, $\overrightarrow{\nu_f}= 0.15$ cm/s, the calculated magnetic field gradient equals 29 T/m, which can be easily achieved with commercially available permanent magnets. We have shown that hybrid NPs can be successfully manipulated in dynamic conditions with external magnetic fields. This fits well with the literature, which reports that for most of the magnetite-based NPs, the magnetic flux densities at the target site must be of the order of 0.2 T, with field gradients of approximately 8 T/m for femoral arteries and greater than 100 T/m for the cartoid arteries [153], which are comparable with our results. Since the magnetic flux decreases exponentially with the distance, it is hard to achieve sufficient magnetic forces for a

controlled manipulation using magnets externally if we want to target internal organs. But there is a possibility that magnetic implants could be located in the vicinity of the target using minimally invasive surgery [74]. Thus, a strong enough local magnetic field can be created to overcome the hydrodynamic forces in the blood stream [75].

Chapter 5

Conclusions

High bulk volume saturation magnetization (M_S) of *fcc* FePt alloy makes this material a very promising candidate for various magnetic applications listed below. However, when in a form of NPs its magnetization (m_s) reduces drastically. After understanding the theoretical aspects, which parameters influence the NP's magnetic properties; we have set down several fabrication paths in order to improve the saturation magnetization of FePt alloy in the nanoparticle form. Having a material with a high saturation magnetization is essential for its efficient performance in applications, such as MRI and magnetic manipulation.

First, we have shown that m_s can be significantly increased by simply increasing the FePt NPs's size. This can be achieved with increasing the surfactants concentration (OLA and OA). However, concentration of OLA and OA cannot be increased infinitely because at a very high surfactant concentrations the free surfactant molecules can cause flocculation of the already surfactant-stabilized NPs, which leads to a NPs agglomeration. With this approach 6 nm large FePt NPs, named "single-core" NPs, with a magnetization of 8 emu/g can be synthesized. The elemental composition determined from the obtained EDXS data of the "single-core" FePt NPs was found to be $Fe_{25\pm1}Pt_{75\pm1}$. Further increase of NPs size up to 10 nm was achieved with the so-called seed-mediated synthesis. FePt NPs prepared in the first step served as the seeds in the second step, where the addition of the metal precursor leads to the increase of the NPs size via heterogeneous nucleation on the already present NPs seeds. The magnetization value after the second step was almost twice as large (14.5 emu/g) as after the first step (8 emu/g), which can be attributed to the larger size of the NPs. Again, size of the NPs cannot be increased infinitely due to the SPL, which was calculated to be approx. 10 nm for *fcc* FePt.

Reports in the literature showed that controlled aggregation of individual superparamagnetic NPs into larger »multi-core« clusters can be beneficially used for the improvement of the magnetic properties. Therefore, we have systematically studied, which experimental conditions would give the optimal »multi-core« FePt NPs with regards to its size and the resulting magnetic properties. We have showed that by changing the ratio and the volume of the added surfactants (OA and OLA) and Fe:Pt salt ratio "multi-core" FePt NPs with saturation magnetization of 19 emu/g can be prepared. By changing the ratio of the added surfactants (OA and OLA) not only morphology but also the elemental composition of the "multi-core" FePt NPs can be varied. The highest amount (54 at.% of Fe) is achieved when no OA was used and, on the contrary, the lowest amount (12 at.% of Fe) at the highest OA addition. Furthermore, the composition of "multi-core" FePt NPs was studied by changing the Fe:Pt salt ratio. With increasing Fe salt addition (Pt:Fe salt ratio 1:1 to 1:2) also the amount of Fe in the samples increases from $Fe_{20}Pt_{80}$ to $Fe_{30}Pt_{70}$, respectively. When Pt:Fe salt ratio = 1:4 was used a non-oxidised FePt alloy phase with a composition $Fe_{35}Pt_{65}$ can be achieved with a higher addition of OA. However, at a higher Pt:Fe salt ratio (1:6 and 1:8) even addition of 4.5 mL of OA is not sufficient to prevent the formation of the Fe oxide phase (Fe_3O_4 cubic inverse spinel structure) due to the large excess of Fe-oleate

complex in the initial reaction mixture. From this study we concluded that the composition of the FePt NPs can be more precisely tuned by changing the OLA:OA ratio, while changes in the Pt:Fe salt ratio do not offer good control over the NPs 'composition and at higher concentration of Fe salt the formation of Fe oxide phase cannot be avoided. Optimal conditions for the preparation of »multi-core« FePt NPs with the highest $m_{(1.5T)}$ (19.5 emu/g) were found to be OLA:OA ratio = 6:2 and Fe:Pt salt ratio = 1:2. The so-prepared sample possesses the elemental composition $Fe_{30\pm1}Pt_{70\pm1}$.

In order to understand the mechanism behind this improvement of the magnetic properties in the case of formation of "multi-core" FePt NPs, room temperature and temperature-dependent magnetic measurements were performed to study the possible magnetic interactions between FePt NPs. The observed enhanced effective magnetic moment in the case of "multi-core" NPs may rule out the dipolar interactions. Upon that and due to the close contact of the cores in the "multi-core" structure and enhancement in the magnetization, we propose the presence of the exchange interactions between the individual cores. These are not uncommon and were already observed in the literature. It has to be pointed out that the samples for the ZFC/FC measurements were in a dry form with the inter-particle distance being reduced, therefore, significant dipole interactions at lower temperature could be expected. If however the magnetic dipolar interactions were significant also at room temperature, they would compromise the superparamagnetic properties and the colloidal stability of the suspension, which was not the case in our study. Comparison between the theoretical calculations and experimentally obtained m_s gave us the direction on how high m_s can be achieved with the preparation of "multi-core" FePt NPs. For example, theoretically calculated m_s for a "single-core" NPs with a size around SPL (10 nm) is 23 emu/g. Therefore, due to the presence of the exchange interactions between the individual cores, combining 10-nm sized cores in a "multi-core" structure would lead to an even further increase in m_s. However, this value is still much lower than the bulk saturation magnetization (75 emu/g) that cannot be obtained in a superparamagnetic regime due to the small size and prevalent surface effects.

In order to obtain biocompatible and stable water suspensions, "single-core" and "multi-core" FePt NPs were functionalized with dopamine-based ligands (zwitterionic dopamine sulphonate or hydrocaffeic acid), or coated with SiO_2 shells of various thicknesses. Homogeneous and heterogeneous nucleation in the SiO_2 coating process was systematically studied to obtain optimal reaction conditions where only SiO_2-coated FePt NPs without core-free SiO_2 NPs were obtained. Whether homogeneous or heterogeneous nucleation occurs it can be regulated with the concentration of added TEOS. Therefore, we have systematically studied the influence of the TEOS concentration on the formation of FePt/SiO_2 NPs and, moreover, C_s and C_{homo} for a given system were determined. It was found that optimal reaction conditions appear at TEOS:NH_3 ratio =1:5. Furthermore, it was shown that tuning of the SiO_2 shell thickness by changing the TEOS concentration offers less control over the coating process than varying the reaction time.

ZDS-functionalized and SiO_2-coated "single core" and FePt "multi-core" NPs have shown promising MRI characteristics, with significant shortening of the transversal relaxation times, i.e., r_2 relaxivities that were equal to 52 $mM^{-1}s^{-1}$ for "single core" FePt and 87 $mM^{-1}s^{-1}$ for "multi-core" FePt NPs, while exhibiting r_2/r_1 ratios above 10, which are ideal for MRI. The nonmagnetic SiO_2 coating "diluted" the magnetic effect of the FePt NPs, resulting in a reduced MRI performance. Taking all of this into account, some fundamental steps towards FePt NPs bio-implementations have been made in our study, especially in the sense of FePt NPs synthesis and m_s improvements, their bio-functionalization and MRI performance, which will positively affect their subsequent in-vitro and in-vivo functioning.

Prior to the hybrid magneto-plasmonically active NPs synthesis their optical responses were theoretically calculated in order to estimate the optimal dimensions with the maximum absorption in the NIR region of the light. Comparison of all simulation results revealed that only few NP's dimensions fit in this optimal range. For the Au shell thicknesses 5, 10 and 15 nm the core-to-shell ratio should be in the range 7 - 15. Those theoretical predictions made on an ideal monodispersed hybrid NPs served as the guidelines for the design of the experiments. However real samples may suffer from imperfection and any degree of polydispersity or agglomeration would influence the optical properties. Therefore, we took into account also the polydispersity of the samples and the performed simulations have shown that this factor has a strong influence not only on the position of the spectra, but also on its shape.

Along those theoretical lines we have demonstrated that by fabricating a magnetic FePt core, embedded in a dielectric SiO_2, and covered with a plasmonically active Au shell, hybrid FePt/SiO_2/Au NPs with combined magnetic and optical properties can be produced. To achieve this, several synthesis steps are needed. First, a positively charged SiO_2 surface has to be obtained, which enables depositing the anionic gold species in the next step. For that purpose the FePt/SiO_2 NPs were functionalized with APTES. In the second step, which is called the "Au seeding", small (1-3 nm) Au NPs are homogeneously attached on the SiO_2 surface. We have shown that the size of Au seeds and coverage of the SiO_2 surface strongly depends on the pH of the gold solution ($HAuCl_4x3H_2O$) and time of the synthesis. Optimal conditions were found to be at pH=7 at 70°C for 5 minutes. However, due to the small size, those Au seeds do not exhibit any significant SPR peak; therefore, a thicker gold layer has to be deposited. In the last step of the synthesis, where gold layer is added on the SiO_2 surface, two different approaches were used. The first approach, gold seeding and sequent reduction of additional gold with a strong reducing agent ($NaBH_4$), resulted in a formation of hybrid NPs with a strong and broad absorption peak in the NIR region. Broad absorption peak was attributed to the polydispersity and agglomeration of the FePt/SiO_2 cores under the common Au shell layer. This was confirmed not only by TEM analysis but also by comparing experimental absorption spectrum with the theoretically predicted ones. In order to overcome this morphological problem and to form thinner Au shell in a more controllable manner, a novel approach, i.e. Au double seeding, was proposed. As-prepared hybrid "multi-core" FePt/SiO_2/Au NPs showed an absorption peak at the edge of the biological window, however, high absorption of the light is measured also within this region. Less broad absorption peak in comparison with the sample prepared via the first synthesis route, i.e. reduction with a strong reducing agent $NaBH_4$, was attributed to the lower polydispersity of the sample and lower degree of agglomeration, which is a prerequisite for further applications.

Biocompatibility and stability of the magneto-plasmonically active hybrid NPs in suspension was achieved with functionalization with mPEG-SH. Water suspension of PEGylated hybrid "multi-core" FePt/SiO_2/Au NPs, with Au shell prepared via two-step Au seeding procedure, was used for the determination of the photo-thermal effect and in the magnetic extraction experiment. Photo-thermal experiments, where laser light of λ=808 nm was used to induce the heating a water suspension of hybrid NPs, showed a very promising photo-thermal effect, i.e., with the highest heating rate (~ 0.8°C/min) at NPs concentration 0.8 mg/mL, which is sufficient to induce photo-thermia. Additionally, the hybrid NPs were successfully retained at the targeted location by using a commercial permanent magnet ($\mu_0 H$= 0.3T). It should be made clear that the dynamic conditions included liquid flow rates of 0.15 cm/s, which exceeds the average velocity of blood in the body by 3 times.

The developed hybrid FePt/SiO_2/Au NPs show great potential for the successful implementation of such multifunctional hybrid inorganic NPs in future nanomedicine applications, since their magnetic properties allow them to be manipulated by an applied external field, while their strong wavelength-specific optical absorption and the expelled heat make them suitable for photo-thermally induced cancer therapies, as shown schematically in Figure 5.1.

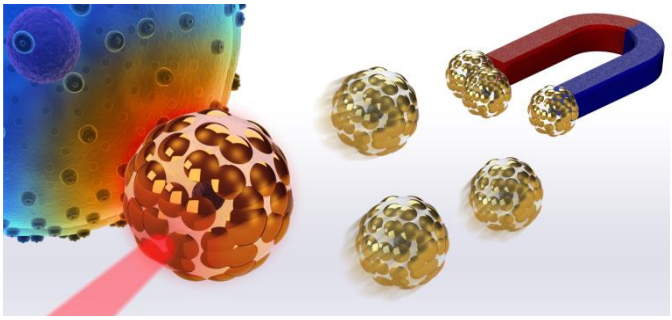


Figure 5.1: Schematic representation of multimodal hybrid FePt/SiO_2/Au NPs′ functionalities for nanomedical applications by combining photothermal stimulation and manipulation with an external magnetic field [154]. Reprinted with permission.

Future perspectives towards using the magneto-optically active hybrid NPs in novel cancer therapies

Work done during my PhD period resulted in fully functional hybrid FePt/SiO_2/Au NPs that are ready to leave "our lab environment" and to be taken onto the next level of experiments, i.e. *in-vitro* cell testing. The first step was done by preparing sterile suspensions of hybrid NPs. For biomaterials sterilization in autoclave is frequently used (at 121°C/30min); however, this approach was found to be destructive for the NP's morphology. Therefore, a nondestructive and efficient method was selected, e.g. sterilization with sterile filters, where besides the sterilization of the NPs suspensions also possible agglomerates are removed.

Along that line the sterilized **PEGylated hybrid NPs** are currently tested on three different cell lines: normal porcine urothelial cells (NPU), low-grade (RT4) and high-grade (T24) cancer urothelial cells. Cell viability together with the internalization mechanism and intracellular fate of NPs was evaluated. Furthermore, NPs were incubated in the presence and absence of the magnetic field (Nd-Fe-B permanent magnet $\mu_0 H$=0.3 T, measured right at the top of the magnet). Preliminary results have shown that the survival of urothelial cells, which were exposed to the hybrid NPs for 2 hours, has been >85 % in the absence as well as presence of the magnetic field. TEM analysis showed (Figure 5.2) hybrid NPs on the apical plasma membrane and in endocytotic structures of urothelial cells. While hybrid NPs were primarily distributed individually or in small clusters (>20 particles) on the apical surface of the urothelial cells, they were also found individually or accumulated in the endosomal compartments of the urothelial cells. High-grade cancer urothelial cells showed higher intensity of endocytosis compared to low-grade cancer and normal urothelial cells, which means that the selectivity between normal and cancerous cells is achieved already in the first stage. The ultrastructure of the cells is normal, confirming non-toxicity of hybrid NPs.

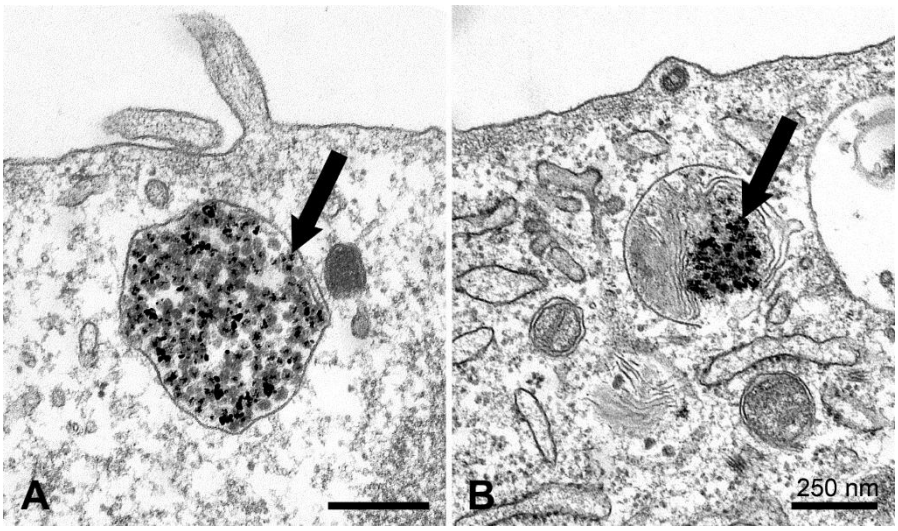


Figure 5.2: Internalization of hybrid NPs into high-grade cancer urothelial cells *in vitro* (A and B). High-grade cancer urothelial cells were grown for 1 week in a growth medium A-DMEM/F12 with additives and incubated with the hNPs for 2 hours in the absence the magnetic field. Arrows indicate hNPs in early endosomes (A) and late endosomes (B) of the cells.

Further, **HCA-functionalized FePt NPs** were tested on low-grade (RT4) cancer urothelial cells. Preliminary results have shown that the survival of urothelial cells, which were exposed to the NPs for 12 hours, has been >93%. Those preliminary results indicate the non-toxicity of HCA-functionalized FePt NPs, which further confirms biocompatibility of such coating. TEM analysis has shown high NPs uptake. Moreover, in order to quantitatively assess the NPs uptake, ICP-MS analysis (content of Fe and Pt) on the suspension of cells was done.

Optimistic preliminary results obtained by *in-vitro* cell testing on HCA-functionalized FePt NPs and PEG functionalized hybrid FePt/SiO_2/Au NPs suspensions gave us an insight in the cell/NPs interaction and about the non-toxicity of our material to the healthy cells and encouraged us to continue in that direction. A more systematic *in-vitro* study on both types of NPs is in progress as we speak.

We have shown that the developed hybrid FePt/SiO_2/Au NPs can produce a significant photo-thermal effect and can be magnetically manipulated in ex-vivo experiments. Therefore, we hypothesize, that similar effects would be pronounced also in in-vitro conditions. For that purpose, cancer cell lines internalized with hybrid NPs will be irradiated with a laser light in the NIR region. Afterwards, the survival rate of the cells will be estimated.

References

[1] J. van der Zee, "Heating the patient: A promising approach?," *Ann. Oncol.*, vol. 13, no. 8, pp. 1173–1184, 2002.

[2] L. a Dykman and N. G. Khlebtsov, "Gold nanoparticles in biology and medicine: recent advances and prospects.," *Acta Naturae*, vol. 3, no. 2, pp. 34–55, 2011.

[3] G. F. Baronzio and E. D. Hager, *Hyperthermia in Cancer Treatment: A Primer*. Boston, MA: Springer US, 2006.

[4] D. L. Miller, N. B. Smith, M. R. Bailey, G. J. Czarnota, K. Hynynen, I. R. S. Makin, and Bioeffects Committee of the American Institute of Ultrasound in Medicine, "Overview of therapeutic ultrasound applications and safety considerations.," *J. Ultrasound Med.*, vol. 31, no. 4, pp. 623–34, Apr. 2012.

[5] T. A. Okhai and C. J. Smith, "Principles and Application of RF System for Hyperthermia Therapy," in *Hyperthermia*, InTech, 2013.

[6] C. L. Brace, "Microwave tissue ablation: biophysics, technology, and applications.," *Crit. Rev. Biomed. Eng.*, vol. 38, no. 1, pp. 65–78, 2010.

[7] A. Hervault and N. T. K. Thanh, "Magnetic nanoparticle-based therapeutic agents for thermo-chemotherapy treatment of cancer.," *Nanoscale*, vol. 6, no. 20, pp. 11553–73, 2014.

[8] M. Bañobre-López, A. Teijeiro, and J. Rivas, "Magnetic nanoparticle-based hyperthermia for cancer treatment.," *Reports Pract. Oncol. Radiother. J. Gt. Cancer Cent. Poznań Polish Soc. Radiat. Oncol.*, vol. 18, no. 6, pp. 397–400, Jan. 2013.

[9] W. J. Atkinson, I. A. Brezovich, and D. P. Chakraborty, "Usable Frequencies in Hyperthermia with Thermal Seeds," *IEEE Trans. Biomed. Eng.*, vol. BME-31, no. 1, pp. 70–75, 1984.

[10] Q. a Pankhurst, J. Connolly, S. K. Jones, and J. Dobson, "Applications of magnetic nanoparticles in biomedicine," *J. Phys. D. Appl. Phys.*, vol. 36, no. 13, pp. R167–R181, 2003.

[11] S. Maenosono and S. Saita, "Theoretical assessment of FePt nanoparticles as heating elements for magnetic hyperthermia," *IEEE Trans. Magn.*, vol. 42, no. 6, pp. 1638–1642, 2006.

[12] G. V Hartland, "Optical studies of dynamics in noble metal nanostructures," *Chem. Rev. (Washington, DC, U. S.)*, vol. 111, no. Copyright (C) 2011 American

Chemical Society (ACS). All Rights Reserved., pp. 3858–3887, 2011.

[13] A. Espinosa, M. Bugnet, G. Radtke, S. Neveu, G. A. Botton, C. Wilhelm, and A. Abou-Hassan, "Can magneto-plasmonic nanohybrids efficiently combine photothermia with magnetic hyperthermia?," *Nanoscale*, vol. 7, no. 45, pp. 18872–18877, 2015.

[14] M. J. Sailor and J.-H. Park, "Hybrid nanoparticles for detection and treatment of cancer.," *Adv. Mater.*, vol. 24, no. 28, pp. 3779–802, Jul. 2012.

[15] L. Li, W. Jiang, K. Luo, H. Song, F. Lan, Y. Wu, and Z. Gu, "Superparamagnetic iron oxide nanoparticles as MRI contrast agents for non-invasive stem cell labeling and tracking," *Theranostics*, vol. 3, no. 8, pp. 595–615, 2013.

[16] S. Laurent, S. Dutz, U. O. Häfeli, and M. Mahmoudi, "Magnetic fluid hyperthermia: focus on superparamagnetic iron oxide nanoparticles.," *Adv. Colloid Interface Sci.*, vol. 166, no. 1–2, pp. 8–23, Aug. 2011.

[17] M. Johannsen, B. Thiesen, P. Wust, and A. Jordan, "Magnetic nanoparticle hyperthermia for prostate cancer," *Int. J. Hyperth.*, vol. 26, no. 8, pp. 790–795, 2010.

[18] S. Chen, L. Wang, S. L. Duce, S. Brown, S. Lee, A. Melzer, S. A. Cuschieri, and P. André, "Engineered biocompatible nanoparticles for in vivo imaging applications," *J. Am. Chem. Soc.*, vol. 132, no. 42, pp. 15022–15029, 2010.

[19] S. Chen and P. Andre, "Colloidal syntheses of FePt nanoparticles," *Int. J. Nanotechnol.*, vol. 9, no. 1/2, p. 39, 2012.

[20] X. Huang, P. K. Jain, I. H. El-Sayed, and M. a. El-Sayed, "Plasmonic photothermal therapy (PPTT) using gold nanoparticles," *Lasers Med. Sci.*, vol. 23, no. 3, pp. 217–228, 2008.

[21] P. K. Jain, K. S. Lee, I. H. El-Sayed, and M. a. El-Sayed, "Calculated absorption and scattering properties of gold nanoparticles of different size, shape, and composition: Applications in biological imaging and biomedicine," *J. Phys. Chem. B*, vol. 110, no. 14, pp. 7238–7248, 2006.

[22] R. Weissleder, "A clearer vision for in vivo imaging Progress continues in the development of smaller , more penetrable probes for biological imaging . Toward the phosphoproteome," *Nat. Biotechnol.*, vol. 19, pp. 316–317, 2001.

[23] A. H. Morrish, "The Magnetic Field," in *The Physical Principles of Magnetism*, John Wiley & Sons, Inc., 2001, pp. 1–30.

[24] N. a Frey and S. Sun, "Magnetic Nanoparticle for Information Storage Applications," *Inorg. Nanoparticles Syntesis, Appl. Perspect.*, no. Richter, pp. 33–68, 2009.

[25] D. Jiles, *Introduction to Magnetism and Magnetic Materials*, vol. 1. 1991.

[26] N. T. K. Thanh, *Magnetic Nanoparticles: From Fabrication to Clinical Applications*. London: CRC Press, Taylor & Francis, 2012.

[27] N. A. Spaldin, *Magnetic Materials*. Cambridge: Cambridge University Press, 2010.

[28] B. D. (Bernard D. Cullity and C. D. (Chad D. . Graham, *Introduction to magnetic materials*. IEEE/Wiley, 2009.

[29] B. Issa, I. M. Obaidat, B. A. Albiss, and Y. Haik, "Magnetic nanoparticles: surface effects and properties related to biomedicine applications.," *Int. J. Mol. Sci.*, vol. 14, no. 11, pp. 21266–305, Jan. 2013.

[30] T. Burkert, O. Eriksson, S. Simak, A. Ruban, B. Sanyal, L. Nordström, and J. Wills, "Magnetic anisotropy of L10 FePt and Fe1−xMnxPt," *Phys. Rev. B*, vol. 71, no. 13, pp. 1–8, 2005.

[31] Y. A. Koksharov, "Magnetism of Nanoparticles: Effects of Size, Shape, and Interactions," in *Magnetic Nanoparticles*, Wiley-VCH Verlag GmbH & Co. KGaA, 2009, pp. 197–254.

[32] F. Bødker, S. Mørup, and S. Linderoth, "Surface effects in metallic iron nanoparticles," *Phys. Rev. Lett.*, vol. 72, no. 2, pp. 282–285, Jan. 1994.

[33] X. W. Wu, C. Liu, L. Li, P. Jones, R. W. Chantrell, and D. Weller, "Nonmagnetic shell in surfactant-coated FePt nanoparticles," in *Journal of Applied Physics*, 2004, vol. 95, no. 11 II, pp. 6810–6812.

[34] Y. Tanaka, S. Saita, and S. Maenosono, "Influence of surface ligands on saturation magnetization of FePt nanoparticles," *Appl. Phys. Lett.*, vol. 92, no. 9, pp. 47–50, 2008.

[35] H. Bin Na, I. C. Song, and T. Hyeon, "Inorganic nanoparticles for MRI contrast agents," *Adv. Mater.*, vol. 21, no. 21, pp. 2133–2148, 2009.

[36] T. Şimşek and Ş. Özcan, "Effective magnetic anisotropy enhancement of FePt nanocrystals through shape control," 2013.

[37] L. Lartigue, P. Hugounenq, D. Alloyeau, S. P. Clarke, M. Lévy, J. C. Bacri, R. Bazzi, D. F. Brougham, C. Wilhelm, and F. Gazeau, "Cooperative organization in iron oxide multi-core nanoparticles potentiates their efficiency as heating mediators and MRI contrast agents," *ACS Nano*, vol. 6, no. 12, pp. 10935–10949, 2012.

[38] S. Mørup, M. F. Hansen, and C. Frandsen, "Magnetic interactions between nanoparticles," pp. 182–190, 2010.

[39] K. Nadeem, H. Krenn, T. Traussnig, R. Würschum, D. V. Szabó, and I. Letofsky-Papst, "Effect of dipolar and exchange interactions on magnetic blocking of maghemite nanoparticles," *J. Magn. Magn. Mater.*, vol. 323, no. 15, pp. 1998–2004, Aug. 2011.

[40] M. S. Seehra, V. Singh, P. Dutta, S. Neeleshwar, Y. Y. Chen, C. L. Chen, S. W. Chou, and C. C. Chen, "Size-dependent magnetic parameters of fcc FePt nanoparticles: applications to magnetic hyperthermia," *J. Phys. D. Appl. Phys.*, vol. 43, no. 14, p. 145002, 2010.

[41] V. Schaller, G. Wahnström, A. Sanz-Velasco, S. Gustafsson, E. Olsson, P. Enoksson, and C. Johansson, "Effective magnetic moment of magnetic multicore nanoparticles," *Phys. Rev. B - Condens. Matter Mater. Phys.*, vol. 80, no. 9, pp.

1–4, 2009.

[42] P. V. Melenev, V. V. Rusakov, and Y. L. Raikher, “Magnetic structure of a spherical cluster of monodomain particles,” *Tech. Phys. Lett.*, vol. 34, no. 3, pp. 248–250, Mar. 2011.

[43] C. B. Rong, N. Poudyal, G. S. Chaubey, V. Nandwana, R. Skomski, Y. Q. Wu, M. J. Kramer, and J. P. Liu, “Structural phase transition and ferromagnetism in monodisperse 3 nm FePt particles,” *J. Appl. Phys.*, vol. 102, no. 4, pp. 3–7, 2007.

[44] P. de la Presa, M. Multigner, M. P. Morales, T. Rueda, E. Fern??ndez-Pinel, and A. Hernando, “Synthesis and characterization of FePt/Au core-shell nanoparticles,” *J. Magn. Magn. Mater.*, vol. 316, no. 2 SPEC. ISS., 2007.

[45] B. Rellinghaus, S. Stappert, M. Acet, and E. F. Wassermann, “Magnetic properties of FePt nanoparticles,” *J. Magn. Magn. Mater.*, vol. 266, no. 1–2, pp. 142–154, 2003.

[46] V. Nandwana, V. Nandwana, K. E. Elkins, K. E. Elkins, N. Poudyal, N. Poudyal, G. S. Chaubey, G. S. Chaubey, K. Yano, K. Yano, J. P. Liu, and J. P. Liu, “Size and Shape Control of Monodisperse FePt Nanoparticles,” *J. Phys. Chem. C*, vol. 111, no. 11, pp. 4185–4189, 2007.

[47] S. Maenosono, T. Suzuki, and S. Saita, “Superparamagnetic FePt nanoparticles as excellent MRI contrast agents,” *J. Magn. Magn. Mater.*, vol. 320, no. 9, pp. 79–83, 2008.

[48] T. Egami and W. L. Johnson, *Elements of Rapid Solidification*, vol. 29. Berlin, Heidelberg: Springer Berlin Heidelberg, 1998.

[49] A. T. Heitsch, D. C. Lee, and B. A. Korgel, “Antiferromagnetic Single Domain L1 2 FePt 3 Nanocrystals,” *J. Phys. Chem. C*, vol. 114, no. 6, pp. 2512–2518, Feb. 2010.

[50] E. E. Carpenter, J. A. Sims, J. A. Wienmann, W. L. Zhou, and C. J. O’Connor, “Magnetic properties of iron and iron platinum alloys synthesized via microemulsion techniques,” *J. Appl. Phys.*, vol. 87, no. 9, p. 5615, 2000.

[51] K. M. Hyie and I. I. Yaacob, “Preparation of iron–platinum nanoparticles in water/triton/cyclohexane microemulsions,” *J. Mater. Process. Technol.*, vol. 191, no. 1, pp. 48–50, 2007.

[52] J. Majeed, F. Syed, O. D. Jayakumar, C. Sudakar, P. S. V. Mocherla, M. S. R. Rao, and A. K. Tyagi, “Direct synthesis of partially ordered tetragonally structured FePt nanoparticles by polyol method for biomedical application,” *Int. J. Nano Dimens.*, vol. 2, no. 0, pp. 61–65, 2011.

[53] S. Sun, “Monodisperse FePt Nanoparticles and Ferromagnetic FePt Nanocrystal Superlattices,” *Science (80-.).*, vol. 287, no. 5460, pp. 1989–1992, 2000.

[54] S. Saita and S. Maenosono, “Formation Mechanism of FePt Nanoparticles Synthesized via Pyrolysis of Iron(III) Ethoxide and Platinum(II) Acetylacetonate,” *Chem. Mater.*, vol. 17, no. 26, pp. 6624–6634, Dec. 2005.

[55] M. Nakaya, M. Kanehara, and T. Teranishi, "One-pot synthesis of large FePt nanoparticles from metal salts and their thermal stability.," *Langmuir*, vol. 22, no. 8, pp. 3485–3487, 2006.

[56] V. Nandwana, K. E. Elkins, and J. P. Liu, "Magnetic hardening in ultrafine FePt nanoparticle assembled films," *Nanotechnology*, vol. 16, no. 12, pp. 2823–2826, 2005.

[57] W. Beck, C. G. S. Souza, T. L. Silva, M. Jafelicci, and L. C. Varanda, "Formation mechanism via a heterocoagulation approach of FePt nanoparticles using the modified polyol process," *J. Phys. Chem. C*, vol. 115, no. 21, pp. 10475–10482, 2011.

[58] E. V Shevchenko, D. V Talapin, H. Schnablegger, P. Svedlindh, M. Haase, H. Weller, and A. Kornowski, "Study of Nucleation and Growth in the Organometallic Synthesis of Magnetic Alloy Nanocrystals : The Role of Nucleation Rate in Size Control of CoPt Nanocrystals Study of Nucleation and Growth in the Organometallic Synthesis of Magnetic Alloy Nanocrystals ," no. 13, pp. 9090–9101, 2003.

[59] H. Zeynali, S. A. Sebt, H. Arabi, and H. Akbari, "Size Control of FePt Nanoparticles Produced by Seed Mediated Growth Process," *J. Clust. Sci.*, vol. 23, no. 4, pp. 1107–1117, 2012.

[60] E. C. Vreeland, J. Watt, G. B. Schober, B. G. Hance, M. J. Austin, A. D. Price, B. D. Fellows, T. C. Monson, N. S. Hudak, L. Maldonado-Camargo, A. C. Bohorquez, C. Rinaldi, and D. L. Huber, "Enhanced Nanoparticle Size Control by Extending LaMer's Mechanism."

[61] C. Wang, Y. Hou, J. Kim, and S. Sun, "A general strategy for synthesizing FePt nanowires and nanorods," *Angew. Chemie - Int. Ed.*, vol. 46, no. 33, pp. 6333–6335, 2007.

[62] S. W. Chou, C. L. Zhu, S. Neeleshwar, G. L. Chen, Y. Y. Chen, and C. C. Chen, "Controlled growth and magnetic property of fept nanostructure: cuboctahedron, octapod, truncated cube, and cube," *Chem. Mater.*, vol. 21, no. 20, pp. 4955–4961, 2009.

[63] L. a. W. Green, T. T. Thuy, D. M. Mott, S. Maenosono, and N. T. Kim Thanh, "Multicore magnetic FePt nanoparticles: controlled formation and properties," *RSC Adv.*, vol. 4, no. 3, p. 1039, 2014.

[64] T. Shin, Y. Choi, S. Kim, and J. Cheon, "Recent advances in magnetic nanoparticle-based multi-modal imaging," *Chem. Soc. Rev.*, vol. 44, pp. 4501–4516, 2015.

[65] C. P. Slichter, *Principles of Magnetic Resonance*, vol. 1. Berlin, Heidelberg: Springer Berlin Heidelberg, 1990.

[66] Nayak, S. Desai, and S. Maheshwari, "Interpretation of magnetic resonance imaging of orbit: Simplified for ophthalmologists (Part I)," *J. Clin. Ophthalmol. Res.*, vol. 1, no. 1, p. 29, 2013.

[67] P. Caravan, J. J. Ellison, T. J. McMurry, and R. B. Lauffer, "Gadolinium(III) Chelates as MRI Contrast Agents: Structure, Dynamics, and Applications.," *Chem. Rev.*, vol. 99, no. 9, pp. 2293–352, Sep. 1999.

[68] G. Huang, H. Li, J. Chen, Z. Zhao, L. Yang, X. Chi, Z. Chen, X. Wang, and J. Gao, "Tunable T1 and T2 contrast abilities of manganese-engineered iron oxide nanoparticles through size control.," *Nanoscale*, vol. 6, no. 17, pp. 10404–12, 2014.

[69] S. Tong, S. Hou, Z. Zheng, J. Zhou, and G. Bao, "Coating optimization of superparamagnetic iron oxide nanoparticles for high T2 relaxivity.," *Nano Lett.*, vol. 10, no. 11, pp. 4607–13, Nov. 2010.

[70] R. N. Muller, P. Gillis, F. Moiny, and A. Roch, "Transverse relaxivity of particulate MRI contrast media: From theories to experiments," *Magn. Reson. Med.*, vol. 22, no. 2, pp. 178–182, Dec. 1991.

[71] S. Balasubramaniam, S. Kayandan, Y.-N. Lin, D. F. Kelly, M. J. House, R. C. Woodward, T. G. St Pierre, J. S. Riffle, and R. M. Davis, "Toward design of magnetic nanoparticle clusters stabilized by biocompatible diblock copolymers for T_2-weighted MRI contrast.," *Langmuir*, vol. 30, no. 6, pp. 1580–7, Feb. 2014.

[72] J.-H. Lee, Y.-W. Jun, S.-I. Yeon, J.-S. Shin, and J. Cheon, "Dual-mode nanoparticle probes for high-performance magnetic resonance and fluorescence imaging of neuroblastoma.," *Angew. Chem. Int. Ed. Engl.*, vol. 45, no. 48, pp. 8160–2, Dec. 2006.

[73] K. E. Scarberry, E. B. Dickerson, Z. J. Zhang, B. B. Benigno, and J. F. McDonald, "Selective removal of ovarian cancer cells from human ascites fluid using magnetic nanoparticles," *Nanomedicine Nanotechnology, Biol. Med.*, vol. 6, no. 3, pp. 399–408, 2010.

[74] R. Fernández-Pacheco, C. Marquina, J. Gabriel Valdivia, M. Gutierrez, M. Soledad Romero, R. Cornudella, A. Laborda, A. Viloria, T. Higuera, A. Garcia, J. A. G. de Jalon, and M. Ricardo Ibarra, "Magnetic nanoparticles for local drug delivery using magnetic implants," *J. Magn. Magn. Mater.*, vol. 311, no. 1 SPEC. ISS., pp. 318–322, 2007.

[75] J. A. Ritter, A. D. Ebner, K. D. Daniel, and K. L. Stewart, "Application of high gradient magnetic separation principles to magnetic drug targeting," *J. Magn. Magn. Mater.*, vol. 280, no. 2–3, pp. 184–201, 2004.

[76] M. Schneider, F. Meder, A. Haiß, L. Treccani, K. Rezwan, and K. Kümmerer, "Physicochemical properties and biodegradability of organically functionalized colloidal silica particles in aqueous environment," *Chemosphere*, vol. 99, pp. 96–101, 2014.

[77] G. Cao and Y. Wang, *Nanostructures and Nanomaterials*. WORLD SCIENTIFIC, 2011.

[78] S. Honary and F. Zahir, "Effect of Zeta Potential on the Properties of Nano-Drug Delivery Systems - A Review (Part 1)," *Trop. J. Pharm. Res.*, vol. 12, no. 2, pp. 255–264, May 2013.

[79] J. Polte, "Fundamental growth principles of colloidal metal nanoparticles – a new perspective," *CrystEngComm*, vol. 17, no. 36, pp. 6809–6830, Sep. 2015.

[80] D. K. Kim, D. Kan, T. Veres, F. Normadin, J. K. Liao, H. H. Kim, S. H. Lee, M. Zahn, and M. Muhammed, "Monodispersed Fe-Pt nanoparticles for biomedical applications," *J. Appl. Phys.*, vol. 97, no. 10, pp. 50–52, 2005.

[81] S. W. Chou, Y. H. Shau, P. C. Wu, Y. S. Yang, D. Bin Shieh, and C. C. Chen, "In vitro and in vivo studies of fept nanoparticles for dual modal CT/MRI molecular imaging," *J. Am. Chem. Soc.*, vol. 132, no. 38, pp. 13270–13278, 2010.

[82] H. Yang, J. Zhang, Q. Tian, H. Hu, Y. Fang, H. Wu, and S. Yang, "One-pot synthesis of amphiphilic superparamagnetic FePt nanoparticles and magnetic resonance imaging in vitro," *J. Magn. Magn. Mater.*, vol. 322, no. 8, pp. 973–977, 2010.

[83] H. G. Bagaria, E. T. Ada, M. Shamsuzzoha, D. E. Nikles, and D. T. Johnson, "Understanding mercapto ligand exchange on the surface of FePt nanoparticles," *Langmuir*, vol. 22, no. 18, pp. 7732–7737, 2006.

[84] T. Togashi, S. Takami, K. Kawakami, H. Yamamoto, T. Naka, K. Sato, K. Abe, and T. Adschiri, "Continuous hydrothermal synthesis of 3,4-dihydroxyhydrocinnamic acid-modified magnetite nanoparticles with stealth-functionality against immunological response," *J. Mater. Chem.*, vol. 22, no. 18, p. 9041, Apr. 2012.

[85] M. Nardini, M. D'Aquino, G. Tomassi, V. Gentili, M. Di Felice, and C. Scaccini, "Inhibition of human low-density lipoprotein oxidation by caffeic acid and other hydroxycinnamic acid derivatives," *Free Radic. Biol. Med.*, vol. 19, no. 5, pp. 541–552, Nov. 1995.

[86] H. Wei, N. Insin, J. Lee, H. S. Han, J. M. Cordero, W. Liu, and M. G. Bawendi, "Compact zwitterion-coated iron oxide nanoparticles for biological applications," *Nano Lett.*, vol. 12, no. 1, pp. 22–25, 2012.

[87] C. Xu, K. Xu, H. Gu, R. Zheng, H. Liu, X. Zhang, Z. Guo, and B. Xu, "Dopamine as a robust anchor to immobilize functional molecules on the iron oxide shell of magnetic nanoparticles," *J. Am. Chem. Soc.*, vol. 126, no. 32, pp. 9938–9939, 2004.

[88] J. C. Y. Kah, N. Phonthammachai, R. C. Y. Wan, J. Song, T. White, S. Mhaisalkar, I. Ahmadb, C. Shepparda, and M. Olivoc, "Synthesis of gold nanoshells based on the depositionprecipitation process," *Gold Bull.*, vol. 41, no. 1, pp. 23–36, 2008.

[89] N. Phonthammachai, J. C. Y. Kah, G. Jun, C. J. R. Sheppard, M. C. Olivo, S. G. Mhaisalkar, and T. J. White, "Synthesis of contiguous silica-gold core-shell structures: Critical parameters and processes," *Langmuir*, vol. 24, no. 9, pp. 5109–5112, 2008.

[90] H. L. Ding, Y. X. Zhang, S. Wang, J. M. Xu, S. C. Xu, and G. H. Li, "Fe 3 O 4 @SiO 2 Core/Shell Nanoparticles: The Silica Coating Regulations with a Single

Core for Different Core Sizes and Shell Thicknesses," *Chem. Mater.*, vol. 24, no. 23, pp. 4572–4580, Dec. 2012.

[91] U. Jeong, X. Teng, Y. Wang, H. Yang, and Y. Xia, "Superparamagnetic Colloids: Controlled Synthesis and Niche Applications," *Adv. Mater.*, vol. 19, no. 1, pp. 33–60, Jan. 2007.

[92] S. Slomkowski, J. V. Alemán, R. G. Gilbert, M. Hess, K. Horie, R. G. Jones, P. Kubisa, I. Meisel, W. Mormann, S. Penczek, and R. F. T. Stepto, "Terminology of polymers and polymerization processes in dispersed systems (IUPAC Recommendations 2011)," *Pure Appl. Chem.*, vol. 83, no. 12, pp. 2229–2259, Jan. 2011.

[93] B. K. Paul and S. P. Moulik, "Uses and applications of microemulsions," *Curr. Sci.*, vol. 80, no. 8, pp. 990–1001, 2001.

[94] K. Osseo-Asare and F. Arriagada, "Growth Kinetics of Nanosize Silica in a Nonionic Water-in-Oil Microemulsion: A Reverse Micellar Pseudophase Reaction Model.," *J. Colloid Interface Sci.*, vol. 218, no. 1, pp. 68–76, 1999.

[95] N. Phonthammachai and T. J. White, "One-step synthesis of highly dispersed gold nanocrystals on silica spheres.," *Langmuir*, vol. 23, no. 23, pp. 11421–11424, 2007.

[96] R. Zanella, A. Sandoval, P. Santiago, V. A. Basiuk, and J. M. Saniger, "New preparation method of gold nanoparticles on SiO2.," *J. Phys. Chem. B*, vol. 110, no. 17, pp. 8559–65, May 2006.

[97] E. F. Vansant, P. Van Der Voort, and K. C. Vrancken, *Characterization and Chemical Modification of the Silica Surface*, vol. 93. 1995.

[98] C.-K. Chang, Y.-J. Chen, and C. Yeh, "Characterizations of alumina-supported gold with temperature-programmed reduction," *Appl. Catal. A Gen.*, vol. 174, no. 1–2, pp. 13–23, Nov. 1998.

[99] L. K. Ono and B. Roldan Cuenya, "Formation and Thermal Stability of Au 2 O 3 on Gold Nanoparticles: Size and Support Effects," *J. Phys. Chem. C*, vol. 112, no. 12, pp. 4676–4686, Mar. 2008.

[100] C. M. Cobley, J. Chen, E. C. Cho, L. V Wang, and Y. Xia, "Gold nanostructures: a class of multifunctional materials for biomedical applications.," *Chem. Soc. Rev.*, vol. 40, no. 1, pp. 44–56, Jan. 2011.

[101] J. Gao, X. Huang, H. Liu, F. Zan, and J. Ren, "Colloidal stability of gold nanoparticles modified with thiol compounds: bioconjugation and application in cancer cell imaging.," *Langmuir*, vol. 28, no. 9, pp. 4464–71, Mar. 2012.

[102] D. T. Thompson, "Using gold nanoparticles for catalysis," *Nano Today*, vol. 2, no. 4, pp. 40–43, 2007.

[103] D. Huang, F. Liao, S. Molesa, D. Redinger, and V. Subramanian, "Plastic-Compatible Low Resistance Printable Gold Nanoparticle Conductors for Flexible Electronics," *J. Electrochem. Soc.*, vol. 150, no. 7, p. G412, 2003.

[104] Y. Tian, X. Shi, C. Lu, X. Wang, and S. Wang, "Charge separation in solid-state

gold nanoparticles-sensitized photovoltaic cell," *Electrochem. commun.*, vol. 11, no. 8, pp. 1603–1605, 2009.

[105] X. Huang and M. a. El-Sayed, "Gold nanoparticles: Optical properties and implementations in cancer diagnosis and photothermal therapy," *J. Adv. Res.*, vol. 1, no. 1, pp. 13–28, 2010.

[106] K. M. Mayer and J. H. Hafner, "Localized surface plasmon resonance sensors.," *Chem. Rev.*, vol. 111, no. 6, pp. 3828–57, Jun. 2011.

[107] G. Mie, "Contributions to the optics of turbid media, particularly of colloidal metal solutions," *Ann. Phys.*, vol. 25, no. 3, pp. 377–445, 1908.

[108] S. Link and M. El-Sayed, "Size and Temperature Dependence of the Plasmon Absorption of Colloidal Gold Nanoparticles," *J. Phys. Chem. B*, vol. 103, no. 21, pp. 4212–4217, 1999.

[109] A. Moores and F. Goettmann, "The plasmon band in noble metal nanoparticles: an introduction to theory and applications," *New J. Chem.*, vol. 30, no. 8, pp. 1121–1132, 2006.

[110] S. Link and M. A. El-Sayed‹, "Shape and size dependence of radiative, non-radiative and photothermal properties of gold nanocrystals," vol. 19, no. 3, pp. 409–453, 2000.

[111] R. Gans, "Über die Form ultramikroskopischer Silberteilchen," *Ann. Phys.*, vol. 352, no. 10, pp. 270–284, 1915.

[112] X. Huang and M. A. El-Sayed, "Gold nanoparticles: Optical properties and implementations in cancer diagnosis and photothermal therapy," *Journal of Advanced Research*, vol. 1, no. 1. pp. 13–28, 2010.

[113] A. L. Aden and M. Kerker, "Scattering of Electromagnetic Waves from Two Concentric Spheres," *J. Appl. Phys.*, vol. 22, no. 10, p. 1242, Apr. 1951.

[114] X. Ji, R. Shao, A. M. Elliott, R. Jason Stafford, E. Esparza-Coss, J. A. Bankson, G. Liang, Z. P. Luo, K. Park, J. T. Markert, and C. Li, "Bifunctional Gold Nanoshells with a Superparamagnetic Iron Oxide-Silica Core Suitable for Both MR Imaging and Photothermal Therapy," *J. Phys. Chem. C*, vol. 111, no. 17, pp. 6245–6251, 2007.

[115] J. Wu, Y. Hou, and S. Gao, "Controlled synthesis and multifunctional properties of FePt-Au heterostructures," *Nano Res.*, vol. 4, no. 9, pp. 836–848, 2011.

[116] K. Yano, V. Nandwana, G. S. Chaubey, N. Poudyal, S. Kang, H. Arami, J. Griffis, and J. P. Liu, "Synthesis and Characterization of Magnetic FePt / Au Core / Shell Nanoparticles," pp. 13088–13091, 2009.

[117] M. Elsabahy and K. L. Wooley, "Design of polymeric nanoparticles for biomedical delivery applications," *Chem. Soc. Rev.*, vol. 41, no. 7, p. 2545, 2012.

[118] O. Peña-Rodríguez and U. Pal, "Enhanced plasmonic behavior of incomplete nanoshells: Effect of local field irregularities on the far-field optical response," *J. Phys. Chem. C*, vol. 115, no. 45, pp. 22271–22275, 2011.

[119] W. Yang, "Improved recursive algorithm for light scattering by a multilayered sphere," *Appl. Opt.*, vol. 42, no. 9, pp. 1710–1720, 2003.

[120] O. P. Rodríguez, "No Title," 2016. .

[121] P. B. Johnson and R. W. Christy, "Optical constants of the noble metals," *Phys. Rev. B*, vol. 6, no. 12, pp. 4370–4379, 1972.

[122] A. Figuerola, A. Fiore, R. Di Corato, A. Falqui, C. Giannini, E. Micotti, A. Lascialfari, M. Corti, R. Cingolani, T. Pellegrino, P. D. Cozzoli, and L. Manna, "One-pot synthesis and characterization of size-controlled bimagnetic FePt-iron oxide heterodimer nanocrystals," *J. Am. Chem. Soc.*, vol. 130, no. 4, pp. 1477–1487, 2008.

[123] Z. R. Dai, S. Sun, and Z. L. Wang, "Phase Transformation, Coalescence, and Twinning of Monodisperse FePt Nanocrystals," *Nano Lett.*, vol. 1, no. 8, pp. 443–447, 2001.

[124] S. Bedanta and W. Kleemann, "Supermagnetism," *J. Phys. D. Appl. Phys.*, vol. 42, no. 1, p. 13001, 2009.

[125] F. Ahrentorp, A. Astalan, J. Blomgren, C. Jonasson, E. Wetterskog, P. Svedlindh, A. Lak, F. Ludwig, L. J. van IJzendoorn, F. Westphal, C. Grüttner, N. Gehrke, S. Gustafsson, E. Olsson, and C. Johansson, "Effective particle magnetic moment of multi-core particles," *J. Magn. Magn. Mater.*, vol. 380, pp. 221–226, 2015.

[126] V. G. Pynko, A. S. Komalov, and L. V. Ivaeva, "Influence of atomic order on magnetic properties of Fe-Pd and Fe-Pt films," *Phys. Status Solidi*, vol. 63, no. 2, pp. K127–K130, Feb. 1981.

[127] Y. Liu, T. Chen, C. Wu, L. Qiu, R. Hu, J. Li, S. Cansiz, L. Zhang, C. Cui, G. Zhu, M. You, T. Zhang, and W. Tan, "Facile Surface Functionalization of Hydrophobic Magnetic Nanoparticles.," *J. Am. Chem. Soc.*, pp. 16–19, 2014.

[128] B. Hirani, J. Li, P. I. Djurovich, M. Yousufuddin, J. Oxgaard, P. Persson, S. R. Wilson, R. Bau, W. A. Goddard, and M. E. Thompson, "Cyclometallated iridium and platinum complexes with noninnocent ligands.," *Inorg. Chem.*, vol. 46, no. 10, pp. 3865–75, May 2007.

[129] N. Shukla, C. Liu, P. M. Jones, and D. Weller, "FTIR study of surfactant bonding to FePt nanoparticles," *J. Magn. Magn. Mater.*, vol. 266, no. 1–2, pp. 178–184, 2003.

[130] T. Rajh, L. X. Chen, K. Lukas, T. Liu, M. C. Thurnauer, and D. M. Tiede, "Surface Restructuring of Nanoparticles: An Efficient Route for Ligand−Metal Oxide Crosstalk," *J. Phys. Chem. B*, vol. 106, no. 41, pp. 10543–10552, Oct. 2002.

[131] B. H. Stuart, "Spectral Analysis," in *Infrared Spectroscopy: Fundamentals and Applications*, John Wiley & Sons, Ltd, 2005, pp. 45–70.

[132] X. Gao, D. W. Metge, C. Ray, R. W. Harvey, and J. Chorover, "Surface Complexation of Carboxylate Adheres Cryptosporidium parvum Öocysts to the Hematite−Water Interface," *Environ. Sci. Technol.*, vol. 43, no. 19, pp. 7423–7429, Oct. 2009.

[133] Y. S. Hwang, J. Liu, J. J. Lenhart, and C. M. Hadad, "Surface complexes of phthalic acid at the hematite/water interface.," *J. Colloid Interface Sci.*, vol. 307, no. 1, pp. 124–34, Mar. 2007.

[134] T. Togashi, T. Naka, S. Asahina, K. Sato, S. Takami, and T. Adschiri, "Surfactant-assisted one-pot synthesis of superparamagnetic magnetite nanoparticle clusters with tunable cluster size and magnetic field sensitivity.," *Dalton Trans.*, vol. 40, no. 5, pp. 1073–8, Feb. 2011.

[135] D. C. Lee, F. V. Mikulec, J. M. Pelaez, B. Koo, and B. A. Korgel, "Synthesis and magnetic properties of silica-coated FePt nanocrystals," *J. Phys. Chem. B*, vol. 110, no. 23, pp. 11160–11166, 2006.

[136] M. Aslam, L. Fu, S. Li, and V. P. Dravid, "Silica encapsulation and magnetic properties of FePt nanoparticles," vol. 290, pp. 444–449, 2005.

[137] R. M. Taylor, D. L. Huber, T. C. Monson, V. Esch, and L. O. Sillerud, "Structural and Magnetic Characterization of Superparamagnetic Iron Platinum Nanoparticle Contrast Agents for Magnetic Resonance Imaging," *J Vac Sci Technol B Nanotechnol Microelectron*, vol. 30, no. 2, pp. 2C101–2C1016, 2012.

[138] S. Liang, Q. Zhou, M. Wang, Y. Zhu, Q. Wu, and X. Yang, "Water-soluble L-cysteine-coated FePt nanoparticles as dual MRI/CT imaging contrast agent for glioma.," *Int. J. Nanomedicine*, vol. 10, pp. 2325–33, Jan. 2015.

[139] K. Tanaka, A. Narita, N. Kitamura, W. Uchiyama, M. Morita, T. Inubushi, and Y. Chujo, "Preparation for highly sensitive MRI contrast agents using core/shell type nanoparticles consisting of multiple SPIO cores with thin silica coating," *Langmuir*, vol. 26, no. 14, pp. 11759–11762, 2010.

[140] H. Chen, J. Yeh, L. Wang, H. Khurshid, N. Peng, A. Y. Wang, and H. Mao, "Preparation and control of the formation of single core and clustered nanoparticles for biomedical applications using a versatile amphiphilic diblock copolymer," *Nano Res.*, vol. 3, no. 12, pp. 852–862, 2010.

[141] J.-F. Berret, N. Schonbeck, F. Gazeau, D. El Kharrat, O. Sandre, A. Vacher, and M. Airiau, "Controlled clustering of superparamagnetic nanoparticles using block copolymers: design of new contrast agents for magnetic resonance imaging.," *J. Am. Chem. Soc.*, vol. 128, no. 5, pp. 1755–1761, 2006.

[142] H. Ai, C. Flask, B. Weinberg, X. Shuai, M. D. Pagel, D. Farrell, J. Duerk, and J. Gao, "Magnetite-loaded polymeric micelles as ultrasensitive magnetic-resonance probes," *Adv. Mater.*, vol. 17, no. 16, pp. 1949–1952, 2005.

[143] P. Tuersun and X. Han, "Optical absorption analysis and optimization of gold nanoshells," *Appl. Opt.*, vol. 52, no. 6, p. 1325, Feb. 2013.

[144] C. Diaz-Egea, W. Sigle, P. A. van Aken, and S. I. Molina, "High spatial resolution mapping of surface plasmon resonance modes in single and aggregated gold nanoparticles assembled on DNA strands.," *Nanoscale Res. Lett.*, vol. 8, no. 1, p. 337, Jan. 2013.

[145] C. J. Stanford, M. Dagenais, J.-H. Park, and P. DeShong, "Real-Time Monitoring

of Siloxane Monolayer Film Formation on Silica Using a Fiber Bragg Grating," *Current Analytical Chemistry*, vol. 4, no. 4. pp. 356–361, 2008.

[146] M. Barisik, S. Atalay, A. Beskok, and S. Qian, "Size Dependent Surface Charge Properties of Silica Nanoparticles," *J. Phys. Chem. C*, vol. 118, no. 4, pp. 1836–1842, 2014.

[147] M. J. Hostetler, J. E. Wingate, C.-J. Zhong, J. E. Harris, R. W. Vachet, M. R. Clark, J. D. Londono, S. J. Green, J. J. Stokes, G. D. Wignall, G. L. Glish, M. D. Porter, N. D. Evans, and R. W. Murray, "Alkanethiolate Gold Cluster Molecules with Core Diameters from 1.5 to 5.2 nm: Core and Monolayer Properties as a Function of Core Size," *Langmuir*, vol. 14, no. 1, pp. 17–30, Jan. 1998.

[148] M. R. Rasch, K. V. Sokolov, and B. a. Korgel, "Limitations on the optical tunability of small diameter gold nanoshells," *Langmuir*, vol. 25, no. 19, pp. 11777–11785, 2009.

[149] J. M. Zook, V. Rastogi, R. I. MacCuspie, A. M. Keene, and J. Fagan, "Measuring Agglomerate Size Distribution and Dependence of Localized Surface Plasmon Resonance Absorbance on Gold Nanoparticle Agglomerate Size Using Analytical Ultracentrifugation," 2011.

[150] K. Rahme, L. Chen, R. G. Hobbs, M. A. Morris, C. O'Driscoll, and J. D. Holmes, "PEGylated gold nanoparticles: polymer quantification as a function of PEG lengths and nanoparticle dimensions," *RSC Adv.*, vol. 3, no. 17, p. 6085, Apr. 2013.

[151] K. Giering, I. Lamprecht, O. Minet, and A. Handke, "Determination of the specific heat capacity of healthy and tumorous human tissue," *Thermochim. Acta*, vol. 251, pp. 199–205, Mar. 1995.

[152] P. K. Ian Power, *Principles of Physiology for the Anaesthetist*, 2nd Ed. Oxford University Press, 2008.

[153] P. A. Voltairas, D. I. Fotiadis, and L. K. Michalis, "Hydrodynamics of magnetic drug targeting," *J. Biomech.*, vol. 35, no. 6, pp. 813–821, Jun. 2002.

[154] N. Kostevšek, K. Žužek Rožman, M. S. Arshad, M. Spreitzer, S. Kobe, and S. Šturm, "Multimodal Hybrid FePt/SiO 2 /Au Nanoparticles for Nanomedical Applications: Combining Photothermal Stimulation and Manipulation With an External Magnetic Field," *J. Phys. Chem. C*, vol. 119, no. 28, pp. 16374–16382, Jul. 2015.

Bibliography

Publications Related to the Thesis

Journal Articles Related to the Thesis

N. Kostevšek, K. Žužek Rožman, M. S. Arshad, M. Spreitzer, S. Kobe and S. Šturm, "Multimodal hybrid FePt/SiO[sub]2/Au nanoparticles for nanomedical applications: combining photothermal stimulation and manipulation with an external magnetic field," *The journal of physical chemistry C*, vol. 119, pp. 16374-16382, 2015.

N. Kostevšek, S. Sturm, I. Serša, A. Sepe, M. Bloemen, T. Verbiest, S. Kobe and K. Žužek Rožman, "Single- and "multi-core" FePt nanoparticles : from controlled synthesis via zwitterionic and silica biofunctionalization to MRI applications," *Journal of nanoparticle research*, vol. 17, pp. 464, 2015.

N. Kostevšek, E. Locatelli, C. Garrovo, F. Arena, I. Monaco, I. Petrov Nikolov, S. Šturm, K. Žuzek Rožman, V. Lorusso, P. Giustetto, P. Bardini, S. Biffi and M. Comes Franchini, "The One-Step Synthesis and Surface Functionalization of Dumbbell-Like Gold-Iron Oxide Nanoparticles. A Chitosan-Based Nanotheranostic System," *Chemical communications*, vol. 52, pp. 378-381, 2016.

Scientific Conference Contribution Abstracts Related to the Thesis

N. Kostevsek, K. Žužek Rožman, S. Šturm and S. Kobe, "Bifunctional FePt/Au nanoparticles with a combined mangeto-photothermal effect" SLONANO 2013, 23-25 October 2013, Ljubljana, Slovenia. *Book of abstracts*. Ljubljana: Jožef Stefan Institute, pp. 71, 2013.

N. Kostevsek, K. Žužek Rožman, S. Šturm and S. Kobe, "Hybrid FePt/Au nanoparticles with a combined magneto-photothermal effect" 21st International Conference on Materials and Technology, 13-15 November 2013, Portorož, Slovenia. *Programme and book of abstracts*. Ljubljana: Inštitut za kovinske materiale in tehnologije, pp. 105, 2013.

N. Kostevsek, K. Žužek Rožman, S. Šturm and S. Kobe, "Hybrid FePt/Au nanoparticles with a combined magneto-photothermal effect" 1st International Symposium on Nanoparticles/Nanomaterials and Applications, 20-22 January 2014, Caparica, Portugal. Proceedings of the ISN_2A, pp. 114, 2014.

N. Kostevsek, K. Žužek Rožman, S. Kobe and S. Šturm, "Magnetically and optically active FePt/SiO2/Au hybrid nanoparticles for photothermal therapy", Gordon Research Conference: Noble Metal Nanoparticles: synthesis, characterization, modeling, and applications, June 15-20, 2014, South Gadley, MA, USA, 2014.

S. Šturm, N. Kostevsek, K. Žužek Rožman and S. Kobe, "Stimuli responsive hybrid nanomaterials with a combined magneto-photothermal effect for nanomedical applications" 16th Annual Conference YUCOMAT 2014, Herceg Novi, Montenegro, September 1-5, 2014, *Programme and the book of abstracts.* Belgrade: Materials Research Society of Serbia, pp. 102, 2014.

N. Kostevšek, S. Sturm, I. Serša, A. Sepe, M. Bloemen, T. Verbiest, S. Kobe and K. Žužek Rožman, "Hydrophilic silica- and zwitterionic catechol-coated single-core and multi-core FePt nanoparticles" 5th International Colloids Conference, Amsterdam, 21-24 June 2015, Amsterdam, The Netherlands. *Programme and the book of abstracts,* 2015.

N. Kostevšek, S. Sturm, I. Serša, A. Sepe, M. Spreitzer, S. Kobe and K. Žužek Rožman, "Single-core and multi-core FePt nanoparticles as MRI contrast agents" 23rd International Conference on Materials and Technology, 28-30 September 2015, Portorož, Slovenia. *Programme and book of abstracts*, Inštitut za kovinske materiale in tehnologije, Ljubljana, pp. 140, 2015.

S. Šturm, N. Kostevsek, K. Žužek Rožman and S. Kobe, Nanotech Tunisia 2015 : International Nanotechnology Conference, "Multimodal FePt/SiO2/Au nanoparticles with a combined magneto-photothermal effect for nanomedical applications" Nanotech Tunisia 2015 : International Nanotechnology Conference, 22-24 April 2015, Hannamet, Tunisia. *Programme and book of abstracts,* 2015.

N. Kostevsek, "Synthesis of hybrid FePt/SiO[sub]2/Au nanoparticles", Small Simposium "Bio-responsive magneto-optically coupled nanomaterial-based systems for innovative skin cancer treatments", 6th November 2015, Ljubljana.

N. Kostevšek, S. Sturm, I. Serša, A. Sepe, M. Spreitzer, S. Kobe and K. Žužek Rožman, "Multimodal hybrid FePt/SiO_2/Au nanoparticles for nanomedical applications : new synthesis approach for imrpoved magnetic and optical properties" 2nd International Symposium on Nanoparticles/Nanomaterials and Applications, 18th-21st January 2016, Carapica, Portugal, *ISN2A 2016 proceedings book*, pp. 146, 2016.

K. Žužek Rožman, N. Kostevšek, S. Šturm, M. S. Arshad, M. Spreitzer, S. Kobe, T. Višnjar and M. Erdani-Kreft, "Multimodal FePt/SiO_2/Au nanoparticles-based cancer theranostic system enabling MRI, magnetic manipulation and thermal stimulation" MMM Intermag 2016 joint Conference, January 11-15, 2016, San Diego, California, *Book of abstracts*, American Institute of Physics, pp. 851, 2016.

N. Kostevšek, S. Šturm, I. Serša, A. Sepe, M. Spreitzer, S. Kobe and K. Žužek Rožman, "Hybrid FePt/SiO_2/Au nanoparticles for nanomedical applications" 13th

International Conference on Nanosciences & Nanotechnologies, NN16, 5-8 July 2016, Thessaloniki, Greece, *Book of abstracts*, pp. 242, 2016.

Other Publications

Journal Articles

N. Kostevšek, K. Žužek Rožman, D. Pečko, B. Pihlar and S. Kobe, "A comparative study of the electrochemical deposition kinetics of iron-palladium alloys on a flat electrode and in a porous alumina template," *Electrochimica Acta*, vol. 125, pp. 320-329, 2014.

D. Pečko, K. Žužek Rožman, N. Kostevšek, M. S. Arshad, B. Markoli, Z. Samardžija and S. Kobe, "Electrodeposited hard-magnetic Fe50Pd50 nanowires from an ammonium-citrate-based bath," *Journal of alloys and compounds*, vol. 605, pp. 71-79, 2014.

D. Pečko, N. Kostevšek, B. Pihlar, Z. Samardžija, S. Kobe and K. Žužek Rožman, "Electrochemical studies of Fe and Pd deposition and their influence on the co-deposition of the Fe-Pd alloy", *Journal of electroanalytical chemistry*, vol. 738, pp. 51-60, 2015.

Conference Paper

N. Kostevšek, K. Žužek Rožman, D. Pečko, B. Pihlar and S. Kobe, "Controlling the composition of electrodeposited Fe-Pd nanowires and thin films via determination of the diffusion and electrode kinetic parameters," in *Procedings of the 7th Jožef Stefan International Postgraduate School Students' Conference, part 2,* pp. 207-217, Ljubljana, Slovenia, 2015.

Scientific Conference Contribution Abstracts

N. Kostevšek, K. Žužek Rožman, B. Pihlar and S. Kobe, "Electrochemical study of deposition of nanowires based on Fe[sub](70)Pd[sub](30) system for medical purposes" SLONANO 2012, 24-26 October 2012, Ljubljana, Slovenia. *Book of abstracts*. Ljubljana: Institut Jožef Stefan, pp. 76, 2012.

N. Kostevšek, K. Žužek Rožman, B. Pihlar and S. Kobe, "Electrochemical study and comparison of kinetics of iron-palladium alloy electrodeposition at flat electrode and porous alumina template" EDNANO 9, 9th International Workshop on Electrodeposited Nanostructures, 8-10th November 2012, Porto, Portugal. *Book of abstracts.* Pp. 60, 2012.

K. Žužek Rožman, D. Pečko, N. Kostevšek, S. Šturm, U. Maver, P. Nadrah, M. Bele and S. Kobe, "Fe-Pd-based nanotubes for drug-delivery applications" 4th International Congress Nanotechnology, Medicine & Biology, 13-15 March 2013, Krems, Austria. *Congress documentation.* Krems: Donau Universität, 2013.

N. Kostevšek, K. Žužek Rožman, B. Pihlar and S. Kobe, "Electrochemical study and deposition of Fe[sub](70)Pd[sub](30) nanowires"7th Young Researchers' Day, 19 February, 2013, Ljubljana, Slovenia. *Programme and abstract book*. Ljubljana: Institut Jožef Stefan, pp. 38, 2013.

N. Kostevšek, K. Žužek Rožman, B. Pihlar, M. Bele, M. Zorko and S. Kobe, Synthesis of silica-coated Fe[sub] (70)Pd[sub](30) nanowires for medical applications. 4th International Congress Nanotechnology, Medicine & Biology, 13-15 March 2013, Krems, Austria. *Congress documentation*. Krems: Donau Universität, 2013.

K. Žužek Rožman, D. Pečko, N. Kostevšek, U. Maver, P. Nadrah, M. Zorko, M. Bele and S. Kobe, "Electroplated ferromagnetic nanostructures for different applications" Fourth Regional Symposium on Electrochemistry, South-East Europe - RSE-SEE, Ljubljana, Slovenia, 26-30 May, 2013. *Programme and book of abstracts*. Ljubljana: National Institute of Chemistry: Centre of Excellence for Low-Carbon Technologies: Jožef Stefan Institute, pp.78, 2013.

D. Pečko, K. Žužek Rožman, N. Kostevšek and S. Kobe, "Electrodeposited hard magnetic Fe[sub](50)Pd[sub](50) nanowires synthesised from the ammonium citrate based bath" 21st International Conference on Materials and Technology, 13-15 November 2013, Portorož, Slovenia. *Programme and book of abstracts*. Ljubljana: Inštitut za kovinske materiale in tehnologije, pp. 144, 2013.

D. Pečko, K. Žužek Rožman, N. Kostevšek and S. Kobe, "Electrodeposition of Fe[sub](50) Pd[sub](50) nanowires and their characterization" 10th International Workshop on Electrodeposited Nanostructures, ED NANO, 20-22 March, 2014, Oberwesel am Rhein, Germany. *Abstract book*, pp. 7, 2014.

K. Žužek Rožman, Š. Trafela, D. Pečko, M. S. Arshad, N. Kostevšek, S. Šturm and S. Kobe, "Tailoring the magnetization distribution in ferromagnetic nanowires and nanotubes for (bio) applications" Nanotech Tunisia 2015 : International Nanotechnology Conference, 22-24 April 2015, Hannamet, Tunisia. *Programme and book of abstracts,* 2015.

K. Žužek Rožman, N. Kostevšek, Š. Trafela, D. Pečko and S. Kobe, "Multifunctional nanodevices for detection, elimination and killing of pathogens from living enviroments" Workshop Smart cities and communities as a development opportunity for Slovenia, *Proceedings of the 18th International Multiconference Information Society - IS 2015, October 12th, 2015, Ljubljana, Slovenia,* Institut Jožef Stefan, vol. H. pp. 38-39, 2015.

B. Ambrožič, N. Kostevšek, M. Bele and S. Šturm, "First dynamic study of yttrium-based nanoparticles formation at the nanoscale by using transmission electron microscopy combined with the liquid cell" *10th Young researchers' day, 31 March, 2016, Ljubljana, Programme and abstract book*. Ljubljana: Institut Jožef Stefan, pp. 13, 2016.